annual report 1981

nuclear physics laboratory
university of washington

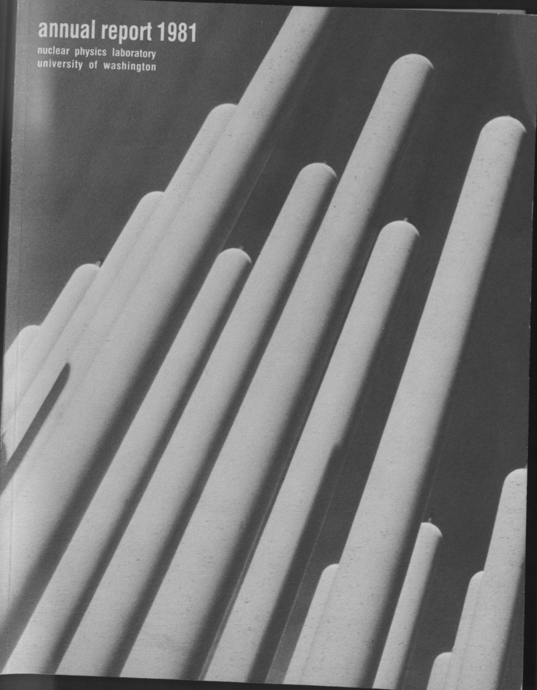

ANNUAL REPORT

Nuclear Physics Laboratory
University of Washington
June, 1981

Supported in part by the United States Department of Energy under contract DE-AC06-76ER01388

INTRODUCTION

This Annual Report covers the period from April 1980 to April 1981 and includes all work done in the Nuclear Physics Laboratory and research performed at other institutions by our staff. The majority of these projects are supported by our Department of Energy contract, but experiments and therapy performed by the Medical School and problems of applied physics pursued by investigators from the College of Engineering and by outside users are also included.

We continue to maintain a strong laboratory-based research program while at the same time we work to achieve an upgrading of our accelerator energy capability. We first proposed such an upgrading nearly 4 years ago. We were pleased last year to have achieved top priority (along with Yale University) from NSAC for funding in FY 82 of our proposal to DOE for an 18 MV folded tandem accelerator. Our pleasure at being included in the outgoing administration's budget recommendation in late 1980 for accelerator "startup" money in FY 82 turned to dismay in early 1981 when our project was omitted from the new administration's budget recommendation. We believe that a new accelerator in our Laboratory is in the national interest, and we will continue to strive to obtain the means necessary to achieve this goal.

Our Laboratory has thrived this past year under the directorship of Prof. Robert Vandenbosch. Our new magnetic momentum filter project is well underway. Optics design was completed a year ago, and the dipole and quadrupole magnets were delivered several months ago. Design of the vacuum system, scattering chamber and support structure is completed and construction is underway. A number of technical improvements to the tandem accelerator and beam handling are underway or completed, including improvements to the tandem generating voltmeter, and computer control of the high energy beam transport.

Our new PDP-11/60 (on-line) and VAX 11/780 (off-line) computer system is working well; particularly noteworthy is our multiparameter coincidence capability using a version of the program "Multi" which has been improved locally. DOE has approved funding of a new high-intensity polarized ion source in FY 82. The qualitative improvement in polarized beam intensities that will be available from this source will have a big impact on our light-ion research.

Our diversified research program remains centered on the use of our FN tandem accelerator and injector, and includes a significant amount of research by some of us at outside institutions and at our Laboratory on the hydrogen parity mixing experiment. Some of the highlights of our research in the past year are given below.

The nucleosynthesis of ^{26}Al is currently a topic of great interest in nuclear astrophysics. While cross sections have been measured for the major ^{26}Al production mechanism, the ^{25}Mg(p,γ) reaction, cross sections for the ^{26}Al destruction reactions have not been measured due to the lack of an ^{26}Al target. However, information on the ^{26}Al(n,p) and ^{26}Al(n,α) destruction reactions can be deduced from measurements of the $^{26}Mg(p,n)$ and $^{23}Na(\alpha,n)$ reactions along with the principle of detailed balance. During the past year we have measured the cross sections for the (p,n) and (α,n) reactions using a large neutron detector array and we have calculated the corresponding cross sections for the astrophysically interesting (n,p) and (n,α) reactions.

Recently we have helped to place the interpretation of parity mixing in light nuclei on a firmer, experimental foundation. Haxton, Gibson and Henley and Brown, Richter and Godwin have previously analyzed the results of our parity mixing experiments in ^{18}F, ^{19}F, and ^{21}Ne. Both groups assumed a parity nonconserving (PNC) nucleon-nucleon (NN) force given by Desplangues, Donoghue, and Holstein and used large-basis shell model calculations to compute the PNC matrix elements. These calculated results had to be reduced by roughly a factor of 3 to agree with the data. This raised the question of whether the discrepancy was due to a shortcoming in the assumed PNC NN force or was it due to inadequacies in the shell model wavefunctions? We have shown that the shell model wavefunctions are deficient by measuring first forbidden β^+ transitions in the decays of ^{18}Ne and ^{19}Ne. These transitions are isospin analogs of the parity mixing in ^{18}F and ^{19}F. In both cases our measured β-decay rates are roughly a factor of 10 smaller than calculations using the wavefunctions employed in the parity mixing calculations. This strongly suggests that the above mentioned factor of 3 is due to deficiencies in the shell model analysis and not in the assumed PNC NN force.

Hardware for the new Mark II hydrogen parity—violation experiment has been completed. This equipment includes a precision two-RF-cavity assembly, a hydraulic system for remote positioning of the cavities inside the vacuum vessel, an RF source for the double cavity assembly with two coherent outputs and both digital and analog control of the relative phase, an NMR stabilizer for the static magnetic field, a precision tape-wound aluminum solenoid, a high-gain phase-space stabilizer for the metastable beam, and a precision voltage source for generating static fields in the RF cavities. These various units have been installed and tested, and the expected $\alpha \rightarrow e \rightarrow \beta$ resonant transitions have been generated. Studies have now begun on the nature of systematic errors encountered with the new apparatus at a level several orders of magnitude smaller than the Mark I system.

We have measured $^{27}Al(^3He,d)$ and $^{27}Al(p,\gamma)$ to the stretched 6^-, T=0 and T=1 states at 11.58 and 14.36 MeV in ^{28}Si, which have strong parentage to the $(d_{5/2}^{-1}, f_{7/2})$ particle-hole configuration. From an analysis of our experiments and other results, we find $a^2 \approx 0.5$ for the $(d_{5/2}^{-1}, f_{7/2})$ intensity in both levels (relative to the ^{28}Si ground state). This indicates that (p,p') and (π,π') reactions excite the 6^-, T=0 state anomalously weakly relative to the 6^-, T=1 state.

A good-resolution study of the $^{24}Mg(\alpha,\gamma_0)^{28}Si$ reaction in the giant resonance region has been completed, with detailed information on E2 strength in good agreement in magnitude and energy dependence with $^{28}Si(\alpha,\alpha'\alpha_0)$ results. This confirms the inelastic scattering extraction of E2 strength, and provides interesting information on the phase coherence of the giant E1 and E2 resonances.

We have begun studies of "second-harmonic" giant dipole resonances, built on highly excited states, with measurements of the $^{27}Al(p,\gamma)$ and $^{27}Al(p,\gamma p)$ reactions. Our singles results near the bombarding energy expected for the peak of the second-harmonic giant resonance provide the first clear evidence that the capture process preferentially populates $1\hbar\omega$ particle-hole final states. This supports the general concept of the existence of second-harmonic giant resonances.

A search for "quasi-molecular" gamma rays in the $^{12}C + {}^{12}C$ system, i.e., enhanced gamma ray emission from a presumed intermediate-lifetime dinuclear state with a large quadrupole moment, has resulted in an upper limit which is smaller than the simplest estimate from a quasi-molecular model. The sensitivity achieved was not sufficient to see the gamma emission rate predicted by Blair and Sherif on the basis of a direct reaction model. The fusion cross section excitation function for the $^{12}C + {}^{28}Si$ system has been measured by two techniques. The excitation function is rather smooth and does not show evidence of structure correlated with structure observed in the back-angle elastic and inelastic channels. The absolute values of the cross sections are appreciably larger than reported previously and are in good agreement with current theoretical expectations.

We have completed a study of the $^{16}O + {}^{16}O$ system in which Time-Dependent-Hartree-Fock calculations predict the presence of non-fusion for the smallest partial waves. We find no experimental evidence for this prediction. Several other systems have been studied to date with negative results. These results provide a constraint that TDHF will have to satisfy if it is to be a successful model for reaction mechanisms in the energy range of 2-10 MeV/A.

Our studies of reactions induced by very heavy projectiles, employing the LBL SuperHILAC, have addressed the questions of fluctuations in deeply inelastic collisions, and the role of nucleon exchange in energy dissipation and angular momentum transfer. On the question of the magnitude of the fluctuations in the dependence of the scattering angle, energy loss and angular momentum transfer on initial orbital angular momentum, we have shown from gamma ray angular correlation measurements for a wide range of scattering angles that there are strong correlations between the scattering angle and the initial orbital angular momentum. A Monte Carlo approach is being used to explore various correlations arising from a nucleon exchange model for energy dissipation and angular momentum transfer. Spin-spin and N-Z correlations are being explored. We have also shown from evaporation model calculations that correlations are expected in the final observables such as the isobaric charge variances which arise from post-reaction evaporative mechanisms as well as from the deeply inelastic collision itself.

As in the past we welcome applications from scientists at other institutions who may wish to use our facilities. At present outside users are active on both the tandem and the cyclotron. Our tandem runs very well, with experiments performed from 0.5 to 9 MV. Other salient characteristics of these machines are listed on a following page. Anyone interested in using the facilities should consult with a potential collaborator from the University of Washington or Dr. William G. Weitkamp, Technical Director, Nuclear Physics Laboratory, GL-10, University of Washington, Seattle, WA 98195 or telephone (206) 543-4080.

Let me remind the reader that the articles in this report describe work in progress and are not to be regarded as publications nor quoted without permission of the investigators. The names of the investigators on each article have been listed alphabetically but where appropriate the name of the person primarily responsible for the report has been underlined.

I would like to thank Bill Weitkamp for editorial assistance. My special thanks go to Ms. Judith Nyman-Schaaf for her excellent typing and managerial skills.

Kurt A Snover

Kurt A. Snover
Editor, 1981 Annual Report

THREE STAGE TANDEM VAN DE GRAAFF ACCELERATOR

(A High Voltage Engineering Corp. Model FN)

Completed: 1967
Funding: Purchased with NSF funds; maintained by DOE funds and some funds from the State of Washington.

Beams currently available: (See also W.G. Weitkamp and F.H. Schmidt, "The University of Washington Three Stage Van de Graaff Accelerator" Nucl. Inst. and Meth. 122, 65 (1974).

Ion	Max. Current 2 Stage (μA)	Max. Practical Energy 2 Stage (MeV)	Max. Current 3 Stage (μA)	Max. Practical Energy 3 Stage (MeV)
p,d	20	18	5	25
polarized p,d	0.1	18		
^{3,4}He	3	27		
^{6,7}Li	0.5	36		
C	2	63	1	70
N	2	72	1	79
O	10	81	3	88
Si	0.2	90		
Cl	0.2	117	0.2	124
Ni	0.5	117		
Br	0.1	125		
Ag	0.01	125		

CYCLOTRON

(A 60-inch fixed energy machine)

Completed: 1952
Funding: Constructed primarily with State funds and subsequently supported by AEC funds. Now sustained by funds from outside users.

Beams currently available:

Ion	Maximum Current (μA)	Maximum Practical Energy (MeV)
p	100	11
d	150	22
^{4}He	30	42

TABLE OF CONTENTS

1. ASTROPHYSICS AND COSMOLOGY

1.1 The Nucleosynthesis of ^{26}Al

T. Chupp, P. Grant, K. Lesko, E. Norman, and P. Schwalbach

We have continued our investigations of the nucleosynthesis of ^{26}Al. Our interest in this nucleus stems from the recent discovery in inclusions from the Allende meteorite of excess isotopic abundances of ^{26}Mg relative to ^{24}Mg. We have studied mechanisms by which ^{26}Al may be destroyed as well as produced. We have studied two reactions, ^{26}Mg(p,n)^{26}Al and ^{23}Na(α,n)^{26}Al, which populate both the ground state ($J=5^+$, $t_{1/2}=7.2 \times 10^5$ years) and the isomeric level at 228 keV ($J=0^+$, $t_{1/2}=6.3$ seconds).

In last year's Annual Report[1] we described measurements of the gamma ray production cross sections for the ^{26}Mg(p,n)^{26}Al reaction. The data from our measurements of gamma ray cascades to both the 0^+ and 5^+ states were combined with previously published data of direct neutron emission to the ground state to obtain the total ground state cross sections.[2] Using these results and the principle of detailed balance, we have calculated cross sections for the (n,p_0) reaction on the three lowest-lying states in ^{26}Al. These calculations, illustrated in Fig. 1.1-1 show the importance of the excited states in the destruction of this nucleus. The (n,p) reaction will populate excited states as well as the ground state of ^{26}Mg. However, to measure the cross sections for these reac-

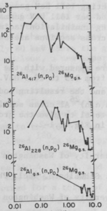

Fig. 1.1-1: Cross sections for the (n,p_o) reaction on the ^{26}Al ground state, 228 keV isomeric level and the 417 keV 3^+ level. Cross sections for these reactions have been calculated using measured (p,n) cross sections and the principle of detailed balance.

tions, the difficult problem of producing a ^{26}Al target must be overcome.

To gain further information on the low energy behavior of the ^{26}Al(n,p)^{26}Mg reaction, we have also begun measurements of the total ^{26}Mg(p,n)^{26}Al cross sections. These measurements are performed with the large graphite pile "long counter" described elsewhere.[3]

Our program of investigation of the ^{23}Na(α,n)^{26}Al reaction includes three different experiments which measure (a) gamma ray production cross sections, (b) isomer production cross sections, and (c) total neutron production cross sections. The gamma ray experiment independently determines the lower limit of ground state and isomer production while the total neutron and isomer production data are combined to determine the ground state and isomer cross sections.

The gamma rays from alpha particle bombardment of a 730 μgm/cm^2 NaF target were observed in a 50 cm^3 coaxial Ge(Li) detector. Angular distributions were measured at 10 angles between 30° and 145° relative to the beam in order to correct the 90° measurements for anisotropy in gamma ray emission. Production was measured at 36 energies from threshold at E=3.97 MeV up to 26 MeV.

The isomer production cross sections were determined with an activation technique. In this measurement, the NaF target was activated for 20 seconds and then counted in place with a pair of 3 in. × 3 in. NaI detectors at 90° and 270°. Gamma ray spectra were routed into 8 successive time bins. The 511 keV gamma rays from the annihilation of the positrons emitted in the ^{26}Al decay were counted in coincidence. The efficiency for detecting the annihilation radiation was determined in a separate activation by producing ^{25}Al, which decays to the 1611 keV state of ^{25}Mg. By measuring the efficiency for detecting 1611 keV gamma rays and by measuring the number of 511 keV gamma rays detected per 1611 keV gamma ray, we determined the efficiency to be 0.011 for detecting annihilation radiation. Data were taken from E=4 MeV up to E=15 MeV. These cross sections are shown in Fig. 1.1-2.

The total neutron production cross sections were measured with the large graphite pile with NaI and PbI_2 targets at energies from 3.5 to 10.5 MeV. The iodine contribution to the NaI yield was subtracted and the resulting sodium yield was differentiated to determine the total ^{23}Na(α,n)^{26}Al cross section. The isomer cross sections were then subtracted from the total to give the ground state cross sections. These results are also shown in Fig. 1.1-2.

References:
1. Nuclear Physics Laboratory Annual Report, University of Washington (1980), p. 1.
2. E. B. Norman, K. T. Lesko, T. E. Chupp, and P. Schwalbach, Nucl. Phys. A357, 228 (1981).
3. Nuclear Physics Laboratory Annual Report, University of Washington (1979), p. 131.

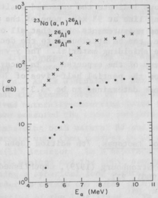

Fig. 1.1-2: Cross sections for the production of $^{26}Al^{g,m}$ from the $^{23}Na(\alpha,n)$ reaction.

1.2 The Half-Life of ^{180}Ta

E. B. Norman

^{180}Ta is an interesting naturally occurring odd-odd nucleus. It is known to have a half-life of $>2\times10^{13}$ years and an abundance relative to that of ^{181}Ta of 1.2×10^{-4}.[1] In addition to this long-lived state, there is a $J_1^\pi = 1^+$ level which β^- and electron-capture decays with a half-life of 8.1 hours. Recently, it has been shown that this short-lived state is actually the ground state of the nucleus and that the long-lived level is an excited state approximately 80 keV above the ground state.[2,3] As a result of the renewed interest in this nucleus, a new experiment was performed in an attempt to determine the half-life of the long-lived ^{180}Ta.

The long-lived ^{180}Ta state is unstable with respect to both electron-capture and β^- decay with decay energies of 935 and 799 keV respectively.[3] Thus, this 9^- level would be expected to decay to the 6^+ state at 641 keV in ^{180}Hf and/or to the $(6)^+$ level in ^{180}W at 688 keV. The electron capture decay of the long-lived ^{180}Ta would produce a cascade of γ-rays with energies of 332.3, 215.3, and 93.3 keV.[1] The β^- decay would produce a similar cascade with γ-rays of energies 350.4, 234.3, and 103.6 keV.[1] In the present work a γ-ray singles experiment was performed for a total of 14 days and a γ-γ coincidence experiment was performed for a total of 11 days to search for these γ-rays. For these experiments, a 30.5 mg sample of Ta_2O_5 enriched to 5.1% in ^{180}Ta was acquired on loan from Oak Ridge National Laboratory.

The low energy portion of the γ-ray spectrum observed during 4.5 days of singles counting is shown in Fig. 1.2-1. Arrows indicate the expected positions of the ^{180}Ta decay γ-rays. Except for a strong line at 93 keV, none of the expected ^{180}Ta decay γ-rays are seen. Background measurements show that all of γ-ray peaks observed including the 93 keV line, can be attributed to the decay of U and Th isotopes probably contained in the shielding material. The γ-γ coincidence spectra also showed no evidence of any of the expected ^{180}Ta decay γ-rays. From these null results, lower limits on the partial half-lives of ^{180}Ta against electron capture and β^- decay have been determined to be $\geq 3.3 \times 10^{14}$ years and $\geq 2.9 \times 10^{14}$ years respectively.

References:

1. C. M. Lederer and V. S. Shirley, Table of Isotopes, 7th edition (John Wiley + Sons, New York, 1978), p. 1130.
2. E. Warde, Thesis, Univ. Louis Pasteur de Strasbourg (1979), unpublished.
3. K. S. Sharma, et al., Phys. Lett. 91B (1980), 211.

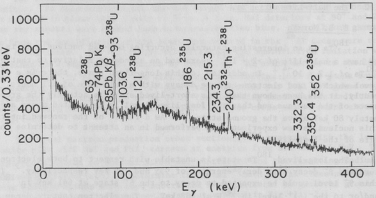

Fig. 1.2-1: Low energy portion of the γ-ray spectrum observed in 4.5 days of singles counting of the ^{180}Ta sample. Arrows indicate the expected positions of the ^{180}Ta decay γ-rays.

1.3 Yields of $^{180}Ta^{g,m}$ From the $^{180}Hf(p,n)$ Reaction

P. J. Grant[+], E. B. Norman, and T. R. Renner[*]

As was discussed in last year's Annual Report,[1] we have conducted a series of measurements of the cross sections for the production of $^{180}Ta^{g,m}$ from the $^{180}Hf(p,n)$ reaction over the energy range $6.5 \leq E_p \leq 10.0$ MeV. This reaction has been suggested as one of the possible astrophysical production mechanisms for ^{180}Ta. As is discussed in Sec. 1.2 of this report, it has been recently shown that the ground state of ^{180}Ta is the $J^{\pi} = 1^+$ 8.1 hour level and that the long-lived naturally-occurring level is an excited state at approximately 80 keV. We have measured the cross sections for the production of the 8.1 hour state by bombarding both natural Hf and enriched ^{180}Hf targets with a proton beam. The targets were then removed to an off-line location and were counted using a Ge(Li) detector. In a separate experiment, a thick ^{180}Hf target was bombarded with protons and the total neutron yield from the (p,n) reaction was measured using a spherical long-counter.[2] The thick-target yield is differentiated in order to obtain the total (p,n) cross sections. The cross sections for the production of the long lived $^{180}Ta^m$ were determined by subtracting the $^{180}Ta^g$ cross sections from the total (p,n) cross sections. Fig. 1.3-1 shows our preliminary results for the total ^{180}Hf (p,n) cross sections and the cross sections for the short-lived ^{180}Ta ground state.

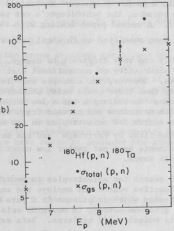

Fig. 1.3-1: Circles represent total $^{180}Hf(p,n)$ cross sections. X's represent cross sections for the production of the short-lived ^{180}Ta ground state.

References:

+ Present Address: The Boeing Company, Seattle, Washington.
* Department of Physics, State University of New York, Stony Brook.
1. Nuclear Physics Laboratory Annual Report, University of Washington (1980), p. 3.
2. Nuclear Physics Laboratory Annual Report, University of Washington (1979), p. 131.

1.4 Investigations of Wheeler-Feynman Absorber Theory

J. G. Cramer

Over the past several years, we have embarked upon a program aimed at testing and generalizing the ideas of Wheeler-Feynman absorber theory.[1,2] The Wheeler-Feynman approach to electrodynamics is to regard the emission and subsequent absorption of electromagnetic radiation as a "transaction" between emitter and absorber through the medium of advanced and retarded electromagnetic waves. The theory has important implications for the origins of the electromagnetic time asymmetry, i.e., the complete dominance of retarded potentials and radiation in electromagnetic processes, and also possible implications for cosmology.

We have shown in a recent paper[3] that a generalized form of the Wheeler-Feynman transaction can be used to explain a number of quantum mechanical paradoxes, e.g., the Einstein-Podolsky-Rosen paradox, the Schrödinger's cat paradox, Wheeler's delayed choice experiments, etc. A second paper dealing with the electromagnetic time asymmetry[4] has just been submitted to Physical Review D.

Experimental tests of absorber theory are very difficult to design, because the Wheeler-Feynman protocol is an alternative to conventional electrodynamics which leads to the same observables. However, the concepts embodied in absorber theory do lead to the possibility that there could exist anisotropies in the emission of radiation, particularly when the radiation has a low probability of ultimate absorption, as is the case with neutrinos and certain frequencies of radio waves. Two experiments involving a search for anisotropies in the emission of radio waves have been performed, the first by Partridge[5] and the second by Schmidt and Newman.[6] Both of these experiments have set rather low upper limits on possible emission anisotropies for radio waves.

We have designed two experiments to search for anisotropies in neutrino emission. The first of these uses a radioactive source and employs the angular correlation between neutrino and beta emission which is present in a pure Gamow-Teller beta decay. In such a process, a given anisotropy in neutrino emission should be reflected in an isotropy in beta emission 1/9 as large. Beta asymmetry measurements with a ^{109}Ru source are made in a search for sidereal correlations associated with the Earth's rotation with respect to the fixed stars. These measurements are presently troubled by 24-hour instrumental effects at the level of 1 part in 10^4. A stabilized light-pulser system is now being installed in the apparatus to remove this effect (see Sec. 11.2 of this report) and a new set of measurements will be made in the next few months.

This beta decay experiment is complicated by the rather weak angular correlation between beta and neutrino directions arising from the 3-body nature of the decay process. We have, in collaboration with groups at LAMPF and the University of Texas, designed a second absorber-theory experiment which involves the 2-body emission of mu-neutrinos and therefore is not troubled by this problem. This is accomplished by observing the direction of muons produced in the decay of a well-collimated pion beam. We are presently seeking approval for this experiment at a meson facility.

References:

1. J. A. Wheeler and R. P. Feynman, Rev. Mod. Phys. 17, 157 (1945).
2. J. A. Wheeler and R. P. Feynman, Rev. Mod. Phys. 21, 425 (1949).
3. J. G. Cramer, Phys. Rev. D22, 362 (1980).
4. J. G. Cramer, submitted to Phys. Rev. D.
5. R. B. Partridge, Nature 244, 263 (1973).
6. J. Schmidt and R. Newman, Bull. Am. Phys. Soc. 25, 581 (1980).

1.5 Cross Sections Relevant to Gamma Ray Astronomy

D. Bodansky, P. Dyer, D. Leach, E. B. Norman, and A. G. Seamster

As described in previous Annual Reports, we have measured gamma-ray production cross sections for proton and alpha-particle induced reactions on ^{12}C, ^{14}N, ^{16}O, ^{20}Ne, ^{24}Mg, ^{28}Si, and ^{56}Fe. These cross sections are required in order to interpret potential astronomical gamma-ray spectra in terms of the abundances and energies of the interacting nuclei. The analysis of the proton data has been completed, and a paper based on this work has been accepted for publication.[1] During the past year we have concentrated on the analysis of the alpha-particle data. Extractions of the yields of the prominent lines seen in the alpha-particle bombardments are currently in progress. As an outgrowth of this analysis, we have recently measured the gamma-ray production cross sections for alphas on ^{27}Al.

Reference:

1. P. Dyer, D. Bodansky, A. G. Seamster, E. B. Norman, and D. R. Maxson, Phys. Rev. C (in press).

2. NUCLEAR TESTS OF FUNDAMENTAL SYMMETRIES

2.1 Test of Time Reversal Invariance with P-A Comparisons in the $^{9}Be(^{3}He,\vec{p})^{11}B$ Reaction

J. G. Cramer, M. Doss, D. W. Storm, T. A. Trainor, and W. G. Weitkamp

At the 5th International Symposium on Polarization Phenomena in Nuclear Physics (Santa Fe)[1] this past summer, the results of a collaboration between groups at Laval University and LBL were presented, showing very large difference between the proton polarization (P) measured in the reactions $^{9}Be(^{3}He,\vec{p})^{11}B_{gs}$ and $^{7}Li(^{3}He,\vec{p})^{9}Bs_{gs}$ and the proton analyzing power (A) as measured in the inverse reactions. This result is very difficult to understand, because time-reversal invariance as embodied in the principle of detailed balance would require that P=A in such reactions. A violation of time reversal invariance of the magnitude reported by the Laval/LBL group is orders of magnitude larger than that which could be reconciled with existing theories or with the CP violation observed in the decay of the K_2° meson. Therefore, followup experiments are very important to determine whether the results should be taken seriously.

The P measurements are quite a bit more difficult and subject to error than are the A measurements because the former involve double-scattering measurements of nuclear reactions with fairly small cross sections (about 100 mb/sr). Further, the Laval/LBL measurements were performed with a polarimeter employing a silicon analyzer/detector, and the proton analyzing power of silicon is rather small and has a rather strong energy dependence. Therefore, we decided to attempt to reproduce these measurements of P in the ^{3}He + ^{9}Be system using a helium polarimeter designed by Prof. Weitkamp, which has been in use at this Laboratory for some time in depolarization measurements in the continuum.

It was first necessary to modify the polarimeter for improved energy resolution to permit resolution of the ground state of the ^{11}B residual nucleus from its first excited state. This was accomplished by modifying the two dE/dx gas counters in each polarimeter arm so that they would serve as position sensitive drift chambers, permitting a determination of the horizontal entrance angle of the reaction-produced protons which was used for correction of the detected proton energy and improved resolution. This modification is described in Sec. 11.9 of this report. This system has worked very well, permitting an improvement in energy resolution by a factor of 2-3 and permitting the resolution of the two states of ^{11}B.

The results of the two accelerator runs on the ^{9}Be + ^{3}He system have been inconclusive, the first because of excessive neutron background in the polarimeter counter nearest the beam and the second because of a malfunction in the PDP 11/60 data collection computer on the last day of the run. We expect to have another run in the near future and to determine whether the polarization value agrees with that determined by the Laval/LBL group.

References:

1. H. E. Conzett, Polarization Phenomena in Nuclear Physics-1980, G.G. Ohlsen, et al., eds., American Institute of Physics, New York (1981), p. 1422.

2.2 $0^+ \to 0^-$ β^+ Decay of ^{18}Ne and the Interpretation of the Parity Mixing in ^{18}F

E. G. Adelberger, C. D. Hoyle, H. E. Swanson, and R. D. Von Lintig

It has been recognized for several years that pion exchange should play a large and calculable role in A_o, the time component of the nuclear axial current.[1,2] The effects will be especially large in $0^+ \to 0^-$ β decays where the one-body (impulse) contributions to A_o are suppressed, being proportional to $\sigma \cdot v/c$ and $\sigma \cdot rk$. Both v (the nucleon velocity) and k (the momentum transferred to the leptons) are small in β decay. On the other hand the π exchange contribution to A_o is not similarly suppressed since the π carries off the same quantum numbers (ΔJ^π; $\Delta I = 0^-$; 1) that A_o brings in. Unfortunately, very little is known experimentally about $0^+ \rightleftarrows 0^-$ β decay. The β decay[3] of $^{16}N^m$ is the only example in a light, well understood nucleus.

We have measured the decay rate of ^{18}Ne ($J^\pi = 0^+$, I = 1) to the 1081 keV ($J^\pi = 0^-$, I = 0) level of ^{18}F. This decay is particularly interesting because:

(A) It is one of the rare cases of a $0^+ \to 0^-$ transition in a theoretically tractable nuclear system. Shell model wave functions (see Ref. 4) predict that pion exchange currents increase the β decay rate by a factor of approximately 2.5 compared to the impulse current alone.

(B) To the extent that exchange currents are important, knowledge of this β^+ decay rate removes most of the nuclear structure uncertainties in extracting F_π, the weak parity nonconserving (PNC) πNN vertex.

The $\pi\pm$ exchange component of the PNC NN force is pure $\Delta I = 1$. The most sensitive probe of this force is our measurement[5] of the parity mixing of the 1042 keV ($J^\pi = 0^+$, I = 1) and 1081 keV levels of ^{18}F. The $0^+ \to 0^-$ decay of ^{18}Ne connects these same levels (assuming isospin symmetry). Moreover the π exchange contribution to the β^+ decay rate and the π exchange contribution to the parity mixing have identical dependence on the nuclear coordinates.[4,6] The $0^+ \to 0^-$ $\beta^\pm$ decay exchange current operator is

$$M^{(2)}_{\beta\pm} = \mp i \left(\frac{m_\pi}{M_N}\right)^2 \frac{g^2}{4\pi} \frac{1}{2F_A} \frac{1}{2} \sum_{i \neq j} [\tau_i \otimes \tau_j]_{1\pm1} (\vec{\sigma}_i + \vec{\sigma}_j) \cdot \vec{r}_{ij} \phi_\pi(r_{ij}),$$

while the $\pi^\pm$ exchange parity mixing operator is

$$H_{PNC} = iF_\pi \left(\frac{m_\pi^2}{M_N}\right) \frac{1}{\pi\sqrt{2}} \frac{1}{2} \sum_{i \neq j} [\tau_i \otimes \tau_j]_{10} (\vec{\sigma}_i + \vec{\sigma}_j) \cdot \vec{r}_{ij} \phi_\pi(r_{ij})$$

(See Ref. 4). In these expressions

$$\phi_\pi(r_{ij}) = \frac{e^{-m_\pi r_{ij}}}{m_\pi r_{ij}} \left(1 + \frac{1}{m_\pi r_{ij}}\right),$$

g is the strong πNN coupling constant and $F_A = -1.23$.

F_π (the strength of the PNC π exchange NN interaction) is poorly determined by existing data and analyses. The measured[5] circular polarization of the 1081 keV γ-ray $P_\gamma = (-0.7 \pm 2.0) \times 10^{-3}$ yields a value $|\langle 0^-|H_{PNC}|0^+\rangle| =$ (.13 ± .36) eV. $|F_\pi|$ has been inferred from this measured matrix element by relying on shell-model calculations of the nuclear wavefunctions. However, the extent that $\alpha \equiv M_\beta^{(2)}/M_\beta^{(1)}$ (the ratio of the 2 body to the 1 body β-decay matrix elements) is known, $|F_\pi|$ can be obtained from P_γ and the β decay rate ω in a way which is otherwise completely independent of the nuclear wave functions - i.e., $F_\pi = K[(\alpha+1)/\alpha]P_\gamma\sqrt{\omega}$ where K is a constant containing kinematic factors and known quantities such as F_A and g. We return to this point below.

We produced ^{18}Ne activity by bombarding natural O_2 gas with 12 MeV ^{3}He ions. The irradiated gas was transferred from the bombardment cell to a lucite chamber placed in a heavily shielded counting station. Beta delayed γ-rays were counted for 1.70 sec. beginning 0.10 sec. after each bombardment ended. γ-rays were detected in Ge(Li) detectors equipped with pileup rejection circuitry. The γ-ray spectrum was "hardened" by 1.27 cm thick Pb absorbers placed in front of the detector. The gas transfer system, which operated on a 2.00 sec. cycle, is similar to those described in Refs. 6 and 7 and is described in Sec. 11.14. Contaminant activities, principally ^{18}F, ^{17}F, and ^{15}O produced by the ^{16}O(^{3}He,p), ^{16}O(^{3}He,d) and ^{16}O(^{3}He,α) reactions respectively, were largely removed by three liquid N_2 traps, one of which was filled with a molecular sieve material. By multiscaling the γ-rays we determined that the dominant background activity was ^{18}F produced by ^{18}Ne decays within the counting chamber. In addition, a small amount of ^{15}O was transmitted through the traps.

A composite spectrum of γ-rays taken with two different detectors is shown in Fig. 2.2-1. Previously observed γ-rays of 511, 659, 1042, and 1700 keV are prominent. Low intensity peaks (see Fig. 2.2-2, also), present in data taken with each detector separately, are observed at (1080.6 ± 0.3) keV, 1357 keV, and 1461 keV. Sliding pulser spectra ruled out any possibility that the 1081 keV peak was due to differential nonlinearity in the ADC. We ascribe the 1357 keV peak to decays of ^{19}O produced in the ^{18}O(^{3}He, 2p) reaction. In a subsidiary measurement with the gas transfer system operating on an 80 sec. cycle, we determined that the 1357 keV peak had a decay half-life of approximately 26 sec. in good agreement with the ^{19}O value of 26.8 sec. The 1461 keV peak arises from ^{40}K room background. We conclude that the 1081 keV peak is from ^{18}Ne decay since its measured energy is in excellent agreement with the accepted value of 1080.5 ± 0.1 keV for the corresponding ^{18}F transition.

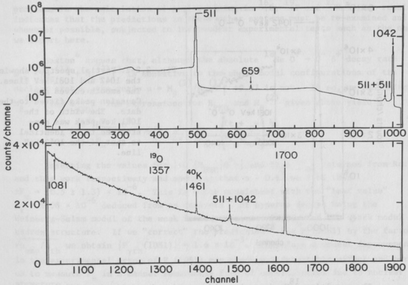

Fig. 2.2-1: Spectrum of γ-rays following ^{18}Ne β^+ decays. This is a sum of data taken with two different detectors in order to improve statistics.

The relative efficiencies of our Ge(Li) detectors plus "hardeners" were measured using known decays[9] of ^{56}Co and ^{207}Bi sources. Relative intensities of the 659, 1042, 1081 and 1700 keV γ-rays are 1.75 ± 0.05, 100.0, $(1.92 \pm 0.32) \times 10^{-2}$ and 0.680 ± 0.011 respectively. These intensities (except for the previously unobserved 1081 keV γ-ray) are in good agreement with the lower-statistics results of Refs. 8 and 10. In addition our value for $R = \Gamma(1700 \rightarrow g.s)/\Gamma(1700 \rightarrow all) = 0.280 \pm 0.007$ is in good agreement with the value R = 0.298 ± 0.013 presented in Ref. 11. The weak 1081 keV γ-ray cannot be due to deexcitation of the 1700 keV level via the 1081 keV level since[11] $\Gamma(1700 \rightarrow 1080)/\Gamma(1700 \rightarrow all) < 2 \times 10^{-3}$. Therefore β^+ feeding of the 1700 keV level can account for at most 546 of the observed 2156 ± 355 counts in the 1081 keV peak. We assume that 273 ± 273 of the 2156 counts arise from decays of the 1700 keV level and ascribe the remaining 1883 ± 488 counts to direct feeding of the 1081 keV level in ^{18}Ne decay.

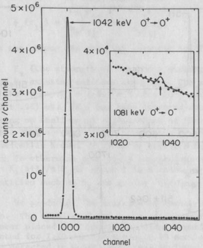

Fig. 2.2-2: Partial spectrum showing the 1042 and 1081 keV lines. The smooth curves are Gaussian peaks fitted to the data. The width of the 1081 keV peak was constrained to be identical to that of the 1042 keV line.

The resulting ^{18}Ne decay branching ratios (normalized to 100 for the superallowed transition to the 1042 keV level) are 100.0, $(1.71 \pm 0.41) \times 10^{-2}$ and 2.47 ± 0.05 for transitions to the 1041, 1081, and 1700 keV levels respectively. Assuming that the superallowed Fermi transition has a partial half-life of 22.00 ± 0.61 sec. and an ft value of 2977 ± 87 sec.[7] we obtain a partial half-life of $(1.29 \pm 0.31) \times 10^5$ sec. and ft = $(1.60 \pm 0.39) \times 10^7$ sec. for the $0^+ \rightarrow 0^-$ transition. We have computed f assuming an allowed β spectrum shape, which is reasonable since the matrix elements of the π exchange and the $\sigma \cdot v/c$ one body currents are both independent of the momentum transferred to the leptons. In what follows we neglect all terms (they are small) which are momentum transfer dependent. For a more complete discussion including the k dependence see Ref. 4.

Now turn to some implications of our result. Haxton[4] has calculated the β^+ decay rate expected using the wavefunctions employed in a recent analysis[12] of the PNC circular polarization in ^{18}F. His predicted rate, $\omega_{th} = 7.5 \times 10^{-5}$ sec^{-1}, is appreciably faster than our measured value, $\omega_{exp} = (5.4 \pm 1.3) \times 10^{-6}$ sec^{-1}. Similar disagreement would occur with other calculations[12] of the parity mixing in ^{18}F. Reasons for this deficiency are given in Ref. 4, along with a more realistic shell model calculation, $\omega_{th} = 4.8 \times 10^{-6}$ sec^{-1}, which is in much better agreement with experiment. To what extent should one expect similar problems in the calculation of parity mixing in ^{16}O, ^{19}F and ^{21}Ne? Our result indicates that the predictions in these other systems must be re-examined and, whenever possible, subjected to independent experimental tests such as the one we report here.

Haxton[4] argues that, although the absolute $^{18}Ne\ 0^+ \rightarrow 0^-\ \beta^+$ decay rate $\omega_{th} \propto |M_\beta^{(1)} + M_\beta^{(2)}|^2$ is sensitive to the shell-model configurations of the nuclear states, the ratio $\alpha = M_\beta^{(2)}/M_\beta^{(1)} \simeq +0.67$ is not. If so, we can deduce $M_\beta^{(2)}$ from ω_{exp}. The expressions for H_{PNC} and $M_\beta^{(2)}$ given above yield

$$F_\pi = \frac{\langle 0^-|H_{PNC}|0^+\rangle}{M_N} \left(\frac{\alpha+1}{\alpha}\right) \frac{g^2}{4\pi} \frac{\pi}{2F_A} \left(\frac{ft_{0^+\rightarrow 0^-}}{ft_{0^+\rightarrow 0^+}}\right)^{1/2} .$$

Inserting the values for $|\langle 0^-|H_{PNC}|0^+\rangle|$ and $ft_{0^+\rightarrow 0^-}$ obtained from Ref. 5 and this work respectively and assuming that $\alpha \simeq 0.67$ we find that $\pm F_\pi = (0.5 \pm 1.3) \times 10^{-6}$. This is quite consistent with the "best value" $F_\pi = 1.08 \times 10^{-6}$ deduced from an analysis[14] of hyperon decays using the Weinberg-Salam model of the weak interaction, and SU(6) and the quark model of hadron structure. If we "correct" the prediction[12] for $P_\gamma(1081)$ by the factor $\sqrt{\omega_{exp}/\omega_{th}}$ we obtain $|P_{\gamma th}(1081)| = 1.6 \times 10^{-3}$. Therefore a modest improvement in the experimental error of $P_\gamma(1081)$ may produce a detectable effect and permit us to measure F_π in a manner remarkably free of uncertainties due to nuclear structure.

We thank C. L. Bennett and M. M. Lowry for pointing out the similarity between H_{PNC} and $M_\beta^{(2)}$. We are grateful to W. C. Haxton for discussions of the physics and for his calculations of the decay rate.

<u>References:</u>

1. K. Kubodera, J. Delorme, and M. Rho, Phys. Rev. Lett. <u>40</u>, 755 (1978).
2. P. A. M. Guichon, M. Giffon, and C. Samour, Phys. Lett. <u>74B</u>, 15 (1978).
3. L. Palffy, J. P. Deutsch, L. Grenacs, J. Lehmann, and M. Steels, Phys. Rev. Lett. <u>34</u>, 212 (1975).
4. W. C. Haxton, Phys. Rev. Lett. <u>46</u>, 698 (1981). The F_π used in our paper and Refs. 4 and 12 is related to the f_π of Refs. 5 and 13 by $F_\pi = gf_\pi/(4\sqrt{2})$.
5. C. A. Barnes, M. M. Lowry, J. M. Davidson, R. E. Marrs, F. B. Morinigo, B. Chang, E. G. Adelberger, and H. E. Swanson, Phys. Rev. Lett. <u>40</u>, 840 (1978).
6. M. M. Lowry, C. L. Bennett, and K. Krien, Bull. Am. Phys. Soc. <u>25</u>, 486 (1980).
7. J. E. Esterl, R. G. Sextro, J. C. Hardy, G. J. Ehrhardt, and J. Cerny, Nucl. Inst. Meth. <u>97</u>, 229 (1971).
8. J. C. Hardy, H. Schmeing, J. S. Geiger, and R. L. Graham, Nucl. Phys. <u>A246</u>, 61 (1975).

9. Y. Yoshizawa, et al., Nucl. Inst. Meth. 174, 109 (1980).
10. S. Gorodetzky, E. Aslanides, A. Gallman and G. Friek, Nucl. Phys. A109, 417 (1968).
11. C. Rolfs, H. P. Trautvetter, R. E. Azuma, and A. E. Litherland, Nucl. Phys. A199, 289 (1973).
12. W. C. Haxton, B. F. Gibson, and E. M. Henley, Phys. Rev. Lett. 45, 1677 (1980).
13. M. Gari, J. B. McGrory, and R. Offerman, Phys. Lett. 55B, 277 (1975), and B. A. Brown, W. A. Richter, and N. S. Godwin, Phys. Rev. Lett. 45, 1681 (1980).
14. B. Desplanques, J. F. Donoghue, and B. R. Holstein, Ann. Phys. 124, 499 (1980).

2.3 $1/2^+ \rightarrow 1/2^-$ Beta Decay of ^{19}Ne and the Interpretation of the Parity Mixing in ^{19}F

E. G. Adelberger, M. M. Hindi, C. D. Hoyle, H. E. Swanson, and R. D. Von Lintig

Recently Desplanques, Donoghue and Holstein[1] have related the PNC emission of mesons by nucleons to the known PNC mesonic decays of the strange baryons. They employed the quark model of hadron structure and the Weinberg-Salam model of the weak interaction to predict the various components of the PNC NN force. Their "best values" are in good quantitative agreement with the measured helicity dependence[2,3] in p + p scattering. However, the p + p results are not sensitive to PNC $\pi^{\pm}$ exchange (which is pure $\Delta I = 1$). At present $\pi^{\pm}$ exchange is best probed by the parity mixed doublets in ^{18}F,[4] ^{19}F[5] and ^{21}Ne[6]. Haxton, Gibson and Henley[7] and Brown, Richter and Godwin[8] have used large basis shell model wavefunctions to compute the parity mixing in these doublets expected from the "best value" parameters of Desplanques, Donoghue and Holstein. These calculations explain several features of the data, among them the sign of the PNC asymmetry in ^{19}F and the observation of a much larger parity mixing matrix element in ^{19}F than in ^{21}Ne. However the predicted effects in ^{18}F and ^{19}F are roughly 3 times larger than the experimental results. Is this due to a deficiency in the nuclear wavefunctions, or because the "best values" of Desplanques, Donoghue and Holstein are too large by a factor of $\sim$3?

There is a way to distinguish between these two possibilities! Consider the first forbidden β decays of ^{18}Ne and ^{19}Ne which connect (assuming isospin symmetry) the same levels involved in the parity mixing in ^{18}F and ^{19}F. These forbidden β transitions are dominated by the $\Delta J^{\pi} = 0^-$ axial charge operator which has a close similarity to the $\Delta J^{\pi} = 0^-$ parity mixing operator. Hence these forbidden β decay rates form an excellent test of the wavefunctions used to analyze the parity mixing in ^{18}F and ^{19}F.

We recently measured[9] the β decay rate of ^{18}Ne to $J^{\pi}=0^-$, I=0 level of ^{18}F. The observed rate was roughly 10 times smaller than that predicted by the wavefunction of Ref. 7! Hence the predicted[7] parity mixing in ^{18}F should be reduced by $\sim\sqrt{10}$ which removes any discrepancy between the experimental upper limit on the parity mixing and the "best value" PNC $\pi^{\pm}$ exchange coupling given in Ref. 1. Haxton[10] has shown that the failure of the wavefunctions was due to neglect of 2 ħω excitations on the ^{18}Ne ground state; when these are included he obtains a result in accord with experiment. Could a related phenomenon explain the discrepancy between experiment and theory in the parity mixing in ^{19}F? We have measured the decay rate of ^{19}Ne to the 110 keV $1/2^-$ level. Our result indicates that the answer to the above question is yes.

We produced ^{19}Ne activity by bombarding SF_6 gas with 6.4 MeV protons. The UW gas transport system operating on a 20 sec. cycle transferred the irradiated gas to a lucite chamber with 9.5 mm wall thickness placed in a well-shielded counting station. We observed triple coincidences between 511 keV annihilation quanta detected in two back-to-back 7.6 cm x 7.6 cm NaI counters and γ-rays registered in a 15% Ge(Li) detector equipped with pileup rejection circuitry. A time-to-amplitude converter was started on fast 2-fold coincidences between 511 keV events in the NaI detectors and stopped by fast triggers from the Ge(Li) detector. Scalers recorded the start and stop pulse rates along with the 3-fold coincidence rate and a rate which gave the pileup losses. From the absence of contaminant lines in the Ge(Li) singles spectra and the observed decay time of activity we conclude that any contaminant activities are negligible for our purposes.

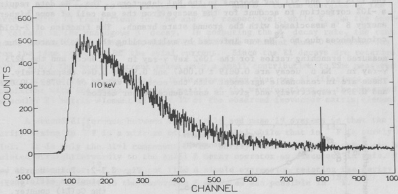

Fig. 2.3-1: Spectrum of events in the Ge(Li) counter in coincidence with 511 keV photons detected in two NaI detectors. Random coincidences have been subtracted. The anomaly around channel 800 is due to the subtraction of random 511 keV events.

A spectrum of γ-rays in the Ge(Li) detector in coincidence with two 511 keV quanta is shown in Fig. 2.3-1. A smooth bremsstrahlung continuum is prominent along with a sharp peak at 110.0 ± 0.3 keV which contains 531 ± 88 counts. We deduced the absolute branching ratio for ^{19}Ne decays to $^{19}F(110)$ by dividing the area of the 110 keV peak in the coincidence spectrum by the product of the absolute efficiency of the Ge(Li) detector for 110 keV γ-rays times the number of 2-fold coincidences in the NaI detector. An ∿30% correction for pile-up losses in the Ge(Li) was incorporated. The absolute point-source efficiency of the Ge(Li) detector and its fast trigger was obtained using calibrated radioactive sources. These sources were placed in the center of the counting cell and singles pulse-height spectra gated by the fast trigger were accumulated and corrected for pileup losses. The measured point source efficiency is shown in Fig. 2.3-2. The ^{19}Ne decay measurement involves an extended source. A -6% correction to the point source efficiency was inferred from the measured change in the detection efficiency as the radioactive sources were moved around within the counting cell. From these results we obtain a branching ratio of $(1.20 \pm 0.20) \times 10^{-4}$ for the $^{19}Ne \rightarrow {}^{19}F(110)$ decay.

We checked our method by using the same apparatus and procedure to measure the known β^+ branching ratios for $^{18}Ne \rightarrow {}^{18}F(1042)$ and $^{22}Na \rightarrow {}^{22}Ne(1275)$. The former activity was made by $^{16}O(^3He,n)$ as described in Ref. 9; the latter was a commercial radioactive source. Both of our checks required corrections to the 2-fold coincidence rate which were not needed in the ^{19}Ne case. The ^{22}Na data required a -13.8% correction to account for summing of the 1275 keV and 511 keV photons in the NaI detectors. The ^{18}Ne data required a -10% correction to account for the escape from the gas cell of some higher energy β^+'s associated with the ground state branch. The fraction of 2-fold coincidences due to ^{18}Ne was inferred by multiscaling the 2-fold rate. Our measured branching ratios for the 1042 keV γ-ray in ^{18}Ne decay and the 1275 keV γ-ray in ^{22}Na β^+ decay are 0.0819 ± 0.0047 and 0.956 ± 0.044 respectively. These are in reasonable agreement with the accepted values of 0.0783 ± 0.0021[11] and 0.999 respectively and give us confidence in our method.

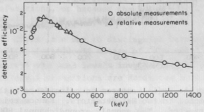

Fig. 2.3-2: Point source γ-ray detection efficiency of the Ge(Li) counter. Uncertainties (∿ 3%) are smaller than the symbols.

Our branching ratio when combined with the 17.22 ± 0.02 sec[12] half life of ^{19}Ne corresponds to an ft value of (1.13 ± 0.19) x 10^{7} sec for the $1/2^+ \to 1/2^-$ decay. We have computed f assuming an allowed spectrum shape which is reasonable since the dominant axial charge operator is independent of the momentum transfer to the leptons.

Now we turn to some implications of our result. The $1/2^+ \to 1/2^-$ β decay of ^{19}Ne and the corresponding parity mixing in ^{19}F differ in some respects from the $0^+ \to 0^-$ β decays of ^{18}Ne and the analogous parity mixing in ^{18}F which we have discussed previously[9]. The ^{19}Ne decay proceeds by both the vector and axial vector weak currents while the ^{18}Ne decay is purely axial. However it is easy to show that the vector weak current makes a negligible contribution to the ^{19}Ne $\to$ ^{19}F(110) decay rate. CVC relates the vector weak current to the isovector electromagnetic current if isospin is a good quantum number for the nuclear states. Thus the vector current contribution to the ^{19}Ne $\to$ ^{19}F(110) β decay can be inferred from the E1 lifetimes[12] of the corresponding $1/2^-$ levels in ^{19}F and ^{19}Ne (see Fig. 2.3-3). Using Siegert's theorem to remove trivial q dependence of the matrix elements we obtain

$$\langle 1/2^- | V^\beta | 1/2^+ \rangle \propto \frac{1}{2e} \left(\frac{E_\beta^{\,o}}{hc} \right) \left\{ \sqrt{\frac{h}{\tau_+} \left(\frac{hc}{E_\gamma^{+}} \right)^3} + \sqrt{\frac{h}{\tau_-} \left(\frac{hc}{E_\gamma^{-}} \right)^3} \right\}$$

where τ_+ and τ_- refer to the lifetimes and E_γ^+ and E_γ^- to the energies of the corresponding E1 transitions in ^{19}Ne and ^{19}F respectively, while $E_\beta^{\,o}$ is the energy release in the analogous β^+ decay. In computing the β^+ decay rate, the rank 1 vector matrix element does not interfere with the dominant rank 0 contribution from the time component of the axial current. Since the E1 decays are retarded ($\sim 10^{-3}$ W.u.) the vector current makes only a small contribution to the measured decay rate and can be neglected. It is reassuring that the E1 lifetimes are consistent with the assumed isospin purity of the wavefunctions -- the observed isoscaler E1 matrix element is only 3% of the observed isovector matrix element.

A second difference between the mass 18 and mass 19 systems is that the parity mixing in ^{19}F is a mixture of $\Delta I=0$ and $\Delta I=1$ while that in ^{18}F is purely $\Delta I=1$. It is only the $\Delta I=1$ component of the parity admixture in ^{19}F which can be related straightforwardly to the axial β decay operator as discussed in Refs. 9 and 10. Hence for ^{19}F one cannot find a simple expression relating the parity mixing matrix element to the forbidden β decay as was possible in ^{18}F.

Nevertheless our ^{19}Ne β decay results are a crucial test of wavefunctions used to interpret the parity mixing in ^{19}F. Our measured decay rate $\omega_{exp} = (4.8 \pm 0.8) \times 10^{-6}\ \mathrm{sec}^{-1}$ is roughly 10 times smaller than the rates $\omega_{th} = 4.13 \times 10^{-5}\ \mathrm{sec}^{-1}$ and $10.4 \times 10^{-5}\ \mathrm{sec}^{-1}$ predicted[14] using the wavefunctions

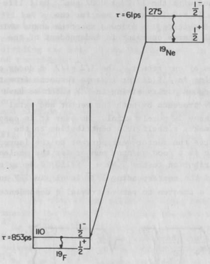

Fig. 2.3-3: Analogue β and γ transitions in ^{19}F and ^{19}Ne.

of Refs. 7 and 13 respectively. A similar situation occurred for ^{18}Ne where the measured $0^+ \rightarrow 0^-$ decay rate was approximately 10 times slower than the rate predicted using the wavefunctions of Ref. 7. In that case the discrepancy was removed by incorporating $2\hbar\omega$ excitations into the wavefunctions of the 0^+ level[10]. Unfortunately a similar calculation for ^{19}F involving 5p-3h configurations is quite tedious and to our knowledge has not yet been performed. However it is probably fair to assume that whatever shell model deficiencies are responsible for overpredicting the β decay amplitude by roughly a factor of 3 also cause the 3-fold overprediction of the parity violation in ^{19}F. If so, the "best value" estimates of Desplanques, Donoghue and Holstein would be in remarkable agreement with experiment.

We are grateful to W. C. Haxton for illuminating remarks and for allowing us to quote his unpublished calculations.

References:

1. B. Desplanques, J. F. Donoghue, and B. R. Holstein, Ann. Phys. 124, 449 (1980).
2. D. Nagle, et al., AIP Conference Proceedings No. 51 (Am. Inst. of Phys., New York, 1978), p. 224.
3. R. Balzer, et al., Phys. Rev. Lett. 44, 699 (1980).
4. C. A. Barnes, et al., Phys. Rev. Lett. 40, 840 (1978).

5. E. G. Adelberger, et al., Phys. Rev. Lett. 34, 402 (1975) and E. G. Adelberger, Proceedings of Fifth Int. Symp. on Polarization Phenomena in Nucl. Phys., Santa Fe, NM, 1980, p. 1367.
6. K. A. Snover, et al., Phys. Rev. Lett. 41. 145 (1978).
7. W. C. Haxton, B. F. Gibson, and E. M. Henley, Phys. Rev. Lett. 45, 1677 (1980).
8. B. A. Brown, W. A. Richter, and N. S. Godwin, Phys. Rev. Lett. 45, 1681 (1980).
9. E. G. Adelberger, C. D. Hoyle, H. E. Swanson, and R. D. Von Lintig, Phys. Rev. Lett. 46, 695 (1981).
10. W. C. Haxon, Phys. Rev. Lett. 46, 698 (1981).
11. J. C. Hardy, et al., Nucl. Phys. A246, 61 (1975).
12. F. Ajzenberg-Selove, Nucl. Phys. A300, 1 (1978).
13. J. B. McGrory and B. H. Wildenthal, Phys. Rev. C7, 974 (1973).
14. W. C. Haxton, work in progress.

2.4 Calibration of Polarimeters For the Mark II ^{21}Ne Parity Violation Experiment

E. G. Adelberger, H. E. Swanson, and R. D. Von Lintig

We have been measuring the analyzing power of the large-solid-angle, transmission-mode polarimeters constructed by our Chalk River colleagues for the Mark II ^{21}Ne parity violation experiment. The procedure used is identical to that used to measure the efficiency of the smaller polarimeters of the Mark I experiment. The polarimeters are arranged so that gamma rays from a ^{24}Na source (produced by irradiation of NaF in the University of Washington Nuclear Reactor) pass through them in series before reaching a 5 in. by 6 in. sodium iodide detector. In this way the first polarimeter, which has steady magnetization, circularly polarizes the gamma rays while the second one, whose magnetic field is reversed each 3 seconds, analyzes the polarization. The measured effect is the square of the analyzing power. Two runs have been completed and we anticipate at least two more will be needed for an accurate measurement of the efficiency.

The results to this point indicate the new polarimeters have about the same efficiency as the smaller ones, but a reduced efficiency per unit length. Equal amounts of data are obtained with either polarity of the steady magnet. The results for each steady magnet polarity and each run are listed below:

Run	Field Normal	Field Reversed	Combined
1	(2.99±.20)%	(3.85±.17)%	(3.40±.15)%
2	(3.12±.23)%	(3.52±.19)%	(3.33±.15)%
Total	(3.05±.15)%	(3.70±.13)%	(3.37±.10)%

The data agree reasonably well with the expected efficiency but the efficiency per unit length is .34 percent per centimeter compared to .41 percent per centimeter for the Mark I polarimeters. A significant difference in the efficiency exists for the two directions of steady magnet polarization. We hope to resolve this in the remaining data runs. Completion of this project has been suspended until bureaucratic difficulties involving the use of radioactive sources throughout the University have been resolved.

The Mark II experiment, to be run this April at Chalk River, will employ 4 of these polarimeters. We expect to achieve a sensitivity of 1×10^{-3} in the circular polarization. This corresponds to a sensitivity of 0.012 eV in the parity non-conserving matrix element connecting the $1/2^{+}$ and $1/2^{-}$ levels.

References:

1. Nuclear Physics Laboratory Annual Report, University of Washington (1979), p. 21.
2. W. C. Haxton, B. F. Gibson, and E. M. Henley, to be published in Phys. Rev. C.

3. PARITY MIXING IN THE HYDROGEN ATOM

3.1 Introduction

E. G. Adelberger and T. A. Trainor

During the last year we have made major revisions to our experiment to detect neutral-current-induced parity mixing between the $2s_{1/2}$ and $2p_{1/2}$ levels of the hydrogen atom. The principles of our new experiment were discussed in last year's Annual Report[1] and have recently been published.[2] Most of our effort during the preceeding year has been devoted to designing and fabricating the new apparatus (cavities, electronics, and solenoid coils) required for the Mark II scheme. Almost all of this construction is now complete. We have tested the components electrically and have recently begun studies using the metastable atomic hydrogen beam. Preliminary results of the beam studies are encouraging, although much work remains to understand, align and refine the apparatus. Nevertheless it is already clear that the new apparatus has much smaller systematic errors than the old. The major projects undertaken in the last year are discussed below.

References:

1. Nuclear Physics Laboratory Annual Report, University of Washington (1980), p. 32.
2. E. G. Adelberger, T. A. Trainor, E. N. Fortson, T. E. Chupp, D. Holmgren, M. Z. Iqbal, and H. E. Swanson, Nucl. Inst. and Meth. 179, 181 (1981).

3.2 Design, Construction, and RF Performance of Dual 1608 MHz Cavities

E. G. Adelberger, D. Holmgren, M. Z. Iqbal, H. E. Simons and T. A. Trainor

In last year's Annual Report[1] we described studies of prototype 1608 MHz cavities needed to drive 2s→2p transitions in the Mark II apparatus. Two cavities are required, each of which must have uniform static and RF $\vec{E}$ fields along the $\hat{z}$ axis. In order to minimize spurious effects in our experiment each cavity must have precise cylindrical symmetry and the axes of the two cavities must coincide. Our prototype studies produced a design concept for a cylindrical cavity operating in the TM010 mode. The static $\vec{E}$ field was generated by splitting the cavity into cylindrical slices each of which was held at a different static potential. Good RF performance was maintained by connecting the different segments with radial $\lambda/4$ chokes (see Ref. 1).

During the last year we have designed, fabricated and tested Mark II cavities based on the concept of Ref. 1. RF performance of the cavities has met or exceeded our expectations in all respects. The copper cavities are divided into 2 in. long segments with 1 in. long end caps. The shorter cavity (cavity I) is 4 in. long and is divided into 3 segments. The longer cavity (cavity II) is 16 in. long and contains 9 segments. The spacing between the segments and the alignment is maintained by 3 Macor pins in each gap. The entire 2 cavity structure is kept under alignment by an external framework which compresses the segments together. The mechanical alignment of the entire structure is exceedingly good. For example, the outside ends of cavities I and II, separated by 12 segments, are parallel to an accuracy of 0.1 mil. A photograph of the partially assembled structure is shown in Fig. 3.2-1.

The RF performance of the cavities is excellent. We measured a Q of 15,900 for cavity II when it was coupled moderately to the RF generator and a power meter. The theoretical value for the unloaded Q of a perfect copper cavity of these dimensions is 34,200.[2] Since our cavity was loaded by the generator and the detector our results indicate that a very small amount of RF power is radiated by the chokes. This conclusion is buttressed by the observation that one cannot appreciably perturb the cavity resonances by shorting the ends of the chokes, etc.

For our parity violation measurement the cavities must be excited coherently but with an adjustable phase between the two cavities. Hence it is very important that any coupling between the two cavities (which, after all,

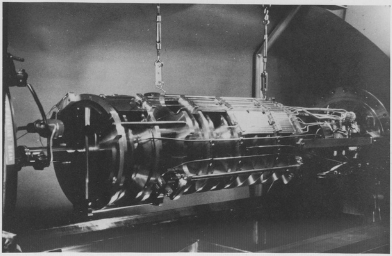

Fig. 3.2-1: Photograph of the Mark II cavity assembly.

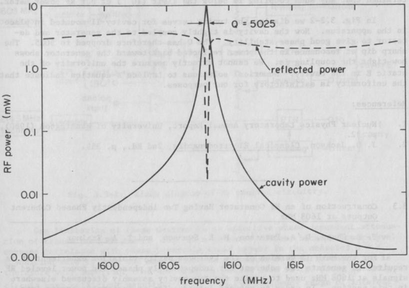

Fig. 3.2-2: Resonance in cavity II. The cavity is mounted inside the solenoid and tightly coupled to the generator and detector. The solid curve (cavity power) is the power absorbed by an inductively coupled pickup loop in the cavity. The dashed curve (reflected power) is the power reflected back toward the generator from the driving loop.

are tuned to the same frequency) be very small. By exciting one cavity at maximum power and looking for a detected signal in the second cavity we have determined that any such coupling is below the limit (10^{-4}) of our RF power meter.

In Fig. 3.2-2 we display the tuning curves for cavity II mounted in place in the apparatus. Now the cavity is tightly coupled to the generator and detector to give good phase stability. The Q has therefore dropped to 5025. The sharp dip at resonance in the power reflected back toward the generator shows how tight the coupling is. We cannot directly measure the uniformity of the static E in the cavity. Numerical solutions to Laplace's equation indicate that the uniformity is satisfactory for our purposes.

References:

1. Nuclear Physics Laboratory Annual Report, University of Washington (1980), p. 32.
2. J. D. Jackson, Classical Electrodynamics, 2nd Ed., p. 359.

3.3 Construction of an RF Generator Having Two Independently Phased Coherent Outputs at 1608 MHz

T. E. Chupp, D. A. Peterson, H. E. Swanson, and T. A. Trainor

For the Mark II version of the hydrogen parity-violation experiment it is required to generate two coherent but independently phased and power leveled RF signals at 1608 MHz used to excite the two-cavity assembly discussed elsewhere in this section. In order to prevent introduction of systematic errors into the experimental result we must control the RF electric field amplitudes (power level) in the cavities with great accuracy ($1/10^5$ or better) especially at certain phase modulation frequencies in a range important to the experiment (DC to 1 kHz). To do this is difficult because of certain limitations of system components. But we have devised a scheme which satisfies our needs as discussed below.

A simplified block diagram of the RF control circuitry is shown in Fig. 3.3-1. The 1608 MHz oscillator produces about 800 mwatts of RF power which are split about evenly between two legs. One leg has a conventional configuration similar to the polarized ion source RF system and delivers leveled power to cavity I (Stark amplitude generator). The second leg (for the PV amplitude generator) contains, in addition, two phase shifters supplied by Vectronics Microwave Corp. One (ϕ_D) is a digital four-quadrant device controlled by two TTL lines in a binary format. Phase shifts of 90° and/or 180° can be inserted with this device. The second (ϕ_A) is an analog phase shifter with a range of about 180° monotonically dependent on a bias voltage (0-60V). With this combination the relative phase of the two coherent 1608 MHz outputs can be arbitrarily set over 2π, and the phase can also be rapidly changed by 180° for asymmetry measurements.

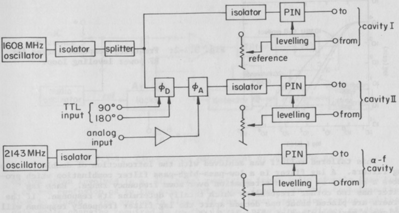

Fig. 3.3-1: Block diagram of RF control circuitry.

One limitation of these devices is an effective phase-dependent attenuation of transmitted RF power. This is a serious problem, because power-level changes correlated with phase reversals would appear in the measured $\alpha \to \beta$ transition rate to have the same effect as a genuine PV interference. It is therefore very important that the noise reduction gain in the power leveling circuit have sufficient magnitude ($\sim 10^4$) in the frequency range of interest (DC-1 kHz). To achieve this is difficult because of the properties of the PIN diodes.

The PIN diodes are used in this system as variable attenuators with the log attenuation proportional to current injected into the intrinsic (I) region. The frequency response of a PIN is flat to about 200 kHz, where it starts to roll off at 20 db/decade (one RC stage).

The situation is clearer in Fig. 3.3-2. We require a noise reduction gain of 10^4 up to 1 kHz. This means the leveling loop must have a gain-bandwidth product of 10 MHz. Typically the loop frequency response rolls off at 20 db/decade (one stage of integration) until unity gain is reached ($\sim$ 10 MHz). However, with the additional equivalent RC stage (and added 90° phase shift) produced by the PIN modulator above about 200 kHz the system so configured (curve A) would oscillate just above 200 kHz. To prevent this the gain at 200 kHz must be reduced to unity, but in a manner that preserves the 10 MHz G-B product at 1 kHz. A simple additional stage of integration (curve B) would only move the oscillation frequency down to 1 kHz. What is required is a careful shaping of the frequency response curve so that the rolloff from 1 kHz to 200 kHz is less than 40 db/decade (-180°) but fast enough to achieve unity gain at 200 kHz (curve C).

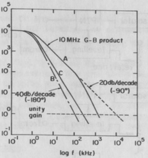

Fig. 3.3-2: Frequency response curves for RF power leveling loop.

This tailored rolloff was achieved with the introduction of double passive lag filters. A lag filter is a low-pass-high-pass filter combination which produces a step up or down in attenuation over some frequency range. Each lag filter has two corner frequencies which totally determine its response. If the corners are placed about one decade apart the lag filter frequency response will achieve a maximum slope of about 15 db/decade midway between corners. If several such lag filters are cascaded (about 1-1/2 decades apart) this 15 db/decade can be maintained over any frequency range of interest. For our purpose two lag filters covered the region from 1 kHz to 300 kHz. The double lag rolloff (15 db/decade) added to the single RC stage equivalent of the high gain stage (20 db/decade) produced an overall rolloff of 35 db/decade (-150°) from 1 kHz (10^4) to 200 kHz (1). The circuit used to achieve the desired open-loop gain is shown in Fig. 3.3-3.

In order to check the performance of this circuit a special measurement technique was developed which depends on a lockin amplifier with very good common mode rejection ratio (CMRR) and a differential input (in this case a PARC 186A). The principle is shown in Fig. 3.3-4. Differential inputs (A and B) of the lockin are used to measure the differential inputs of the leveling circuit gain stage under closed-loop operation. An audio signal is added to the system DC reference at input A and also supplied as the lockin reference. The lockin output is then A-B and (A-B)/A = 1/(1+G) where G is the open-loop gain. The advantage of this system is that trying to measure performance in an open loop configuration is almost impossible due to the high levels of amplifi-

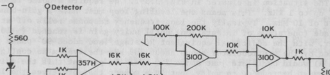

Fig. 3.3-3: RF power leveling circuit.

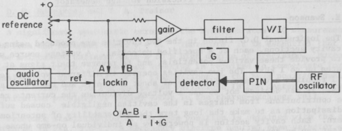

Fig. 3.3-4: Closed-loop measurement of open-loop gain.

cation often involved (e.g. 10^4 here) requiring input audio signals less than 1 mV and confusion as to the true input signal level. In this technique the loop is closed. The system is always in the linear operating region and the only scale changing required is on the lockin, providing a direct reading of the gain.

The result of this procedure for the design circuit is shown in Fig. 3.3-5. It can be seen that G is $>10^4$ at DC, about 8×10^3 at 1 kHz and rolls off smoothly to unity at 200 kHz. We observe unleveled phase-dependent power modulations of order 5% at 1 kHz. This leveling circuit reduces these modulations in power (and hence in electric field amplitude) to less than $1/10^5$.

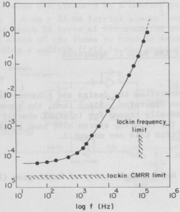

Fig. 3.3-5: Frequency response curve for leveling circuit of Fig. 3.3-3.

3.4 Design and Construction of a Precision Voltage Generator

E. Swanson

The logitudinal D.C. fields in the two cavities are produced using insulated cavity sections, each at a specified potential. A voltage source was built to provide these various potentials, and to reverse their signs at modulation rates up to 1 kHz. The two cavities operate in different voltage regimes. Cavity I requires a voltage difference of about 150 volts and cavity II about 10 volts. It was decided not to use a voltage divider,as the currents required to make contributions from charges in the cavities negligible caused sufficient power dissipation as to make the long term thermal stability of potentiometers a concern. Each cavity section is powered by an individual op-amp whose gain and offset can be controlled. Teledyne-Philbrick model 1022 op-amps capable of plus and minus 150 volt operation were used for cavity I and we are presently evaluating both National LM-11's and Teledyne Philbrick 1322's for cavity II. The power supplies for both the high and low voltage op-amps float with respect to chassis ground, hence the common on one supply may be connected to a cavity section of the other for series operation.

Each cavity's set of op-amps is driven from an adjustable reference source. In the case of cavity II, where the total voltage difference is small, an LM-3999Z provides the stable reference (about a factor of ten better than a good zener diode). The reference is inverted, and FET switches select whether the plus or minus polarity is used. An optically isolated TTL signal selects the state.

The panel shows the cavity selections schematically and provides inspection jacks for measuring potentials.

3.5 Construction of a New Solenoid for the Mark II Apparatus

T. E. Chupp

In last year's Annual Report[1] we described the design and construction status of the new solenoid for the H-atom apparatus. Since then, the twenty coil elements have been wound and individually tested for internal shorts. All of the necessary pieces for adapting to the existing system have been built. In the near future, we will install and trim this new solenoid.

Reference:

1 Nuclear Physics Laboratory Annual Report, University of Washington (1980), p. 31.

3.6 Feedback Stabilization of the Atomic Beam Position

D. W. Holmgren, and T. A. Trainor

A significant systematic error in the hydrogen atom PNC measurement arises from the motional field $\vec{v} \times \vec{B}$.[1] Therefore, it is essential that the beam axis be maintained colinear with $\vec{B}$ to a high degree of precision. Moreover, continuous correction of the beam steering is required to compensate for slow (thermal) drift as well as for ac fluctuations in the beam position due to electronic noise in the ion source and variations in the degree of space-charge neutralization provided by cesium vapor in the charge-exchange cell.

Feedback stabilization of the beam position is obtained with the system illustrated in Fig. 3.6-1. A secondary electron neutral beam detector yields a current proportional to the atomic beam incident on each of four sectors. Detector currents are converted to voltages by special fast logarithmic preamplifiers.[2] The difference between the log outputs for the left and right sectors is $(I_L - I_R)/(I_L + I_R) = \delta_H$. The currents in the top and bottom sectors likewise determine the difference δ_V in the vertical channel. In either channel the difference δ is added to a dc offset δ_o, and the result is amplified (0-60db dc gain, 100 Hz corner). This correction signal $G(\delta+\delta_o)$ controls the current delivered to the magnetic beam steerers in the ion source.

The atomic beam can be steered by a deflecting field applied to the charged proton beam between the duoplasmatron and the cesium cell. An electric field in this region would remove the space-charge neutralizing electrons from the beam, resulting in beam blow-up. Magnetic deflection of the protons is successfully achieved with fields of a few tens of gauss applied over 5 cm. The fields are produced by a compact picture-frame magnet consisting of four 6 mm × 6 mm × 25 mm ferrite blocks[3] enclosing a 19 mm square aperture. Two coils, each 20 turns of #24 enameled copper wire, are wound in series on opposite sides of the frame to produce opposing fields in the magnetic material, yielding a uniform field in the aperture.

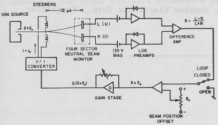

Fig. 3.6-1: Feedback stabilization in the horizontal plane. An identical system provides stabilization in the vertical plane.

The steering magnets are driven by fast bipolar power amplifiers (see Fig. 3.6-2), which are in turn controlled by the correction signal $G(\delta+\delta_0)$.

The system may be run open-loop to provide beam steering of ± 20 mr. In the closed-loop mode the system provides -40 db noise reduction from 0-100 Hz and -6 db at 10 kHz.

The deflecting magnets are designed and placed to minimize eddy currents, providing a magnetic field proportional to driven current at all frequencies of interest. A 5 ampere square wave current driving a prototype steering magnet has been used successfully as a neutral-beam chopper. The detector signal rise time was 2 μs, which is fast compared to the 12 μs flight time of the 500 eV atoms from source to detector, allowing beam speed distribution studies.

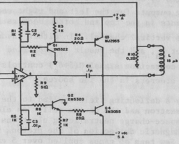

Fig. 3.6-2: Fast bipolar power amplifier. The load L represents the steering magnet.

References:

1. Nuclear Physics Laboratory Annual Report, University of Washington (1980), p. 14.
2. These preamps are described in Nuclear Physics Laboratory Annual Report, University of Washington (1980), p. 180.
3. Available from Ferroxcube Div., Amperex Electronic Corp., Saugerties, New York 12477.

3.7 Remote Positioning Device for the RF Cavities

M. Z. Iqbal, and T. A. Trainor

In hydrogen parity experiment all the unwanted amplitudes would vanish in the ideal situation where the applied field directions are perfectly aligned along the beam direction. The magnetic field direction could be considered fixed, so one needs to align independently the beam direction and the cavity axis, of which the latter defines the direction of both RF and static electric field. This report describes a scheme for aligning the cavity along the magnetic field using a hydraulic system.

Inside the solenoid the cavity sits on four stainless steel bellows which are supported on four wheels inside the solenoid. The bellows can move the cavity up or down by expanding or contracting depending on the hydraulic pressure. The pressure is exerted from outside the ultra-high vacuum system through 1/8 in. copper tubing. For coarse movement a piston and cylinder is used which is common to all four bellows. For finer movements each bellows can be isolated and a piston in cylinder system of smaller cross section can be used separately. The movement of pistons are noted as the number of rotations in rotation counters.

Pumping oil is chosen as the hydraulic fluid for its low vapor pressure. To fill the hydraulic system with oil it is pumped down carefully and then is exposed to an oil reservoir. Special care is taken to expell the air dissolved in the oil as a small air bubble could make the whole system look much less incompressible.

For each bellows the displacement and the pressure of hydraulic fluid inside the bellows is then plotted as the function of the position of piston which is given in terms of number of turns in rotation counters (see Figs. 3.7-1 and 3.7-2). The graphs are of hysterisis nature and are reproducible within a few thousandths of an inch. It is possible to predict the position of cavity inside the ultra high vacuum from the same hysterisis graphs. However, the final position would be adjusted by minimizing an atomic signal.

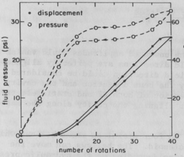

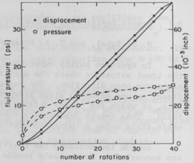

Fig. 3.7-1: A typical hysteresis curve of displacement and pressure as a function of piston position (rotation) for an upstream bellows.

Fig. 3.7-2: Hysteresis curve for a down stream bellows which works at lower pressure because the down stream bellows supports less weight.

3.8 Improved Cryopump for Mark II Apparatus

E. G. Adelberger, M. Z. Iqbal, and T. A. Trainor

A new cryopump has been constructed for use in the upstream region of the hydrogen parity experiment. The helium expansion module is about 2 feet away from the pumping surface located inside the solenoid. Moreover, the pump contains the ion deflector and a set of beta quench plates so it must have the same complicated shape as before.[1] The new pump is made as light as possible to reduce the cooling time. The OFHC copper along with indium in the joints still ensures good conductivity although the mass is reduced by half. The improved design reduced the surface area by more than 40%. All the exposed surfaces are nickel and gold plated, so the radiation load is much smaller. To adsorb hydrogen, activated charcoal is attached to the cold part with sodium silicate as before. The pump works satisfactorily and is a clear improvement over the original. It cools down within 2-3 hours and stays at 15° K at about 2×10^{-8} torr pressure.

Reference:

1. Nuclear Physics Laboratory Annual Report, University of Washington (1979), p. 31.

3.9 Frequency Stabilization of the RF Generator-Cavity System

E. Swanson

Typically, an oscillator is locked in frequency to a resonant cavity by modulating the frequency about its nominal value, and measuring the correlation between power in the cavity and the modulation. Near resonance, power varies with frequency as one moves up and down the skirts of the resonance curve and the sign of the correlation tells whether the nominal oscillator frequency is above or below resonance. Thus, minimizing the correlation, constrains the oscillator to have the same frequency as the cavity.

As seen in the phasor representation, both frequency and phase modulation affect the angle of the vector representing the oscillator's output, and thus similar properties are expected from phase modulation. This can be seen by first considering a sinusoidal phase modulation. The output of an ideal phase shifter (one having no attenuation which varies at the modulation frequency) is given by

$$RF(t) = A_c \cos[w_c t + \beta \sin(w_m t)]$$

w_c and A_c are the nominal RF frequency and amplitude, β is one half of the total phase shift, and w_m is the frequency of the phase modulation. The instantaneous frequency w_c can be obtained by differentiating the argument of the cos function with respect to time.

$$w_c' = w_c + \beta w_m \cos(w_m t)$$

The frequency deviation about w_c is proportional to both the modulation frequency and the total phase shift and is 90° out of phase with the modulation.

In the experiment, the P.V. signal results from modulating the phase of the RF in cavity II with respect to cavity I. This provides a "ready made" phase modulation for locking the oscillator to the frequency of the second cavity. The modulation wave-form in this case is a square wave having zero and 180° as its two states. The instantaneous frequency shift now occurs only in the immediate vicinity of the transition but the phase relationship to the modulation is the same as the sinusoidal case.

A signal inversly proportional to the power in the cavity is obtained using the power reflected from the input coupling loop. A directional coupler is placed in the line allowing a Shottkey Barrier detector to measure only the reflected power. This power is a minimum at resonance, and tends toward zero if the impedance matches that of the transmission line. Presently this is fed to a lock-in amplifier with the modulation frequency as its reference. The output is considered as an error signal and added to the signal controlling the oscillator's nominal frequency such as to lock the frequency to the minimum in the power. A block diagram of this is shown in Fig. 3.9-1.

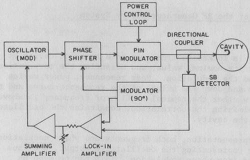

Fig. 3.9-1: Frequency control loop.

The above analysis assumes an ideal phase shifter which in practice was not the case. The attenuation of the shifter was found to vary with the amount of shift provided. Thus as the power in the cavity is constrained to be constant, the oscillator is required to provide more or less power in the different phase shifted states and this leads to a shift in frequency correlated to the phase. The frequency stabilization scheme operates in this manner; however, the frequency shift is now in phase with the modulation. We plan to reduce this dependence by isolating the oscillator with a buffer amplifer.

3.10 Preliminary Measurements of Systematic Effects in the Mark II Apparatus

E. G. Adelberger, T. E. Chupp, D. A. Holmgren, M. Z. Iqbal, H. E. Swanson, and T. A. Trainor

Systematic errors are suppressed by several features of the Mark II apparatus. The most important of these is the choice of field geometry. All applied fields are predominantly axial. This means that unwanted amplitudes caused by stray transverse fields must contain these small fields in second order. The contributions from transverse fields are further reduced by carefully maintaining all fields coaxial with the average beam momentum. This is done by on-line adjustments of the solenoid and RF-cavity orientations and by stabilization of the metastable beam phase space distribution.

Further suppression of systematic errors is achieved with the phase-reversal system shown in Fig. 3.10-1. There are three phase reversals shown in this figure. A fourth reversal (of the 570G magnetic field) is not shown. The parity violating part of the $\alpha \rightarrow \beta$ transition rate built up in cavity II is odd under reversal of E_I, ϕ_D, and the 570G B-field. The reversal frequencies are f_ϕ($\sim$1 kHz), f_I($\sim$ 100 Hz) and f_B($\sim$ .1 Hz).

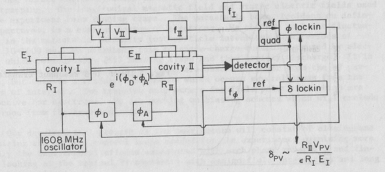

Fig. 3.10-1: Block diagram of phase-reversal system.

An expression proportional to the $\alpha \to \beta$ transition amplitude is

$$\beta \propto 2\epsilon\, R_I E_I + e^{i(\phi_D + \phi_A)}\, R_{II}(2\epsilon\, E_{II} + iV_{pv}).$$

Because of their relative phase E_{II} cannot interfere with V_{pv}. E_{II} is used here to monitor the beam average relative phase between cavities I and II. This phase can be determined from the asymmetry in the β-state yield correlated with a periodic reversal of E_{II}. The phase is chosen to make this asymmetry zero, so that the Stark amplitude $R_I E_I$ build up in cavity I interferes maximally with $R_{II}\ V_{pv}$ in cavity II and, what is most important, interferes minimally with E_{II} and other stray axial static fields in cavity II that might mimic V_{pv}. This relative phase is in fact controlled by a servo loop in which the E_{II} correlated asymmetry is fed back with gain to the analog phase shifter (ϕ_A). In this way the asymmetry can be made very small and the overall phase very accurately controlled.

This phase control loop has been implemented, but with a lockin having an 18 db/octave rolloff inherent in the phase-sensitive detector. This means that the maximum stable gain was limited to unity, and the unwanted E_{II} asymmetry noise was only reduced by 50%. A new lockin with the proper 6 db/octave rolloff has been purchased and should permit substantial improvement in this control loop.

Generation of $\alpha \to \beta$ resonant transitions by each of the two cavities separately can be seen in Fig. 3.10-2. The cavity I resonance is 1G FWHM and the cavity II resonance is four times narrower, consistent with the relative lengths of the two cavities. The structure on the narrower cavity II resonance is thought to be due to B-field inhomogeneities produced by our original solenoid.

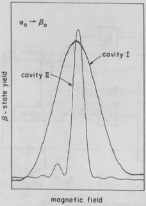

Fig. 3.10-2: α→β resonant transitions.

Asymmetries correlated with reversal of ϕ_D are shown in Fig. 3.10-3. For this figure fields E_I and E_{II} are static and ϕ_D changes by π at a rate of 500 Hz. An additional phase of π/2 has been added to ϕ_D between one scan and another, and ϕ_A has been adjusted so that the overall relative phase was close to 0° or 90°. This figure shows the shapes of asymmetries associated with E_{II} (odd) and V_{pv} (even) under proper experimental conditions. The E_{II} asymmetry passes through zero near the resonance center, and this signal is fed back with the proper sign to ϕ_A to maintain the asymmetry at zero.

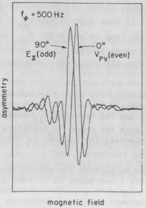

Fig. 3.10-3: ϕ_D-correlated asymmetries.

One effect currently under study has to do with what we believe is electron trapping. The longitudinal magnetic field and static electric fields used in the experiment form Penning traps. The metastable beam, incident on defining apertures, is a copious source of electrons. We observe periodic fluctuations in the metastable intensity (not particle intensity) with periods of order 10-1000 ms. We attribute this to space-charge quenching caused by electrons which periodically fill Penning traps and then rapidly discharge. It is also possible that the trapped electrons are absorbing power from the RF cavities, but this is a resonant phenomenon which occurs several gauss from the region of interest. The trapping only occurs for field polarities which are attractive for electrons. We are working on biasing schemes which will exclude electrons from the trapping regions.

Our developmental program in the near future will consist of closing and optimizing the several control loops needed for the experiment, examining more closely the instrumental effects associated with each phase reversal, and finally looking at the nominal PV asymmetry with design field intensities and long integration times.

---

4. NUCLEAR STRUCTURE AND REACTIONS

4.1 J^{π} Assignments in ^{29}P and ^{25}Al and the Giant G-T Resonance in the β^+ Decay of ^{29}S and ^{25}Si

E. G. Adelberger, C. D. Hoyle, P. G. Ikossi, A. Ray, and K. A. Snover

We have continued our investigation of the Giant Gamow-Teller resonance in the β^+ decay of ^{29}S and ^{25}Si. The method and motivation for this investigation was reported in detail in previous Annual Reports.[1,2] Briefly, delayed proton spectra for these decays were obtained in a series of experiments at Lawrence Berkeley Laboratory.[3,4] In order to infer the β^+ decay scheme from the delayed proton spectra, one needs to know the spins, parities and proton branching ratios of the states in the daughter nucleus. We have been studying the spectroscopy of the β^+ daughters ^{25}Al and ^{29}P. We obtained thin target excitation functions for the polarized proton reactions $^{24}Mg(\vec{p},p)$ ^{24}Mg and $^{28}Si(\vec{p},p)$ ^{28}Si at lab angles ranging from 55° to 155°. Our experimental method is described in ref. 1.

A large amount of data was taken for both the ^{24}Mg and ^{28}Si scattering reactions. For both targets we have cross section and analyzing powers at six angles and approximately one thousand energies between 2.3 and 7.9 MeV. We have performed a phase shift analysis of the ^{28}Si data to obtain the resonance energies, widths and branching ratios of the resonances in the $^{28}Si(\vec{p},p)$ ^{28}Si reaction. The results of this analysis are summarized in Table 4.1-1. An example of the calculated fit and data at 70° lab angle are plotted together for comparison in Fig. 4.1-1 and Fig. 4.1-2. The phase shifts fit the resonances below $E_{P(LAB)} \sim 6.2$ MeV; however, above that energy no reasonable fits were obtained. To do a better job of analyzing the ^{28}Si data an R matrix analysis of the data has begun at Los Alamos Scientific Laboratory. We have no results from this analysis yet, but we hope the R matrix code can do a better analysis than the phase shift code. If the R matrix works for the ^{28}Si data we hope to perform a similar analysis of our ^{24}Mg data.

References:

1. Nuclear Physics Laboratory Annual Report, University of Washington (1979), p. 47.
2. Nuclear Physics Laboratory Annual Report, University of Washington (1980), p. 39.
3. D. J. Vieira, R. A. Gough and J. Cerny, Phys. Rev. C19, 177 (1979).
4. R. G. Sextro, Ph.D. Thesis, University of California, Berkeley, 1973 (unpublished).

Table 4.1-1
Level Parameters for ^{29}P

	This Work				Previous Values			
Ep (keV)	Ex (keV)	Γ (keV)	Γ_{po}/Γ	J^{π}	Ex (keV)	Γ (keV)	Γ_{po}/Γ	J^{π}
2876	5523±6	436±33	1.0	$1/2^-$	5527±20	400±20	1.0	$1/2^-$
3105	5744±6	11±3	.22±.03	$7/2^-$	5739±3	12.5±0.7	.304	$7/2^-$
3341	5972±6	11±2	.81±.08	$3/2^+$	5968±3	9.5±1.5	.84	$3/2^+$
3582	6204±7	75±8	.16±.02	$3/2^-$	6191±5	95±6	.19	$3/2^-$
3719	6337±7	49±6	.13±.07	$3/2^+$	6328±5	73±5	.23	$3/2^+$
4026	6633±8	200±16	1.0	$1/2^+$	6577±5	200±20	1.0	$1/2^+$
4237	6837±8	8±2	.61±.06	$3/2^+$	6828±5	4.9±0.4	.59	$5/2^+$
4360	6956±9	143±11	1.0	$1/2^+$	6956±10	120±10	1.0	$1/2^+$
4436	7029±10	57±12	.13±.02	$3/2^+$	7021±5	100±8	.3	$3/2^-$
4682	7266±9	5±3	.08±.03	$5/2^+$	7272±5	<3		
4886	7463±9	12±3	.25±.03	$7/2^-$	7456±5	8.4±0.7	.35	$5/2^-$
4955	7530±10	∿4	∿.1	$3/2^+$	7523±5	7±3		$(1/2^-)$
5087	7657±10	132±11	.91±.09	$1/2^+$	7641±40	165±25		$1/2^+$
5200	7767±10	5±3	.27±.08	$5/2^+$	7755±5	∿2		$3/2^+$
5399	7959±10	9±3	.38±.06	$3/2^-$	7950±15	14±4		$3/2^-$
5435	7993±11	124±10	.49±.05	$5/2^-$	7998±30	125±25		$3/2^-$
5558	8112±11	28±7	.26±.05	$5/2^+$	8104±15	36±10		$(3/2,5/2)^+$
5689	8238±11	24±3	.93±.11	$3/2^+$	8220±15	20±4		$(3/2,5/2)^+$
5761	8308±11	44±5	1.0	$1/2^-$	8297±15	∿40		$(1/2,3/2)^-$
5999	8537±12	24±4	.71±.10	$3/2^+$	8529±15	25±7		$(3/2,5/2)^+$
6179	8711±12	89±8	1.0	$1/2^+$	8693±30	120±30		$1/2^+$

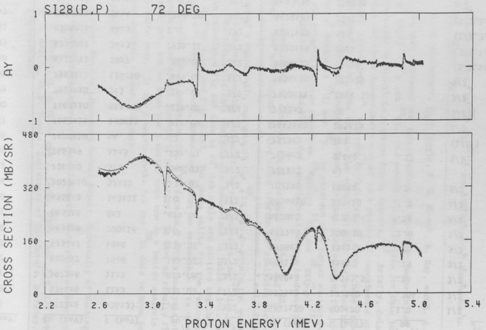

Fig. 4.1-1: Comparison of the phase shift analysis fit and the data for the $^{28}Si(\vec{p},p)$ ^{28}Si reaction.

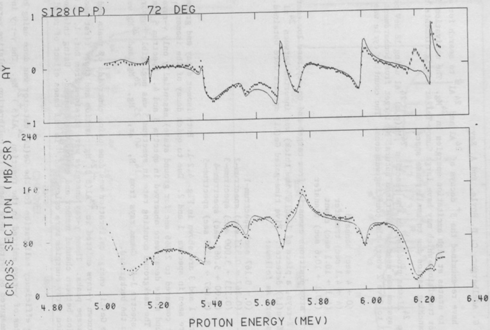

Fig. 4.1-2: Comparison of the phase shift analysis fit and the data for the $^{28}Si\ (\vec{p},p)\ ^{28}Si$ reaction.

4.2 Beta Decay of ^{24}Al and ^{24}Al^m

E. G. Adelberger, C. D. Hoyle, and A. Ray

We have re-examined the β^+ decays of ^{24}Al and ^{24}Al^m to search for weak branches to states at high excitation energies in ^{24}Mg. The motivation is to search for transitions which may have large Gamow-Teller matrix elements but have small branching ratios due to small phase space.

The ^{24}Al was produced in the reaction ^{24}Mg(p,n)^{24}Al using 18 MeV protons. A rabbit system was used to shuttle a natural Mg target from bombardment station in Cave 1 to Cave 2 where the counting was done. The counting cycle was as follows:

(0 → 4 sec) bombard
(4 → 4.1 sec) transfer
(4.1 → 10.1 sec) count
(10.1 → 10.6 sec) transfer

In order to stop positrons emanating from target and to suppress low energy γ-rays and X-rays, a piece of lead (1 in. thick) was inserted between ^{24}Al source and a 15% Ge(Li) detector. Five time-gated Ge(Li) spectra were obtained. The time bins were as follows:

(0 → 0.167 sec) spectrum-1
(0.167 → 0.333 sec) spectrum-2
(0.333 → 3.000 sec) spectrum-3
(3.00 → 5.667 sec) spectrum-4
(5.667 → 8.333 sec) spectrum-5

The spectra 1 and 3 are shown in Fig. 4.2-1. Both isomer decay and ground state decay were seen in spectra 1 and 2. Due to quick decay of the isomer ($\tau_{1/2}$ = 0.130 sec compared to 2.066 sec for ground state) essentially only γ-rays coming from ground state decay were observed in spectra 3 and 4. Spectrum 5 was a background. The background counting rate in spectrum 5 was negligible compared to those in spectra 1-4. Gamma rays from ^{14}N, ^{40}Ar, ^{25}Mg, ^{26}Mg, and ^{24}Mg were detected in the background.

The Ge(Li) energy calibration was done using centroids of peaks and energies of known γ-rays emitted in ^{24}Al(β^+)^{24}Mg reaction and their first escape and double escape peaks. These γ-ray energies were obtained from Ref. 1. A quadratic relation between channel number and energy was assumed. Using this energy calibration γ-ray energies were calculated. In all cases effect of recoil was included.

The efficiency calibration for the Ge(Li) detector was done using known intensities of γ-rays emitted in the reaction ^{24}Al(β^+)^{24}Mg. The γ-ray intensities as measured by Detraz[2] were used in the calibration. Relative γ-ray intensities from the β decay of the ^{24}Al ground state were calculated using peak areas from spectra 3 and 4. Then the intensities and corresponding errors were

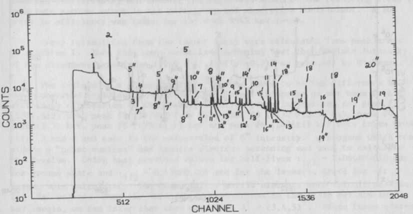

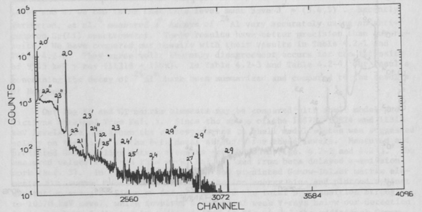

Fig. 4.2-1: Spectrum 1 of γ-rays from the decay of ^{24}Al.

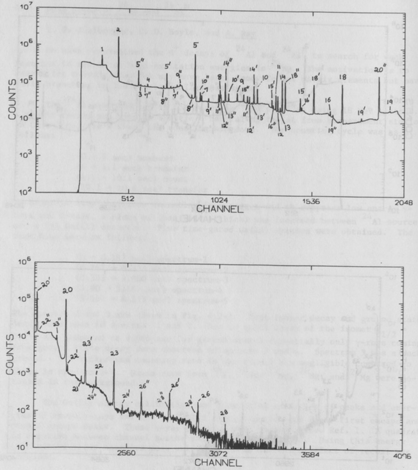

Fig. 4.2-1: Spectrum 3 of γ-rays from the decay of ^{24}Al.

combined statistically and another 10% error was added to the resulting error to take into account error in the efficiency and absorption coefficient. A 20% error in efficiency was taken for the weak 9945 keV γ-ray.

γ-ray intensities from the isomer decay were calculated from peak areas in spectrum 1. Then they were normalized assuming that the absolute intensity of the strongest transition (9966 → 0) is=(1.6±0.2)% as measured by Honkanen.[3]

The β-yield to a given level of ^{24}Mg was taken to be the difference between observed γ-yields to and from that level. Since we do not have Ge(Li) efficiency calibration at low energy, relative γ-ray intensities for peak #1 (1079.6±2) keV, peak #2 (1370.7±2.5) keV, peak #3 (1772.8±1.5) keV, peak #4 (1900±1.5) keV, peak #5 (2753±1.4) keV and peak #6 (2428±1) keV were taken from Refs. 2 and 3 and used in the calculation of β^+ intensity. A program which considers a "point nucleus" and ignores electron screening was used to calculate the F-value. Using best previous values for half-lives $\tau_{1/2}$ = 2.066±0.010 sec for ground state and $\tau_{1/2}$ = 0.130±0.004 sec for the isomeric state log ft values were calculated. The Gamow-Teller matrix elements were calculated from log ft values. From the strength of transitions to the 11318 keV and 10824 keV levels, we can infer that they must have $J^\pi = (3,4,5)^+$. Since these states do not decay by α-emission, their J^π is probably $(3,5)^+$. We have seen the β^+ transition to the 10578 keV level also. Although we could not measure the total strength of the transition due to our inability to measure weak low energy γ-transitions from this level, we have set a lower limit on the strength of transition and so we can infer that this level must have $J^\pi = (3,4,5)^+$. Recently Warburton, et al.[4] measured β^+ decays of ^{24}Al very accurately using an anticompton Ge(Li) spectrometer. Their results have better precision than our results. We have compared our results with their results in Table 4.2-1 and Table 4.2-2. They agree well; the only disagreement occurs for the intensity of 9945 keV γ ray (11318 → 1369). In Table 4.2-3 and Table 4.2-4, our results concerning the decay of $^{24}Al^m$ have been summarized and compared to the results of Honkanen.[3]

Our log ft and GT matrix elements may be compared with shell model predictions obtained from Ref. 5. Since the spins of the 10578, 10824 and 11318 keV levels are not known the correspondence to shell model states was suggested solely on the basis of the beta decay strength for these levels. Measured and predicted Gamow-Teller matrix elements are shown in Figs. 4.2-2 and 4.2-3. The measured values are from this work, Ref. 4, and from beta delayed α-emission work (Ref. 3). In Fig. 4.2-3, measured and predicted Gamow-Teller matrix elements are summed over 0.5 MeV wide excitation energy bins and plotted against excitation energy. Since we did not measure the total β^+ transition strength to 10578 keV level, which involves a number of weak γ-rays below our detection limit, we have indicated by a dashed line in Fig. 4.2-3 the additional Gamow-Teller strength to that level obtained from Ref. 4. From the clustering of beta strength at ∿ 11 MeV excitation energy, one can see evidence for the GT giant resonance.

Table 4.2-1
Gamma Transitions from $^{24}Al(\beta^+)^{24}Mg$

Peak No	Energy (keV)	Assignment	Intensity (%) (our work)	Intensity (%) Brookhaven work (Ref 4)
7	2868±2	4238→1368.6	1.14±0.12	1.097±.028
8	3202±1	8437→5236.1	3.02±.31	3.085±.066
9	3505±1	9515→6010	2.19±.22	1.98±.06
10	3867±1	5236→1368.6	5.50±0.55	5.26±0.22
11	4201±1	8437→4238	4.17±.42	4.02±.22
12	4238±1	4238→0	3.61±.36	3.61±0.21
13	4280±2	9515→5236	0.67±.07	0.66±.04
14	4317±2	8437→4123	15.2±1.5	14.20±.86
15	4642±2	6010→1368.6	3.74±.37	3.42±.25
16	5178±2	9298→4123	0.96±0.1	0.98±0.10
17	5339±2	10578→5236	.07±.03	0.115±.013
18	5395±2	9515→4123	19.6±2.0	18.3±1.8
19	6248±1.5	7616→1368.6	0.53±.06	0.54±0.04
20	7069±2	8437→1368.6	43.1±4.3	43.0±1.3
21	7347±2	7349→0	0.14±.02	0.153±.016
22	7615±2	7616→0	0.20±.02	0.224±.015
23	7928±2	9298→1368.6	1.35±0.14	1.34±0.10
26	9451±3	10824→1368.6	0.14±.02	0.110±.02
28	9945±3	11318→1369	.05±.01	0.027±.006

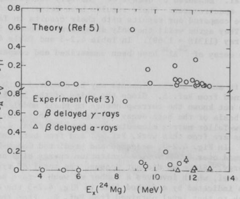

Fig. 4.2-2: β^+ decay strength $|(g_A/g_V)Mg_T|^2$ of individual transitions for ^{24}Al decays as a function of excitation energy in ^{24}Mg. Top: Theoretical result (Ref. 5). Bottom: Experimental result from this work, Ref. 3 and Ref. 4.

Table 4.2-2

β^+ Decay of ^{24}Al to γ-Decaying Levels in ^{24}Mg

EXPERIMENT						THEORY (B)		
J^π	Ex (^{24}Mg) (keV)	β^+ Intensity (%) (our work)	β^+ Intensity (%) Brookhaven (Ref. 4)	log ft (our work)	log ft Brookhaven (Ref. 4)	J^π	Ex (keV)	log ft
4^+	4123	7.1±4.6	7.7±1.0	6.16±0.28	6.13±.06	4^+	4420	5.811
3^+	5236	1.8±0.6	1.40±.13	6.48±.14	6.59±.04	3^+	5170	6.473
4^+	6010	1.03±0.40	1.2±0.1	6.50±0.17	6.43±.04	4^+	5890	5.983
4^+	8437	49.2±4.7	50.0±2.0	3.93±.04	3.93±.02	4^+	8790	4.026
4^+	9298	2.3±0.2	2.5±0.2	4.84±.04	4.80±.04	4^+	9620	4.565
4^+	9515	38.4±2.5	37.0±1.5	3.49±.03	3.510±.018	4^+	9740	3.485
$(3,4,5)^+$	10578	>0.07±.03	0.67±.06	<5.49	4.50±.04	5^+	11050	4.466
$(3,5)^+$	10824	0.14±.02	0.11±.01	4.97±.06	5.08±.08	3^+	11070	4.973
$(3,5)^+$	11318	.05±.01	.026±.008	4.89±.09	5.19±.14	5^+	11330	5.026

Table 4.2-3

γ-Transitions From $^{24}Al^{m}$ (β^{+}) ^{24}Mg

Peak No	Energy (keV)	Assignment	Relative* Intensity (%) (our work)	Absolute Intensity (%) Honkanen's work (Ref 3)
24	8593±3	9966→1368.6	0.46±.08	0.6±.1
25	8687±3	10059→1368.6	0.18±0.10	0.2±0.1
27	9825±3	9827→0	0.29±.10	0.2±0.1
29	9965±2	9966→0	1.6±0.2	1.6±0.2

*Peak 29 is normalized to that of Ref. 3

Table 4.2-4

β^{+} Decay of $^{24}Al^{m}$ to γ-ray Decaying Levels

EXPERIMENT							THEORY (B)		
J^{π}	Ex (^{24}Mg) (keV)	β^{+} Intensity (%) (our work)	β^{+} Intensity (%) Honkanen (Ref 3)	log ft (our work)	log ft Honkanen (Ref 3)		J^{π}	Ex (keV)	log ft
1^{+}	9824	0.29±0.10	0.2±0.1	4.48±.15	4.6±0.3				
1^{+}	9966	2.06±0.22	2.2±0.2	3.55±0.05	3.51±.04		1^{+}	10220	3.387
2^{+}	10059	0.18±0.1	0.2±0.1	4.55±0.24	4.5±0.3				

References:

1. P. M. Endt and C. Van der Leun, Nucl. Phys. A310, 113 (1978).
2. C. Detraz, Nucl. Phys. A188, 513 (1972).
3. J. Honkanen, M. Kortelanti, J. Aysto, K. Eskola, and A. Hautojarrei, Physica Scripta 19, 239 (1979).
4. E. K. Warburton, C. J. Lister, D. E. Alburger, and J. Wolness, Phys. Rev. C23, 1242 (1981).
5. B. H. Wildenthal, private communication.

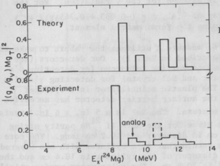

Fig. 4.2-3: β^+ decay strength $|(g_A/g_V)M_{GT}|^2$ in 0.5 MeV wide bins for ^{24}Al decays as a function of excitation energy in ^{24}Mg. Top: Theoretical result (Ref. 5). Bottom: Experimental result from this work, Ref. 3 and Ref. 4.

4.3 β-γ Circular Polarization Correlation in $^{24}Al \overset{\beta^+}{\to} {}^{24}Mg$ and $^{28}Al \overset{\beta^-}{\to} {}^{28}Si$

E. G. Adelberger, C. D. Hoyle, K. A. Snover, H. E. Swanson and R. D. Von Lintig

The most rigorous way to measure isospin mixing is to measure the Fermi matrix element for an isospin forbidden decay. In ^{24}Al the ground state has $J^\pi = 4^+$, T=1. In ^{24}Mg the analog state occurs at an excitation energy of 9.515 MeV. Besides the analog state, there are three low-lying 4^+, T=0 states in ^{24}Mg at 4.123, 6.010, and 8.437 MeV. We are attempting to measure the Fermi matrix elements for the isospin forbidden decays to each of these 4^+, T=0 states and "map out" the anti-analog distribution as a function of excitation energy in ^{24}Mg.

To do this one needs, in addition to the ft values, to determine a quantity that depends on $Y = |G_V/G_A|M_F/M_{GT}$, where G_V = vector coupling constant, G_A = axial vector coupling constant, M_F = Fermi matrix element = $\langle f|T^+|i\rangle$, and M_{GT} = Gamow-Teller matrix element = $\langle f|\sum_j \vec{\sigma}(j)t^\pm(j)|i\rangle$. For a $J \overset{\beta}{\to} J' \overset{\gamma}{\to} J''$ transition, the β-γ circular polarization correlation function is given by $W(\theta,\tau) = 1 + \tau\, v/c\, A\cos\theta$, where θ = angle between β and γ, τ = ±1 for right/(left) handed circular polarization, v/c = ratio of β speed to the speed of light, and

$$A = \frac{\sqrt{3}}{6}\,\frac{1}{1+y^2}\left(\mp\frac{J'(J'+1) - J(J+1) + 2}{\sqrt{J'(J'+1)}} - 4Y\right) F(\lambda\lambda J''J')$$

where F is an angular correlation coupling coefficient.

A single multipole radiation is assumed for the γ radiation. For the $4^+ \xrightarrow{\beta^+} 4^+ \xrightarrow{\gamma} 2^+$ transition in the decay of ^{24}Al, $A = (-0.083 + 0.7454Y)/1+Y^2)$. Hence by measuring A, one can determine the Fermi matrix element.

Our experimental arrangement to measure A utilizes the rabbit to make the radioactive sample (the rabbit is described in Ref. 1). Our detectors (see Fig. 4.3-1) consist of a plastic-surface barrier telescope for detecting β's and a Compton transmission polarimeter and NaI crystal for detecting γ's of a particular circular polarization. The plastic scintillator is a cylinder 12.7 cm in diameter and 5 cm deep; the surface barrier detector has an active area of 300 mm^2 and a depth of 700 microns. The NaI is a 5 in. × 6 in. crystal. The polarimeter (developed at Chalk River for the Mark II ^{21}Ne parity mixing experiment) has a core that is 7.3 cm in diameter and 10.2 cm long. The core and windings are enclosed in a flux return that is a cylinder with one tapered end (see Fig. 4.3-1). The outside diameter of the cylinder is 18.4 cm and the outside diameter of the tapered end is 10.8 cm. The polarimeter preferentially transmits right handed or left handed γ's depending on the direction of the $\vec{B}$ in the core. The polarimeter magnetization is synchronized with the rabbit. The direction of $\vec{B}$ is reversed every rabbit cycle just after the rabbit leaves the counting station. Therefore alternate counting cycles of the rabbit preferentially transmit γ's of opposite handedness.

The electronics for taking data is shown schematically in Fig. 4.3-1. We require a coincidence of the fast negative outputs of the plastic and surface barrier detector to identify a β in the telescope; γ rays are rejected with high efficiency since they have a small probability of generating a signal in the surface barrier detector. We then require a coincidence between the plastic-surface barrier coincidence and the γ ray signal. When this 3-fold coincidence condition is satisfied (i.e., β-$\Delta\beta$-γ) the output of the coincidence circuitry is used to start a TAC and gate the computer. The TAC is stopped by the NaI signal with an appropriate delay.

For each event generating a 3-fold coincidence output, we record the energy signal from the plastic, the surface barrier, the NaI and the TAC signals as well as a voltage proportional to the magnetization of the polarimeter. This information for each event is written on tape event-by-event using MULTI. In order to obtain a coincidence rate that will allow us to do the ^{24}Al decays in about one week of running time, the singles rate in the plastic and surface barrier detectors must be approximately 10^6 sec^{-1}. The singles rate in the NaI is on the order of 25 KHz and the TAC rate, which is the same as the coincidence rate is about 325 Hz. The low rates in the NaI and TAC allow us to convert the standard slow linear signals from the NaI and TAC to digital form in the Tracor-Northern ADC's. The TAC signal is also routed according to the state of the polarimeter. This keeps track of the polarimeter state for each event.

The singles rates in the plastic and surface barrier detectors are so high that standard slow linear signals would be severely piled up. Therefore we have interfaced a LeCroy Model 2249A ADC with our computer to convert the plastic and surface barrier signals. The LeCroy 2249A is a charge sensitive ADC that integrates fast negative signals of 100 ns or less. The plastic signal is only

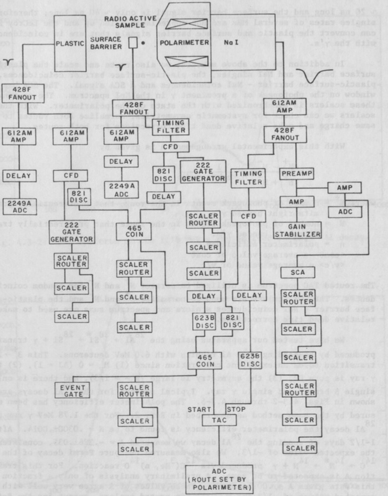

Fig. 4.3-1: Schematic diagram of detectors and electronics. Number in blocks refer to LeCroy module number. All routes are synchronized with the polarimeter.

$\sim$ 20 ns long and the surface barrier signal is only $\sim$ 40 ns long; therefore singles rates of several MHz are not appreciably piled up and the LeCroy 2249A can convert the plastic and surface barrier signals that are in coincidence with the γ's.

In addition to the above spectra, we also route and scale the plastic, surface barrier and NaI singles, the plastic-surface barrier coincidences, the plastic-surface barrier - NaI coincidences and a SCA signal. The SCA has its window on the photopeak of a prominent γ in the NaI spectrum. The routing of these scalers is synchronized with the state of the polarimeter. With these scalers we can check for systematic asymmetries, normalize both routes to the same charge and make relative dead time corrections for both routes.

With this experimental arrangement A is given by

$$A = \frac{N^+ - N^-}{N^+ + N^-} \frac{1}{\eta \langle\cos\theta\rangle \langle v/c\rangle}$$

where N^+ = number of photopeak events in the route that preferentially transmits right handed γ's.

N^- = number of photopeak events in the route that preferentially transmits left handed γ's.

η = polarimeter efficiency

$\langle\cos\theta\rangle$ = average value of $\cos\theta$

$\langle v/c\rangle$ = average value of v/c

The routed TAC spectrum is utilized to correct N^+ and N^- for random coincidences. The SCA scalers are used to normalize N^+ and N^- and the plastic-surface barrier - NaI coincidences scalers and spectrum sums are used to make relative dead time corrections.

We have tested our apparatus using the $^{28}Al \rightarrow {}^{28}Si^* \rightarrow {}^{28}Si + \gamma$ transition produced by bombarding thin Al rabbits with 6.0 MeV deuterons. This $3^+ \rightarrow 2^+ \rightarrow 0^+$ transition forms an excellent calibration since (1) $M_F = 0$ ($\Delta J = 1$), (2) the γ ray is pure E2, (3) the asymmetry is large ($A = -1/3$), and there is only a single β branch and single γ ray. Typical spectra for the ^{28}Al decays are shown in Figs. 4.3-2 through 4.3-5. The polarimeter efficiency has been measured by the same method as described in Ref. 2. For the 1.78 MeV γ ray of the ^{28}Al decay the polarimeter efficiency is found to be N = .0300±.0014. After 1-1/2 days of running the ^{28}Al decay we measured A = -.326±.035, consistent with the expected value of -1/3. We also measured the pure Fermi decay of the $^{14}O \rightarrow {}^{14}N^* \rightarrow {}^{14}N + \gamma$ produced via $^{12}C(^3He, n)^{14}O$ reaction. For this transition A is expected to be zero. A preliminary analysis of only a fraction of this data gives A = .0015±.0049. These values of A agree very well with the expected values of -1/3 and 0. All the routed scalers, except for the β-$\Delta\beta$-γ coincidence scalers where there is an asymmetry for ^{28}Al decays, had asymmetries of .001 or less. With these results, we are confident that we have a very good apparatus for measuring the Fermi matrix elements in mixed Fermi-

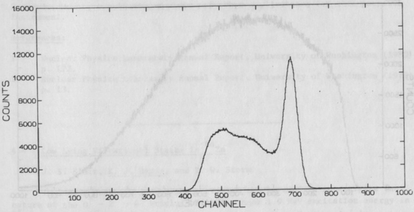

Fig. 4.3-2: NaI spectrum of the 1.78 MeV γ ray emitted in the ^{28}Al decay.

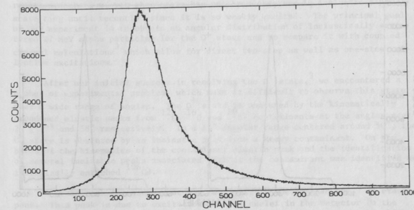

Fig. 4.3-3: Surface barrier spectrum of the β's emitted in the ^{28}Al decay.

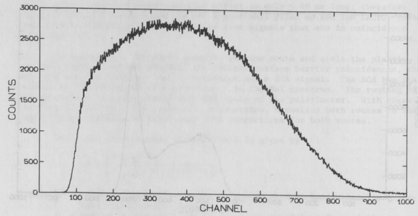

Fig. 4.3-4: Plastic spectrum of the β's emitted in the ^{28}Al decay.

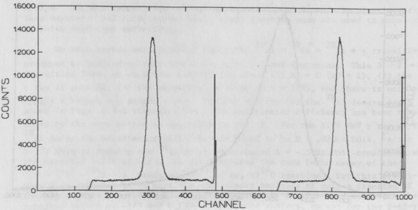

Fig. 4.3-5: TAC spectrum. The TAC is started by a β-Δβ-γ coincidence and stopped by the γ signal with an appropriate delay.

Gamow-Teller decays and that the ^{24}Al measurement will be relatively straightforward. We are considering a number of other applications for this powerful instrument.

References:

1. Nuclear Physics Laboratory Annual Report, University of Washington (1980), p. 172.
2. Nuclear Physics Laboratory Annual Report, University of Washington (1979), p. 13.

4.4 Low Lying Vibrational States in ^{64}Zn

J. S. Blair, K. J. Davis, and D. W. Storm

Inelastic scattering of alpha particles can be used to investigate the nature of the $0^+ - 2^+ - 4^+$ triplet of states near 1.9 MeV excitation energy in ^{64}Zn. The triplet is thought to be a set of "two-phonon" vibrational states which may be excited by a two-step reaction process. The angular distribution of alpha particles in a two-step process is predicted to be out of phase with that of a single-step process.[1] This has been verified in a previous experiment which measured the angular distribution of the 2^+ and 4^+ states.[2] The angular distribution of the 0^+ state is more sensitive to the details of the reaction mechanism, yet that state has not been observed in inelastic alpha scattering until recently[3] since it is so weakly excited. The principal goal of our experiment is to obtain an angular distribution of inelastically scattered 27 MeV alpha particles for the 0^+ state and to compare it with coupled channel calculations[3] which allow for direct two-step as well as one-step collective excitations.

After our initial success in resolving the 0^+ state,[3] we encountered a number of experimental problems which make it difficult to observe this state over a wide range of angles. The 0^+ state is obscured by the kinematically broadened elastic peaks from ^{12}C, ^{16}O and ^{28}Si contaminants at the angles near 29°, 37° and 58° respectively. In a 10° angular range centered around 50°, the 0^+ state is obscured by an inelastic peak from a heavy contaminant. On the basis of the kinematics of the contaminant elastic peak and the identification of several inelastic peaks associated with it the contaminant was identified as isotopically enriched ^{106}Cd.

A broad peak is observed at ∿ 2 MeV lower in energy than the ^{64}Zn elastic peak. This peak is due to excitation of ^{28}Si nuclei in the detector to the first excited state at 1.78 MeV followed by the emission of a gamma-ray which escapes from the detector. This peak is difficult to resolve from the 0^+ state and is particularly serious at angles less than 35° where the ^{64}Zn elastic peak is $\geq 10^4$ times bigger than the 0^+ state.

Our recent efforts have been directed towards solving these problems and improving the overall counting rate.

The use of rolled targets with a thickness of 500 $\mu g/cm^2$ increased the counting rate by a factor of five without significantly degrading the resolution.

The C and Si contaminants are most likely due to the cracking of vacuum pump oil and can be minimized by taking the data near 37° and 58° first and by using a cold finger to improve the vacuum in the vicinity of the target.

The source of the ^{106}Cd contaminant was identified by making targets by the direct evaporation of ^{64}ZnO onto a carbon backing. The targets made by this method showed no evidence of ^{106}Cd contamination so we concluded that the contaminant was introduced during the target preparation. We are in the process of having new targets made.

A factor of four increase in counting rate was obtained with a variable width nickel detector aperture with rounded edges of 1/8 in. radius which subtends a larger solid angle without worsening the slit scattering.

We are currently investigating techniques for rejecting events associated with nuclear reactions in the detector. This can be done by placing a ΔE-detector in front of the E-detector aperture. A comparison of $E + \Delta E$ and the energy inferred from ΔE can be used to distinguish events where energy is lost by nuclear reactions in the detector or by slit scattering from the E-detector aperture. By using a custom MBD-11 program we will be able to take data using the SINGLES data acquistion program. The viability of this technique will depend upon the obtainable energy resolution with the added ΔE detector.

References:

1. J. S. Blair, in Lectures in Theoretical Physics, Vol. VIII-C, Nuclear Structure Physics, P. D. Kunz, et al., eds., University of Colorado Press, Boulder (1966) p. 343.
2. N. Alpert, et al., Phys. Rev. C2, 974 (1970).
3. Nuclear Physics Laboratory Annual Report, University of washington (1980), p. 54.

4.5 Elastic and Inelastic Polarized-Proton Scattering via Isobaric Analog Resonances in ^{207}Bi and ^{209}Bi

N. L. Back, H. C. Bhang, J. G. Cramer, D. D. Leach, T. A. Trainor, and R. D. Von Lintig

As reported previously,[1] cross sections and analyzing powers have been measured for the elastic scattering of polarized protons from ^{206}Pb and ^{208}Pb, and for the inelastic scattering to the lowest 2^+ and 3^- states of ^{206}Pb and the lowest 3^- state of ^{208}Pb. The energy region over which these measurements were performed (14.25 to 18 MeV) includes the isobaric analog resonances (IARs) corresponding to the low-lying single-neutron states in ^{207}Pb and ^{209}Pb.

Some care was taken in determining the normalization of the cross-section data. The data were taken during four different series of runs; each of these series contained a run at 4 MeV for each target, and three of them contained unpolarized runs at 13.75 MeV for each target. The 4 MeV runs were used to obtain the relative normalization of the five detectors at 35° (monitor), 120°, 135°, 150°, and 165°. In most cases, the geometric solid angles had to be adjusted by 2% or less as a result of this procedure. The error in the relative normalization is ±0.25%, assuming that the cross sections are all Rutherford at 4 MeV.

Because of the large amount of multiple scattering in the target at 4 MeV, it was not possible to determine the absolute normalization at that energy. However, optical-model calculations showed that the monitor cross section was still within 0.5% of Rutherford at energies as high as 10 MeV. Therefore, the absolute normalization was determined by comparing the monitor yields at 8 and 10 MeV (for each target) with the optical-model predictions. Typically, the product of charge × target thickness × detector solid angle was found to be 8 - 12% higher than the independently-determined value [charge from the BIC charge integrator, solid angle from geometry, target thickness at 4 MeV from the separation of the carbon (and oxygen) contaminants on the front and back surfaces of the target]. Because of possible inaccuracies in the optical-model predictions and possible variations of the BIC with scale and beam current, the absolute normalization is assigned an error of ±2%.

Once the overall normalization was determined for one series of runs, the other series could be normalized to it by comparing the yields at 13.75 MeV. Finally, a monitor calibration was performed, in which the (unpolarized) monitor cross section for each target was measured between 13.75 and 18 MeV in energy steps of 0.25 MeV or less. Since the monitor cross sections vary smoothly in this region, with only small perturbations due to the IARs, this calibration was used to determine the normalization for all of the polarized runs. This was necessary because the multiple scattering at higher energies, though negligible for unpolarized runs, was significant when the polarimeter was placed between the target and the Faraday cup for the polarized runs, so that the BIC tended to understate the charge passing through the target. The errors used in the data analysis include the charge-normalization error, which comes from the statistical error in the monitor yield for a particular run and from the statistical errors in the nearest monitor calibration points; they do not include the absolute or relative normalization errors discussed earlier.

The ^{208}Pb elastic-scattering excitation functions have been analyzed with the program IAR4. This program calculates the cross section and analyzing power by adding the resonance amplitudes to background amplitudes which are simple functions of the energy. The "spin-flip" amplitude is represented by a third-order Taylor series expansion about the midpoint of the energy region of interest; the same is true for the "non-spin-flip" amplitude, except that it is multiplied by E^{-1} to take out the E^{-2} dependence of the Rutherford cross section. Each of the four angles has its own independent background; also, the phase between the background and each resonance is different at each angle (this phase cannot easily be related to the resonance mixing phase ϕ_R). The program performs a non-linear least-squares fit to all four of the cross-section and/or analyzing-power excitation functions, varying background and resonance parameters simultaneously.

Table 4.5-1 shows the results of this procedure for ^{208}Pb. The only resonance parameters which were kept fixed were the total width and energy for the weak $i_{11/2}$ and $j_{15/2}$ resonances. The errors quoted for the parameters reflect only the statistical errors in the data, including the charge-normalization errors mentioned above. In particular, the errors in E_R do not include an error in the analyzing-magnet calibration constant, which would move all of the values of E_R up or down by the same factor. The numbers in Table 4.5-1 are in good agreement with the values of Γ_p found by Baker, et al.[2] and with the values of Γ and E_R found by Wharton, et al.[3]

In Table 4.5-2 is a comparison of the level structure of ^{209}Pb as found in this work with that found in the literature.[3,4] In each case, the $g_{9/2}$ energy is taken as zero; the error is simply the sum (in quadrature) of the errors in E_R for the ℓ_j and $g_{9/2}$ resonances. Note that the values of E_R for the $i_{11/2}$

Table 4.5-1
Resonance Parameters for IARs in $^{209}Bi^*$

ℓ_j	Γ_p (keV)	Γ (keV)	E_R (MeV-c.m.)	ϕ_R (deg)[a]
$g_{9/2}$	21.59±0.21	260.5±2.3	14.8527±0.0012	1.10±0.26
$i_{11/2}$	1.828±0.071	224	15.632	-4.27±2.14
$j_{15/2}$	0.850±0.089	201	16.276	-8.17±4.54
$d_{5/2}$	49.03±0.42	304.5±2.3	16.4136±0.0012	-0.29±0.18
$s_{1/2}$	51.01±0.96	323.6±4.7	16.8867±0.0026	-0.27±0.34
$g_{7/2}$	32.77±0.57	281.3±3.5	17.3409±0.0016	2.98±0.23
$d_{3/2}$	46.32±0.74	298.2±3.9	17.3922±0.0022	-1.89±0.25

[a] ϕ_R comes from RESFIT; Γ_p, Γ, and E_R come from IAR4.

Table 4.5-2

^{209}Pb Level Scheme Comparison
(Excitation Energies in MeV)

ℓ_j	This Work	Wharton, et al.[a]	Table of Isotopes[b]
$g_{9/2}$	0	0	0
$i_{11/2}$	0.7793±.0012	0.794±.012	0.779
$j_{15/2}$	1.4233±.0012	1.411±.016	1.423
$d_{5/2}$	1.5609±.0017	1.570±.010	1.567
$s_{1/2}$	2.0340±.0029	2.037±.015	2.032
$g_{7/2}$	2.4882±.0020	2.500±.012	2.491
$d_{3/2}$	2.5395±.0025	2.546±.012	2.537

[a]Ref. 3 [b]Ref. 4

and $j_{15/2}$ resonances given in Table 4.5-1 were chosen so as to make the excitation energies of these levels agree with those given in Ref. 4.

In order to proceed with the analysis of the inelastic-scattering data, it is necessary to obtain a good optical-model description of the elastic scattering. This is done using two additional programs: (1) GENOAB, which performs a search on the optical-model parameters to obtain the best fit to the angular distributions at a small number of energies, and (2) RESFIT, which uses a fixed set of optical-model parameters and obtains the best fit to the four excitation functions by varying the resonance parameters. In each case, the cross sections and analyzing powers are calculated by adding the resonance amplitudes to the optical-model amplitudes, i.e.,

$$\sigma(E,\Theta) = |A(E,\Theta)|^2 + |B(E,\Theta)|^2,$$

$$P(E,\Theta) = 2\,\mathrm{Re}\,[A(E,\Theta)B^*(E,\Theta)]/\sigma(E,\Theta),$$

where $A(E,\Theta) = A_{OM}(E,\Theta) + \sum_i A_{RES,i}(E,\Theta)$

and $B(E,\Theta) = B_{OM}(E,\Theta) + \sum_i B_{RES,i}(E,\Theta)$.

For ^{208}Pb, GENOAB used five energies far from the major resonances (13.75, 14.25, 15.5, 16.0, and 18.0 MeV), fitting only to the four back angles. We started with the optical-model parameters given in Ref. 2, the values of Γ_p, Γ, and E_R given by IAR4, and the ϕ_Rs all set equal to zero. By varying the optical-model parameters in GENOAB, then varying the ϕ_Rs in RESFIT, then going back to GENOAB, and so on, we were able to obtain a consistent set of parameters. The values of ϕ_R are shown in Table 4.5-1; the optical-model parameters are given in Table 4.5-3.

Table 4.5-3

Optical-Model Parameters for ^{208}Pb+p

Parameter	Value	Error
U (MeV)	$57.78-.072*E_{lab}$	$(1.97, .087)^a$
W_v (MeV)	0	not varied
W_s (MeV)	$2.07+.794*E_{lab}$	$(2.47, .156)^a$
$U_{s.o.}$ (MeV)	6.99	0.54
r_R (fm)	1.24	0.01
r_I (fm)	1.23	0.02
$r_{s.o.}$ (fm)	1.07	0.02
r_c (fm)	1.19	not varied
a_R (fm)	0.71	0.01
a_I (fm)	0.57	0.02
$a_{s.o.}$ (fm)	0.53	0.06

[a] The two numbers are the errors in the intercept and the slope, respectively.

The data for one of the four angles (165°) are shown in Fig. 4.5-1, along with the best-fit calculations from IAR4 (solid curve) and RESFIT (dashed curve).

References:

1. Nuclear Physics Laboratory Annual Report, University of Washington (1980), p. 50.
2. Nuclear Physics Laboratory Annual Report, University of Washington (1974), p. 85.
3. W. R. Wharton, P. von Brentano, W. K. Dawson, and P. Richard, Phys. Rev. 176, 1424 (1968).
4. Table of Isotopes, 7th Edition, C. M. Lederer and V. S. Shirley, eds., John Wiley and Sons, New York, 1978.

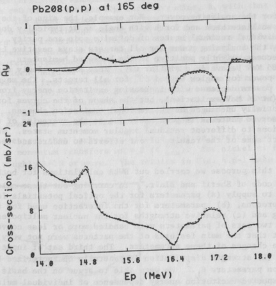

Fig. 4.5-1: Cross-section and analyzing-power excitation functions for ^{208}Pb $(\vec{p}, p_o)$ at 165°. The solid curve is a fit using seven IARs and a parameterized background. The dashed curve is a fit using the same IARs and an optical-model background.

4.6 <u>Analyzing Power of Proton Scattering to the Continuum</u>

H. C. Bhang, <u>I. Halpern</u>, and T. Trainor

Some years ago[1] we initiated a program to study analyzing powers in the continuum with polarized protons of the highest energy (18 MeV) available at our accelerator. Since then there have appeared[2] the results of a similar investigation at Osaka at the higher energy of 65 MeV.

Since we have reported the details of our measurements and data analysis in earlier reports, we will confine the present account to matters related to the interpretation of results. Both our results and those of Osaka show simple patterns for the analyzing power. For example, the sign of the analyzing power does not oscillate back and forth with angle as it typically does for scattering to individual residual states of definite spin and parity. For our results, at 18 MeV, the analyzing power for all targets stays negative between 30° and 90° and becomes slightly positive in the backward hemisphere. The Osaka results at 65 MeV behave in a similar way. They show a slowly varying positive analyzing power for angles beyond 60° for all targets. The magnitudes of the analyzing powers decrease with increasing excitation energy from values as high as +0.20 (at 14 MeV excitation), but the shape of the curves for Ay vs. θ remain essentially unchanged as the residual excitation changes. The simplicity of the observed patterns is presumably due to the averaging of the oscillatory contributions to different residual angular momentum states. We describe in this report some of the results of our efforts to understand these simple patterns.

For this purpose we carried out DWBA calculations for both sets of data using the code of Sherif and Blair.[3] In carrying out these calculations it was necessary to supply (a) parameters for the optical potentials for incoming and outgoing protons, (b) parameters for the interaction used for the inelastic scattering and (c) relative strengths for the nuclear multipoles being excited. The first two sets of parameters were handled more or less conventionally. It turned out that the main features of the patterns were not very sensitive to reasonable changes of these parameters. The third set of input numbers, the multipole (L) strength distribution is generally characterized by values of the deformation parameters β_L^2. We were able to argue on the basis of sum rules and the expected excitation energy dependence of individual multipoles that this distribution should be represented roughly by the form $L \exp(-L^2/2\gamma^2)$. The details of these arguments as well as other details of the analysis are to be found in the recent Ph.D. thesis of one of us (H.C.B.).[4] The best value for the single parameter, γ^2, which governs the strength distribution as a function of L was determined for each target by fitting the computed analyzing powers to the measured ones. These fitted γ^2 values turned out to be quite reasonable on the basis of crude microscopic estimates of the particle-hole level density spectrum as a function of L and excitation energy. With these fitted values for γ^2, it was found that the DWBA calculations reproduced the angular dependence of the measured analyzing powers rather well, especially for heavier targets and higher incident energies. The latter point is presumably due to the increased validity of taking smooth averages over L for distributions containing a larger number of L's.

In general the DWBA was in better quantitative accord with the 65 MeV data than with the 18 MeV data, and we therefore began by trying to understand the most conspicuous feature of the higher energy data, namely the sizeable and rather uniform back-angle positive analyzing power. This feature was a persistent result of the calculations in the sense that any reasonable excursions of parameters left it more-or-less intact. By "understanding" this feature, we mean identifying those elements in the DWBA calculation that are responsible for it.

To study the inner workings of the DWBA calculation we made cuts on critical input parameters. For example we compared the scattering from the region in radial space r=0 to r=0.8 times the nuclear radius, R, with that from the region r>0.8 R. The inner region gave a negative analyzing power and the outer region a positive one. Although making such cuts is sometimes misleading, since it tampers with interference effects, our calculations involved sufficient numbers of independent terms so that one could safely assume that the averages of interference terms remained negligible. The DWBA calculation was also cut according to incident angular momentum, ℓ. Here it was found that the positive analyzing powers come from the range $\ell>6$. For $\ell\leq 6$ the analyzing power was negative. These results point to glancing collisions as the source of the observed positive analyzing power. Finally we made cuts on the angular momentum transfer, L, and a typical set of results is shown in Fig. 4.6-1. Clearly the positive analyzing powers are associated with small angular momentum transfer.

One would expect that backward scattered grazing particles would correspond to angular momentum transfers of $\sim 2\ (\ell^{inc}_{max})$. For nickel at 65 MeV, this would be roughly L=10 or more. The results in Fig. 4.6-1 make us wonder

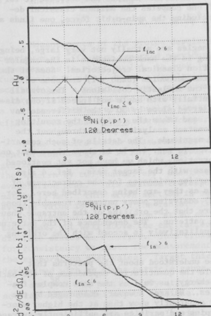

Fig. 4.6-1: The calculated analyzing power and differential cross-section for $(\vec{p},p')$ on nickel, as a typical backward angle, as a function of angular momentum transfer, L. The incident angular momentum, ℓ, was divided into two groups, one with $\ell\leq 6$ and the other with $\ell>6$.

how backward scattering could instead be dominated by scatterings with L less than four or five. A mechanism which suggests itself is that somehow the particles responsible for the positive analyzing power manage to orbit around to the opposite side of the nucleus before being emitted into the backward hemisphere. This picture is not unlike that recently discussed in connection with elastic deuteron scattering at comparable energies.[5] The idea is that the backward yield at the Osaka energy is dominated by events due to the particle flux orbiting around the nuclear periphery. There will not be very many such orbiting particles but when they scatter, it is their forward rather than backward scattering which contributes to the backward-emerging particles. Since the forward scattering probability far exceeds that for back scattering, a relatively small flux of orbiting projectiles can dominate the observed backward emission.

But why would these orbiting particles show a left-right asymmetry? Clearly it must arise from the spin-orbit forces. It is easy to appreciate that these forces essentially increase the radius of the effective optical potential for particles incident on one side of the nucleus and decrease it for those incident on the other side. If one computes the maximum classical deflection in the assumed potential, including the spin-orbit force, one finds a 30° difference for Ni at 65 MeV!

Now these classical deflection angles are actually not very large, being typically $\sim 50°$, and what one is seeing in the back hemisphere is the angular tail of the cluster of maximum deflection classical trajectories. Some of the angular width is associated with quantum mechanics ($\Delta\ell\Delta\theta \sim 1$) and some of it comes from the spread in angle due to the inelastic collisions. The overall angular distribution falls off exponentially with angle and indeed if one displaces two identical curves of the observed slope by 30°, the difference in classical deflections, left and right, and takes the ratio of the resulting cross sections, one finds a roughly constant analyzing power throughout the back hemisphere of about the observed magnitude. The details of such comparisons for the different targets are given in Ref. 4. It is shown there that one can reproduce quantitatively the observation, which we have not yet mentioned here, that the analyzing powers increase with the target mass. Ref. 4 also discusses a number of additional supporting evidences for the correctness of the interpretation of the DWBA results as they are being described here. For example, the fact that $(\vec{p},\alpha)$ and $(\vec{p},d)$ analyzing power patterns resemble those for $(\vec{p},p')$ fits nicely with the picture that the orbiting of the entrance channel $\vec{p}$'s is responsible for all of the patterns. The dependence of the patterns on incident energy also seems to be qualitatively in accord with the orbiting interpretation.

There is clearly much more to be understood about the patterns that Osaka and we have observed, for example the quantitative dependence of the backward patterns on residual excitation energy, as well as the more complex features of the patterns at forward angles. We are, however, encouraged by the results of our analysis so far. They apparently show that at the higher energies of the continuum, the residual spins and parities are sufficiently averaged that none of them dominates the analyzing power patterns. One can therefore hope to learn in sharper detail about aspects of the reaction mechanisms than is possible at the more commonly studied low-lying excitation energies. The use of polarization techniques at continuum excitations represents a sorely needed addition to the available tools to study reactions in which there is substantial energy loss, since the spectra and angular distributions of such reactions tend to carry very little information.

References:

1. Nuclear Physics Laboratory Annual Report, University of Washington (1976), p. 105. See also subsequent years.
2. H. Sakai, et al., Phys. Rev. Lett. 44, 1193 (1980).
3. H. Sherif, Ph.D. Thesis, University of Washington, 1968.
4. H. C. Bhang, Ph.D. Thesis, University of Washington, 1981.
5. E. J. Stephenson, et al., Fifth International Symposium on Polarization Phenomena in Nuclear Physics, Santa Fe, 1980, p. 481.

4.7 Inelastic Scattering of Protons from Nuclei with $46 \leq A \leq 102$

S. Laubach+, Z. Liu, R. M. Tromp*, T. A. Trainor, and W. G. Weitkamp

Measurements of the proton depolarization in inelastic scattering to the continuum of ^{63}Cu were reported previously.[1,2] It is desirable to extend these measurements to other nuclei, to look for variations of the depolarization as a function of Z and A. Because depolarization measurements involve the double scattering of a polarized beam, measurements are only feasible on nuclei giving a large yield of inelastic protons. Consequently, we have measured spectra for a variety of medium weight nuclei, looking for inelastic cross sections at excitation energies above a few MeV comparable or larger than those for ^{63}Cu.

The results of our measurements, which were made at 4 angles at an incident proton energy of 18 MeV, are given in Table 4.7-1. Inelastic spectra are generally rather complicated, but for ease of comparison, we have characterized the spectra by two quantities. One is the cross section at the maximum of the evaporation peak. This maximum corresponds to an excitation energy of approximately 15 MeV. This cross section is nearly constant at all angles, so the average value is given in the table. The second quantity is the cross section in the pre-equilibrium region, at an excitation energy just below the evaporation peak, but well above the excitation energy where inelastic scattering to discrete states is observed. This cross section is strongly forward peaked, so for consistency we quote the measurement at 90°. It is about 1 to 2 percent of the evaporation peak value. Target thicknesses for these measurements were determined with an alpha particle gauge. The results in the table show that ^{54}Fe and ^{58}Ni are particularly attractive for depolarization measurements, and several other nuclei may be feasible.

The cross section for inelastic proton scattering, especially for proton evaporation, should be related to the proton excess in a nucleus. Proton excess is the difference between the Z of the nucleus and the most stable (non-integer) value of Z calculated from the semi-empirical mass formula. Proton excesses for each of the nuclei are given in the table. However, the correlation is small.

Table 4.7-1
Inelastic Proton Scattering (E_p = 18 MeV)

Target Nucleus	Maximum Evaporation Cross Section (mb/sr-MeV)	90° Pre-equilibrium Cross Section (mb/sr-MeV)	Proton Excess
^{46}Ti	10	0.13	0.8
^{48}Ti	10	0.09	0
^{51}V	5	-	-0.3
^{54}Fe	17	0.17	1.4
^{56}Fe	4	0.06	0.6
^{58}Ni	18	0.18	1.7
^{60}Ni	9	0.15	0.9
^{63}Cu	10	0.19	0.6
^{68}Zn	3	-	-0.5
^{91}Zr	4	-	0.2
^{92}Mo	8	0.07	1.8
^{102}Pd	4	0.08	1.8

References:

+ Present address: University of Darmstadt, West Germany
* Department of Physics, University of Washington

1. Nuclear Physics Laboratory Annual Report, University of Washington (1980), p. 56.
2. W. G. Weitkamp, T. A. Trainor, I. Halpern, H. Bhang, and S. K. Lamoreaux, in Polarization Phenomena in Nuclear Physics-1980, G. G. Ohlsen, et al., eds., AIP Conference Proceedings 69, p. 511.

4.8 K-Shell Ionization Effects in p - ^{12}C Elastic Scattering

R. Anholt+ and J. S. Blair

In an experiment similar to one[1] performed several years ago in our laboratory, Duinker, et al.[2] have observed a substantial change in the probability for K-shell ionization as the incident proton energy is varied over the broad $s_{1/2}$ resonance in ^{13}N which occurs at an incident energy of 0.461 MeV. Unlike the situation in our earlier experiment[1] (3.15 MeV protons on ^{58}Ni), no appreciable variation due to "time delay" is expected in the p - ^{12}C experiment. Here, the width of the resonance, 38 keV, is much larger than the K-shell ionization energy, 284 eV; thus, since the corresponding nuclear time delay, $\hbar/\Gamma$, is far less than the characteristic atomic time, one predicts from semi-classical considerations[3] that the probability for K-shell ionization will be nearly the same as what would be found were there no nuclear resonance.

Duinker, et al.[2] have recognized that "time-delay" cannot account for their observations but have advanced the hypothesis that the variation is due to angular momentum exchange between the projectiles and the electron. Conceivably, the incident and final projectile waves might be "scrambled" when the K-shell electron is excited into $\ell \geq 1$ continuum states since the projectile must then transfer one unit of angular momentum to the electron.

We have been rather skeptical of this hypothesis. Exchange of angular momentum was considered in the fully quantum-mechanical time-independent derivation of the formula for the K-shell ionization probability quoted in Ref. 1. With somewhat altered notation, that formula may be written

$$P_K = \int_0^\infty d\varepsilon_f \sum_{\lambda\mu} \left| a_{\varepsilon_f\lambda\mu} \; [f(\Theta,E-\Delta E)/f(\Theta,E)] + b_{\varepsilon_f\lambda\mu}(\Theta) \right|^2 \qquad (1)$$

Here, P_K is the probability for ionizing the electron when a projectile with incident energy E is scattered to center-of-mass angle Θ; $f(\Theta,E)$ is the corresponding nuclear elastic scattering amplitude; $\varepsilon_f,\lambda,\mu$ are the final electron energy, angular momentum, and projection of angular momentum; a and b are equivalent to the atomic ampliudes of the semi-classical theory[3] for ionizing on the "way in" and "way out", respectively, including the monopole contributions when the projectile is inside the nucleus. For the relatively small energy transfer, ΔE, involved in carbon ionization there will be only a small change in the scattering amplitudes, even at resonance; thus one expects the ionization probability to show the slow energy variation of the semi-classical prediction in the limit where the "time delay" approaches zero.[3]

The observations of Duinker, et al.[2] had also caught the attention of R. Anholt of Stanford. Correspondence has led to a collaboration, in which we have looked for possible weak links in the arguments leading to eq. 1.

In this investigation we have formulated the problem of joint ionization and nuclear ionization in a fashion somewhat different from the approach originally[1] considered; specifically, we have assumed that the nuclear scattering could be described by a spherically symmetric potential, $V_N(R)$, rather than through an S-matrix description, which abjured knowledge of the nuclear wave functions in the nuclear interior. Such a potential description does not suffice to describe most nuclear resonances, but for the case at hand, it is a rather good approximation to consider the 461 keV $s_{1/2}$ resonance as a slightly unbound 2s single particle state. The virtue of the potential model is that the nuclear wave function is then presumably calculable over all values of the internuclear coordinate and thus one can use the standard methods of DWBA theory.

This is not the place to give a detailed account of the DWBA calculation but we do wish to indicate the main physical considerations and our conclusions.

Crucial to making a useful calculation is the recognition of the various lengths which characterize the electron-nuclear system. The most important parameters governing the electronic excitation are the radius of the K-shell orbit and the inverse minimum momentum transfer, $(1/q) \equiv 1/(K-K') \cong \hbar v/\Delta E$. The nuclear scattering is characterized by three distances: the distance of closest approach for a head-on Coulomb collision, the wavelength for relative nuclear motion, $(1/K)$, and some radius parameter for the specifically nuclear potential.

For the p - ^{12}C experiment, the electronic lengths are of the order of 10^{-9} cm or larger while the nuclear lengths are of the order 10^{-12} cm or less. Thus one can introduce a "matching" radius, R_m, intermediate between electronic and nuclear lengths, which cleanly separates the radial space into an exterior and an interior region.

We have gone on to show that the exterior contributions to the DWBA amplitude yield Eq. 1 with the qualification that the monopole sticking contribution is absent now from a and b. In particular, since we are permitted to use asymptotic radial wave functions in the exterior region, we find that there is no angular momentum exchange effect which alters Eq. 1 when the angular momentum transfer is non-zero.

Further, we have found that for $\ell \geq 1$ the interior contributions are negligibly small. The interior monopole contribution, however, may be appreciable but again does not modify the form of Eq. 1; rather, it restores the monopole sticking contributions to the atomic amplitudes, $a_{\varepsilon_f 00}$ and $b_{\varepsilon_f 00}$. The presence of those terms does cause a change in the ionization probability in the vicinity of the 0.461 MeV resonance in ^{13}N but the effect is small; a calculation retaining only monopole excitations shows a 4% dip in P_K at the minimum of the scattering cross section, an effect smaller by an order of magnitude and opposite in sign to the deviation observed in Ref. 2.

In summary, a DWBA calculation of the probability for K-shell ionization does not account for the results claimed by Duinker and collaborators. In particular their suggestion that the variation be attributed to angular momentum transfer is not supported by detailed calculation.

References:

+ Stanford University
1. J. S. Blair, P. Dyer, K. A. Snover, and T. A. Trainor, Phys. Rev. Lett. 41, 1712 (1978).
2. W. Duinker, J. Van Eck, and A. Niehaus, Phys. Rev. Lett. 45, 2102 (1980).
3. G. Ciocchetti and A. Molinari, Nuovo Cimento 40, 69 (1965).

4.9 $^{27}Al(^{3}He,d)^{28}Si$ to the 14.36 MeV (6^-,1) and the 11.58 MeV (6^-,0) Levels

Y. Fujita[+], M. Fujiwara[+], M. N. Harakeh[*], K. Hosono[+], M. Noumachi[++], M. Sasao[++], and K. A. Snover[**]

The so-called "stretched" particle-hole excitations, which have the maximum possible total J for a 1 particle-1 hole 1ħω excitation, are particularly interesting due to their simplicity. In particular, in a particle-hole model only one configuration may contribute. These states have been studied in a number of different nuclei, in inelastic electron, proton and pion scattering. In this report, we discuss ^{28}Si, where the 6^-, T=0 and T=1 levels at 11.58 MeV and 14.36 MeV have been previously identified as predominately stretched ($d_{5/2}^{-1}$, $f_{7/2}$) configuration. Inelastic electron[1] and proton[2,3] scattering excites the 6^-,1 level with comparable intrinsic strength, while proton and pion[4] scattering to the 6^-,0 level suggests that it is much less pure ($d_{5/2}^{-1}$, $f_{7/2}$) than the 6^-,1 level, by a factor of 2-3. Our (^{3}He,d) results show comparable cross section for population of the 6^-, T=1 and T=0 levels, indicating comparable spectroscopic strength for these levels.

The $^{27}Al(^{3}He,d)^{28}Si$ reaction was studied in the region of the 6^-, T=0 and T=1 states, at bombarding energies of E(^{3}He) = 39.72 and 60.06 MeV. The ^{3}He beam was obtained from the Research Center for Nuclear Physics (RCNP) cyclotron at Osaka, and the deuterons were detected in a position-sensitive focal plane detector[5] in the magnetic spectrograph RAIDEN.[6] Elastic scattering was measured at forward angles $\Theta_{c.m.} \sim 10° - 40°$ and the absolute cross section was determined by normalizing the elastic scattering results to optical model calculations. This normalization (the same at both energies) is consistent within 10% with absolute elastic scattering cross sections previously deduced at 60 MeV, and with cross sections deduced using a weighed target thickness and the nominal spectrometer acceptance.

Results for the 6^-, T=0 level at 11.58 MeV and the 6^-, T=1 level at 14.36 MeV are shown in Fig. 4.9-1. The measured cross sections are similar in magnitude and shape over the measured angular range. The 6^-, T=0 state is bound by ≈ 9 keV and hence poses no problem for DWBA analysis. The 6^-, T=1 level is, however, unbound and hence must be treated as such in order to obtain

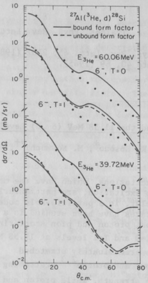

Fig. 4.9-1: Cross sections for the $^{27}Al(^3He,d)^{28}Si$ reaction to the 6^-, T=0 (11.58 MeV) and 6^-, T=1 (14.36 MeV) levels, measured at two different bombarding energies. Solid curves are calculated with a bound form factor for the transferred proton, and dashed curves with an unbound form factor.

accurate spectroscopic strengths. A wide variety of optical model parameters were tried for the ^{3}He and d channel, and for the transferred proton. For the best fit potentials, the results of Table 4.9-1 were obtained using the expression $d\sigma/d\Omega/_{exp} = NC^2S\ [(2J_f+1)/(2J_i+1)](d\sigma_{DWUCK}/d\Omega)/(2j+1)$ where N = 4.42.

The extracted spectroscopic factors showed little variation as a function of optical model parameters - from extensive parameter variations in the DWBA analysis and from the absolute cross section uncertainty, we estimate the overall uncertainty in these spectroscopic factors to be ≤ 20%. These results do show a substantial difference in $S_{T=1}$ depending on whether a bound or unbound form factor is used, illustrating the necessity for the latter. Our adopted spectroscopic factors are S = 0.41 and 0.35 for the T=0 and T=1 states, re-

Table 4.9-1

Spectroscopic Factors for the 6^-, T=0 and T=1 States in ^{28}Si

$E(^3He)$ (MeV)	$S_{T=0}$	$S_{T=1}$
39.72	.43	.33 (.53)[a]
60.06	.38	.37 (.53)[a]

[a]The first value shown was obtained with an unbound form factor for the transferred proton. The value in parenthesis was obtained using a bound form factor.

spectively, obtained from the average of the results at the two different bombarding energies.

The results for the 6^-, T=1 spectroscopic factor may be compared to our measured decay width $\Gamma_{po} = 3.78 \pm 0.17$ MeV for this level (see Sec. 5.3 of this report). From the form factor parameters $r_o = 1.325$ fm and $a_o = 0.5$ fm for the transferred proton, we calculate a single particle width $\Gamma_{s.p.} = 13.4$ keV. Our stripping results then predict

$$\Gamma_{po} = C^2 S \Gamma_{s.p.} = 1/2\ (0.35)(13.4\ \text{keV}) = 2.35\ \text{keV},$$

which is substantially less than the measured value quoted above. The sensitivity of the calculated Γ_{po} to form factor parameters was tested by doing calculations with different values of r_o and a_o. The result of choosing values of r_o and a_o which lead to larger $\Gamma_{s.p.}$ lead also to larger values of $d\sigma/d\Omega$(DWUCK) and correspondingly smaller values of S such that the product $C^2 S \Gamma_{s.p.}$ is stable within a few percent. Similar results obtain for adjustments leading to smaller $\Gamma_{s.p.}$. At present we have no explanation for this disagreement. If we use the measured Γ_{po} and the calculated single particle width $\Gamma_{s.p.} = 13.4$ keV to solve for S, we obtain S = 0.56. Thus we find $S_{T=1}$ lies between 0.35 and 0.56.

Perhaps the most reliable measurement from which the $(d_{5/2}^{-1}, f_{7/2})$ strength in the 6^-, T=1 state may be extracted is the measured electron scattering strength,[2] which corresponds to $S_{ee'} = 0.56/1.87 = 0.30$. This value is reduced from unity in part because the $d_{5/2}$ orbital has a nucleon occupancy n<12. In fact, mass-27 has about 68% of the full $d_{5/2}$ pickup strength[7] from ^{28}Si deduced from single nucleon transfer. This means that $a^2_{T=1} \cong 0.30/0.68 = 0.44$ where $a^2_{T=1}$ is the $(d_{5/2}^{-1}, f_{7/2})$ particle-hole intensity relative to the physical ground state of ^{28}Si. In order to compare the measured (^{3}He,d) strength to the (ee') strength, one should note that the mass-27 ground state gets only ≈ 78% of the total $d_{5/2}$ pickup strength.[7] Thus we may conclude that our best estimate of $a^2_{T=1}$ from stripping data is that it lies between $S_{T=1}$ and $S_{T=1}/0.78$. From above, we see that the range of values for $a^2_{T=1}$ deduced from stripping brackets the value of 0.44 deduced from (e,e').

Our best estimate for the 6^-,0 $(d_{5/2}^{-1}, f_{7/2})$ intensity is $a^2_{T=0} = a^2_{T=1} \cdot S_{T=0}/S_{T=1}$ where $S_{T=0}/S_{T=1} = 0.41/0.35 = 1.17$ as deduced from stripping, and for $a^2_{T=1}$ we use 0.44 deduced from (e,e'). The result is $a^2_{T=0} = 0.52$. Further support for these particle-hole intensities is given in Sec. 5.3 of this report, where it is shown that the measured M1 strength for the (6^-, T=1) → (6^-, T=0) transition is in good agreement with the a^2 values given above, assuming a reasonable value for M1 core polarization.

Finally, it is interesting to note that, although proton inelastic scattering[2] has been shown[3] to lead to a 6^-, T=1 spectroscopic strength close to that obtained from (e,e'), the 6^-, T=0 level is excited much more weakly. In fact, $S_{pp'}(T=0)/S_{pp'}(T=1) = 0.34$! The large disagreement between this (p,p') ratio and the value 1.17 obtained from $a^2_{T=0}/a^2_{T=1}$ (or, equivalently, $S_{T=0}/S_{T=1}$ from proton stripping) suggests that the effective interaction for inelastic scattering of intermediate energy 135 MeV protons is not well understood. A similar problem exists[4] in the relatively weak degree to which inelastically scattered 162 MeV pions excite the 6^-, T=0 level relative to the 6^-, T=1 level.

References:

+ Research Center for Nuclear Physics, Osaka, Japan

* KVI, Groningen, The Netherlands

++ Faculty of Science, Osaka University, Osaka, Japan

** Japan Society for the Promotion of Science Research Fellow, Osaka University, May-June, 1980

1. S. Yen, R. Sobie, H. Zarek, B. O. Pich, T. E. Drake, C. F. Williamson, S. Kowalski, and C. P. Sargent, Phys. Lett. 93B, 250 (1980).
2. G. S. Adams, A. D. Bacher, G. T. Emery, W. P. Jones, R. T. Kouzes, D. W. Miller, A. Pickelsimer, and G. E. Walker, Phys. Rev. Lett. 38, 1387 (1977).
3. F. Petrovich, W. G. Love, A. Picklesimer, G. E. Walker, and E. R. Siciliano, Phys. Lett. 95B, 166 (1980).
4. C. Olmer, B. Zeidman, D. F. Geesaman, T. S. H. Lee, R. E. Segel, L. W. Swenson, R. L. Bondrie, G. S. Blanpied, H. A. Thiessen, C. L. Morris, and R. E. Anderson, Phys. Rev. Lett. 43, 612 (1979).
5. Y. Fujita, K. Nagayama, S. Morinobu, M. Fujiwara, I. Katayama, T. Yamazaki, and H. Ikegami, Nucl. Inst. and Meth. 173, 265 (1980).
6. H. Ikegami, et al., RCNP Annual Report (1976), p. 113, and submitted to Nucl. Inst. and Meth.
7. P. M. Endt, Atomic and Nuclear Data Tables 19, 23 (1977).

5. RADIATIVE CAPTURE

5.1 Search for "Second Harmonic" Giant Resonances in the $^{27}Al(p,\gamma)$ and $^{27}Al(p,\gamma p)$ Reactions

D. Dowell, G. Feldman, and K. A. Snover

Recent work by Kovash and coworkers[1] has shown the existence of strong transitions to isolated high-lying states in the radiative capture of intermediate energy protons. In particular, they have observed capture gamma rays to states near E_x=19.2 MeV in $^{11}B(p,\gamma)$ with a dependence on proton energy which shows a broad resonance near $E_x \approx 42$ MeV. It has been speculated that these transitions are a result of "second harmonic" giant resonances, i.e., collective excitations built upon excited nucleon configurations. This is in analogy to the well known giant resonances formed from ground state configurations. While the resolution of this experiment was not sufficient to resolve the final states of the capture, it has been conjectured that the transitions are to negative parity states of high spin. The gamma ray energies agree well with decays to 1p-1h $1\hbar\omega$ excitations. The population of the "stretched" 1p-1h $1\hbar\omega$ states may be enhanced because of the 2J+1 multiplicity of magnetic substates.

It would be extremely interesting to look for similar effects in a somewhat heavier nucleus. We are interested in a case where one might be able to prove experimentally that the high spin 1p-1h $1\hbar\omega$ residual states are preferentially populated. In addition, a true collective resonance should be a general phenomenon observable in other nuclei. We have chosen to investigate the $^{27}Al(p,\gamma)$ and the $^{27}Al(p,\gamma p)$ reactions, as illustrated in Fig. 5.1-1. An intermediate energy proton ($E_p \approx 25$ MeV) may be captured by the ^{27}Al nucleus to form a

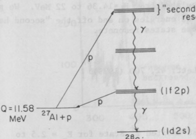

Fig. 5.1-1: Radiative capture reaction for producing the "second harmonic" resonance.

"second harmonic" resonance at approximately $3\hbar\omega$ excitation energy. This resonance may then photon decay to states which are excited by $1\hbar\omega$ relative to the ground state. Our objective is to make singles measurements with good gamma ray energy resolution and to measure the proton decays of the $1\hbar\omega$ "final" states that are coincident with the populating gamma rays.

Fig. 5.1-2 shows our spectra of capture gamma rays from $^{27}Al(p,\gamma)$ at E_p=17 and 23.5 MeV. The 10 in. × 10 in. NaI spectrometer was placed at 90° to the beam direction and beam currents of 50 to 100 nA were used on a 0.7 mg/cm^2 target of commercial aluminum foil. The ground state and first few excited state transitions are clearly seen, as well as transitions to higher excited states. The E_p=23.5 MeV spectrum is taken near the expected maximum of the second harmonic giant resonance. The positions of some of the known high spin $1\hbar\omega$ $(1f)^1(1d)^{-1}$ final states are indicated in the figure. The correlation of structure in our E_p=23.5 MeV spectrum and the location of these 1p-1h states suggests that they indeed are preferentially populated.

Also shown in Fig. 5.1-2 is the neutron background present in these spectra. At E_p=17 MeV this background was directly measured using pulsed beam time-of-flight techniques. At E_p=23.5 MeV where a pulsed beam is not available, this background was estimated from measurements with a thick Pb absorber placed between the detector and the target. This eliminates all gamma rays produced at the target. Neutron attenuation in the Pb absorber was measured at lower bombarding energies using pulsed beams, and extrapolated to higher bombarding energies.

We have also made exploratory measurements of the $^{27}Al(p,\gamma p)$ reaction. The protons were detected in an energy telescope consisting of a 150 micron ΔE detector and a 2 mm E detector. We have collected limited statistics in about 10-12 hours of beam time with an average beam current of 200 nA. We observe γ-p coincidences corresponding to states populated from E_x=14.36 to 22 MeV. We plan to measure such spectra at incident proton energies on and off the "second harmonic" resonance to observe which of these states resonate.

Reference:

1. M. A. Kovash, et al., Phys. Rev. Lett. 42, 700 (1979).

5.2 $^{11}B(p,\gamma)^{12}C$ to the Ground and First Excited 2^+ State for E_p = 2.5 to 5.4 MeV

D. Dowell, G. Feldman, M. M. Hindi, and K. A. Snover

Using the 10 in. × 10 in. NaI photon spectrometer and a bare 5 in. × 6 in. NaI crystal, we measured the yield of capture gamma rays to the ground state and first excited state in $^{11}B(p,\gamma)^{12}C$ from E_p=2.4 to 5.4 MeV. We originally

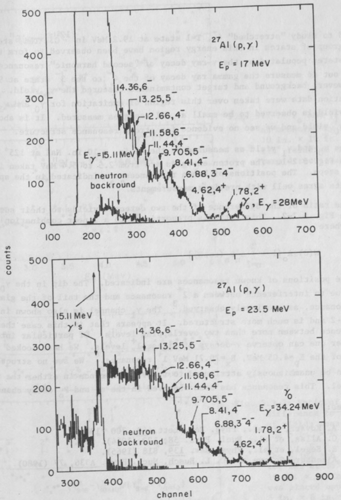

Fig. 5.1-2: NaI spectra for E_p=17 and 23.5 MeV. The neutron background in the 17 MeV spectrum was determined by pulsed beam time-of-flight techniques. The 23.5 MeV spectrum background was estimated from a thick lead absorber measurement.

intended to study "stretched" 4^-, T=1 state at 19.2 MeV in ^{12}C. This state and/or group of states in this energy region have been observed to form the residual states populated by the γ-ray decay of "second harmonic" resonances.[1] We had set out to measure the gamma ray decay of the 4^- to the 3^- state at 9.64 MeV; however, background and target contaminants obscured the γ_3 yield. Angular distribution data were taken over this region of excitation for γ_0 and γ_1 decays. The γ_2 yield is observed to be small at all energies measured. It is about 10% of the γ_0 yield and we see no evidence for strong resonance structure.

The γ_0 and γ_1 yield as measured by the 10 in. × 10 in. NaI at 125° is shown in Fig. 5.2-1. The proton energies are from 2.5 to 5.4 MeV taken in 50 to 100 keV steps. The positions of known resonances are indicated in the spectra. These data agree well with previous measurements.[2,3]

The ratio of the difference of the two detector yields to their sum is shown in Fig. 5.2-2. This ratio is proportional to a linear combination of a_1 and a_3 where

$$W(\Theta) \simeq A_o[1 + \sum_{n=1}^{4} a_n P_n(\cos\Theta)]$$

Again the positions of known resonances are indicated. The dip in the γ_0 channel is due to interference between a 2^+ resonance and the tail of the giant dipole resonance, as previously observed.[3] The γ_1 channel is also shown in Fig. 5.2-2 and is much more structured. It appears that in this case there is interference between more than two overlapping levels. Of particular interest is whether one can observe γ-decays of higher 1^+ levels. We have looked for the γ-decay of the E_p=4.05 MeV, E_x=19.71 MeV 1^+ resonance.[4] We see no structure which can be unambiguously attributed to this 1^+ resonance in either the γ_0 or γ_1 channel. This resonance has been observed in the n_o and P_o decay channels.[4]

References:

1. M. A. Kovash, et al., Phys. Rev. Lett. 42, 700 (1979).
2. R. G. Allas, et al., Nucl. Phys. 58, 122 (1964).
3. R. E. Segel, et al., Phys. Rev. 139, 818 (1965).
4. F. Ajzenberg-Selove and C. L. Busch, Nucl. Phys. A336, 77 (1980).

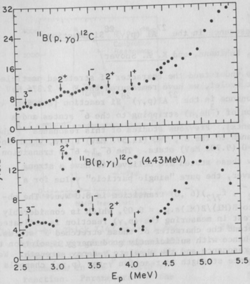

Fig. 5.2-1: γ_o and γ_1 yields as measured by the 10 in. × 10 in. NaI at 125° relative to the beam direction.

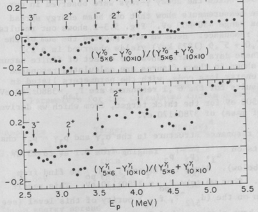

Fig. 5.2-2: Ratio of the difference to the sum of yields measured by the 5 in. × 6 in. NaI and 10 in. × 10 in. NaI. The 5 in. × 6 in. detector was at 55° and the 10 in. × 10 in. crystal was placed opposite the 5 in. × 6 in. at 125°.

5.3 The Stretched 6^-, T=1 Resonance in the $^{27}Al\ (p,\gamma)^{28}Si$ Reaction

G. Feldman, M. Hindi, E. Kuhlmann, and K. A. Snover

As part of our effort to understand the character of stretched particle-hole 1 $\hbar\omega$ excitations in light nuclei, we have remeasured the E_p = 2.876 MeV (Ex = 14.356 MeV) 6^-, T=1 resonance in the $^{27}Al(p,\gamma)^{28}Si$ reaction [see Sec. 4.9 of this report for a discussion of (^3He,d) stripping to the 6^- states and a comparison with other experiments]. Previous studies of this resonance[1,2] show that it has a 100% γ-decay branch to the 6^-, T=0 (11.577 MeV) state, which in turn decays 100% to the 5^-, T=0 (9.702 MeV) state. The $6^-,1 \rightarrow 6^-,0$ transition was found[1] to be pure M1. Now these states are believed to have a strong $(d_{5/2}^{-1}, f_{7/2})$ component; however, the pure "single particle" value for a $(d_{5/2}^{-1}, f_{7/2})(6^-,1) \xrightarrow{M1} (d_{5/2}^{-1}, f_{7/2})(6^-,0)$ transition is 8.0 W.u. The observed strength[1] corresponds to $B(M1)/B(M1)_{s.p.} \approx 0.09$, which is considerably smaller than unity. Our interest in measuring the (p,γ) reaction is motivated by the desire to better understand the character of these stretched 6^- states. We remeasured the 6^-, T=1 resonance with sufficiently good energy resolution to deduce the total width of the resonance and the absolute γ-decay strength. We also looked for possible resonance strength in reaction γ-ray (p,xγ) channels and for weak γ-decay branches.

Our experimental results on the total width are shown in Figs. 5.3-1 and 5.3-2. Fig. 5.3-1 shows our results for a narrow (Γ<230 eV) "calibration" resonance[3] at E_p = 3670 keV, for which the decay γ-rays were observed in our large NaI spectrometer. These measurements show that our beam energy spread (assumed Gaussian) lies in the range 450-800 eV. Fig. 5.3-2 shows our results for the E_p = 2876 keV 6^-, T=1 resonance. Here we have plotted the sum of the $6^-,1 \rightarrow 6^-,0$ (2779 keV) and $6^-,0 \rightarrow 5^-,0$ (1875 keV) yields observed in a 15% Ge(Li) detector at Θ_γ=90°. These data clearly show the effect of finite natural resonance width. The curves shown in these figures are calculated resonance yields using a discontinuous energy loss code, with the parameters listed in Table 5.3-1. Our best fit results for the 6^-,1 resonance are Γ_{Lab}=3880±200 eV for the thin target and 4250±500 eV for the thick target, from which we derive a total level width (center of mass) of 3780±170 eV.

From the absence of any resonance structure in the $\alpha_1\gamma$ and $p_1\gamma$ - $p_3\gamma$ channels we may set 1σ upper limits on Γ_{α_1}, Γ_{p_1}-Γ_{p_3} ranging from 0.1 eV to 25 eV (assuming Γ_γ = 0.54 eV - see below). Since $\Gamma = \Sigma\Gamma_i$ and $\Gamma_\gamma \ll \Gamma_{po}$ we find from these limits that $\Gamma_{po}/\Gamma>0.987$. Thus we take Γ_{po} = 3780±170 eV. This result provides important information on the $(d_{5/2}^{-1}, f_{7/2})$ purity of this level (see Sec. 4.9 of this report). We have also searched for weak γ-decay branches of this resonance. For example, we find that the γ-branching ratio for the $6^-,1 \rightarrow 5^-,0$ (9.70 MeV) transition is <3% of the $6^-,1 \rightarrow 6^-,0$ decay, corresponding to a ratio of reduced M1 strengths of <0.6%. It is surprising that this transition is so strongly hindered.

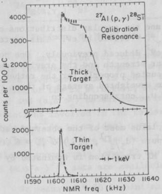

Fig. 5.3-1: Thick (147 μg/cm^2) and thin (12.6 μg/cm^2) target data over the narrow E_p = 3.671 MeV resonance in the $^{27}Al(p-\gamma)$ reaction. Parameters for the calculated curves are shown in Table 5.3-1

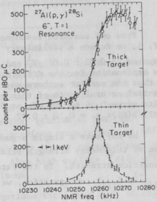

Fig. 5.3-2: Thick and thin target data over the E_p = 2.876 MeV 6^-, T=1 resonance. Parameters for the calculated curves are shown in Table 5.3-1.

Table 5.3-1

Parameters for the Calculated Curves Shown in Figs. 5.3-1 and 5.3-2

Resonance	Target	BES(eV)[a]	Γ(eV)[b]	t(μg/cm^2)[c]
3.671 MeV	thick	700	130	147
	thin	450	175	15
2.876 MeV	thick	800	4250±550	147
	thin	450	3915±200	15

[a]beam energy spread
[b]laboratory resonance width
[c]target thickness

From our measured resonance strengths and the angular distributions of Ref. 1, we deduce a preliminary value of $\Gamma_p\Gamma_\gamma/\Gamma = 0.54 \pm 0.11$ eV. This is to be compared to 0.32 ± 0.07 eV[1] and 0.23 ± 0.08 eV[2] deduced previously. One possible explanation for the difference between our strength and the previous values is that the earlier authors may not have accounted properly for the rather substantial natural width of this resonance. An unweighted average of these results gives 0.36 ± 0.09 eV, or 0.80 ± 0.20 W.u., corresponding to $B(M1)/B(M1)_{s.p.} = 0.10 \pm 0.02$.

We may make a simple argument which explains most of the observed reduction of this decay strength relative to the pure $(d_{5/2}^{-1}, f_{7/2})(6^-,1 \rightarrow 6^-,0)$ transition strength. To the extent that the M1 transition is dominated by the $(d_{5/2}^{-1}, f_{7/2})$ configuration, we may write

$$B(M1)/B(M1)_{s.p.} = a^2_{6^-,1} \cdot a^2_{6^-,0} \cdot f_{cp}$$

where $a_{6^-,T}$ is the amplitude for the $(d_{5/2}^{-1}, f_{7/2})$ configuration (relative to the physical ground state of ^{28}Si) in the $6^-,T$ level and f_{cp} is a core-polarization factor which accounts for admixtures in these states of the giant M1 resonance. In fact the $(d_{5/2}^{-1}, f_{7/2})(6^-1 \rightarrow 6^-,0)$ single particle M1 strength is just proportional to the sum of the isovector magnetic moments of a $d_{5/2}$ and an $f_{7/2}$ nucleon. Hence we may estimate $f_{cp} \simeq [\mu_{IV}/\mu_{IV}\ (\text{Schmidt})]^2$ where μ_{IV} is the measured isovector magnetic moment of the mass-27 $5/2^+$ ground state. This yields $f_{cp} \simeq (0.67)^2 = 0.45$. Taking $a^2_{6^-,1} \simeq 0.44$ and $a^2_{6^-,0} \simeq 0.52$ (see Sec. 4.9 of this report) gives a calculated value of 0.10 for $B(M1)/B(M1)_{s.p.}$, in good agreement with experiment.

References:

1. G. F. Neal and S. T. Lam, Phys. Lett. 45B, 127 (1973).
2. C. Miche, J. P. Gonidec, A. Huck and G. Walter, Revue de Physique Appliquée 8, 307 (1973).
3. J. L. Osborne, E. G. Adelberger, and K. A. Snover, Nucl. Phys. A305, 144 (1978).

5.4 A High Resolution Study of the Giant Quadrupole Resonance in the $^{24}Mg(\alpha,\gamma_o)^{28}Si$

G. Feldman, M. M. Hindi, E. Kuhlmann, and K. A. Snover

Our motivation for continued study of (α,γ) reactions in the giant quadrupole resonance (GQR) region is primarily 2-fold: (a) most previous (α,γ) studies have been made in coarse energy steps insufficient for a clear understanding of the E2 structure, and (b) more detailed comparisons of analogous (α,γ) and $(\alpha,\alpha'\alpha_o)$ measurements are necessary in order to better understand the limitations involved in the inelastic α-scattering studies of the GQR. $^{24}Mg(\alpha,\gamma_o)^{28}Si$ is an ideal case to study since previous measurements of this reaction (Ref. 1; see also Ref. 2) are quite old, in coarse energy steps, and indicate anomalously large E2 cross sections. Also high quality $^{28}Si(\alpha,\alpha')$[3,4] and $(\alpha,\alpha'\alpha_o)$[5,6] data are available for comparisons.

We measured ∿ 50 5-point angular distributions for $^{24}Mg(\alpha,\gamma_o)^{28}Si$ from $E_\alpha \cong 4.1 - 14.0$ MeV ($E_x = 13.5 - 22.0$ MeV) and extracted E1 and E2 cross sections and the relative phase factor cos δ. Targets of 242 ± 19, 524 ± 34 and 1250 ± 90 μg/cm^2 rolled ^{24}Mg (>99%) were used, with thicknesses deduced from a narrow $^{24}Mg(p,p'\gamma)$ resonance. Absolute cross sections were deduced to ± 10% using the known[6] (± 3%) $^{12}C(p,\gamma)$ resonance strength to calibrate the γ-detector efficiency. Energy step size was equal to the energy loss in the target and varied from $\Delta E_x = 130$ near the lowest energies to 290 keV near the highest energies. Results are shown in Fig. 5.4-1, where we plot cross sections and the relative E1-E2 phase factor cos δ for the inverse $^{28}Si(\gamma,\alpha_o)^{24}Mg$ reaction obtained using detailed balance.

Several interesting features of Fig. 5.4-1 are immediately apparent: (a) both E1 and E2 cross sections show a lot of structure, (b) cos δ shows strong deviations from zero. The E1 structure is known from an autocorrelation analysis of higher resolution data[1] to have a strong (Γ ∿ 65 keV) "compound nucleus" component and perhaps also a weaker Γ ∿ 300 keV intermediate structure component. Our E2 results show strong variations with energy indicating semi-isolated resonances (or intermediate structure). At lower energies sharp structure is apparent with width Γ ≤ ΔE (target) ∿ 130 keV, while at higher energies most of the structure is broader. The fact that cos δ shows substantial deviations from zero shows that substantial phase information remains in both the E1 and E2 channels averaged over ΔE (target). Hence neither channel can be dominated by fluctuations arising from very narrow overlapping resonances.

Our E1 and E2 cross sections are (on the average) lower by a factor of 2 and 3, respectively, than the corresponding cross sections measured at Argonne[1,2]. In particular, our E2 cross sections do not show a strong peak near the center of the GQR, as previously observed.[2] The difference in E1 cross sections is related to the overall absolute cross section normalization, while

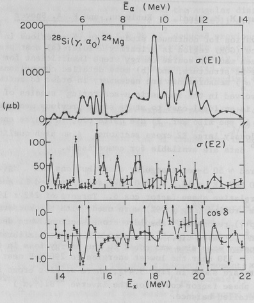

Fig. 5.4-1: E1 and E2 cross sections, and the phase factor cos δ for the $^{28}Si(\gamma,\alpha_o)^{24}Mg$ reaction obtained from the measured inverse cross sections using detailed balance.

the additional discrepancy in E2 cross sections must be related to differences in angular distribution shapes. Our NaI spectrometer, with good energy resolution, ∿ 4% FWHM (and correspondingly good separation of γ_o and γ_1) and excellent cosmic ray suppression, produced clean spectra at all energies and angles. Our confidence in our results is supported by the number of energies at which we extract a value of zero for σ_{E2} (within errors). The Argonne spectra, taken with poorer resolution and no cosmic ray suppression, would have been much harder to use to obtain γ_o with a systematic uncertainty of less than several percent. Such precision is necessary for the reliable extraction of E2 cross sections which are of the order of 10% (or less) of the E1 cross sections.

In Fig. 5.4-2 our results are compared with the Heidelberg decay-coincidence $^{28}Si(\alpha,\alpha'\alpha_o)$ measurements.[5] One may express the E2 energy-weighted sum rule (EWSR) equivalently in terms of $\int\sigma_{E2}(\gamma,x)dE/E^2$ and Σ E·B(E2). Making the approximation in the inelastic α-scattering that the sum rule fraction E·B(E2)

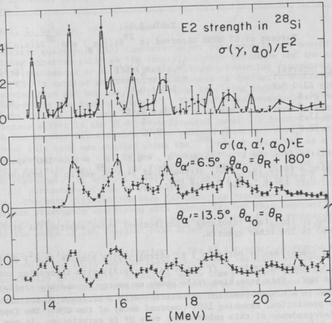

Fig. 5.4-2: (Top Part): $\sigma_{E2}(\gamma,\alpha_o)/E^2$
(Bottom Parts): $E\cdot\sigma(\alpha,\alpha'\alpha_o)$ where $\sigma(\alpha,\alpha'\alpha_o)\equiv d^3\sigma_L(\alpha,\alpha'\alpha_o)/d\Omega_{\alpha'}d\Omega_{\alpha o}dE$, from Ref. 5. For $\Theta_{\alpha o} = \Theta_R + 180°$, the vertical scale is chosen to give the same %EWSR per MeV as in the (γ,α_o) plot.

contained in an interval ΔE at energy E is proportional to $E\cdot d^3\sigma_L(\alpha,\alpha'\alpha_o)/d\Omega_{\alpha'}d\Omega_{\alpha}dE$, we arrive at the middle plot for the antirecoil ($\Theta_{\alpha o}=\Theta_R + 180°$) spectrum, normalized to an overall strength[4,5] of 3.7 ± 0.9% of the EWSR for E = 15.4 - 24.8 MeV (we use $R^2_{rms} = 9.61$ fm^2 in the sum rule). The similarity in total strength and shape of $\sigma(\gamma,\alpha_o)/E^2$ and $E\cdot\sigma(\alpha,\alpha'\alpha_o)$ is impressive (see also Table 5.4-1) and confirms the detailed accuracy of the inelastic scattering technique for extracting E2 strength. The bottom of Fig. 5.4-2 shows a similar plot for $\Theta_{\alpha o} = \Theta_R$ (with an arbitrary vertical scale). This spectrum, which is known to contain quasi-free scattering contributions (in

Table 5.4-1

Percent of E2 EWSR Observed in $^{28}Si(\gamma,\alpha_0)$ and $^{28}Si(\alpha,\alpha'\alpha_0)$

Energy Interval	$\int\sigma_{E2}(\gamma,\alpha_0)dE/E^2$	$\int E\cdot\sigma(\alpha,\alpha'\alpha_0)dE^*$
13.45 - 22.0 MeV	3.8 ± 0.4%	
15.4 - 24.8		3.7 ± 0.9%
14.1 - 22.0	3.8 ± 0.4%	4.2 ± 1.0%
14.1 - 17.9	2.4%	2.5%
17.9 - 22.0	0.9%	1.7%

*Calculated from the E_α = 155 MeV, $\Theta_{\alpha'}$ = 6.5°, $\Theta_{\alpha o} = \Theta_R$ + 180° spectrum,[5] assuming a total (α,α') E2 strength[4] of 34 ± 6% and an α_o branching ratio[5] of 0.11 ± 0.02 for E = 15.4 - 24.8 MeV.

addition to the giant resonance contribution) shows substantial differences compared to the other spectra.

A comparison of our (γ,α_o) E2 strength with singles (α,α') E2 strength[3] shows a branching ratio $\Gamma_{\alpha o}/\Gamma$ which falls rapidly with increasing energy above E_x = 16 MeV. This branching ratio shows an energy dependence similar to that obtained in a Hauser-Feshbach calculation with a strength approximately twice the HF prediction, assuming 100% compound decay of the GQR. The (approximate) energy independence of this enhancement over HF is surprising. It may arise from the doorway (particle-hole) GQR configuration, which would produce an energy dependence similar to HF in the limit where the total nonstatistical decay probability of the GQR into all channels is small compared to the compound part.

References:

1. L. Meyer-Schutzmeister, Z. Vager, R. E. Segel, and P. P. Singh, Nucl. Phys. A108, 180 (1968).
2. L. Meyer-Schutzmeister, R. E. Segel, K. Raghunathan, P. T. Devebec, W. R. Wharton, L. L. Rutledge, and T. R. Ophel, Phys. Rev. C17, 56 (1978).
3. K. Van der Borg, M. N. Harakeh, S. Y. Van der Werf, A. Van der Woude, and F. E. Bertrand, Phys. Lett. 67B, 405 (1977).
4. K. T. Knopflë, G. J. Wagner, A. Kiss, M. Rogge, C. Mayer-Boricke, and Th. Bauer, Phys. Lett. 64B, 263 (1976).
5. G. J. Wagner, in Giant Multipole Resonances, F. E. Bertrand, ed., Harwood Academic Publishers, 1980, p. 251; H. Riedesel, Ph.D. thesis, Heidelberg, 1979, and private communication.
6. R. E. Marrs, E. G. Adelberger, and K. A. Snover, Phys. Rev. C16, 61 (1977).

5.5 The E2 Isovector Giant Resonance as Seen Through the Capture of Fast Neutrons*

K. Aniol, I. Halpern, and D. Storm

The electric quadrupole (E2) isovector giant resonance is not nearly so well established experimentally as the electric dipole resonance and the electric isoscalar resonances up to E3. This is because isovector resonances are not so easily excited as isoscalar resonances in inelastic scattering of the common projectiles and because, in reactions involving photons, the E2 tends to be overshadowed by the much stronger E1. To avoid this overshadowing one typically looks for the isovector E2 in radiative capture reactions by searching for a conspicuous effect in the E1-E2 interference; namely, a front-to-back asymmetry in the angular distribution of the emitted photons. Some years ago an asymmetry of this kind was studied using the $^{208}Pb(p,\gamma)$ reaction[1] as a function of excitation energy up to ~ 28 MeV. The excitation function for the asymmetry showed a definite bump which was reasonably interpreted as being due to an E2 isovector resonance. It was not possible, however, to establish the values of the critical parameters of the E2 resonance on the basis of the experimental observations. The main difficulties were (a) that the resonance bump sat on a large background presumably associated with direct (rather than resonant) E2 capture, and (b) model calculations of the expected shape of the resonance did not resemble the shape of the residual bump after background subtraction.

We report here the first observation of the E2 isovector resonance in a heavy nucleus using the (n,γ) capture reaction. (This reaction has been used earlier successfully to survey E2 strengths below the isovector resonance.)[2] Although our preliminary measurements are not crisp enough to allow the extraction of the critical parameters of the E2 resonance, they are qualitatively clear and very encouraging.

The (n,γ) reaction is unquestionably more difficult experimentally than (p,γ) but it is expected to be much easier to interpret. As we have pointed out earlier,[3] there is almost no direct capture E2 background at all when neutrons are captured. Thus for neutrons the front-to-back asymmetry is due to resonant (collective) E2 excitation exclusively and there is not the uncertain subtraction problem that occurs in (p,γ).

It is easy to provide a rough framework for the interpretation of the (n,γ) measurement. It shows what one should expect to see in an asymmetry measurement and what this expectation depends on. The amplitude $F(\Theta)$, for dipole plus quadrupole capture which leads to a particular residual state depends on the angle Θ at which the capture photon is observed. Aside from factors common to $F(\Theta)$ and $F(\pi-\Theta)$, this amplitude can be represented as the sum of two terms

$$F(\Theta) = \frac{1}{E - E_D + i\frac{\Gamma}{2}D} + \frac{R}{E - E_Q + i\frac{\Gamma_Q}{2}} \cos\Theta$$

Here E_D, E_Q, Γ_D and Γ_Q are the dipole and quadrupole resonance energies and widths; E is the energy of the emitted photon and the factor $\cos\Theta$ reflects the fact that classically (i.e., for high J states) the quadrupole capture distribution goes as $\sin^2\Theta\cos^2\Theta$ while the dipole distribution goes as $\sin^2\Theta$. The constant R can be complex. It basically gives the ratio of quadrupole to dipole amplitude. In simple models in the high energy limit, R is expected to be real and positive. Its expected magnitude can be crudely estimated from sum rules. A value $R \simeq 0.2$ is not unreasonable.

What one typically measures is the asymmetry

$$A(\Theta) = \frac{Y(\Theta) - Y(\pi-\Theta)}{Y(\Theta) + Y(\pi-\Theta)}$$

where the yields Y are proportional to the absolute squares of $F(\Theta)$. Factors in the amplitude other than those shown in $F(\Theta)$ drop out in the ratio $A(\Theta)$. It is customary to use $\Theta = 55°$ (and therefore $\pi-\Theta = 125°$). [These angles are close to where $P_2(\cos\Theta)=0$.] The asymmetry $A(55°)$ can then be expressed as a function of the various parameters which appear in the expression for F. Fig. 5.5-1 shows a series of curves for $A(55°)$ in ^{208}Pb (n,γ) in the energy region where the E2 isovector resonance is expected to be. For all curves in the figure, $|R|$ was taken to be $0.2 \exp(i\delta)$ with various choices for δ. When δ=0, the curve goes through a minimum with negative values for A and then rises sharply to a maximum well over 1/2 in magnitude. This rise takes place in an energy interval which matches the assumed quadrupole resonance width. If δ

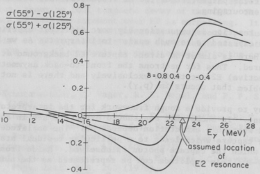

Fig. 5.5-1: Calculated curves for the expected asymmetry of photon yields for ^{208}Pb according to the simple interference model. The E2 isovector giant resonance was assumed to lie at 23 MeV and the magnitude of the E2 amplitudes was taken to be 1/5 that of the E1 amplitude. Various assumptions were made about the phase δ (in radians) of the E2 amplitude with respect to that of the E1 amplitude.

differs from zero the expected curves change their shapes as shown in the figure. If the magnitude of R is increased the minima deepen and the maxima grow larger.

Now the actual expectations for A(Θ) in n + ^{208}Pb have been studied in great detail by Longo and Saporetti and their collaborators.[4] They have done extensive calculations using the so-called direct-semi-direct model for nucleon capture with carefully chosen optical model parameters for the incoming projectile. The A(Θ)'s they find all resemble those shown in Fig. 5.5-1. Longo and Saporetti also find that if one includes a third amplitude in the E2 isovector resonance region, namely one for the tail of the isoscalar E2 resonance, the curves tend to lose their negative undershoot below resonance - i.e., they look like the curves of positive phase shift in Fig. 5.5-1. (This effect is just what one must expect when one adds to the two terms in F(Θ) an E2 amplitude from a resonance at an energy much lower than the E2 isovector energy.)

Longo and Saporetti have also investigated how the curves for A(Θ) are expected to depend on the spin and parity of the residual state in ^{209}Pb. They find that for the very highest angular momentum residuals, A(Θ) resembles the curve for δ=0, but that as the angular momentum decreases, δ seems to grow. The important point is that for all of the states, one sees the same dramatic upswing in A(Θ) in the immediate neighborhood of the E2 giant resonance. A(Θ) goes very quickly from very low, sometimes negative values, to values approaching the maximum possible, namely A=1.

It is because one can expect such a huge and characteristic effect that we have persisted[5] in trying to measure these asymmetries even though the expected counting rates in (n,γ) experiments are very low and the backgrounds tend to be quite high.

The measurements were performed with the (n,γ) detection system at the tandem accelerator at Los Alamos. The neutrons were produced by a ∿ 1μa beam of 18 MeV deuterons hitting a 3 cm long gas cell containing 8.5 atm of deuterium. (The d,d) reaction was chosen over the (d,t) reaction despite the higher neutron energies from the latter because the neutron production is five times higher for the (d,d) reaction. The high energy of the neutrons made it necessary to improve the already extensive shielding around the NaI detector system. In the final arrangement the singles rates (and associated dead times) were very nearly the same at 55° and 125°. The main phototube was run with 7 milliamps in the resistor string and was cooled, all to provide stability in the presence of the high singles counting rates.

The target was a 350 gm cylinder of ^{208}Pb with axis perpendicular to the beam. There was a hole drilled on axis to minimize neutron and photon attenuation. The calculated attenuation correction was ∿ 13%. The attenuation calculations were checked by observing the 2.6 MeV inelastic scattering line (and in a carbon target, the 15.1 MeV line). As expected these inelastic lines showed symmetry fore and aft (aside from Doppler and attenuation corrections).

Making use of fast coincidences between the NaI detector and the surrounding (NaI) annular shield, it was possible to supplement the normal photopeak events with one-escape events, thus doubling the counting rate (to ~ 2.5 counts/hour in the γ_o peak). The beam was pulsed with 400 ns between pulses. Good events were accepted within a 2.5 ns interval and were corrected for random events by using a displaced time gate.

The pulse height spectra P(Θ) seen at 55° and 125° are plotted in Fig. 5.5-2 where we have also plotted the asymmetry for these spectra

$$\mathcal{A} = \frac{P(55°) - P(125°)}{P(55°) + P(125°)}$$

It is seen that the spectra cut off crisply beyond the highest photon energy expected, showing that there is no significant pileup in the measurements.

The quantity $\mathcal{A}$ plotted in the figure is not the asymmetry A of the earlier discussion. It is determined from the pulse height spectra whereas A must be determined from the cross section spectra - i.e., from the spectra after they have been unfolded with the help of the measured response function for the detector. It is seen that in the neighborhood of γ_o, the asymmetry $\mathcal{A}$ is quite substantial (and therefore so must A be). Part of the observed asymmetry in $\mathcal{A}$ at energies just below γ_o must be associated with the tail of the γ_o line. Thus A must have an even sharper dependence on energy than the sharp dependence

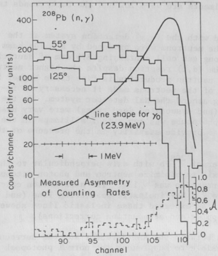

Fig. 5.5-2: The pulse height distributions from high energy γ's in the bombardment of ^{208}Pb with 20 MeV neutrons observed at 55° and 125°. It is necessary to correct these raw spectra for total beam charge and attenuation in the lead sample. The ratio $\mathcal{A}$ of the difference to the sum of the corrected spectra is plotted at the bottom of the figure. The plot shows a dramatic rise in $\mathcal{A}$ at pulse heights corresponding to ~ 23 MeV indicating the presence of a strong E2 resonance. Shown at the top of the figure is the line shape of a monochromatic photon line as seen in the detector. It is necessary to unfold the observed spectra using this line shape to obtain the asymmetry as a function of photon energy instead of pulse height.

we see for $\mathcal{A}$. On the basis of these observations we can tentatively say that the peak of the E2 resonance responsible for the asymmetry lies within an MeV of 23 MeV. It is seen from the figure that below ∼ 21 MeV, the average $\mathcal{A}$ falls to ∼ 0.1 or less, consistent with our earlier results for this lower energy interval.[5] During the present run we were able to make the apparently critical step of raising the incident neutron energy about 3 MeV above that of the early run, with the result that the energy γ_0 has entered the E2 resonance region. We are currently examining various schemes for the approximate unfolding of the pulse height spectra to obtain the actual photon spectra at 55° and 125°. From these we hope to construct the asymmetry function A which characterizes the E2 isovector resonance in Lead.

References:

* We are collaborating in this experiment with Dr. D. M. Drake at Los Alamos National Laboratories and with members of his group.

1. K. A. Snover, K. Ebisawa, D. R. Brown, and P. Paul, Phys. Rev. Lett. 32, 317 (1974).
2. E. D. Arthur, D. M. Drake, and I. Halpern, Phys. Rev. Lett. 35, 914 (1975); H. R. Weller, R. A. Blue, P. L. Von Behren, N. R. Roberson, C. R. Gould, D. R. Tilley, and S. A. Wender, Phys. Rev. 17, 1260 (1978).
3. I. Halpern, Proceedings Int. Conf. on Photonuclear Reactions (1973), p. 909.
4. G. Longo and F. Saporetti, Nuovo Cimento 46, 509 (1978).
5. Nuclear Physics Laboratory Annual Report, University of Washington (1978), p. 55.

6. MEDIUM ENERGY

6.1 Survey of Continuum Inelastic Scattering with 50 to 100 MeV Positive Pions

K. Aniol, K. Doss, I. Halpern, J. Julien+, M. Khandaker, and D. Storm

We have been engaged in a broad survey of the inelastic scattering of positive pions between 50 and 100 MeV. The general thrust of our measurements is to learn about the probabilities of the different possible interactions of pions with nuclear constituents as the pion passes through nuclear matter. These include absorption and scattering from neutrons, protons and larger aggregates. It is our hope that one can deduce a fairly definite picture of the elementary interaction probabilities as a function of energy by a consistent examination of the full spectral shapes in inelastic scattering, of their energy dependence and their dependence on target mass.

The specific energy range we have investigated was set, at the bottom end, by the properties of the LEP channel at LAMPF. At energies lower than 50 MeV the channel pion flux is too low and the background too high to permit the efficient collection of data. The maximum incident energy was set by the properties of the intrinsic germanium telescope used to detect the scattered pions. This detector belongs to our collaborators in this measurement, the Carnegie-Mellon University Intermediate Energy Group. The investigation was restricted to positive pions because the stars made by negative pions at the end of their range make difficult their identification and the determination of their energy in a telescope.

This past summer we had our last run on this survey (LAMPF Experiment 191) and we are now busy analyzing and interpreting the extensive collection of data. The 1980 run was devoted to filling in significant gaps in earlier runs and to the extension of the earlier measurements to 100 MeV.

The measurements spanned targets from carbon to lead and the angular range from 40° to 150°. It was not possible to take useful data forward of 40° because of the intense muon background from pion decays in flight. Even at 40° it was necessary to examine, in detail, two-dimensional scatter plots of Particle-Identification-Signal vs. Energy in order to properly subtract the muon background. It was not possible to measure outgoing pions with energies below 20 MeV, the low energy cutoff of the telescope. To estimate total inelastic cross-sections, it was therefore necessary to slightly extrapolate measured spectra downward in pion energy and to extrapolate angular distributions to 0° and 180°. The uncertainties of the latter extrapolation are eased substantially by the $\sin\theta$ factor in the integration over solid angle.

A plot of our preliminary results for the integrated inelastic cross-sections as a function of incident pion energy is shown in Fig. 6.1-1 for four targets (C, Ca, Sn and Pb). The curves drawn through the data are just to guide the eye. Among the most significant features of these curves is their slope. If the curves are compared with locally tangent straight lines, i.e. with curves

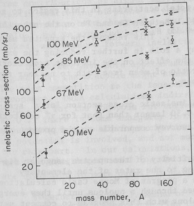

Fig. 6.1-1: The dependence of the integrated pion inelastic scattering cross-section on target mass number, A (C •, Ca Δ, Sn x, Pb o). The curves have been drawn in to guide the eye. They are reasonably linear at large A (i.e., $d\sigma/d\Omega = k\ A^n$) and have n values close to 0.4.

of the form $\sigma = \sigma_o A^n$, the values of n between Ca and Pb are very nearly 1/3 for all of the incident energies. (Between C and Ca the slope is close to n = 2/3.) The high A behavior is in contrast to that for the pion absorption cross-sections which go very nearly as $A^{2/3}$ in this energy range.

The fact that the slope is lower for the scattering than for the absorption arises from a number of factors. One of the main factors comes about because low energy positive pions scatter mainly from protons rather than neutrons in the nucleus. If the scattering were equally probable from all nucleons, one would expect an integrated scattering cross-section that goes roughly as $A^{2/3}$. This is because most of the scattering is backward for pions in this energy range. The overall scattering cross-section would then be expected to be something like $\sigma_{inel} = \mu_s \Delta X \cdot \pi R^2 = 1/2\ \mu_s/\mu_a\ \pi R^2$ where μ_s is the absorption coefficient for inelastic scattering events and ΔX is half the density-weighted mean free path, $1/\mu_a$, for pion absorption in nuclear matter. (This relation is based on the reasonable assumption that single scattering dominates over multiple scattering.) Since μ_s and μ_a presumably do not depend on nuclear size, the scattering cross-section in this picture would go simply as $A^{2/3}$.

However since positive pions scatter from protons with strong preference, μ_s will be proportional to Z/A. The coefficient μ_a, on the other hand, is relatively insensitive to the mix of neutrons and protons as long as they are roughly comparable in number. Thus the total positive pion scattering cross-section should go roughly as Z/A $A^{2/3}$. Now, between C and Ca, Z/A remains very close to 1/2. One therefore expects the total scattering in this region to go as $A^{2/3}$ as it apparently does (Fig. 6.1-1). Between Ca and Pb on the other hand Z/A behaves more like a constant times $A^{-0.15}$. This reduces the expected slope to close to $A^{1/2}$. Other factors that play a role in further reducing the exponent to the measured value include (1) the effect on the incident trajectories of the Coulomb field and (2) the larger ratio of mean free path to nuclear radius for smaller nuclei than for larger ones.

According to this picture the total inelastic cross-section for π^- scattering would have an exponent n at least 0.30 larger than that for π^+ scattering. It would be of interest to carry out a π^- survey comparable to the present one for π^+.

In order to study in detail the sensitivity of the spectra, angular distributions etc. in the inelastic scattering to the rates of the elementary interaction processes, we have undertaken a program of Monte Carlo calculations in which many individual pions are followed through a nucleus until they emerge or are absorbed. We are not far enough along with this program to comment seriously on spectra and angular distributions. We can say however that the shapes of the curves in Fig. 6.1-1 are well reproduced by the calculations. These shapes are not very sensitive to the values of assumed interaction parameters nor to the exact shape of the assumed nuclear matter distribution. This is what one might expect on the basis of our earlier rough account of the shape of these curves.

Reference:

+ Permanent address: CEA Saclay, Gif-sur-Yvette, France

6.2 Development of Techniques for Studying Giant Monopole Resonances with Pions*

K. G. R. Doss, M. Khandaker, I. Halpern, and D. W. Storm

The observation of the Giant Isoscalar Monopole excitation with inelastically scattered alpha particles has been reported.[1] It is difficult in alpha particle experiments to determine quantitative details of the monopole excitation due to the presence of a strong continuum and a relatively large, nearby quadrupole resonance. We are therefore attempting to observe the resonance with low energy pions. Since pions are 28 times lighter than alpha particles, it is possible that the excitation of the giant monopole resonance may be cleaner. In particular, with alpha particles of 120 MeV, the momentum transfer at 0° for 15 MeV excitation is about .35 F^{-1}, so excitation of multipoles of L less than 3 for heavy nuclei is not suppressed. With 67 MeV pions, however, the momentum transfer at 0° is less than 0.1 F^{-1}, while at 10° it is 0.15 F^{-1}, so one would expect L=1 excitations to become important (for lead) only beyond about 10°. Thus if it were possible to measure inelastic pion scattering cross sections at 10° and forward, one might expect to observe the giant monopole resonance relatively free from contributions of higher multipoles. Furthermore, excitation due to quasi-elastic scattering of pions is expected to be relatively low at forward angles. This trend has been observed in our studies of inelastic scattering at larger angles, and is expected because the basic pion-nucleon cross section is backward peaked, and because forward inelastic scattering is suppressed by Pauli blocking.

Distorted wave Born approximation calculations support the view we have just argued that the monopole might stand out at forward angles. (See Fig. 6.2-1.) The main competition to the isoscalar giant monopole is from the giant dipole resonance. DWBA calculations indicate that the dipole cross section will be less than that for the monopole for angles forward of 10 to 14° and substantially less at 0°. There is some ambiguity in the expected magnitude of the cross section, especially for the dipole excitation, since the isovector part of the pion-nucleus potential is involved, and not much is known about the best parameterization for this part. In our calculations, we have used the free pion-nucleon parameters in a Kisslinger model for the isovector ptoential. The DWBA calculations are discussed in more detail in David Chiang's thesis.[2]

Together with Dr. J. Amann of the Los Alamos Laboratory, we carried out some work on EPICS (Energetic Pion Channel and Spectrometer) in order to develop a technique for measuring pion inelastic scattering around 10°. The main problem that we addressed so far was the muon background. Since the pion decay length at 67 MeV is about 8 m, and since the maximum laboratory decay angle is about 15°, there is a very large muon background in the spectrometer at 10°. In a previous test, we determined that the counters in the spectrometer could operate in this intense flux, but that the muon events would have to be vetoed in order to main-

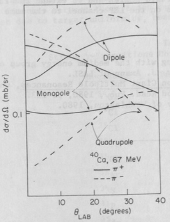

Fig. 6.2-1: Predicted differential cross sections for excitation of Giant Monopole and Giant Dipole resonances, using fitted parameters for all but the isovector excitation, as described in Ref. 2.

tain a reasonable computer trigger rate. The muons at the focal plane of the spectrometer are fairly well localized by energy, so it is possible to differentiate between muons and pions by range, although it is necessary to use an absorber whose thickness varies with position along the focal plane. By installing and adjusting such an absorber, it was possible to veto from 95 to 98% of all muons, while losing only about 10% of the pions. The rate of non-vetoed muons was then comparable to the pion rate, and they could be identified by computing the mass associated with the measured time of flight from the spectrometer entrance and particle trajectory.

When the muons were satisfactorily eliminated, it became possible to study the pion spectra at forward angles. We found a large background resulting from degraded elastically scattered pions. It appears that about 0.2% of the flux of elastically scattered pions which enter the spectrometer is degraded by hitting flanges or walls of the vacuum system in the quadrupole triplet at the entrance to the spectrometer. Because of the focusing in the quadrupole, combined with multiple scattering in the timing scintillation counter immediately after the triplet, it is impossible to project the trajectories backward to the site of the scattering in the quadrupoles. Thus it will be necessary to use veto counters at the flanges to eliminate this background. Since the 10° elastic scattering cross section is around 20 barns/sr (for lead) whereas the giant monopole resonance cross section is expected to be only about 1 mb/sr, a reduction of this background by about two orders of magnitude will be required.

Although measurements at 10° are not possible with the present setup of EPICS, we were able to demonstrate the feasibility of measurements on C and Pb at 20°. We plan to continue these studies in the summer, in order to determine how large the dipole excitation really is at forward angles and to extend the range of our previous inelastic scattering studies on the LEP channel to the more forward angles already available at EPICS.

References:

* In this experiment we are collaborating with the medium energy group of the Carnegie-Mellon University and with Dr. J. Amann of LASL.

1. D. H. Youngblood, Topical Conference on Giant Multipole Resonances, Oak Ridge, TN, F. E. Bertrand, ed., Harwood Acad. Pub., 1980, p. 113.
2. David Chiang, Ph.D. Thesis, University of Washington, 1980.

7.1 Energy Dependence of $^{12}C + ^{28}Si$ Fusion Cross Reactions by Gamma Ray Measurement

A. Lazzarini, K. Lesko, D.-K. Lock, and R. Vandenbosch

We have determined the energy dependence of the fusion cross section for the $^{12}C + ^{28}Si$ reaction by summing the yields of the major fusion products as determined by in-beam gamma-ray yield measurements. Although this method does not achieve as high an absolute accuracy as does the method of direct observation of evaporation residues (see Sec. 7.2), it is a more efficient way of studying the detailed energy dependence of the fusion cross section. We were particularly interested to see if the fusion cross section exhibits structure similar to that observed at back angles in the elastic and inelastic channels.[1,2]

The target consisted of 100 $\mu g/cm^2$ of ^{28}Si evaporated onto a thick Ta backing. The target and small scattering chamber were electrically connected but isolated from the beam line and served as a Faraday cup. A 50 cc Ge(Li) detector was placed at 90° with respect to the beam. The transitions used in determining the individual fusion yields are given in Table 7.1-1. The total fusion cross sections, obtained by summing the individual product yields, are shown in Fig. 7.1-1. The circles represent the values observed in continuous measurements, and should provide the best representation of the energy dependence of the fusion cross section. The purely statistical errors are no larger than the size of the symbols plotted. Triangles represent the values obtained in repeat measurements at later times, in some cases using different charge states for the beam. The differences between these cross sections provide an indication of the uncertainties due to target uniformity, beam focusing, etc. The absolute yields are

Table 7.1-1
Strong γ-Transitions Observed in the $^{12}C + ^{28}Si$ Reaction

Nucleus	Transitions ($J_i^\pi - J_j^\pi$) E_γ(keV)
^{34}Cl	$(4^+ \rightarrow 3^+)$ 2230
^{34}Cl	$(2^+ \rightarrow 3^+)$ 2465
^{35}Cl	$(5/2^+ \rightarrow 3/2^+)$ 1763
^{35}Cl	$(7/2^+ \rightarrow 3/2^+)$ 2646
^{35}Cl	$(7/2^- \rightarrow 3/2^+)$ 3163
^{38}Ar	$(2^+ \rightarrow 0^+)$ 2168
^{34}S	$(2^+ \rightarrow 0^+)$ 2127
^{31}P	$(3/2^+ \rightarrow 1/2^+)$ 1266
^{35}Ar	$(1/2^+ \rightarrow 3/2^+)$ 1184
^{37}Ar	$(7/2^- \rightarrow 3/2^+)$ 1611

believed to be good to only 20% due to uncertainties in the target thickness and to missed yield to products whose cross section could not be measured (e.g. ^{28}Si, ^{32}S). A considerable uncertainty also arises from the integration of the ^{34}Cl line, which is not well resolved from other structures. The relative yields for the sequential series of measurements are believed to have a precision of 3-5%. No evidence for structure correlated with that in other channels is observed.

In order to estimate the yield to unobserved channels, we have performed evaporation calculations and compared the resulting individual product yields with our experimental observations. We have used two evaporation codes, LPACE[3] and LILITA.[4] We find that the evaporation calculations have a consistent tendency to overestimate the yields of channels involving α emission, e.g. ^{34}S, as compared to channels involving nucleon emission, e.g. ^{38}Ar. The results of a calculation with LPACE using its standard parameter set are compared with experiment in Fig. 7.1-2. We have made a number of attempts to improve the fits by changing various parameters. We first tried using a different optical potential for alpha emission, as these channels were poorly predicted. We tried several potentials from Chang, et al.[5] Some channel yields improved but others deteriorated and the overall improvement was modest. We tried lowering the yrast line by changing the r_o parameter in the moment of inertia expression from 1.225 to 1.4 fm. We also tried adding the known levels of ^{38}Ar up to 4 MeV since this channel was poorly predicted. We tried replacing the Gilbert and Cameron level density parameters with those of Dilg, et al.[6] None of these changes gave dramatic improvements to the fits. Calculations with the LILITA code with various level density parameter sets also failed to give a consistently significant improvement to the fit. We conclude that it is not possible to use evaporation calculations to make quantitative predictions of individual product yields in this mass region.

References:

1. J. Barrette, M. J. LeVine, P. Braun-Munzinger, G. M. Berkowitz, M. Gai, J. W. Harris, and C. M. Jachcinski, Phys. Rev. Lett. 40, 445 (1978).
2. M. R. Clover, R. M. DeVries, R. Ost, N. J. A. Rust, R. N. Cherry, Jr., and H. E. Gove, Phys. Rev. Lett. 40, 1008 (1978); R. Ost, M. R. Clover, R. M. DeVries, B. R. Fulton, H. E. Gove, and N. J. Rust, Phys. Rev. C19, 740 (1979).
3. A. Gavron, Oak Ridge National Laboratory
4. R. Stokstad, Oak Ridge National Laboratory
5. H. H. Chang, B. W. Ridley, T. H. Braid, T. W. Conlon, E. F. Gibson, and N. S. P. King, Nucl. Phys. A270, 413 (1976).
6. W. Dilg, W. Schantl, and H. Vonach, Nucl. Phys. A217, 269 (1973).

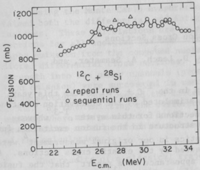

Fig. 7.1-1: Fusion excitation functions for $^{12}C + ^{28}Si$.

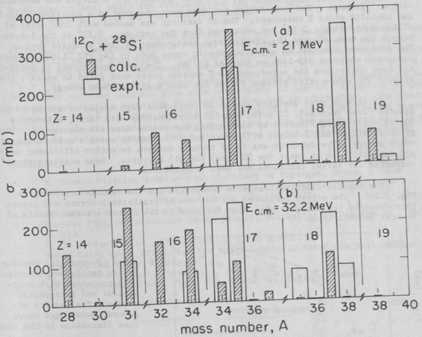

Fig. 7.1-2: Comparison of experimental residue yields with LPACE calculated yields (cross hatched histograms) at two energies.

7.2 $^{12}C + ^{28}Si$ Evaporation Residue Fusion Cross Sections

H. Doubre[+], A. Lazzarini, K. Lesko, D. Leach, A. Seamster, and R. Vandenbosch

We are continuing our investigation in the $^{12}C + ^{28}Si$ system this year. Our original interest in this system was stimulated by the observation of structure in the elastic and inelastic cross sections for this system,[1-3] whereas presently the heaviest system to exhibit structure in the fusion excitation function is the $^{16}O + ^{16}O$ system. The statistics in our original measurement[4] were inadequate to resolve the structure suggested by the elastic cross sections. An additional motivation was the subsequent appearance of a report[5] that the fusion cross sections were anomalously low for this system. A ^{12}C target was bombarded with a ^{28}Si beam. The evaporation residues were observed in a position sensitive gas ΔE-solid state E telescope. The ΔE detector was masked with four vertical slits, subtending $\approx 0.32°$ and separated from the next by $\approx 0.85°$ in the laboratory. The mask allowed the simultaneous measurement of four separate angles. The data were recorded on magnetic tape in event mode by the PDP 11/60 computer, and later analyzed off-line on the VAX 11/780. The data were sorted to separate the four angles and the subsequent ΔE-E scatter plots were gated to extract the elastic and evaporation residue yields for each angle and beam energy.

At each of nine energies chosen to correspond with maxima or minima of the elastic cross sections, 22 point angular distributions were taken, with every fourth angle being repeated by overlapping successive detector placements. Energy calibrations and detector efficiency were obtained by using a gold target at every energy. The detector was found to have uniform detection efficiency across all four slits to at least the 2% level for all energies. Beam monitors at ±8° corrected for target thickness and beam fluctuations.

The angular distributions were integrated and the results are shown in Fig. 7.2-1. The errors indicated are the sum of statistical errors and errors introduced by the integration. Also included in the figure are the results of several calculations.

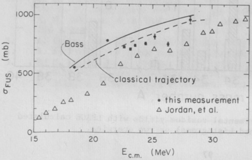

Fig. 7.2-1: Evaporation residue fusion excitation function. Data are shown with statistical and integration errors. The results of several models are shown (see discussion in the text).

Using the Monte Carlo evaporation code[6] obtained last year, we have obtained both the differential and integrated cross sections for the evaporation residues. These calculations are in good agreement with the differential cross sections for all energies measured with the exception that they over-predict alpha emission from the compound nucleus, which results in a shoulder on the predicted differential cross sections. Attempts to reapportion the alpha emission strength into the other channels (proton, neutron, and multiple proton and neutron emission) were successful in removing the shoulder from the differential cross sections, but lowered the differential and integrated cross sections by $\approx 50\%$. By renormalizing the differential cross sections to the data at small angles, where the measured $d\sigma/d\theta$ peaks, we were able to produce integrated cross sections which were lower than, but still within, the uncertainty of the calculations.

The results of a classical trajectory model incorporating nuclear proximity potential and one-body promimity friction are shown in the figure.[7] The Bass model predictions, which are obtained from the Monte Carlo code, also show qualitative agreement with the experimental results.

While all the models agree qualitatively with the measured excitation function, and the classical trajectory model is in good agreement with the data, there still exists some structure in the excitation function which is not reproduced by the models. A nonresonant interpretation of the inelastic scattering of $^{12}C + ^{28}Si$ was supported by another measurement made here.[8] The evaporation residue cross sections obtained from this measurement do not have structure of great enough regularity or magnitude to support a resonant interpretation. The absolute magnitude of our cross sections are considerably larger than that of a previous measurement,[5] particularly at low energies. The dip we observe at ≈ 26 MeV seems to correlate, however, with a dip observed in the previous measurement.

References:

+ H. Doubre visiting Seattle from Institute de Physique, Orsay, France
1. P. Braun-Munziner, et al., Phys. Rev. Lett. 38, 944 (1978).
2. J. Barrette, et al., Phys. Rev. Lett. 40, 445 (1978).
3. T. Renner, et al., Phys. Rev. Lett. 18, 1927 (1978).
4. Nuclear Physics Laboratory Annual Report, University of Washington (1980), p. 113.
5. W. J. Jordan, et al., Phys. Lett. 87B, 38 (1979).
6. Monte Carlo code, LPACE, written by A. Gavron at Oak Ridge National Laboratory, Oak Ridge, Tennessee.
7. R. Vandenbosch, Nucl. Phys. A339, 167 (1980).
8. R. Vandenbosch, et al., Phys. Rev. Lett. 46, 5 (1981).

7.3 A Search for Non-Fusion in the $^{16}O + {}^{16}O$ System

A. Lazzarini, H. Doubre+, K. Lesko, V. Metag*, A. Seamster, and R. Vandenbosch

We have studied the $^{16}O + {}^{16}O$ system at $E_{c.m.}$=34 MeV to determine whether the fusion L-window predicted by time dependent Hartree-Fock calculations[1,2] exists. At $E_{c.m.}$=34 MeV Koonin and Flanders[2] have calculated that the partial waves L=0-6 do not lead to the formation of a compound nucleus. Instead the two heavy ions separate with a kinetic energy determined by their Coulomb barrier. Unlike symmetric fission, the angular distribution does not increase towards smaller scattering angles. We are interested in determining if such a process does indeed occur in nature or whether the effect is an artifact of the model or of the approximations used therein. Several attempts to infer the presence of a fusion L-window from the behavior of the energy dependence of the fusion-evaporation cross section have not been conclusive.[3,4] The magnitude of the effect for the $^{16}O + {}^{16}O$ system is predicted to be 132 mb - an effect that should be directly, if not easily, observable.

We have scanned a large portion (roughly 30-40%) of the entire phase space (all angles and Q-values) available to the O + O exit channel, centered at 90° in the c.m. This covers the domain where the contribution to deep inelastic scattering arising from the fusion L-window is expected to be focused. Fig. 7.3-1 presents the Wilczynski plot for the system. E_0 is the initial c.m. energy for the reaction, V_C is the Coulomb barrier for the $^{16}O + {}^{16}O$, and the 'X' marks indicate the TDHF trajectory for the non-fusing low partial waves. Our data indicate that the bulk of the two body final state is dominated by inelastic scattering via single and double excitation of the $(0^+,3^-)$ and $(2^+,1^-)$ doublets at 6.1 and 7 MeV in ^{16}O. The single excitation has a yield of 35.9 mb and the double excitation contributes 19.8 mb; the elastic scattering cross section over its limited range is 4.6 mb. By comparison the total inelastic yield for $Q \leq -15.0$ MeV is only 5.9 mb. Fig. 7.3-2a presents the angle-integrated yield of the Wilczinski plot while Fig. 7.3-2b presents angular distributions for the most deeply inelastic events. The observation of such a small inelastic cross section for the Q-value range predicted for the deep inelastic scattering following non-fusion is significantly different from the theoretical expectations of 132 mb. We have looked very briefly at transfer channels which might be expected to compete with the O + O final state for the non-fusion cross section and which are suppressed in theoretical calculations because of the mean field approximations that are employed. We do not expect, however, that a fractionation of the deep inelastic yield over several two body final states can account for 132 mb of cross section. It is also improbable that the missing cross section lies at angles forward of $\Theta_{c.m.}$=40°; if this were the case the differential cross section would have to increase by a large factor (≃ 500-1000) in the range not experimentally observed. Another possibility is that a dispersion in the partition of excitation between the two oxygen ions would affect the two-body yield since then it becomes increasingly more probable that one of the ions α-decays in flight. TDHF calculations themselves predict a negligible and unreasonably small dispersion. Independent estimates for the dispersion using level density

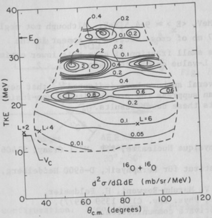

Fig. 7.3-1: Wilczynski plot for $^{16}O + {}^{16}O$ system at $E_{c.m.}$ =34MeV. Dashed lines reflect coincidence limits for experiment. "X" marks denote TDHF predictions for different partial waves.

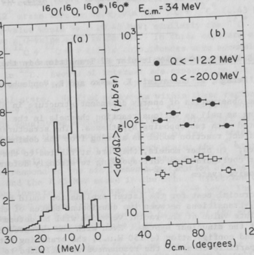

Fig. 7.3-2: Projections of Wilczynski plot for (a) angle integrated yield for all Q-values and (b) differential cross section for selected Q-windows.

arguments indicate that for $-Q = 18$ MeV, $\langle E_x \rangle = 9\pm4.5$ MeV. Although not negligible, the effect still allows for $\simeq 27$ mb of cross section to appear in the $^{16}O + ^{16}O$ final state. We see only a small fraction of even this lower estimate. Our data are consistent with a lower L-value cutoff to fusion of $L < 2$.

During the time of our work several authors have indicated[3,4] that certain refinements to TDHF approximations can suppress the probability of non-fusion for head-on collisions. Our work supports these newer results.

References:

\+ Present address: Institut de Physique Nucleaire, B.P. N° 1 Orsay, 91406 France

* Present address: Max Planck Institut für Kernphysik, D-6900 Heidelberg, P.O. Box 103980, West Germany

1. S. E. Koonin, K. T. R. Davies, V. Maruhn-Rezwani, H. Feldmeier, S. J. Krieger, and J. W. Negele, Phys. Rev. C15, 1359 (1977).
2. S. E. Koonin and B. Flanders, private communication.
3. A. K. Dhar and B. S. Nilsson, Nucl. Phys. A315, 445 (1978).
4. P. Grangé, J. Richert, G. Wolschin, and H. A. Weidenmüller, Nucl. Phys., in press; also H. S. Köhler, Nucl. Phys. A343, 315 (1980).

7.4 A Search for Quasi-Molecular E2 Transitions in the $^{12}C + ^{12}C$ System

V. Metag[+], A. Lazzarini, K. Lesko and R. Vandenbosch

The observation of energy dependent structure in elastic and inelastic scattering as well as various reaction channels in the $^{12}C + ^{12}C$ system has been interpreted with two opposing hypotheses. The structures are explained in a simple direct reaction model as arising from the dominance of the grazing partial waves;[1] in other models, they are attributed to the population of quasi-molecular configurations corresponding to strongly deformed rotational states in the composite system ^{24}Mg.[2-4]

A crucial test for the latter explanation would be the observation of collective γ-transitions between two quasibound states of the 24 nucleon system. The absolute value of the radiative width will be determined by the quadrupole moment of the dinuclear system. Even with the expected enhancement for a strongly deformed configuration ($\simeq$ 150 W.u.), the branching ratio for gamma decay to charged particle decay of the resonances is estimated to be only on the order of 2×10^{-5}.

The experiment was performed at $E_{c.m.} = 25.2$ MeV, at which energy has been reported the presence of the postulated 14^+ member of the quasimolecular band in ^{24}Mg ($E_x \simeq 39$ MeV). Fig. 7.4-1 presents a schematic of the experimental

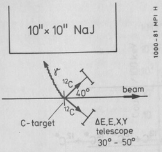

Fig. 7.4-1: Experiment arrangement for $^{12}C + ^{12}C \rightarrow ^{12}C + ^{12}C + \gamma$.

configuration. A collective E2 transition of γ-ray energy $\simeq$ 6-7 MeV, populating the lower lying 12^+ member of the same band ($E_x \simeq$ 33 MeV) would be experimental evidence for the presence of such a rotational band in ^{24}Mg (see Fig. 7.4-2). The Q-value for such an event (C + C + γ) is expected to be 6-7 MeV; if the subsequently populated 12^+ state were to decay via the $^{12}C + ^{12}C^*$ (4.43 MeV) channel, then the total Q-value would be $\simeq$ 10.43 MeV; similarly the $^{12}C^* + ^{12}C^* + \gamma$ final state would have a Q-value of $\simeq$ 14.86 MeV. In three separate experiments a total of 1.05×10^6 $^{12}C + ^{12}C + \gamma$ triple coincidences were accumulated. Most of the coincidences observed came from the single and double excitation of the 2^+ state at 4.43 MeV in ^{12}C. Events of interest are expected to lie within the regions marked I, II, and III in Fig. 7.4-3 depending on the excitations of the ^{12}C nuclei in the final state. We find no events within these regions. Events that occur with $E_\gamma \simeq$ 7-9 MeV and $-Q \simeq$ 12.7 and 12.1 are observed both on resonance ($E_{c.m.}$=25.2) and equally as strongly in a run performed off resonance at $E_{c.m.}$=27 MeV. We attribute these events to γ decays of the 1^+ state at 12.7 MeV in ^{12}C via the 2^+ state at 4.43 MeV to the ground state; the 0^+ state at 7.65 MeV also decays with a small probability via a γ cascade of 3.21 and 4.43 MeV. Events at 12.1 MeV correspond to the simultaneous excitation of the 4.43 MeV state in one nucleus and the 7.65 MeV state in the other; detection of 2 of the 3 γ rays produced thus leads to a total γ ray energy of 7-9 MeV. The cluster of of events near $-Q \simeq$ 15 MeV arises from the $^{12}C(^{12}C,^{11}C^{(*)})^{13}C^{(*)}$ reaction. The yield at this Q value in Fig. 7.4-3 is suppressed because of the kinematic constraints placed on events that appear in this plot.

Our observation of no events identifiable as quasi-molecular γ decays (1±1 event) allows us to place an upper limit on the γ-decay branching ratio for this system. We obtain, at the level of three standard deviations, a value $(\Gamma_\gamma/\Gamma_{tot})^{14^+} \leq 7 \times 10^{-6}$.

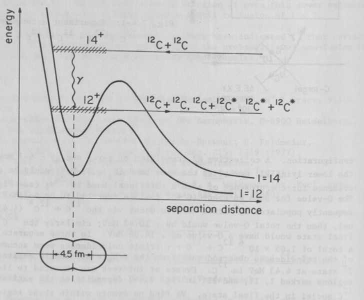

Fig. 7.4-2: Schematic representation of an electric quadrupole transition in the quasimolecular configuration.

Strutinsky-type calculations by Chandra and Mosel[5] have predicted a quadrupole moment of 1.8 b (to be compared with 0.64 b for the ground state) for the molecular configuration of two touching spheroidal ^{12}C nuclei. This is in good agreement from estimates which can be made from experimentally determined spacings between the ^{12}C + ^{12}C resonances. The resonance width from the intermediate structure is $\Gamma_{tot} \approx$ 300 keV. From this information one estimates a B(E2, I→I-2)=2.3×10^{-5}. Our upper limit quoted above is three times smaller than this expected value. The assumptions made in this calculation should hold if quasi-molecular states in ^{24}Mg do indeed exist.

Blair and Sherif[6] have recently calculated the yield of E2 nuclear bremsstrahlung emitted in the collision of two ^{12}C nuclei with angular momenta L = 14 ħ in the entrance channel and L = 12 ħ in the exit channel. They calculate a branching ratio for the production of γ-rays to elastic scattering at

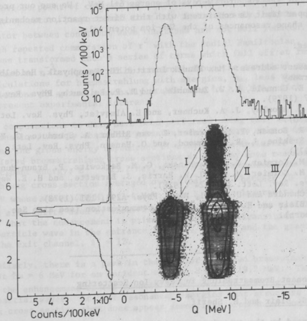

Fig. 7.4-3: Contour plot of coincidences $^{12}C + {}^{12}C + \gamma$ where Q was obtained from particle energies and E_γ from NaI detector. See text for explanations.

$\Theta_{c.m.}$=90° of 1×10^{-6} for γ-rays of energy 6±1 MeV. We see our present experimental upper limit is consistent with this direct reaction mechanism associated with the shape resonances of the ion-ion potential.

References:

+ Present address: Max Planck Institut für Kernphysik, Heidelberg, West Germany

1. L. E. Cannell, R. W. Zurmuhle, and D. P. Balamuth, Phys. Rev. Lett. 43, 837 (1979).
2. D. A. Bromley, J. A. Kuchner, and E. Almqvist, Phys. Rev. Lett. 4, 365 (1960).
3. E. R. Cosman, T. M. Cormier, K. van Bibber, A. Sperduto, G. Young, J. Erskine, L. R. Greenwood, and O. Hansen, Phys. Rev. Lett. 35, 265 (1975).
4. T. M. Cormier, C. M. Jachinski, G. M. Berkowitz, P. Braun-Munzinger, P. M. Cormier, M. Ga, J. W. Harris, J. Barrette, and H. E. Wegner, Phys. Rev. Lett. 40, 924 (1978).
5. H. Chandra and U. Mosel, Nucl. Phys. A298, 151 (1978).
6. J. Blair and H. Sherif, private communication (see also Sec. 7.5 of this report).

7.5 Resonant Bremsstrahlung in Heavy Ion Scattering

J. S. Blair and H. Sherif+

Spurred by the experiment searching for γ-rays from a quasi-molecular $^{12}C + ^{12}C$ system (see Sec. 7.4 of this report), we have set up a calculation of the quadrupole bremsstrahlung produced by the acceleration of the ^{12}C ions in their spherically symmetric nuclear and Coulomb potentials.

It is familiar that many of the "resonant" phenomena observed in heavy ion reactions have been described in terms of direct interaction theories. For example, the gross structure in the energy dependence of total inelastic cross sections in $^{16}O + ^{16}O$ collisions has been duplicated by calculations making use of the Austern-Blair approximation.[1] Crucial for the appearance of "resonant" structure in a direct interaction description is the large role assumed by the grazing angular momenta and by the relatively small absorption in such partial waves.

Thus, while the primary motivation for the $^{12}C - ^{12}C - \gamma$ experiment has been the hope that quasi-molecular states in ^{24}Mg would thereby be revealed, it has also seemed worthwhile to investigate the alternative direct interaction description. The formulation of a quantum-mechanical bremsstrahlung calculation is straight-forward;[2] the angular momentum structure of the reaction amplitudes is the same as that found in DWBA calculations of inelastic scattering and thus much of the required computer code could be "lifted" from the DWBA program "HELMY".[3]

An obvious point of concern has been the radial dependence of the quadrupole moment operator, proportional to $r^2 Y_2^m(\hat{r})^*$. Clearly, matrix elements of this operator between continuum wave functions are not well behaved. Fortunately, through repeated commutation of r^2 with the radial Hamiltonian, the radial operator was transformed into a series of terms which fell off at large r at least as fast as r^{-3}. We are still concerned about the numerical reliability of our calculations for bremsstrahlung with energies, $\hbar\omega$, less than 4 MeV, but the calculations do appear reasonably stable for $\hbar\omega > 4$ MeV, which is the range of present experimental interest.

All computations to date have been performed using the "Reilly" potential,[4] a shallow, weakly absorbing potential which enjoys only modest success in matching the gross energy dependence of elastic and inelastic[5] scattering. The calculated bremsstrahlung cross sections do display some resonant features: For an incident energy, $E_{c.m.}$ =25.2 MeV, there is a pronounced peak in the bremsstrahlung cross section averaged over final $\theta_{c.m.}$ between 70° and 110° at $\hbar\omega$ = 7 MeV whose width (FWHM) ∿ 3-4 MeV; when $E_{c.m.}$ is lowered to 23.2 MeV, this peak also shifts down by about 2 MeV. Inspection of the radial integrals indicates that the enhancement is primarily due to the transition between the grazing particle wave in the entrance channel, ℓ =.14, and the grazing partial wave in the exit channel, ℓ' = 12.

Similarly, there is a peak in the angular averaged bremsstrahlung cross section at $\hbar\omega$ = 6 MeV for an incident energy, $E_{c.m.}$ = 19.2 MeV. This is attributed to the enhancement of the transition between the grazing ℓ = 12 and ℓ' = 10 partial waves. At "off resonance" energies what structure in the bremsstrahlung cross section that does appear seems less pronounced and rather washed out.

But although the calculated cross sections do exhibit resonant behavior, their magnitudes are small. Even at peaks in the bremsstrahlung spectra, the ratio of the angle-averaged bremsstrahlung cross section, integrated over final γ-ray directions, to the elastic cross section, angle-averaged over the same range, is slightly less than 10^{-6}/(MeV). While these results are consistent with the present upper limits on the observed bremsstrahlung cross sections, they also imply that a marked advance in the experimental procedures will be required in order to demonstrate the existance of shape resonant enhancement of bremsstrahlung.

References:

+ Permanent address: University of Alberta, Alberta, Canada
1. R. L. Phillips, K. A. Erb, D. A. Bromley, and J. Weneser, Phys. Rev. Lett. 42, 566 (1979).
2. K. Alder, A. Bohr, T. Huus, B. Mottelson, and A. Winther, Rev. Mod. Phys. 28, 77 (1956).

3. H. Sherif, Nucl. Phys. A131, 532 (1969).
4. W. Reilly, R. Wieland, A. Gobbi, M. W. Sachs, J. Hamor, R. H. Siemssen, D. Mingay, and D. A. Bromley, Nuovo Cim. A13, 897 (1973).
5. L. E. Cannell, R. W. Zurmühle, and D. P. Balamuth, Phys. Rev. Lett. 43, 837 (1979).

7.6 Search for High Spin States in ^{32}S Using an Alpha Transfer Reaction

S. Gil, M. Hindi, A. Lazzarini, K. Lesko, D.-K. Lock, and R. Vandenbosch

The location of high spin states in the s-d shell nuclei is of interest for a variety of reasons. Of particular interest to us is the determination of the yrast line. It is needed in order to understand the angular momentum limitations imposed on the fusion cross sections of light nuclei at energies above the Coulomb barrier. The yrast line is also of importance regarding possible explanations for the nature of postulated quasi-molecular states or resonances in these nuclei. These high spin states in s-d shell nuclei are also important for testing several theoretical models such as the shell, cluster and rotational models.

Experimentally, very few states of spin higher than J=4 are known in this mass region. This is particularly true for $^{32,34}S$. States with spin greater than ≈ 6 are usually above the particle emission threshold for these light systems, making them difficult to observe electromagnetically. Although ^{32}S is a midshell nucleus, its low-lying states exhibit vibrational rather than rotational character. Predictions[1-3] for yrast states in ^{32}S are presented in Table 7.6-1.

Table 7.6-1
Predictions of the Excitation Energies (in MeV) for the Yrast Line in ^{32}S

Spin	2^+	4^+	6^+	8^+	10^+	Threshold for part. emission α	p	n
Source								
Goerke et al.[1]	1.19	3.48	6.56	9.8				
Schmid et al.[2]	1.37	3.68	7.1	10.9				
Arima et al.[3]	(2.23)	(4.46)	7.0	10.0	12.5			
experimental[4,5]	2.23	4.46				6.95	8.86	15.04

The experimental method we chose for beginning this study was to use the $^{28}Si(^{16}O,^{12}C)^{32}S$ reaction to populate high spin states in the region E_x ≈ 6-12 MeV of ^{32}S. Previous studies of this transfer reaction in this region of the s-d shell have shown a high degree of selectivity for populating states of high spin.[6] Particle-γ coincidences were measured using an E-ΔE solid state telescope with both a Ge(Li) and a NaI(Tl) γ-ray detector. In this manner, it was possible to correlate reaction Q-value as determined by the energy of the ^{12}C ions detected in the telescope, with γ-ray energy, from which the decay scheme could, in principle, be determined.

Three experimental runs were performed. The earlier runs were surveys to determine optimal operating conditions for the experiment (i.e. angles, beam energy, geometry and rates). It was determined that E_{lab}=65 MeV and Θ_{lab}=20° were the most favorable conditions. Data were event-mode-recorded on tape for subsequent off-line analysis.

The particle energy resolution suffered from poor detector performance. Nevertheless, the coincidence γ-ray spectrum has been very useful in determining our results. Preliminary indications are that we see a strong enhancement of the α transfer to the 3^- state at 5.01 MeV in ^{32}S. However, the bulk of the transfer yield occurs at energies in ^{32}S between 5 and 16 MeV of excitation. Surprisingly, we have not seen any evidence for an enhancement of transfer to higher spin states. A more careful analysis must be performed, however. Furthermore, we are considering other possible reactions with which the ^{32}S system can be studied. ^{34}S is a more attractive system in some ways because the gamma rays de-exciting the first 2^+ and 4^+ states differ in energy, whereas they happen to coincide in energy in ^{32}S.

References:

1. K. Goerke, J. Garcia, and A. Faessler, Nucl. Phys. A208, 477 (1973).
2. K. W. Schmid, L. Satpathy, and A. Faessler, Z. Physik 267, 345 (1974).
3. A. Arima, G. Scharff-Goldhaber, and K. W. McVoy, Phys. Lett. 40b, 7 (1972).
4. C. M. Lederer, et al., Table of Isotopes, John Wiley + Sons, Inc., New York, 1978.
5. P. M. Endt and C. Van der Leun, Nucl. Phys. A214, 1 (1973).
6. N. Anyas-Weiss, et al., Phys. Reports 12C, 201 (1974).

7.7 Search for Low Spin ^{12}C - ^{8}Be Cluster States in ^{20}Ne

D. H. Dowell, M. M. Hindi, and K. A. Snover

In a recent publication Hindi et al.[1] suggested the existence of a new rotational band in ^{20}Ne which has a large component of ^{12}C - ^{8}Be cluster structure. The band was based on three states (see Table 7.7-1) all of which have very small reduced widths for decay to $\alpha + {}^{16}O_{g.s.}$, while they have large reduced widths for α-decay to 4p-4h states in ^{16}O and/or to the $^{12}C_{g.s.} + {}^{8}Be_{g.s.}$ channel. The moment of inertia of this $K^\pi = 0_6^+$ band is the largest of all the rotational bands in ^{20}Ne and is approximately equal to the classical moment of inertia of two touching spheres with the masses and radii of ^{12}C and ^{8}Be. The proposed $K^{\pi}=0_6^+$ band would serve as a gauge for new extended cluster model calculations[2] and as a link between the simple α cluster bands in light nuclei (^8Be, ^{12}C, ^{16}O, ^{20}Ne) and the ^{12}C - ^{12}C quasi-molecular bands[3] in ^{24}Mg.

To put the proposed $K^{\pi}=0_6^+$ band on a firmer experimental basis, however, appropriate 2^+ and 4^+ members will have to be found. These are expected to be at ≈ 12.7 and 13.9 MeV, respectively. We have conducted a preliminary experiment to search for α decays of the known states at 12.84 MeV and 13.343 MeV[4] to the 6.05 MeV(0^+) and 6.92 MeV(2^+) 4p-4h states in ^{16}O. The 4^+ (13.343 MeV) state in ^{20}Ne($\Gamma_{c.m.}$=20±5 keV) has a reduced width[5] for decay to the α + $^{16}O_{g.s.}$ channel of 0.005, and hence was a likely candidate for the 4^+ member of the $K^{\pi}=0_6^+$ band; the spin of the state at 12.84 MeV ($\Gamma_{c.m.}$=55 keV) is not known, but if its spin were 2^+ it would have a maximum reduced width to α + $^{16}O_{g.s.}$ of 0.011, which is also small and would make it a likely candidate for the 2^+ member. If these two states had reduced widths of order unity for decay to the 6.05 MeV(0^+) and 6.92 MeV(2^+) 4p-4h states of ^{16}O (which should be the case for the sought-after 8p-4h states) then they would have branching ratios of ≈ 12% to ^{16}O(6.05 MeV) and 9% to ^{16}O(6.92 MeV) for the ^{20}Ne(13.343 MeV, 4^+) state, and ≈ 20% to ^{16}O(6.05 MeV) and 0.5% to ^{16}O(6.92 MeV) for the ^{20}Ne[12.83, (2^+)] state. Hence the decay of both states to the 6.05 MeV(0^+) level should be readily observable, and in addition the decay of the 13.343 MeV state to the 6.92 MeV level should also be observable.

With the above branches in mind we sought to measure the excitation function of gamma rays from the $^{16}O(\alpha,\alpha'\gamma)$ reaction. A relatively thin (≲ 16 keV at 10.8 MeV) Ta_2O_5 target was bombarded with an α beam from the University of

Table 7.7-1
Experimental Properties of States
Belonging to the Proposed $K^{\pi}=0_6^+$ Band in ^{20}Ne [a,b]

J^{π}	E_x(MeV)	$\Gamma_{c.m.}$ (keV)	$\theta^2_{\alpha_0}$	$\theta^2_{\alpha_1}$	$\theta^2_{\alpha_2}$	$\theta^2_{\alpha_3}$	$\theta^2_{12_C}$
0^+	12.436	23.2	0.0033	0.51			
6^+	15.159	60	<8×10^{-4}		0.05	0.91	
8^+	18.538	125	0.0029		0.08	0.22	1.36

[a] Data taken from Hindi, et al.[1] and references therein.
[b] The reduced width for a level λ to a channel c was calculated as

$$\theta^2_{\lambda c} = \Gamma_{\lambda c}\left[\frac{3}{2}\frac{\hbar^2}{\mu_c R_c^2}\;\frac{2k_cR_c}{F_\ell^2(k_cR_c)+G_\ell^2(k_cR_c)}\right]^{-1}$$

evaluated at R=5.134 fm for the α + ^{16}O channel and R=6.005 fm for the ^{12}C + ^8Be channel.

Washington FN-tandem accelerator. The 10 in. × 10 in. NaI spectrometer was placed at ≈ 48 cm and $\Theta = 135°$ and was used to observe the 6-7 MeV γ-rays from ^{16}O, while a 5 in. × 6 in. NaI detector was placed at ≈ 17 cm and 90° and was used to observe the 511 keV γ-rays produced from the annihilation of positrons associated with the pair decay of the 6.05 MeV(0^+) state of ^{16}O. A cylindrical sleeve of 1.91 cm thick lucite surrounded the target ladder to insure the annihilation of positrons near the target.

The 511 keV γ-rays showed a delayed activity of half-life 2.50 minutes, which most probably comes from the β^+ decay of ^{30}P, the phosphorus being formed from the $^{27}Al(\alpha,n)^{30}P$ reaction due to the interaction of the beam halo with the Al target ladder and/or the scattered beam with the aluminum walls of the target chamber. Since the delayed activity consituted ≈ 20-30% of the prompt yield of 511 keV γ-rays, the interpretation of that yield was very difficult and was not pursued any further in this preliminary experiment.

The yields of γ-rays from the 6.13 MeV(3^-) and 6.92 MeV(2^+) states of ^{16}O at the two resonances are shown in Figs. 7.7-1 and 7.7-2. For the 13.343 MeV (4^+) state the ratio $\Gamma_{\alpha 3}/\Gamma_{\alpha 2}$ extracted from the data (taking into account the different angular distributions of the two γ-rays) was less than 2×10^{-3}.

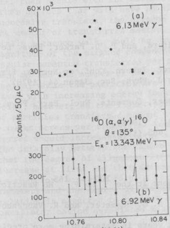

Fig. 7.7-1: Relative yields of 6.13 MeV γ-rays (upper panel) and 6.92 MeV γ-rays (lower panel) in the vicinity of the E_x=13.343 MeV (4^+) state in ^{20}Ne.

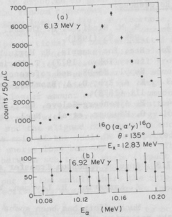

Fig. 7.7-2: Relative yields of 6.13 MeV γ-rays (upper panel) and 6.92 MeV γ-rays (lower panel) in the vicinity of the E_x=12.84 MeV state in ^{20}Ne.

Using the value $\Gamma_{\alpha 2}$=6±3 keV[5] an upper limit of 0.01 can be placed on the reduced width of the 13.343 MeV(4^+) state for α-decay to the 6.92 MeV(2^+) 4p-4h state in ^{16}O. Hence unless the reduced width of the 13.343 MeV state for α-decay to the ^{16}O(6.05 MeV,0^+) 4p-4h state is ≈ 2 orders of magnitude larger than the above reduced width for decay to the 6.92 MeV(2^+) state, which is unlikely since the 6.05 MeV and 6.92 MeV states are members of the same 4p-4h band in ^{16}O and hence have the same intrinsic structure, the above result would indicate that the 13.343 MeV(4^+) state is not the sought-after 4^+ member of the $K^\pi=0_6^+$ 8p-4h band in ^{20}Ne.

A cursory inspection of the angular distribution of the 6.13 MeV γ-rays at the E_x=12.84 MeV resonance was made and was found to be consistent with that expected from a 2^+ resonance. However, the spin cannot be uniquely determined from the singles angular distribution.

We are currently planning a more systematic search for low spin 8p-4h states in the excitation region 12.5 - 14.5 MeV and a measurement of α-γ angular correlations to get rid of delayed activities and to determine the spins uniquely.

References:

1. M. M. Hindi, J. H. Thomas, D. C. Radford, and P. D. Parker, Phys. Lett. 99B, 33 (1981).
2. See, for example, H. Horiuchi, in: Proc. Intern. Conf. on Nuclear Structure (Tokyo, 1977), T. Marimori, ed.; J. Phys. Soc. Japan 44 (1978) Suppl. 85-98, and references therein.
3. K. A. Erb, D. A. Bromley, and J. Weneser, Comments. Nucl. Part. Phys. 8, 111 (1978).
4. F. Ajzenberg-Selove, Nucl. Phys. A300, 1 (1978).
5. O. Häusser, et al., Nucl. Phys. A179, 465 (1972).

7.8 Angular Momentum Transfer and Alignment in the ^{100}Mo + ^{165}Ho Reaction

A. Lazzarini, R. Loveman, V. Metag[+], A. G. Seamster, and R. Vandenbosch

Much effort has been spent in recent years in determining more precisely the mechanism of energy loss in deeply inelastic collisions. Our present interests have addressed themselves to this question by determining subtleties of the collision process that have direct bearing on which models for the energy dissipation mechanism may be the most reasonable. Different theoretical approaches have argued that different processes are responsible for the effect. One view is that the dissipation occurs by multiple excitation of the different collective modes of vibration/rotation of the two interacting nuclei.[1] In other cases the mechanism is viewed as the transfer back and forth between the nuclei of individual nucleons; their relative momentum is brought across and then redistributed by collisions within the other nucleus.[2,3]

A question of current experimental interest is whether the semiclassical correlations between impact parameter and energy loss persist or whether fluctuations destroy them. The fact that an experimental Wilczynski plot has a ridge with a finite width shows both that the concept of a deflection function exists (semiclassical) but that there are dispersions present which give it a finite width. Fluctuations in the model by which collective degrees of freedom are excited arise from the zero point motion of the nuclear slope. On the other hand, fluctuations present in the particle exchange model arise from the stochastic nature of the process. It is interesting to determine how serious these fluctuations may be.

The transfer of orbital angular momentum into internal spin of the fragments promotes an alignment of their spin along the normal to the reaction plane defined by the beam and the observed scattered heavy ion. Rotational transitions in nuclei thus excited will reflect this alignment by their corresponding anisotropy; simultaneously, the total number of γ-rays produced is a measure of the total angular momentum imparted to the fragments during their interaction. In the model invoking the exchange of nucleons, one envisions the dynamic interplay between a component of aligned angular momentum arising from the relative orbital velocity of a nucleon in one nucleus with respect to the other oppositely traveling nucleus. At the same time, however, there is also a component of angular momentum associated with the intrinsic Fermi motion of the nucleon inside the parent nucleus; this essentially randomly oriented component will then couple with the aligned orbital component, imparting a spin to the other nucleus that will have an aligned, coherent part and a random part. With successive transfers, the aligned component is expected to grow linearly with the amount of transferred matter, whereas the random component, executing essentially a random walk, would be expected to grow less rapidly. Furthermore, the magnitude of the aligned component is determined by two factors; the amount of angular momentum transferred per particle (proportional to initial orbital momentum) and the number of particles transferred. Hence for the quasi-elastic region, where few particles are transferred, the aligned component will grow at first with increasing energy loss and decreasing impact parameter. At some point, however, as the impact parameter decreases sufficiently, the large number of particles transferred cannot balance the lesser amount of aligned component brought across per transfer. Hence the amount of aligned angular momentum transferred should increase at first and then decrease with increasing energy loss. The interplay between the random component and the aligned component is such that the degree of alignment induced in the spin of the nucleus is expected to increase at first and then decrease as the energy loss becomes greater. There is therefore expected to be a correlation between scattering angle (impact parameter) and the degree of alignment during the collision process. Such a correlation is expected to be lost or washed out in the models where the zero-point oscillator motion associated with the collective degrees of freedom is important.

To date several experimental results[4,5] exist lending credence to both models; undoubtedly both mechanisms contribute. It is our interest to establish the degree to which either of the mechanisms dominates the deep inelastic process. The experimental results obtained thus far were not obtained in the most favorable experimental conditions that would allow a fairly clear and well defined test of the two hypotheses. Our work on the $^{100}Mo + {}^{165}Ho$ system was designed to be able to make such a distinction. We determined the variation in the γ-ray angular anisotropy and multiplicity with scattering angle of the coincident heavy ion recoil. In this manner, the assumption that the degree of alignment, arising from the dominant partial wave, varies with scattering angle because different impact parameters scatter to different angles could be tested. Fig. 7.8-1 presents our experimentally determined deflection function and compares it to expectations from the nucleon exchange model of Randrup. From this figure, we can estimate the dominant partial wave, L, as a function of the experimental observables ($Q, \Theta_{c.m.}$). Fig. 7.8-2 presents our results for M_γ and W(in-plane/out-of-plane). The upper axes allow one to locate the point in Fig. 7.8-1 at which any particular M_γ or W was measured. We have indeed found a pronounced sensitivity of the degree of alignment to the scattering angle of the accompanying fragment. At the same time, the multiplicity is seen to remain saturated at a constant value; these two pieces of information, taken together, constitute compelling evidence that the correlation between scattering angle, initial orbital angular momentum, and energy loss survives any dispersive effects that quantal energy loss mechanisms may introduce. The dashed curve drawn along with the anisotropy data comes from a Monte Carlo calculation modeling the fermion exchange mechanisms.

References:

+ Present address: Max Planck Institut für Kernphysik, Heidelberg, West Germany

1. H. Esbengen et al., Phys. Rev. Lett. 41, 296 (1978).
2. J. Randrup, Nucl. Phys. A307, 319 (1978).
3. J. Randrup, Nucl. Phys. A327, 409 (1979), and to be published.
4. D. V. Harrach, et al., Phys. Rev. Lett. 42, 1728 (1979).
5. P. Dyer, et al., Phys. Rev. Lett. 39, 392 (1979) and Nucl. Phys. A322, 205 (1979).

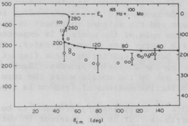

Fig. 7.8-1: Comparison of theoretical Wilczynski plot (solid line) and experimentally determined ridge (open circles). Error bars reflect experimental uncertainties in determining the ridge. Values on the solid dots along the curve denote incident orbital angular momentum, L.

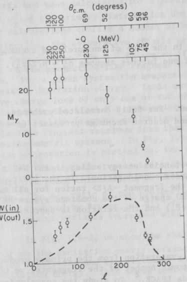

Fig. 7.8-2: Multiplicity, M_γ, and γ-ray anisotropy W(in plane)/W(out-of-plane), for the Mo + Mo system at $E_{c.m.}$ = 454 MeV. Horizontal scales interrelate ℓ, Q, and $\Theta_{c.m.}$

7.9 Particle Evaporation Effects on Z and A Distributions in Deeply Inelastic Collisions

A. Lazzarini, D.-K. Lock, and R. Vandenbosch

Information on the degree of correlation between neutron and proton exchanges in deeply inelastic collisions can, in principle, be obtained from the variances σ_A^2, σ_Z^2, and σ_N^2 of the mass, charge and neutron number distributions at fixed values for the energy loss. The experimentally observed variances, however, reflect any changes in these quantitites due to subsequent particle evaporation. We have performed calculations to explore the relation ship between the variances of the mass and charge distributions of the primary fragments for deeply inelastic collisions and the variances of the final fragments after evaporative de-excitations. We have also explored evaporation modification the isobaric charge distributions $\sigma_Z^2(A)$. There has been considerable interest recently in whether the energy loss dependence of the isobaric variances is indicative of quantal fluctuations.

The variance of the mass distribution can be related to that of the neutrons and protons by

$$\sigma_A^2 \equiv \sigma_N^2 + \sigma_Z^2 + 2\rho\sigma_N\sigma_Z \qquad (1)$$

where ρ is the correlation coefficient. In the case of uncorrelated exchange of protons and neutrons, ρ equals zero. If one further assumes $\sigma_N^2 = N/Z(\sigma_Z^2)$, one obtains

$$\sigma_A^2/\sigma_Z^2 = A/Z, \qquad (2)$$

where A and Z refer to the combined system. For fully correlated exchange, i.e., a strong interdependence between proton and neutron exchange processes (ρ = 1), we have[1]

$$\sigma_A^2 = (1 + dN/dZ)^2\sigma_Z^2, \qquad (3)$$

where dN/dZ represents the slope of the potential energy valley in the N-Z plane, averaged over the particular mass range under consideration. In the limit of a uniform charge density assumption, where the fragment <A/Z> ratios for all mass asymmetries are given by the total mass and charge of the combined system as $(A_1+A_2)/(Z_1+Z_2)$, dN/dZ equals $(N_1+N_2)/(Z_1+Z_2)$ and the relation is approximated by

$$\sigma_A^2/\sigma_Z^2 = (A/Z)^2. \qquad (4)$$

To determine the effect of particle evaporation from the primary products on the correlation between the mass and atomic number of the fragments, we use the Monte Carlo simulation evaporation code LPACE.[2] To study the correlations introduced by particle evaporation, we started with an uncorrelated distribution P_I for the production of a given primary fragment (Z_I,N_I) expressed as a product of Gaussian distributions in Z and N,

$$P_I(Z_I,N_I) \propto [e^{-(Z_I-Z_0)^2/2\sigma_Z^2}] \cdot [e^{-(N_I-N_0)^2/2\sigma_N^2}] \qquad (5)$$

The quantities Z_0 and N_0 determine the centroid of the primary distribution. For a given fixed initial fragment excitation energy, E^*, the final distribution is obtained by

$$P_F(Z_F,N_F,E^*) = \sum_{N_I}\sum_{Z_I} H(Z_I,N_I,Z_F,N_F,E^*)P_I(Z_I,N_I),$$

where $H(Z_I,N_I,Z_F,N_F,E^*)$ is a transformation matrix which represents the probability that the primary fragment (Z_I,N_I) with excitation E^* will end up as a final fragment with Z_F and N_F by the process of evaporation. To obtain the transformation matrix we performed Monte Carlo evaporation calculations for a 7 × 7 matrix of Z_I and N_I values representing possible combinations of the N and Z values.

We have performed calculations for the ^{56}Fe + ^{56}Fe and ^{56}Fe + ^{165}Ho systems with ^{56}Fe as the projectile at E_{lab}=464 MeV, and for the ^{86}Kr + ^{92}Mo system with ^{86}Kr as the projectile at E_{lab}=430 MeV. Once the transformation matrix had been calculated for a particular excitation energy, we varied the σ_N^2 and σ_Z^2 of the primary distribution and determined the post-evaporative widths. The calculations confirm a number of qualitative expectations. For ^{56}Fe as a projectile, the evaporative effects are less important for the $^{56}Fe + {}^{165}Ho$ system than for the $^{56}Fe + {}^{56}Fe$ system if one takes into account the tendency of A/Z of the projectile-like fragment to drift toward that of the composite system. For a given system the evaporative effects become more important with increasing excitation energy. It is surprising, however, that an average evaporative charge loss of only one or two charge units can result in a sizeable correlation in the final N-Z populations. In interpreting the results at a given projectile-like fragment excitation energy, one must remember that the projectile-like fragment receives less than half of the total excitation energy for mass asymmetric systems. In Fig. 7.9-1, the variance of the charge distribution after evaporation is plotted vs. the charge variance before evaporation for the $^{56}Fe + {}^{165}Ho$ system at selected excitation energies of the projectile-like fragment. In these calculations we have kept σ_N^2/σ_Z^2 = N/Z for the primary distribution. The A/Z ratio of the projectile-like fragment was chosen to reflect the drift observed by Breuer, et al.[3] for the $^{56}Fe + {}^{165}Ho$ system. As expected, the total charge variance increases with excitation energy.

In Fig. 7.9-2, we show the charge variance for fixed A, $\sigma_Z^2(A)$. We note that as the excitation energy increases, the post-evaporation variances at constant A decrease and are virtually independent of the initial variances at high excitation energy. This shows that there is a focusing of the final distribution

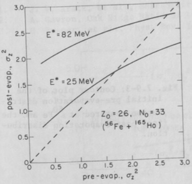

Fig. 7.9-1: Dependence of the post-evaporation charge distribution variance on the pre-evaporation variance for two different projectile-like fragment excitation energies.

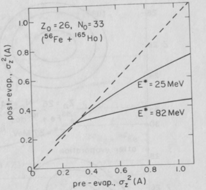

Fig. 7.9-2: Dependence of post-evaporation charge distribution variance for fixed A on pre-evaporation variance.

towards the valley of beta stability. This focusing effect increases with excitation energy of the fragment. In Fig. 7.9-3, we show contour plots of the primary distribution and the final distribution after evaporation for the primary fragment ^{60}Fe, which corresponds to the most likely projectile-like fragment for ^{56}Fe and ^{165}Ho. In this representation we can see the focusing effect more clearly. We can also see the shift in position of the maximum of the distribution in addition to the focusing into the N=Z valley.

In Fig. 7.9-4, we have plotted the post-evaporative ratio σ_A^2/σ_Z^2 vs. excitation energy for the ^{56}Fe + ^{56}Fe system for two different assumptions about the initial distribution. The evaporative effects are the largest for this less neutron-rich system, and Breuer et al.[3] have already cautioned about drawing quantitative conclusions for this system. It is, however, the most tractable system because there are no uncertainties in the average division of the energy loss between the two fragments, and because there is no drift of the Z/A ratio of the projectile due to charge equilibration with a more neutron rich target. For uncorrelated exchanges of neutrons and protons, ρ=0, we should expect σ_A^2/σ_Z^2 =A/Z and for fully correlated exchange, ρ=1, and $\sigma_A^2/\sigma_Z^2 = (A/Z)^2$. Inclusion of pairing and shell corrections can result in σ_A^2/σ_Z^2 values which are smaller than

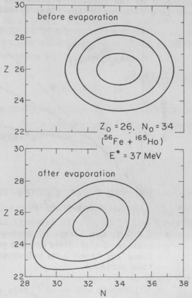

Fig. 7.9-3: Contour plot of the initial pre-evaporation distribution centered at ^{60}Fe and the final post-evaporation distribution.

$(A/Z)^2$ for fully correlated exchange of nucleons based on equation (3) above.[1] We see that if we start out with an uncorrelated system, $\sigma_A^2/\sigma_Z^2 = A/Z$, a considerable correlation in the final distribution appears after evaporation. Also shown in Fig. 7.9-4 is the effect evaporation has for a somewhat correlated initial distribution obtained from the program FERMEX, which calculates the primary distribution for deeply inelastic reactions using a Monte Carlo method (see Sec. 7.10 of this report). We see that most of the correlation of the final distribution comes from the focusing effect due to the evaporation of particles. Because of the nearly complete loss of memory in going from the primary N-Z distributions following the deeply inelastic collision to the post evaporative distributions for this system, it is impossible to infer any information about how correlated the exchanges are in the deeply inelastic collision.

Finally we illustrate how this loss of memory complicates the interpretation of the dependence of the variances for fixed A on excitation energy. Such dependences have been discussed in the context of evidence for quantal fluctuations. In a preliminary exploration of this aspect we consider an assumed initial distribution proportional to the temperature, $[T\propto(E_{loss})^{1/2}]$, and show in Fig. 7.9-5 how evaporative effects lead to final variances nearly independent of the excitation energy, as would also be expected if the initial primary fragment variances had been independent of excitation energy due to quantal effects. Preliminary calculations for the $^{86}Kr + ^{92}Mo$ system, however, indicate that the evaporative effects are less severe for this system.

References:

1. J. V. Kratz, et al., Zeitshrift für Physik A, 296 (1980).
2. A. Gavron, Oak Ridge National Laboratory
3. H. Breuer, et al., Phys. Rev. Lett. 43, 191 (1979).

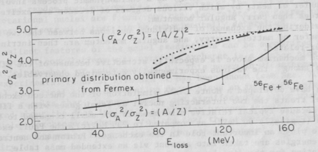

Fig. 7.9-4: The dotted curve (.....) represents the secondary distribution obtained using the FERMEX output as the primary distribution. The dotted-dashed curve represents the secondary distribution obtained using an uncorrelated primary distribution with $\sigma_A^2/\sigma_Z^2 = A/Z$.

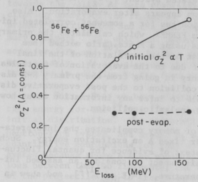

Fig. 7.9-5: Illustration of the dependence of post-evaporation charge-distribution variances at fixed A assuming an initial distribution with the variance proportional to temperature.

7.10 A Monte Carlo Fermion Exchange Calculation

A. Lazzarini and R. Vandenbosch

The mechanism by which energy, mass, and angular momentum are transferred between two nuclei in a deeply inelastic collision has been the object of much conjecture and study. Different possibilities have been postulated in the literature;

(a) Considering the excitation of collective modes of the dinuclear complex.
(b) Treating the exchange of energy as a thermodynamic process involving the transfer of heat, by which various degrees of freedom are excited. These degrees then carry angular momentum.
(c) Considering the exchange of individual nucleons between the two nuclei. The transfer of matter, energy, and angular momentum are then intrinsically inter-related.

The third mechanism above is especially attractive because of the direct relationship among the various experimentally determined observables.

We have developed a Monte Carlo simulation of the nucleon exchange model. The model treats the two interacting nuclei as Fermi gases with a finite temperature. Because typical relative c.m. momenta are small compared to the Fermi momentum (typically 90 MeV/c as compared to 235 MeV/c), the Pauli exclusion principle plays an important role in the exchange. Proton and neutron nuclear binding energies are taken into account via an extended mass table. The spatial configuration for the dinuclear complex is modeled as two touching spheres. The nucleon exchange probabilities are determined by considering the relative amount of available phase space for transfer of particles (neutrons vs. protons and exchange to and from one of the two nuclei). The particle exchange directly determines the mass transfer; the formation of particle-hole pairs (hole in the donor nucleus and particle in the acceptor nucleus) transforms the kinetic energy of relative motion into internal excitation in the fragments; the cross product of position at which transfer occurs ($\vec{r}$), and the total momentum of the transferred nucleon ($\vec{k}_{total}=\vec{k}_{relative}+\vec{k}_{Fermi}$) allows one to calculate the angular momentum associated with the transfer.

The method of calculation is as follows. For an initial orbital angular momentum one allows the two systems to interact by nucleon exchange while keeping track of the cumulative energy loss (Q-value). By stopping the calculation at a given Q-value, one then has an ensemble of Monte Carlo events (typically 500-1000) from which any of various experimentally observable quantities can be projected.

By determining the variances σ_A^2, σ_Z^2, and σ_N^2 it is possible to calculate the degree of proton-neutron correlation in the exchange process:

$$\rho \equiv (\sigma_A^2-\sigma_Z^2-\sigma_N^2)/(2\sigma_Z\sigma_N)$$

For small energy losses (few transferred nucleons, $\hat{N}$), ρ is very close to zero. As the energy loss becomes greater, ρ grows slowly but eventually saturates at ρ=1. In a similar manner one can project the yield $\hat{Y}(Z,N)$ as a function of Q-value or $\hat{N}$ to observe the (Z,N) distribution of the deeply inelastic collision. The angular momentum distribution of the ensemble can also be studied. Because of the interplay between transfer of aligned orbital angular momentum from the relative motion and the transfer of randomly oriented angular momentum from the Fermi motion, the total angular momentum, $\vec{J}$, will not be completely aligned along an axis normal to the reaction plane, but will be distributed with a spread determined by the number of exchanged particles and their internal angular momentum within the nuclei from which they are transferred. The degree of alignment is measured by the alignment parameter, defined as

$$P_{zz} \equiv (3<M^2/J^2>-1)/2$$

The alignment parameter then will vary with Q, reflecting the relative importance of aligned and random angular momenta. In domains of the periodic table where deformed rotational nuclei are found, one can also relate the degree of alignment to γ-ray anisotropies that can be experimentally determined.

The salient features of the model predictions can be summarized as follows.

(a) The growth of correlations with particle exchange is a rather slow function of particle number, or equivalently, Q. This seems in disagreement with some experimental results, although it has been shown (see Sec. 7.9 of this report) that final state evaporative decay plays an important role in the measured results that, in some cases, can significantly alter what is to be inferred about the deep inelastic scattering process itself.

(b) The nucleon exchange mechanism predicts that the correlation between the spin of one fragment, $\vec{I}_1$, and that of the other fragment, $\vec{I}_2$, is strong; the quantity

$$\beta \equiv (\vec{I}_1\cdot\vec{I}_2)/|\vec{I}_1|\ |\vec{I}_2|$$

should be nearly 1.0.

(c) The partition of excitation energy between the two fragments approaches an equilibrium partition ($E^*_2/E^*_1=M_2/M_1$) only during the later stages of the collision process; initially, excitation energy is partitioned more nearly equally between the two nuclei. This behavior follows naturally from phase space considerations of the nucleon transfer and from the particle-hole nature of the excitation in this model. The degree to which this equi-partition is observed experimentally is currently an important issue in deep inelastic scattering. Neutron evaporation studies would indicate nearly thermal equilibration at early states of the collision process; there is some question, however, how much final state evaporative decay may influence such measurements.

Work on the program is not totally complete; several modifications come to mind which would improve the physics of the model. One important point is the consideration of spatial deformation of the dinuclear complex which, in general, is a time-dependent property which varies continuously as the collision proceeds. The program's current ability to reproduce measured observables is good. Several results are quoted in the article outlining our ^{165}Ho + ^{100}Mo measurements.

7.11 The Role of Nucleon Exchange in Angular Momentum Transfer in Heavy Ion Collisions

R. Vandenbosch

We have previously developed a simple model based on nucleon exchange for calculating the fragment angular momentum components in the quasi and deeply inelastic scattering.[1] In this model the damping of the relative motion of the colliding nuclei results in transfer of orbital angular momentum into intrinsic fragment angular momentum perpendicular to the reaction plane. Additional angular momentum is developed in the fragments as a consequence of the Fermi motion of the exchanged nucleons. If the exchange occurs through a window whose radius is small compared to the fragment radius, the components from the Fermi motion will be localized in a plane perpendicular to the internuclear axis. The component of the total angular momentum arising from the relative motion grows linearly with the number of exchanged particles. The component from the Fermi motion grows only as the square root of the number of exchanged particles, due to the random walk nature of the vector addition of the contributions from each exchange. This dependence of the angular momentum transfer on the number of exchanged particles leads to an increase in both the magnitude and the alignment of the fragment angular momentum with increasing energy loss. If the largest energy losses are associated with lower partial waves, the aligned component from the relative motion can eventually decrease for very large energy losses.

A recent study[2] of the gamma ray multiplicity and out-of-plane gamma ray anisotropy for the Ho + Ho system exhibits a qualitative behavior consistent with these expectations. We have therefore performed a quantitative calculation of the gamma ray anisotropy and total angular momentum transfer for this system. We have used the one-body dissipation model of Randrup[3] to calculate the number of nucleons exchanged and the orbital angular momentum transfer as a function of energy loss. This model incorporates a neck degree of freedom and includes the effect of Pauli blocking on the nucleon exchange rate. It does not, however, include the contribution to the angular momentum transfer. This contribution has been calculated from the number of particles exchanged and an estimate of the average angular momentum carried by each particle. The latter quantity has been taken from an average over the single particle j values for the nucleons in the last major shell. An alternative approach is to employ an average Fermi energy and the nuclear radius. The only arbitrary parameter in the calculation is the fraction of the stretched gamma rays in the de-excitation cascade which are dipole rather than quadrupole. The results of the calculation for two choices of this parameter are shown in Fig. 7.11-1. It is seen that with a reasonable choice of this parameter the results can be remarkably well accounted for. The dependence of the total angular momentum transfer on energy loss is also given quite well, with the discrepancy in the absolute magnitude being within the uncertainty in the original deduction of the angular momentum from the multiplicity data. The large decrease in the anisotropy with increasing energy loss is a consequence of the smaller aligned component due to lower ℓ-values contributing, together with an increasing randomly oriented component from the increased number of particle exchanges for large energy losses. The total angular momentum remains rather constant due to the near-cancellation of the decrease in J from the aligned component and the increase from the Fermi motion component.

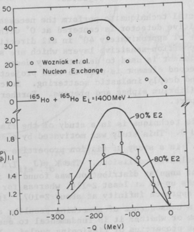

Fig. 7.11-1: Comparison of nucleon exchange model calculations with the total spin per fragment (upper) and anisotropy (lower) data of Ref. 2

References:

1. R. Vandenbosch, Phys. Rev. C20, 171 (1979).
2. G. Wozniak, et al., Phys. Rev. Lett. 45, 1081 (1980).
3. J. Randrup, private communication

7.12 Saddlepoint Properties of Rapidly Rotating Nuclei

A. Lazzarini, K. Lesko, V. Metag, A. Seamster, M.-Y. B. Tsang, and R. Vandenbosch

We have embarked on a new program to measure fusion-fission angular distributions and total cross sections with the ability to discriminate against incomplete fusion-fission or sequential fission from deeply inelastic collisions. Interpretation of heavy ion reactions seeking to learn the properties of compound nuclei near the high-Z or high angular momentum limits of stability are complicated and compromised by the fact that often only a fraction of the mass and charge of the projectile is captured by the target, resulting in a compound nucleus which does not have all the mass, charge, and angular momentum expected. It is important, therefore, to devise some method for isolating those events for which complete fusion of the projectile and target occurs. Our approach is to look for fission fragments from the compound nucleus while also detecting any possible pre-equilibrium particles such as projectile-like fragments or light charged particles (α,p) with projectile-like velocities. Events in which projectile-like fragments (either from deeply inelastic collisions or incomplete fusion reactions) are also observed would then be rejected.

We have devised an experimental technique to perform the necessary rejection. A large-area position sensitive detector is centered at 0° with respect to the beam. It subtends an angle of approximately 40° in all directions. The detector consists of four active position-sensitive layers which are separated by graded absorbers. The first element is used to detect heavy decay fragments from the compound nucleus. The second element is used to veto projectile-like fragments associated with quasi and deeply inelastic scattering. Successive elements are used to veto pre-equilibrium alphas and protons. Further details are given in Sec. 11.7 of this report.

Our first application of this technique is in a study of the fission properties of a system with high Z and J. This study was motivated by a surprising result obtained by Glässel, et al.[1] in a study of fission properties of very heavy nuclei produced in deeply inelastic collisions. The $K_o=(J_{eff}T/\hbar^2)^{1/2}$ parameter characterizing the fragment angular distribution was found to increase only very slowly with Z for Z values up to at least Z=114, whereas for the J values involved K_o is expected to approach infinity at about Z=107. It is not clear whether this discrepancy is a consequence of something peculiar about the deeply inelastic reaction mechanism or whether it is fundamental to our understanding of the role of saddlepoint properties of fissioning nuclei. It seemed of great interest therefore to explore this effect in a compound nuclear fusion reaction. We are measuring the angular distribution of fission fragments in the ^{40}Ar + ^{238}U reaction. This reaction forms a compound nucleus with Z=110. It is known, however, from previous studies that only about half of the total reaction cross section leads to fusion-fission,[2,3] the remainder being associated with fission following incomplete fusion or deeply inelastic scattering. It is therefore important to establish the two-body nature of the desired events. This is being accomplished by the veto technique described above. Although the data analysis is not complete, we have obtained a preliminary angular distribution in anti-coincidence with projectile-like fragments which appears to exhibit an angular distribution close to 1/sin Θ. The distribution is shown in Fig. 7.12-1. The vetoing of alphas and protons, however, was not completely successful. We were unable to veto all protons and alphas over their large dynamic range of energies. We are planning to replace the last two elements of the detector with a thicker E detector which will allow complete vetoing of protons and alphas. We would like to repeat our measurement with this detector to determine the angular distribution of fission fragments resulting from complete fusion of the target and projectile, i.e. excluding those events where some energy and angular momentum was carried away by light particles. If the large anisotropy persists after more complete discrimination against incomplete fusion, several possibilities would have to be considered. One would be that our expectations for the saddlepoint shape are incorrect. A second is that K is not conserved from the descent from saddle to scission. A third possibility is that the dynamics of the collision is such that a true compound nucleus, with a deformation inside that of the compound nucleus saddlepoint, is never achieved.

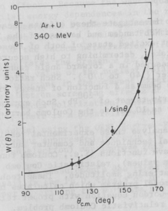

Fig. 7.12-1: Angular distribution of fission fragments in anticoincidence with projectile-like fragments.

References:

1. P. Glässel, et al., Phys. Rev. Lett. 43, 1483 (1979).
2. B. Tamain, C. Ngô, J. Peter, and F. Hanappe, Nucl. Phys. A252, 187 (1975).
3. J. V. Kratz, J. O. Liljenzin, A. E. Norris, and G. T. Seaborg, Phys. Rev. C13, 2347 (1976).

7.13 Relativistic Wave Equation Effects in Sub-Coulomb Heavy Ion Scattering

J. G. Cramer and W. G. Lynch

We have continued the experimental and theoretical investigation of effects which can be experimentally observed as deviations from Rutherford scattering in the sub-Coulomb scattering of heavy ions, as reported in previous reports.[1,2]

Our initial interest was focused on the effects arising from the description of the scattering process with a relativistically invariant wave equation such as the Klein-Gordon equation (for bosons) or the Dirac equation (for fermions) rather than the usual non-relativistic Schrödinger equation. We have shown that the dynamics of the relativistic wave equation produces deviations from Rutherford scattering which have a characteristic dependence on energy and angle and can be observed at backward angles in scattering experiments having a relative accuracy on the order of 0.1%.

The system $^{16}O + ^{208}Pb$ was selected to investigate these effects because of its suitability for measurements with the NPL tandem and because of the large energy gap between the ground state and first excited state of both of these nuclei. Experimental measurements were undertaken, determining to high accuracy the ratio of the scattering cross section measured in a forward angle counter (30°) to that measured in a back angle counter (140° to 170°). Such ratios were measured simultaneously on both sides of the beam as a function of energy with projectiles of ^{12}C, ^{14}N, ^{15}N, and ^{16}O and a strip target of ^{208}Pb. Such excitation functions were measured from energies as low as 10 MeV to the Coulomb barrier.

As described in previous reports,[1] to analyze these experimental results it has been necessary to develop new numerical techniques and computer subroutines for calculating relativistic Coulomb wave functions (i.e., Coulomb functions of complex non-integer angular momentum values), relativistic Coulomb phase shifts, and relativistic Rutherford scattering amplitudes. These techniques have been incorporated in an optical model program which calculates heavy ion scattering cross sections from the Klein-Gordon equation with proper relativistic kinematics and proper treatment of the relativistic Coulomb problem.

We have also calculated contributions to sub-Coulomb heavy ion scattering due to other effects which would give effects of the same order as the wave equation contribution. We have determined that nuclear polarization (i.e., virtual excitation of the giant dipole resonance), electron screening of the target by inner-shell electrons, and vacuum polarization effects would be expected to make such contributions. However, each of these effects has different (and, in principle, distinguishable) angle and energy dependences.

The result of these investigations is that statistically significant deviations from Rutherford scattering have been observed, and these deviations are completely consistent with the predicted contributions from relativistic wave equation effects, nuclear polarization, and electron screening. This is illustrated by the chi-squared contour plot shown in Fig. 7.13-1. Here the horizontal axis variable a_1 is the strength factor for the wave equation effect, with a_1=1.0 corresponding to the predicted strength of the effect, and the vertical

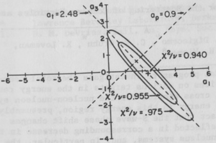

Fig. 7.13-1: Two-dimensional contour plot of χ^2/ν vs. the parameters a_1 (strength of wave equation effect) and a_3 (strength of nuclear polarization effect).

axis variable a_3 is the corresponding strength factor for the nuclear polarization effect. Because the wave-equation and nuclear polarization effects have similar energy dependences in the region of maximum sensitivity, the quantities best determined by the measurement are two orthogonal linear combinations of the strength factors a_1 and a_3. For the purposes of this plot, the strength factor A_2 for the vacuum polarization effect is taken as equal to 1.0. The analysis demonstrates the presence of the relativistic effect and is consistent with the expected value of the nuclear polarization. Vacuum polarization effects were not important in the present experiment, primarily because the uncertainties in the electron screening effects at low energies completely masked possible effects from vacuum polarization, which are only important at the lowest energies. However, there is a possibility that a recent re-calculation of the screened Coulomb potential using the ORNL Hartree-Fock program[3] with the exchange terms in the screening suppressed (because the particle responding to the screened field is not an electron) may improve this situation.

The measurements described above are completed, and have been described in detail in the Ph.D. thesis of Dr. William G. Lynch. A letter and a longer paper describing the work are now in preparation.

References:

1. Nuclear Physics Laboratory Annual Report, University of Washington (1979), p. 93.
2. Nuclear Physics Laboratory Annual Report, University of Washington (1980), p. 129.
3. C. C. Lu, et al., Atomic Data 3, 1 (1971).

7.14 Total Reaction Cross Sections for the Scattering of Complex Particles at 50,000 MeV/A

J. G. Cramer, R. M. DeVries[+], N. Digiacomo[+], C. R. Gruhn[*], R. Loveman, J. C. Peng[+], J. Sunier[+], and H. H. Wieman[*]

We are continuing our experimental program to investigate the total reaction cross sections of complex projectiles on various targets in the energy range from 20 MeV/A to 200 MeV/A. The total cross section for the nucleon-nucleon system becomes progressively smaller with energy in this energy region, presumably because of hard-core effects and the fact that the S-wave phase shift changes sign in this region. This should be reflected in a corresponding decrease in the reaction cross sections for nucleus + nucleus systems, and, in particular, the very strong absorption which is a predominant characteristic of heavy ion reactions at lower energies should be reduced.

It is important to verify experimentally that such a reduction in the total reaction cross section does, in fact, exist, for if it does, the "transparency" which it gives to elastic scattering at energies near 100 MeV/A will permit more detailed investigation of nuclear processes and more sensitivity to new and "exotic" phenomena than would be the case in an energy region dominated by strong absorption. As a first step to investigating the behavior of the reaction cross section in this energy region, two of our group (RMD and JCP) have assembled a body of light ion (p,d,α) elastic scattering data and the optical model parameters from the analyses of these data used to infer a set of total reaction cross sections. These inferred total reaction cross sections are found: (a) to be in good agreement with the few measured total reaction cross sections available for these systems, (b) to be in good agreement with simple Glauber-model calculations based on measured electron-scattering distributions for the target and projectile and on measured nucleon-nucleon total cross sections; and (c) to show a clear tendency toward a significant decrease in the total reaction cross section in the region where the nucleon-nucleon total cross section becomes small.

The experimental program of measuring these cross sections has gone through a development phase, using the ^{3}He beam of the LBL 88 in. cyclotron and the "local" ^{4}He beam of the low energy beam line of the LBL Bevalac. The work entered the production phase, with two data-collection runs at the Bevalac. The first data-collection run, which occurred in December, 1979, was successful in obtaining measured values for the total reaction cross section for α + C at 65 MeV/A (CM) to about 8% and for α + Pb at 85 MeV/A (CM) to about 13%. The second run, which was in March, 1980, collected data for 135 MeV/A α on targets of carbon, nickel, zirconium, and lead. The results of this work were presented[1] in an invited paper at the Minneapolis DNP Meeting last fall, and a paper describing the work is presently in preparation. We find that the total reaction cross sections which we have measured in this energy region are indeed considerably smaller than "geometric", and in fact appear to be somewhat smaller than but consistent with Glauber-model predictions.

Further measurements in this program will be continued as accelerator time on suitable accelerators (LBL, MSU, Saturn) becomes available.

References:

+ Los Alamos Scientific Laboratory, Los Alamos, New Mexico
* Lawrence Berkeley Laboratory, Berkeley, California
1. R. M. DeVries, Bull. Am. Phys. Soc. 25, 721 (1980).

8. RESEARCH BY OUTSIDE USERS

8.1 Theoretical and Experimental Neutron Dosimetry

A. Rubach[+] and H. Bichsel[*]

The average energy needed to produce an ion pair for neutrons, W, and the dose conversion factor, r, for neutrons incident on spherical ionization chambers were calculated, using the NPL Vax computer. These quantities are necessary to convert measured ionization J per unit mass m in a cavity ionization chamber into dose D_w absorbed in the wall material of this chamber:

$$D_w = r\,W\,J/m.$$

The most important result is that r·W is a function of m. Cavities in tissue equivalent (TE) material filled with either tissue equivalent gas or air, and graphite chambers filled with carbon dioxide were studied. Chamber sizes ranging from the Bragg-Gray case (infinitesimal) to the infinite cavity were considered. Results for finite cavities of .01, .1, 1, and 10 cm^3 were obtained in addition. The neutron energies used for the calculations ranged from 0.4 to 14 MeV. Several energies which show strong resonances for the production of heavy charged particles are included. The ionization chambers considered for the calculation were a tissue equivalent plastic (nylon and polyethylene) chamber filled with either air or tissue equivalent gas (methane, carbon dioxide, and nitrogen) and also a graphite chamber filled with carbon dioxide.

For 14 MeV neutrons, the following results were obtained:

Dose conversion factor r

wall/gas \ cavity size*:	0.0	.01	.1	1.0	10.	infinite
TE/TE	1.00±.07	0.99	0.99	1.00±.04	1.00	1.02±.00
TE/air	1.21±.08	1.18	1.18	1.19±.06	1.22	4.65±.00
C/CO_2	1.06±.08	1.05	1.09	1.14±.03	1.19	1.23±.00

Average W (in eV)

wall/gas \ cavity size:	0.0	.01	.1	1.0	10.	infinite
TE/TE	31.2	31.3	31.3	31.3±1.6	31.3	31.3
TE/air	35.0	35.1	35.2	35.2±2.1	35.2	37.9
C/CO_2	35.1	35.7	35.9	36.0±1.4	36.1	36.1

* The cavity size is given in cm^3. Standard temperature and pressure (101 kPa, 22°C) are assumed. The independent parameter for the calculation is the cavity diameter (mg/cm^2).

The neutron sensitivity k_u can be computed from the information obtained in this work. This quantity is necessary for the discrimination of the gamma component in a neutron beam.

The stopping powers and W data necessary for the calculations were gathered and their uncertainties were estimated. This information is necessary for the calculation of r and W and their uncertainties. The uncertainty due to errors in the primary particle spectrum was not included (this also includes the uncertainty in "kerma", the kinetic energy released per unit mass by one neutron/cm^2).

The NPL cyclotron was used for the experimental work. This cyclotron produces a neutron spectrum with an average energy of about 8.5 MeV by bombarding a beryllium target with 21 MeV deuterons. Two cavity ionization chambers, a 1 cm^3 tissue equivalent chamber and a 2 cm^3 graphite chamber, were employed. These chambers were placed in a pressure vessel filled with either tissue equivalent gas, air or carbon dioxide. The number of ion pairs J produced in these cavities (per unit mass of gas) filled with different amounts of gas, i.e., at different gas pressures, and exposed to the same neutron fluence was compared with the calculated number of ion pairs per unit mass for one neutron incident per square centimeter for the same neutron spectrum.

Good agreement is achieved between experiment and theory for the tissue equivalent chamber filled with air and for the graphite chamber filled with CO_2. The experimental result for the tissue equivalent chamber filled with tissue equivalent gas shows a large discrepancy with the calculated result at low gas pressures (Fig. 8.1-1). The experiment indicates an increase of the number of ion pairs produced per unit mass of gas in the cavity by approximately 2% at gas pressures below 10 kPa (75 Torr), while the calculation shows a maximum increase of 0.7%. Calculations at a neutron energy of 14 MeV indicate that the large uncertainty of the stopping power of heavy ions in tissue equivalent plastic is probably responsible for this difference.

References:

\+ Medical Radiation Physics, University of Washington

* 1211 - 22nd Ave. E., Seattle, WA 98112

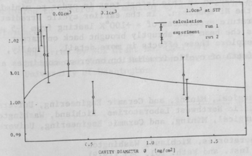

Fig. 8.1-1: Number of ion pairs produced per unit mass in a TE/TE cavity ionization chamber (EG&G) exposed to d(21 MeV)+Be neutrons plotted vs. cavity size Ø.

8.2 Light Ion Irradiation Creep

C. H. Henager,[+] R. G. Stang,[*] E. P. Simonen[++], and E. R. Bradley[++]

Materials placed under stress and subjected to the elevated neutron fluxes of both breeder and fusion reactors exhibit a form of accelerated deformation termed irradiation creep. Due to the difficulty, cost, and time required to make precise in-reactor creep measurements, there is a world-wide interest in simulating in-reactor creep by bombarding materials of interest with energetic light ions under well-controlled conditions. Such experiments enhance our understanding of the operating creep mechanisms and permit screening of potential reactor alloys. The Radiation Effects on Metals program supported by the Division of Basic Energy Sciences, U.S. Department of Energy at Battelle, Pacific Northwest Laboratories (PNL) is conducting an irradiation creep experiment using the tandem Van de Graaff accelerator at the U.W. Nuclear Physics Laboratory.[1,2]

The initial series of experiments to determine the stress dependence of irradiation creep in pure, 90% cold-worked Ni has been completed this past year. Ten continuous irradiations with 17 MeV deuterons have been performed at 473°K with applied tensile stresses ranging from 250 to 134 MPa. Each specimen was tested at a constant stress level and, therefore, a separate irradiation for each stress level was performed. The stress dependence data consists of plotting the irradiation creep rates vs. applied stress with a fit given by the semi-empirical relation $d\varepsilon/dt = A\sigma^n$. In this manner, the stress exponent, n, was determined to be 1.02±.44. Microstructural examination of the irradiated specimens using transmission electron microscopy has begun at PNL. This will be coupled with theoretical models of irradiation creep in order to fully understand this initial series of experiments.[3]

At the present time, the comparison between cyclic and continuous irradiations is being further explored. A recently completed experiment in which a specimen was irradiated continuously for 15 hours and then irradiated under cyclic conditions for 8 hours gave the unexpected result[4] of no creep rate enhancement due to cycling, in contrast to a previous report. The manner in which the deuteron beam is pulsed was changed in this latest test in order to minimize temperature excursions of the Ni specimen. In the earlier cyclic irradiations it was probable that temperature excursions of ≈ +100°K lasting from 1-5 sec occurred in the specimen as the beam was abruptly brought back on target. Further tests are planned to explore these effects in more detail. Finally, theoretical modeling of the effects of cyclic irradiation on creep continues at PNL.[5]

References:

+ Department of Metallurgical, Mining, and Ceramic Engineering, University of Washington and Pacific Northwest Laboratories, Richland, Washington

* Department of Metallurgical, Mining, and Ceramic Engineering, University of Washington

++ Pacific Northwest Laboratories, Richland, Washington

1. P. L. Hendrick, Nuc. Inst. and Meth. 161, 345 (1979).
2. C. H. Henager, J. L. Brimhall, E. P. Simonen, J. Nucl. Mat. 90, 290 (1980).

3. C. H. Henager, E. P. Simonen, E. R. Bradley, R. G. Stang, abstract accepted for presentation at 2nd Topical Meeting on Fusion Reactor Materials, Seattle, WA, August 9-12, 1981.
4. E. P. Simonen and P. L. Hendrick, J. Nucl. Mat. 85 & 86, 873 (1979).
5. E. P. Simonen and C. H. Henager, op. cit.

8.3 Fast Neutron Beam Radiotherapy-Medical Radiation Physics*

J. Eenmaa,+ P. Wootton,+ and P. Wiest+

The Medical Radiation Physics Division continued its routine support of treatment of cancer patients and neutron beam radiobiology. During the course of the year, the computer programs for treatment control and monitoring were updated and the computer systems equipment repaired. This made it possible to turn the operation of the treatment control station over to the radiotherapy technicians, with the physics technologist remaining responsible for the daily machine calibration check.

Automatic readout of ambient temperatures and pressure was installed for ion chamber dose measurement calculations.

An X-ray port filming system was installed on the neutron therapy system. The system consists of a Picker PX-8B Shock Proof Rotating Anode X-ray tube and Picker GX-325 X-ray Generator. The system allows for the taking of X-ray pictures through the neutron beam collimator system, thereby verifying the application of the proper field to the specified area of the patients' anatomy. The X-ray tube can be positioned upstream of the neutron beam collimator, and retracted, by remote control.

A spectrum analyzer and display unit was acquired and installed on the cyclotron as part of the cyclotron RF system equipment overhaul.

Work continues on the installation of the TI Process Controller on the cyclotron to control and monitor cyclotron turn-on and operational sequences.

References:

* Supported by NCI Grant No. CA-12441
+ Division of Medical Radiation Physics, Department of Radiation Oncology, University of Washington

---

8.4 Fast Neutron Beam Radiation Therapy Clinical Program[*]

G. E. Laramore[+]

During the time period April, 1980 through March, 1981, 92 patients received all or a part of their planned radiation therapy using the neutron beam produced by the University of Washington cyclotron. An additional 31 patients were treated with conventional photon radiation in the control arms of certain randomized, prospective clinical trials designed to compare neutron radiotherapy with the results of "state-of-the-art" photon radiotherapy. The majority of the studies utilize neutrons as part of a mixed beam regime (neutrons twice a week and photons three times a week) but some studies include treatment arms utilizing neutrons alone. Including data from the other U.S. institutions participating in neutron radiotherapy, the following information has been obtained for various tumor sites:

A. Squamous Cell Carcinomas of the Head and Neck (Inoperable)

This study randomizes patients between the mixed beam regime and photon radiation alone. Thus far approximately 250 patients have been entered on the study with there being approximately a 6% difference in the local control rates at one year from completion of treatment. The code on this study has thus far not been broken.

B. Malignant Gliomas

During the first part of the study period patients received 5000 rad_γ whole brain photon irradiation and then were randomized to receive either a 1500 rad_γ photon boost or 400-480 $rad_{n\gamma}$ neutron boost to the primary tumor volume. This study is now closed. A preliminary analysis of the uncorrected data indicates that the median survivals were 9.2 months for the neutron boost group and 8.1 months for the photon boost group. Autopsy data indicates that the majority of the neutron boost patients had apparent local control of their disease while the photon boost patients died of progressing disease. This information has been used to develop a new dose-searching study utilizing concomitant neutron and photon irradiation.

C. Advanced Prostate Cancer

In this study patients are randomized to receive either mixed beam or photon irradiation. The study is still ongoing and the code has not been broken but a preliminary analysis indicates a disease-free rate of 72% on one arm and 65% on the other arm.

D. Inoperable Non-Oat Cell Lung Cancer

In this study patients are randomized among three treatment arms: neutrons alone, the mixed beam regime, or photons alone. The group treated with neutrons alone continues to show a more rapid and greater degree of tumor regression than patients on the other treatment arms. Considering only the patients that have died, the median survival is about 2 months longer on the neutron-only treatment arm. Three of four autopsied patients on the neutron-only arm were free of disease in the radiation treatment volume and died of distant metastases. This underscores the need for finding an effective chemotherapeutic agent for this tumor system.

Other tumor systems that were studied include the soft-tissue sarcomas, esophageal cancer, bladder cancer, uterine cervical cancer, salivary gland tumors and malignant melanomas.

Problems with low neutron output and episodic breakdowns of the cyclotron have limited patient treatments over the last year. Several patients have been referred to other neutron treatment facilities in order to complete their planned protocol treatments.

References:

* Supported by NCI Grant No. CA-12441
+ Department of Radiation Oncology, University of Washington

8.5 Neutron Radiotherapy of Experimental Tumors

J. S. Rasey[+]

The Experimental Biology Division of the Department of Radiation Oncology continues to perform radiobiology experiments in support of the radiotherapy of human cancer with the 21.5 MeV d + Be neutron beam from the NPL cyclotron. Most experimental work concerning response of tumors to X-rays and neutrons has focused on the protection that hypoxic tumor cells provide against X- or gamma rays and the smaller radioprotective effect provided by such cells against neutrons. We are investigating additional aspects of cellular radiation response to determine if there are other biological bases for a favorable tumor response to neutron radiotherapy.

In the past year, we have compared the effect of gamma rays and neutrons in causing progression delay (temporary growth delay) in EMT-6 mouse tumor cells irradiated in tissue culture with doses of gamma rays and neutrons which kill the same proportion of cells. Greater progression delay for a given level of cell kill with a particular type of radiation would allow fewer new tumor cells to be born between fractions of radiotherapy. In internally controlled experiments, where gamma rays and neutrons can be compared directly, the two types of radiation appear to produce equivalent progression delay when doses are matched for equal cell kill.

Potentially lethal damage (PLD) caused by radiation may be repaired if cells or tumors are maintained under the appropriate conditions for the first few hours immediately following radiation. These conditions generally include maintaining the cells without encouraging them to divide. This type of repair has generally been reported to be greatly reduced or absent after neutrons or other high LET radiation but present following gamma irradiation. To the extent that this type of repair may be more common in tumors than in dose-limiting normal tissues, it offers a potential source of therapeutic gain with neutrons. In the past year, we have completed studies with the EMT-6 mouse sarcoma under a variety of growth conditions in mice and in tissue cultures. PLD repair following gamma irradiation occurs under all experimental conditions examined. Following neutron irradiation, PLD repair occurs under some but not all growth conditions and in some cases is as extensive as that occurring after gamma irradiation.[1]

Additional studies with the RIF-1 tumor, another mouse sarcoma growing in tissue culture, shows that a small amount of PLD repair occurs following neutron irradiation of this tumor line as well, although the amount is far less than that occurring after gamma irradiation of crowded plateau phase cultures. This is the more commonly observed result with neutrons, and this suggests that different tumor lines or types may have vastly differently capacities for PLD repair following high LET radiation.[2]

References:

+ Department of Radiation Oncology, University of Washington

1. J. S. Rasey, and N. J. Nelson, Rad. Res. 85, 69 (1981).
2. J. S. Rasey, N. J. Nelson, and R. E. Carpenter, Int. J. Rad. Onc. Biol. Phys. 4, 1023 (1978).

8.6 Neutron Induced Squamous Cell Carcinoma of the Skin in Rats

J. P. Geraci[+] and K. L. Jackson[+]

Radiation used in cancer therapy is a double edged sword in that radiation can kill tumor cells but is also itself a potent carcinogen. Therefore a unique possible late effect of radiation therapy is the induction of secondary cancers in the treatment site. This may be especially true with experimental neutron therapy since neutrons are more carcinogenic than the photons used in conventional radiation therapy. In the last year we have tried to determine the relative potency of neutrons as compared to photons in producing skin tumors in rats. For this purpose a surgically prepared flap of skin on the back of rats was exposed to graded doses of 137-Cesium gamma rays (0-4,500 rad) or to 1,250 rad of neutrons. No tumor development occurred at the irradiated site of gamma irradiated animals. Fifty percent of animals irradiated with neutrons developed frank squamous cell carcinoma in the irradiated site 6 to 14 months post exposure. The relative biological effectiveness of neutrons with respect to photons and the estimated probability values are shown in Table 8.6-1. These data indicate there is a reasonable probability that the neutron RBE for skin tumor induction is higher than the RBE used in clinical therapy to calculate treatment doses. Further studies using large numbers of animals and higher radiation doses to accurately determine the neutron RBE for tumor induction in the skin are currently underway.

Table 8.6-1
Neutron RBE for Skin Tumors

RBE	Probability
<3.6	<.30
<3.0	<.10
<2.4	<.05
<1.8	<.02

Reference:

\+ Division of Radiological Sciences, Department of Environmental Health, School of Public Health and Community Medicine, University of Washington

8.7 ^{81m}Kr Production for Respiratory Physiology

M. M. Graham[+], H. I. Modell[*], and R. Murano[+]

^{81m}Kr is produced by α-bombardment of NaBr at the University of Washington cyclotron for studies in respiratory physiology. Sixty to 80 millicuries of ^{81}Rb are produced, from which the 13 sec. ^{81m}Kr is extracted as needed.[1] The high activity produced is an advantage over commercially available materials.

References:

\+ Division of Nuclear Medicine, University of Washington
* Department of Physiology and Biophysics, University of Washington
1. Nuclear Physics Laboratory Annual Report, University of Washington (1980), p. 145.

8.8 Total Body Calcium by Neutron Activation

D. J. Baylink[+], C. H. Chesnut[+], T. K. Lewellen[+], R. Murano[+], and W. B. Nelp[+]

The Division of Nuclear Medicine is continuing its studies of bone wasting disease. The in vivo total body neutron activation technique has been described in previous Annual Reports.[1] A pilot study of the drug dichlormethane diphosponate (Proctor & Gamble) conducted in cooperation with R. R. Recker of Creighton University was completed. Based on the positive results of this study, a more extensive investigation involving 60 patients was begun.

References:

\+ Division of Nuclear Medicine, University of Washington

1. Nuclear Physics Laboratory Annual Report, University of Washington, 1968-1980.

8.9 (α,n) Yield Measurements of Importance to Reactors*

T. E. Chupp, P. J. Grant+, D. L. Johnson++, K. T. Lesko, E. B. Norman, and G. L. Woodruff+

As described in last year's Annual Report,[1] we have begun a series of (α,n) yield measurements of importance to reactors. These measurements are performed with an apparatus consisting of ten ^{3}He proportional counters embedded in a 1.5 m-diameter graphite hemisphere. During the past year we have measured thick-target (α,n) yields from Be, C, O, and F. Preliminary results for the (α,n) yield from C is shown in Fig. 8.9-1.

We have also done a number of tests to determine the energy dependence of the neutron detection efficiency. To date, we have shown that for $E_n \leq 3$ MeV the efficiency is independent of neutron energy. A test of the efficiency at higher neutron energies was recently carried out using the ^{3}H(p,n)^{3}He reaction. Analysis of this data is currently in progress.

References:

* Work supported by Department of Energy, Contract EY-76-S-2225 TA45

\+ Department of Nuclear Engineering, University of Washington

++ Westinghouse, Hanford

1. Nuclear Physics Laboratory Annual Report, University of Washington (1980), p. 142.

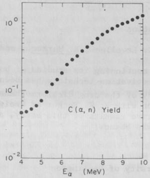

Fig. 8.9-1: Thick target (α,n) yield from carbon.

9.1 Accelerator Radiochronology and Ultrasensitive Mass Spectrometry

G. W. Farwell, P. M. Grootes[+], D. D. Leach, F. H. Schmidt, and R. Stoner

Application of the tandem Van de Graaff as an ultra-sensitive mass spectrometer to measurement of minute isotopic abundance ratios, particularly for the isotopes ^{14}C and ^{10}Be which are of interest in radiochronology, was begun in 1977. (See Nuclear Physics Laboratory Annual Reports for 1979 and 1980.) Our progress and activities up to August 1979 are described in two papers.[1,2] Our program has been conducted in collaboration with the Quaternary Isotope Laboratory of the Quaternary Research Center at the University of Washington.

The major efforts during the past year have been in the following areas:

A. Accurate normalization of ion beams.
B. Removal of contaminant ions.
C. Beryllium studies.

A. Accurate normalization of ion beams

A crucial element in the accurate measurement of isotopic abundance ratios is the normalization of one ion beam against another. During the past year we have worked with three systems of normalization. The first method is based upon the sequential transmissions of radioactive (rare) and stable (abundant) isotopic ion beams. This method provides a means of measuring directly the absolute isotopic abundance ratio for a given sample as well as for measuring the ratio indirectly by comparison with a sample of known isotopic composition. In the discussion that follows we shall refer to this as the "sequential transmission" method.

In the second or "concurrent monitoring" method, the stable isotope beam from a radioactive source - for example, ^{12}C for ^{14}C or ^{9}Be for ^{10}Be measurements - is monitored at the low-energy end of the electrostatic accelerator while the radioactive ion beam is measured simultaneously by particle detectors following acceleration to high energy and appropriate ion analysis (selection) in the beam handling system. We have built and are testing such a system; it includes a sample changer in the ion source which permits rapid alternation of standard and unknown samples to minimize the effects of fluctuations in ion transmission through the accelerator.

In the third or "hybrid" method, the ion source sample alternator is used in measuring successively (a) the relative strengths (after acceleration and ion analysis) of the stable isotope ion beams from the two sources being compared, and (b) the relative strengths of the radioactive isotope beams from the same two samples. Both comparisons are made in the scattering chamber at the terminus of the high-energy beam-handling system, the former through comparison of Faraday cup currents and the latter through comparison of detector counting rates.

Some of our experience to date with each of these methods is discussed below.

Sequential transmission method

The accuracy of the sequential transmission method depends critically upon constant ion source output during each measurement of both beams from one sample, and upon constant and equivalent ion transmission through the accelerator and beam handling system during the measurements of both samples. A rapid-sequencing system for switching all isotope-dependent machine parameters (six, in our case) would minimize the effects of fluctuations in ion source output and ion transmission, but we do not yet have the resources to develop such a system. Nevertheless, reasonable precision has been achieved in the measurement of $^{10}Be/^{9}Be$ and $^{11}B/^{10}B$ ratios. Thus, in the $^{10}Be/^{9}Be$ results reported in Ref. 1, the internal precision of measurements on various samples ranged from ±2% to ±5% (standard deviation) while isotopic ratio measurements made several weeks apart differed by 2%, 5%, and 15%, respectively, for three different samples. In tests with boron, in which both stable isotope beams (^{10}B and ^{11}B) were measured after acceleration and analysis, $^{10}B/^{11}B$ results with an internal precision of better than 1% were achieved several times but measurements made on different occasions sometimes differed by 5% to 10%. The absolute $^{10}B/^{11}B$ ratios determined by this method were always within 10% of the accepted range of values.

Because the hybrid method (see below) offers the same capabilities as the sequential method but is less sensitive to ion source and accelerator fluctuations, we shall probably abandon the latter in favor of the former for work on beryllium and on elements heavier than carbon. In the case of carbon another option is also being pursued, the concurrent monitoring method.

Concurrent monitoring method

This newly developed system permits monitoring of the ^{12}C (or ^{13}C) ion source output from a carbon sample while, concurrently, the ^{14}C ions are injected, accelerated, analyzed, and counted. The required ^{12}C - ^{14}C mass separation at low energy is achieved by utilizing the existing low-energy injection magnet as a low-resolution mass spectrometer. The system permits systematic alternation of unknown and standard samples, thereby minimizing the effects of fluctuations in ion transmission through the accelerator. The first test of the method (using the $^{13}C/^{12}C$ isotopic ratio) was very promising, but it demonstrated the necessity for very accurate repetitive positioning of the unknown and standard samples. Our existing sample changer was inadequate to achieve the requisite precision and a completely new mechanism was designed and constructed.

The new changer is coupled to an industrial-type programmable controller which alternates the samples in a manner to avoid backlash errors, gates and routes the detectors, steers the beam into or away from the accelerator at the appropriate times, and signals any mechanical malfunction during the operational cycle. Though in principle the system is quite simple, its implementation required extensive studies of the beam optics of both the sputter ion source and the beam transport system to the accelerator, followed by design and construction of the necessary sample changer, beam deflectors, and beam-line monitor. The changer is now in place and the entire system is undergoing tests by measuring $^{14}C/^{12}C$ ratios for both known and unknown pairs of samples.[3]

Fig. 9.1-1 shows a simplified diagram of the ion optics of the system. The abundant isotope beam (^{12}C, in our work so far) is integrated in the Faraday cup (FC), and the rare isotope (^{14}C) is accelerated. Note that the focal point for the ^{14}C beam lies at a different distance downstream from the focal point of the normalizing $^{12}C^-$ beam. In order that the ^{12}C beam to the low-energy Faraday cup be a proper monitor of the $^{14}C^-$ beam, the shape of the transmission curves [beam vs. inflection magnet (IM) field] at the Faraday cup and at the (virtual) "entrance pupil" (EP) of the Van de Graaff should be identical for all samples.[2] The entrance pupil is the effective aperture through which ions must pass in order also to pass through the stripper aperture (ST) at the high-voltage terminal.

The necessity to maintain constancy for these two transmission curves for all samples placed in the ion source imposes very strict conditions on providing accurately reproducible geometry for all samples. It means that when two samples are alternately placed in the ion source, the positions of both relative to the accelerating electrodes in the ion source must be the same to within a few mils. Moreover, the emitting surfaces of the samples must also be very closely matched. (See Sec. 9.4 of this report for a discussion of the effects of curved surfaces.)

In addition to precise geometry, the system requires a high degree of stability for each electrical component. During the past year improvements have been made in almost every component: a new focus power supply, changes in steering elements to improve reliability, better monitoring for the einzel lens

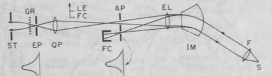

Fig. 9.1-1: S - Source; F - Focus Lens; IM - Inflection Magnet, EL - Einzel Lens; AP - Aperture Plate; FC - Faraday Cup; LEFC - Normal Low Energy Faraday Cup Monitor; QP - Quadrupole Triplet; EP - Entrance Pupil (Virtual); GR - Gridded Lens; ST - Stripper Aperture. All electrical elements are electrostatic except IM. In addition to the elements shown are five electrostatic steerers.

(a new power supply is on order), a quadrupole triplet (QT) in place of a doublet (see Sec. 9.5 of this report).

The most important improvement for the radiochronology program was the installation of a grid lens (GR) in the first accelerating tube of the Van de Graaff (see Sec. 9.5 of this report). With the grid the carbon beam stability (usually monitored by accelerating ^{13}C) is 2 to 3 times better, and the percent transmission is doubled. The position of the aperture plate (AP) was determined with the grid in place, and we are thus committed now to continued use of the grid.

Since in the continuous monitoring method of normalization we do not directly compare the rare isotope beam with the abundant isotope beam, it is necessary to compare an unknown sample with a standard sample whose isotopic ratio is known from beta counting, or from other data. To reduce errors introduced by fluctuations (both short and long term) in accelerator transmission, the unknown and standard samples must be exchanged many times during the course of a comparison measurement.

To achieve this, we have designed and built a new sample changing mechanism. The salient features are shown schematically in Fig. 9.1-2. The key parts are a detent arm and a detent wheel. Two detents at 180° are cut in the wheel; the wheel is coupled by means of an insulated drive shaft to the gear drive on the source sample holder wheel. Two changes were made in the original Extrion design: (1) a sample holder wheel with 20 sample positions was installed in place of the original 18. This change was necessary so that the drive shaft rotates 180° between adjacent pairs of samples; (2) finer teeth (32 pitch) gears (pinion and ring) were installed to reduce backlash. (This turned out to be insufficient. See below).

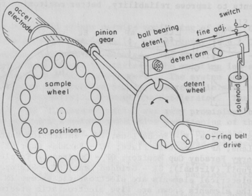

Fig. 9.1-2: Simplified schematic diagram of sample changer mechanism.

An O-ring (flexible) drive is necessary to provide (1) resilience when the detent abruptly falls into the detent wheel notch; (2) clutch action should the internal or external mechanism jam or malfunction (e.g., detent arm fails to rise, sample wheel sticks). The ball bearing detent is necessary to provide smooth insertion into the wheel slot while the belt drive is coming to rest. Mechanical clearances are minimal in order to achieve sample positioning accurate to within a few mils.

The sample changer can be operated (forward or backward) by manually initiating the motion drive mechanism, or automatically by an accurately timed cycle controlled by an industrial-type programmable controller (5TI 2301).

One cycle of operation consists of the following steps:

Time-Sec	Operation
0	Mass-14 beam from sample #1 deflected into tandem
5	Computer on routing to #1 set of counters and timers. On for 30 sec. of time counted only if terminal potential=7,000±2.5 keV
35	Computer and counters gated off
35.1	All beams deflected out. Changer starts shift to sample #2
44.1	Sample change completed - sample #2 in position. Forward motion - no anti-backlash. Mass-14 beam deflected into tandem
49.1	Computer on, routing to #2 set of counters and timers
79.1	Computer and counters gated off
79.2	All beams deflected out. Changer starts shift back to sample #1
88.2	Sample change completed - sample #1 in position from forward motion (anti-backlash operation)
88.2-0	Next cycle starts

Note that 5 seconds is allowed for the ion output of the source sample to stabilize. During this time, if desired, the mass 14 beam ($C^{13}H$ and $C^{12}H_2$) can be quickly monitored at the high energy exit of the tandem. The magnitude of this beam is a measure of the "cleanliness" of a particular source sample.

From the above operational sequence, it turns out that the fraction of time for sample counting is 60/88.2 = 73%. The counting time or the stabilization time can be altered quickly if found desirable. As yet, we have not made any studies to determine the optimum time intervals.

Hybrid method

This method has the advantages of the sequential transmission method (comparison of transmitted stable with transmitted radioactive ion beams; capacity for absolute isotopic ratio determinations). However, it has the potential for much greater precision in comparisons between two samples - an unknown and a standard, for example - through use of the ion source sample alternator developed for the concurrent monitoring method. In one sequence of measurements of, say, $^{10}Be/^{9}Be$ for Sample A against $^{10}Be/^{9}Be$ for Sample B, the following measurements are made (all are on accelerated and analyzed ions detected at the scattering chamber):

1.	^{9}Be (Sample A) to Faraday cup ^{9}Be (Sample B) to Faraday cup	Many alternations - 10, say, over a period of about 15 minutes
2.	^{10}Be (Sample A) to detector ^{10}Be (Sample B) to detector	Many alternations - 20, say, over 30 minutes
3.	Repeat 1	
4.	Repeat 2	

Continue until the desired numbers of ^{10}Be counts are obtained.

This method lends itself well to a comparison of the $^{14}C/^{13}C$ ratios for two samples. In a recent series of tests of the method, the following results were obtained for a pair of graphitized samples from 1939 wood:

$$\frac{^{14}C/^{13}C(\text{Sample A})}{^{14}C/^{13}C(\text{Sample B})} = 1.01 \pm 0.03 \qquad \text{Expected value: } 1.00$$

Absolute ratios can be obtained as well. Data for the same 1939 samples, taken in seven different determinations during two accelerator runs several weeks apart, yielded an average value for $^{14}C/^{13}C$ which translates to

$$^{14}C/^{12}C = (1.15 \pm 0.01) \times 10^{-12}.$$

The expected value, from the currently accepted β-counting data, is 1.15×10^{-12}.

The probable errors (standard deviation) given above were determined from the counting statistics (^{14}C count rates) and the internal consistency of the ^{13}C beam currents as measured over many successive intervals.

Thus, the hybrid method appears very promising; we are using it in our current beryllium work (see below) and, as one alternative, in our carbon work as well.

B. Removal of contaminant ions

Another of the major experimental problems in accelerator radiochronology or ultrasensitive mass spectrometry is the removal of unwanted ions that masquerade as ions of the desired radioisotope and find their way to the detector. They are created in the tandem accelerator beam tubes[1] and have the same magnetic rigidity as the radioisotope ions, so that magnetic analysis of the beam does not remove them. Accordingly, we have added ion velocity selection, and have constructed a temporary Wien filter which is installed just upstream from the detectors. It reduces unwanted ions by at least a factor of 100.

Although our earlier work with carbon has shown that by proper sample preparation (graphitizing at very high temperatures[2]), we could produce beams adequately free of contaminant ions, we found once such "clean" samples were placed in the ion source they had to be used in measurements almost immediately, and could never be removed and reinserted for additional measurement; otherwise they became contaminated, i.e., they acquired hydrogen and the capacity to produce CH^- and CH_2^- ions in great abundance. This property severely limits the usefulness of samples (which are time-consuming to make) and imposes a requirement for prompt, reliable accelerator operation which is not yet possible to achieve. The temporary Wien filter has eliminated this problem.

In the case of ^{10}B beams the Wien filter easily removes beryllium (^9Be), carbon, and oxygen contaminants that would otherwise enter the detector. However, it cannot remove the ubiquitous and abundant ^{10}B ions that emerge from every material we have studied. We have explored several methods for eliminating ^{10}B: (a) absorption by a foil placed just ahead of the detector, leaving a short residual ^{10}Be range with which to work; (b) differential energy degradation of ^{10}B and ^{10}Be ions by a carbon foil (1,000 $\mu g/cm^2$) placed at the image slits just upstream from the switching magnet, whose dispersion at 30° for ^{10}Be then eliminates the ^{10}B; and (c) differential degradation of ^{10}B and ^{10}Be ions by a 400 $\mu g/cm^2$ carbon foil placed at the object slits upstream from the 90° analyzing magnet, whose dispersion then eliminates ^{10}B. The last option seems to be the best choice if we consider both the need for maximum ^{10}Be beam intensity [we lose no more than about half in this method, as compared with about four-fifths for option (b)] and the need for absolute particle identification in our $\Delta E,E$ detector system [the short residual range in option (a) makes this more difficult].

C. Beryllium studies

We have continued our studies of the production and detection of ions of the radioisotope ^{10}Be (half-life 1.5×10^6 years). Our best operation was originally achieved[1] by using Be metal sources while maintaining a flow of very low-pressure O_2 gas through the ion source chamber. Recently, acting upon a suggestion by colleagues at Simon Fraser University (Canada), we found that a mixture of BeO powder and finely-ground silver, compressed into a pellet and used with O_2 gas, produces beams almost as large (up to 25 nA Be^{+3}, analyzed) as those from Be metal sources. BeO/Ag is much easier to prepare than the metal, so this approach is very advantageous. Though we have not yet established the ultimate durability of sources made by this method, some have run very steadily for several hours.

In recent weeks we have been working toward the measurement of ^{10}Be in samples of snow and ice from two locations in Antarctica. The ^{10}Be (with ^9Be carrier) is extracted from the melt water by standard techniques, precipitated as BeOH, and ignited to BeO; an ion source sample is then prepared as described above. In our most recent accelerator run we detected ^{10}Be from one such sample which contained less than 5 mg of Be (largely ^9Be carrier). While we have not had time to make quantitative measurements, this approach looks very promising and we are pursuing it.

References:

+ Quaternary Isotope Laboratory, Quaternary Research Center and Department of Geological Sciences, University of Washington
1. G. W. Farwell, T. P. Schaad, F. H. Schmidt, M. Y. B. Tsang, P. M. Grootes, and M. Stuiver, Radiocarbon 22, 487 (1980).
2. P. M. Grootes, M. Stuiver, G. W. Farwell, T. P. Schaad, and F. H. Schmidt, Radiocarbon 22, 838 (1980).
3. F. H. Schmidt, G. W. Farwell, and P. M. Grootes, Bull. Am. Phys. Soc. 26, 593 (1981).

9.2 Van de Graaff Accelerator Operations and Development

J. F. Amsbaugh, H. Fauska, W. B. Ingalls, C. E. Linder, G. E. Saling, F. H. Schmidt, D. Storm, R. E. Stowell, T. A. Trainor, and W. G. Weitkamp

A number of major development and maintenance projects have been carried out on the tandem accelerator and its ion sources during this year. Some of these are described in Secs. 9.1, 9.3-9.9 and 9.11-9.14 of this report.

During the early part of 1981, we began observing unstable terminal voltages at voltages above 8 MV, accompanied by intense bursts of X-rays. This instability was similar to that observed in 1978, which led us at that time to replace the beam tubes.[1] Because beam tube section number 2 appeared to be the source of the X-rays, we replaced it with a reconditioned tube section in November 1980. The machine runs satisfactorily at 9 MV again.

In addition, the following accelerator projects have been completed:

A. A large mercury diffusion pump at the high energy end of the accelerator has been replaced with a cryopump. Not only was advancing age making the mercury pump difficult to maintain, but it presented a significant health hazard. The cryopump has proven to be reliable and easy to use, and it will pay for itself in liquid nitrogen savings in the course of the next two years.

B. An oil cooling system for the image slits has been built to eliminate electrical noise injected into the terminal voltage control system by air blowing across the slits.

C. A TI programmable controller with a larger capacity has been installed on the accelerator control system. It can now accommodate additional equipment such as the automatic target changer on the sputter source. The old controller is useful for testing new programs before entering them in the on-line system.

During the year from April 16, 1980 to April 15, 1981, the tandem operated 4623 hours and the injector operated 505 hours. Other statistics of the accelerator operation are given in Table 9.2-1.

Table 9.2-1
Tandem Accelerator Operations
April 16, 1980 to April 15, 1981

Activity	Days Scheduled	Percent
A. Nuclear Physics Research		
1) Light Ions	123	34
2) Polarized Ions	26	7
3) Heavy Ions	38	10
4) Radiochronology	43	12
Total	230	63
B. Outside Users		
1) Battelle Northwest Laboratories	9	2
2) University of Washington Nuclear Engineering	7	2
Total	16	4
C. Other		
1) Accelerator Development	28	8
2) Accelerator Maintenance	23	6
3) Unscheduled Time	68	19
Total	119	33
GRAND TOTAL	365	100

Reference:

1. Nuclear Physics Laboratory Annual Report, University of Washington (1979), p. 133.

9.3 Computer Control System for the High Energy Beam Transport System

S. Lamoreaux and T. A. Trainor

The IEEE 448 databus system associated with our recently installed PDP 11/60 on-line data acquisition computer makes it relatively simple to interface a substantial number of manual control and readout systems for computer controlled operation. The first few systems adapted for IEEE bus operation have been directly associated with data acquisition, such as a general experiment control panel and control and readout of scalers.

More recently we have turned our attention to computer control of more general accelerator subsystems such as the high-energy magnetic beam transport system. This last is desirable in general to facilitate accelerator setup, but is especially important during generation of excitation curves, for example, when many rapid beam energy changes are required, or when good energy reproducibility is essential, in which case magnets can be cycled through a known hysteresis pattern under computer control.

Several design restrictions were placed on the new control system. It should be possible to operate each magnet control panel in a stand-alone mode in case of system failure. Remote control of the overall system should be by computer or manual digiswitch, again in case of (computer) system failure. Controlled elements should be independently or universally addressable to handle a variety of possible system configurations. And, an interrogation facility should be incorporated to check on the remote/local status of each controlled device. In the interest of design simplicity it was decided not to require full closed-loop information on the actual power-supply outputs. A power-supply failure is usually rare, and dramatic enough to produce immediately observable effects.

Three address lines are used to accommodate a total of seven independent devices (0 is a general address for all devices in the system). The data consist of the first four digits of the analyzing magnet NMR frequency corresponding to selected beam energy. These digits are BCD encoded onto 16 data lines and ultimately transmitted to 16-bit, BCD, digital-to-analog converters (DAC), one for each power supply reference. This four-digit resolution corresponds well to the typical $1/10^4$ stability of the magnet supplies.

Data and addresses are transmitted from the PDP 11/60 CPU to one of several series M6800 microprocessors (μP) now installed on the IEEE bus (see Fig. 9.3-1). This μP contains microcode required to retransmit the data and addresses with the proper timing and sequencing to the Magnet System Remote Controller (MSRC) on a cyclical basis and to do rudimentary error checks.

The MSRC contains a data/address buffer with front panel LED display of contents, and a three-state device for databus operation. The buffer can be loaded either from a front-panel digiswitch (manual control) or by action of the μP, depending on switch selection. The buffer is transmitted to the MSRC bus when the three-state device is gated open, either manually or by action of the μP. In addition, a two-wire interrogation system checks all magnet control panels for remote/local status. Any panel identified as included in the remote system, but found to be in local control mode, causes an error status at the μP.

The MSRC bus is a 24-line bus, of which 16 lines carry the 4 digit BCD datum, 3 lines (expandable to 4) carry the controlled device binary address, one line is a strobe, two lines are used for checking the remote/local status of each controlled device, one line is spare, and the last line is ground.

Each magnet control panel has a receiver unit consisting of optical isolation for all digital input lines, a 16 bit BCD DAC, various linear stages for buffering, gain and offset adjustments, and a zener reference for local operation. Careful attention has been paid to common-mode noise rejection, proper forced-air cooling of the DACs, elimination of ground loops, general use of low-

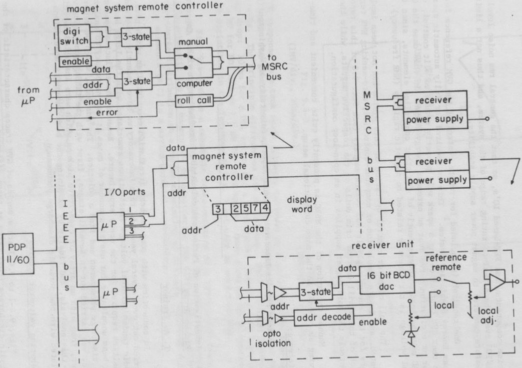

Fig. 9.3-1: Magnet system remote controller block diagram.

noise components, and FET-based IC's, so that the general rms noise level is $<1/10^5$ over the normal operating range of the system, and thus not a limiting feature compared to magnet power supply stability.

One receiver is included for remote control of the GVM reference for the Beam Energy Stabilizer System.[1] This is required for fully automatic operation so that GVM control during a spark will properly return to slit control, even for an excitation curve over an extended energy range. In this case the GVM DAC must be loaded independently of the other controlled elements, since terminal voltage is not linearly related to magnetic rigidity (NMR frequency).

The full computer control operation of this system has not been implemented, and awaits completion of computer-controlled, auto-seeking NMR regulators for the energy analysis and switch magnets (see Sec. 9.8 of this report). Each of these will control trim coils on the respective magnets, while the MSRC controls the main magnet supplies in an open-loop configuration.

Manual operation of the MSRC is presently quite convenient and time-saving as opposed to the more conventional setup.

Reference:

1. Nuclear Physics Laboratory Annual Report, University of Washington (1980), p. 180.

9.4 Investigation of Periodic Acceleration Tube Discharges with a Capacitive Pickup Array

T. A. Trainor

In connection with some in-beam irradiation creep studies which have been carried out over several years in this Laboratory we have recently observed periodic tandem terminal voltage fluctuations associated with the large beam intensities required for the creep experiments. Because these fluctuations made the beam unsuitable for use in a number of cases it was necessary to analyze the discharge phenomenon and find a solution. The analysis, which we report here, was carried out in several stages, first with the tandem generating voltmeter, then with an array of capacitive pickups which were installed especially for this analysis, and finally by examining the beam intensity modulations associated with the periodic discharge phenomenon.

Generating voltmeter studies

Figs. 9.4-1 to 9.4-3 are a series of GVM traces characteristic of the periodic discharges (PDs) taken at three different sweep rates to illustrate various trace constants. For these GVM traces the accelerator ran in GVM control at 7.5 MV with a 10μA proton beam. For comparison Fig. 9.4-4 shows the

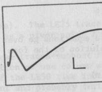

Fig. 9.4-1
(1MV/div., 1s/div.)

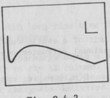

Fig. 9.4-2
(1MV/div., 0.2s/div.)

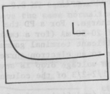

Fig. 9.4-3
(1MV/div., 10ms/div.)

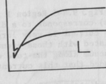

Fig. 9.4-4
(2MV/div., 0.1s/div.)

GVM response to a tank spark (closely followed by a second spark) from about 9.5 MV. The general features of Fig. 9.4-1 are common to both PDs and tank sparks. The principle differences are as follows. Fall time for initial voltage drop: 10 ms for a PD, <<1 ms for a tank spark. Magnitude of initial drop: 3-4 MV for PD, almost 7.5 MV for tank spark. Over a series of 30 monitored PDs the variations in the features of Fig. 9.4-1 were no more than 10%.

Fig. 9.4-5 shows a schematic representation of a typical GVM trace for the PD with four regions identified by Roman numerals. The qualitative features of this schematic can be understood by considering the differential equations for the charge distribution on a column consisting of discrete resistive and capacitive elements (R,C) in a series-parallel combination.

$$\dot{Q}_i = [Q_{i+1} - 2Q_i + Q_{i-1}] \frac{1}{RC}$$

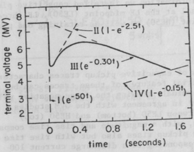

Fig. 9.4-5: Discharge time constants.

In the limit of a continuous R-C distribution these equations go over to the one-dimensional diffusion equation with general solution of the form

$$Q(z,t) = \sum_n q_n \cos(nz + \phi_n)e^{-kn^2t} + Q_o(z)$$

Generally, the most complicated features of the departure from equilibrium charge distribution Q_o decay very rapidly (n>1) compared to the characteristic decay rate of the column as a whole (∿ 5-10 seconds, n=1).

In Fig. 9.4-5 Region I is the initial discharge. For a PD the fall time (10-20 ms) corresponds to a discharge current of 20-50 mA (for a tank spark the discharge current is very large). Because significant terminal gamma radiation is associated with these events we ascribed them to an electron current traveling in vacuum along the tube center. Because the voltage drop is several MeV we concluded that this current must travel over 1/2-2/3 of the column length.

Immediately following the initial discharge (and firing of column spark gaps) the voltage (charge) distribution along the column is roughly trapezoidal. This decays in Region II in about 0.4 seconds to a cosine distribution with maximum at the terminal (n=1 term in the general solution to the diffusion equation). In Region III the cosine distribution continues to decay to an equilibrium distribution Q_o=0 until ∿ 1.5 sec after the initial event. At this point charge delivery to the terminal is restored, and decay toward the distribution Q_o=k $(z-z_o)$ proceeds in Region IV until corona discharge begins about 8 seconds after the initial event. At this point GVM control is restored. Note that the curve in Region IV is decaying toward an unregulated terminal voltage of ∿ 9.2 MV and proceeds from a virtual point at the initial event corresponding to the amount of charge lost from the column in the PD (i.e., ∿ 2-4 MV). For a tank spark the virtual starting point for the Region IV curve is near the origin (0 MV).

From the GVM traces then we learned the discharge current involved, the magnitude of the voltage drop, and hence the length of column involved. There was no information on which column (LE, HE) was involved and no confirmation of the discharge model. To provide this information we installed capacitive pickups (mushrooms) along the pressure vessel at the LE midpoint (LE50), LE three-quarter point (LE75), and the HE midpoint (HE50) as well as retaining one pickup at the terminal (TERM).

Capacitive pickup studies

Figs. 9.4-6 to 9.4-9 are a series of capacitive pickup traces characteristic of a PD. In Fig. 9.4-6 the essential features of these traces can be identified. The second trace is the terminal, showing the large negative voltage drop (here differentiated of course) in agreement with the GVM studies. The most illuminating comparison is that between LE50 (bottom) and HE50 (top) traces. The LE50 voltage rises sharply, with a magnitude and rise time comparable to that of the terminal. The HE50 pickup rises also but with rise time and magnitude much less than LE50 (corresponding to a discharge current 100 times less). The LE75 trace is actually bipolar with long rise time indicating its role as a pivot point for the LE column voltage swings.

These traces support the idea of an electron discharge along a significant portion of one column and point unequivocally to the LE column. The magnitude of the LE50 rise indicates that the discharge proceeds at least down to this point and probably further, so that terminal charge is delivered near this point, causing a momentary voltage equilibrium between the two points as a result of the PD. The LE75 trace confirms this point as being near the center of the discharge. Figs. 9.4-7 and 9.4-8 show the response of the pickup array to a 9.8 MV tank spark. The results indicate that the various pickup signals have the same normalization.

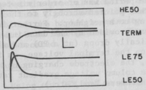

Fig. 9.4-6
Capacitive pickup traces for a PD

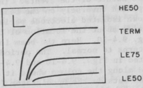

Fig. 9.4-7
Capacitive pickup traces for a 9.8 MV tank spark

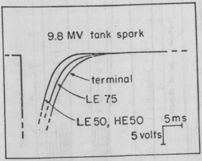

Fig. 9.4-8: Pickup responses to 9.8 MV tank spark adjusted to common zero

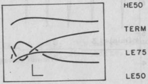

Fig. 9.4-9
Capacitive pickup traces for a PD

Fig. 9.4-9 shows the same traces on a shorter time scale for comparison of rise times. The very fast glitch just after the trigger in the LE50 and LE75 traces should be noted. Also to be noted in Fig. 9.4-6 is the fact that the LE50 and LE75 traces start below their baselines. These provide clues to the nature of the trigger for a PD. There is apparently an initial very fast discharge in tube section 1 and part of section 2 which causes a small voltage drop at LE50 and LE75 and no radiation. The pickups provide no information about the true initiator of a PD.

Beam fluctuation studies

Further clues to the nature of a PD trigger were obtained from the periodic nature of the events. In most cases the period was of order minutes and depended inversely on the beam intensity. This pointed strongly to the well known isolated electrode periodically sparking to a neighbor. Further information about the location of the electrode was provided by the data in Fig. 9.4-10. Here the beam intensity periodically drops (at a PD) and slowly returns to normal. The periodicity depends on the terminal voltage, as indicated in Figs. 9.4-10 and 9.4-11. Therefore, the electrode charging up must lie along the column where it experiences the column voltage gradient rather than outside the accelerator (e.g. a broken steerers lead, etc.)

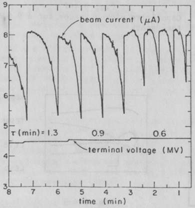

Fig. 9.4-10: Beam current fluctuations at various terminal voltages.

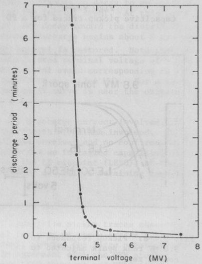

Fig. 9.4-11: Discharge period vs. terminal voltage.

Fig. 9.4-12 shows beam position shifts associated with a PD. The beam has been deflected first one way, then the other (+, -) by the LE X and Y steerers. Note that the pitch of the beam current modulation changes from + to -, and that the modulation occurs for either X or Y deflection. This means that the beam is periodically being swept rapidly along a diagonal, and then slowly returning to equilibrium after a fast discharge.

The column was inspected and no isolated electrodes found. Also, various model calculations indicate that the beam charge alone is insufficient to produce the periods observed. The best possibility available was that secondary electrons from a high-transmission grid at the entrance to tube 1 were producing the periodic fast breakdown and beam deflections. The fast event in turn triggered the general electron discharge along 2/3 of the LE column. Replacement of tube 2 eliminated the electron discharge but not the trigger event. Removal of the high-transmission grid eliminated the trigger breakdown and all periodic beam fluctuations. The "isolated electrode" required for the model was not located.

Conclusion

Using our GVM and an array of capacitive pickups we were able to characterize in some detail a multi-component column discharge, locate its source to within a small region of the column and, from the nature of the discharge periodicity, point directly at the component at fault. From our experience we

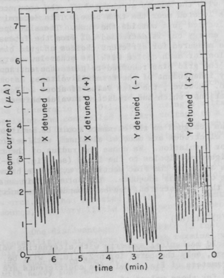

Fig. 9.4-12: Discharge-induced beam position shifts.

conclude that availability of the pickup array is very useful for diagnosing column discharge difficulties, and that the ultimate diagnostic system is achieved by replacing the pickups by a GVM array. The required quality (and hence the expense) of the additional GVMs would be considerably less than the existing precision GVM involved in control of the terminal voltage. The optimum GVM distribution would be seven, with three equally spaced along each of the LE and HE column lengths.

9.5 Improvements to the Low Energy Optics of the Tandem

G. L. Anderson, J. Amsbaugh, M. Q. Tang, and D. W. Storm

In last year's Annual Report,[1] we presented calculations which indicated that we could improve the transmission of ions from the sputter source by making some changes in the low energy optics. We proposed installing a grid at the entrance to the low energy acceleration tube, and presented plans to replace the small bore quadrupole doublet with a larger bore quadrupole triplet lens. Both these changes have been made, with positive results.

The grid is powered by a 0 to 10 kV supply, to which spark protection has been added. We found that with the supply at about 7 kV, the entrance pupil of the low energy tube is located near the tank base. This determination was made using the slits located just outside the tank. The slit opening at which the beam at the high energy cup is decreased 10% from the intensity with the slits wide open can be measured for different choices of grid bias, after optimizing the transmission for each choice with the other low energy parameters. It was found that the grid bias required to place the entrance pupil at those slits was nearly independent of the terminal voltage, as our previous calculations indicated. However, the bias value of about 7 kV was not consistent with the calculations, which had predicted a value between 2 and 3 kV.

The quadrupole triplet was designed so the elements could be built of tubing and flat material. The electrodes are made of aluminum, with teflon screws and mica washers used for insulation. We chose the radius of the tube to minimize contributions of higher multipoles to the field (see Fig. 9.5-1). We studied the influence of the angle of the flat sections, α, on the harmonics, and we found that a choice of 90° was adequate. The potential in an infinitely long section, such as that illustrated, can be expanded in a multipole expansion

$$V(r,\Theta) = V_0 \sum_n a_n (r/R)^n \sin(n\Theta)$$

If there is a true four-fold mechanical symmetry with alternating voltage from one quadrant to the next, only the terms for n=2,6,10... will be present. For the optimized parameters of Fig. 9.5-1, the coefficients are 1.0, 0.3×10^{-3}, and 3.6×10^{-3} for those values of n, respectively, Thus the

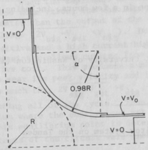

Fig. 9.5-1: One electrode of the quadrupole. We varied R'/R and α to minimize contributions from multipoles higher than quadrupole. The optimum occurred for α=90° and R/R' = 1.02.

aberrations associated with higher multiples will be very small.

The previous quadrupole doublet had been operated with an unregulated power supply. The drifts in the settings were noticable, so we decided to use regulated supplies for the triplet. Since we desired to include steering in the lens, we required six power supplies, and we wanted the outputs to be appropriately controlled by four controls: vertical steering, horizontal steering, lens strength, and balance. Since each of these controls will effect the output of two or more supplies, we decided to build six supplies, three positive and three negative, which could be controlled by several inputs. Basically, there is a summing junction into which up to four control inputs are fed, and the output is proportional to the sum of the control inputs. This way the steering settings are not dependent on the lens strength settings, except that the supplies are of unique polarity and the output will go to zero if the control input sums to the opposite polarity from normal. The power supplies are based on a 10 kHz switching scheme. The voltage which is switched at 10 kHz is controlled and applied to the primary of a step-up transformer. The turns ratio is 10:1, and by using a voltage doubler on the output while applying the controlled primary voltage to a center tap, a step-up of 40 is achieved. Thus a 6 kV output is achieved while controlling an input of about 150 volts. The transformers are built around a Ferroxcube EC 70-3C8 ferrite core.

The improvement in transmission for ions from the sputter ion source is about a factor of 1.4. That is the ratio of the present transmission to that previously obtained, before these changes, for ions from the sputter ion source. We had expected similar improvements for ions from the polarized ion source, but very little improvement has been noted in that case.

One disadvantage of the grid is that electron emission causes beam tube instabilities at moderate to high terminal voltage (over about 6 MV) and at high currents (5 to 10 microamperes for protons). Studies of this phenomena are reported in Sec. 9.4 of this report. In order to be able to use the grid with heavy ions but to remove it readily for intense light ion operation, a tool was built to insert the grid into the beam tube from outside the tank. With this tool, removal or insertion can be done in a few hours, including pumpdown time.

Reference:

1. Nuclear Physics Laboratory Annual Report, University of Washington (1980), p. 163.

9.6 New Electronics for the Beam Profile Monitor System on the Tandem

S. Lamoreaux

New electronics for the vibrating-wire type beam profile monitor system are being developed for the tandem. The existing vacuum tube electronics have several severe problems, including frequent failures, noisy signal preamps, and unreliable hold circuitry. Also, the hold circuit, when operated, generates noise which interferes with other equipment. The new system is being designed to overcome these difficulties.

The new monitor system will retain the present monitor heads. These heads include two isolated perpendicular wires and a ferromagnetic armature mounted on a flat spring. This is a mechanical oscillator which oscillates at about 15 Hz. The wires are arranged so as to traverse the ion beam when the oscillator is set in motion. The currents picked up by these wires are amplified and displayed to the operator. In addition, there are two coils located on opposite ends of the vibration arc. One coil is used to drive the oscillator and the other to pull the wires, when not being used, out of the beam path. There is a small induction pickup coil mounted on the spring support which detects the velocity of the ferromagnetic armature.

A. Driving Circuitry for the Mechanical Oscillator

The driving circuitry, from a published article,[1] was redesigned to improve noise immunity, improve stability, and to be compatible with our monitor heads. All of the driving circuitry is located near the monitor head, next to the beam line.

The circuit first amplifies the voltage signal from the velocity pickup. This amplified signal (approximately sinusoidal) is passed through an active bandpass filter with ω_o=15 Hz and Q=0.5. The output of the bandpass filter (V_{sig}) branches into three paths. One goes to a buffer amplifier and is sent to the control room display circuitry. Another is amplified by a factor of minus two and has a constant settable voltage (V_{set}) subtracted. It is then half-wave rectified and filtered with a parallel RC circuit with τ=0.5 sec. This signal $(\overline{2V_{sig}-V_{set}})$ then goes to the minus input of a comparator. The final branch of the bandpass output goes to the plus input of the comparator.

When the amplitude of the velocity signal (amplitude of vibration) goes below some value, the absolute value of the output of the rectifier for some part of a cycle near the peak greater than the output of the rectifier $(2V_{sig} - V_{set} < V_{sig})$. During this time, the output of the comparator is positive and a high current high voltage transistor is switched on. This transistor allows current from a 250 volt regulated supply to pass through the drive coil. This produces a magnetic field which pulls the armature while it is near its peak velocity and increases its kinetic energy. If the amplitude is such that $2V_{sig} - V_{set} > V_{sig}$, then the output of the comparator is negative during all of the cycle. Thus, the amplitude of vibration reaches an equilibrium where the energy lost per cycle is equal to the energy input per cycle. This equilibrium point is determined by V_{set}. The time constants in various stages of the circuit were chosen to prevent oscillation about the equilibrium point.

The x-y signals from the wires are amplified with current to voltage amplifiers constructed from CMOS input op-amps. These amplifiers have breakpoint at 10 kHz with sensitivity 1V/100 nA and dynamic range of 20 V p-p.

Preliminary tests show this circuit to be quite stable with respect to temperature and time. The oscillation of the wires is offset due to the asymmetric drive by about 3 mm. This can easily be corrected by initially offsetting the stationary equilibrium point by this amount from the beam axis.

B. Hold Circuitry

For the hold circuit to work effectively, a large current must pass through the hold coil for a short period. This pulls the wires against the support very strongly. This current then must be reduced to some value that will hold the wires securely against the support but not burn out the hold coil.

The circuit used achieves this by using a comparator which drives a relay. When the hold control line is made negative (switched with a relay controlled from the display unit), the comparator is turned on and a large current passes through the hold coil. Also, a transistor in parallel with the relay contacts is on while the control line is negative. The control signal is also sent to an integrator. The output of this integrator goes to the comparator. After about a second, the integrator output voltage exceeds the voltage of the control line and the relay is switched off. The transistor remains on and allows sufficient current to pass through the coil to hold the wires out of the beam path.

C. Display Circuitry and Switching

The display circuitry will be located in the tandem control console. Six different monitors can be switched into the display. These monitors can be independently activated regardless of whether they are being displayed. This allows rapid switching between the different monitors.

The signals from the monitor in use are optically isolated at the input to the display circuitry to eliminate ground loops. These signals include the velocity, x current, and y current. The method used gives a common mode rejection ratio of 70dB and a 3% linearity over a 10 volt p-p dynamic range.[2]

The velocity signal is passed through an AC coupled amplifier to remove any DC components. This signal is then continuously integrated. There is a large resistance in parallel with the integrating capacitor to prevent slight offsets in the op-amp from charging the capacitor to saturation. The output of the integrator is then passed through another AC coupled amplifier to eliminate any DC components due to the integrator.

The integrated velocity is proportional to the position of the wires relative to their equilibrium position. Any phase shifts in the velocity signal and integrated velocity create errors in the displayed position. Thus, phase shifts are minimized throughout the circuitry.

The integrated velocity, after passing through an automatic gain control (AGC) circuit, is displayed on the horizontal channel of an X-Y oscilloscope. The AGC is needed to keep the horizontal display constant when switching between different monitors. The AGC consists of a CdS photocell in the feedback loop of an op-amp. The output of the op-amp is rectified, filtered, and is compared to a settable voltage. The photocell is illuminated with an increasing intensity as the difference between these voltages increase. The gain is high enough so that the output remains constant over about a 25dB variation of input voltage amplitude.

The x and y signals are displayed on the vertical channels of the X-Y scope. These signals are displayed only over the half of the vibration cycle where there is no current in the drive coil. This is to prevent the electromagnetic interference generated by the drive from appearing on the display. The x and y signals are turned off when the velocity is less than zero by using a CMOS bilateral analog switch.

Development of the circuitry has almost been completed. Two display units and twelve monitor units will go into production in spring 1981. Construction and installation should be completed before August 1981.

<u>References:</u>

1. J. H. Broadhurst, Nucl. Inst. and Meth. <u>172</u>, 459 (1980).
2. Hewlett-Packard Application Note 951-2.

9.7 Recent Improvements Controlling the Tandem Terminal Potential by the Generating Voltmeter

H. Fauska

The technique of adding the two GVM (generating voltmeter) stator signals as described previously[1] performs well if the control is through the corona tube. The corona circuit frequency response starts to roll off at 10 Hz and the higher frequency noise is averaged out. The higher frequency noise is a cause of instability when the GVM signal is used to control the terminal for A.C. variations via an optical coupled link to the terminal (the terminal derippler). The high frequency cutoff of the terminal derippler is 1 kHz.

High frequency noise is developed by the GVM stator and rotor shapes. The original shapes were sections of a circle with the edges always along a diameter. Our method of clamping and adding the two stator signals to provide a D.C. type signal with good high frequency response allows the perturbations caused by the collective crossing of the rotor from shadowing to unshadowing the adjoining stator sections to be amplified and retained. Another source of high frequency noise is a result of mechanical inequality of rotor and stator area. The delta area shows in the output as a ripple with the amplitude proportional to the magnitude of the area unbalance, and the frequency is the fundamental determined by the motor speed and the number of rotor/stator sections.

The collective section crossing error can be reduced by making the rotor sections other than pie sections. Since we made our rotor a sinusoidal shape, the crossings will be continuous, and the resultant signal will be sinusoidal rather than triangular as the original signal.

By increasing the number of rotor sections one can make the frequency higher than the flat response portion of the terminal derippler. We designed a new rotor with 14 rotor sections and 28 stator sections. The motor speed is 3600 rpm or 60 rps, therefore the fundamental signal frequency is 60×14 or 840 Hz. While a higher frequency would be better we chose this because of mechanical reasons.

The demands of machining equality were solved by machining the rotor in the setup shown in Fig. 9.7-1. The rotor disk was supported on an arbor held in a divider head. The cutter item A was ground to have a shape determined by the greater and smaller disk diameters of the rotor and a sine squared function of the number of rotor blades. The cutter is like a fly cutter with one cutting edge, and since the both edges of the rotor section are cut by the same cutter the equality is only limited by the setability of the dividing head. The last cutting was very light to assure uniformity.

The stators were made of copperclad as used in etched circuit board. The stator sections were left as pie sections with the alternate sections connected together. The layout was done with a dividing head. A typical 8-section stator is shown in Fig. 9.7-2.

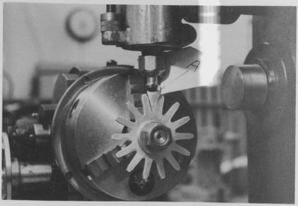

Fig. 9.7-1: Rotor machining setup

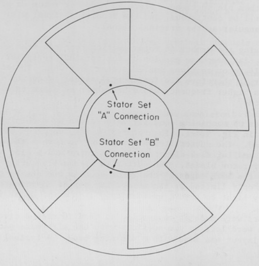

Fig. 9.7-2: A typical 8-section stator

Assembly was done with a dial indicator to insure no wobbling. Wobbling shows as a slow ripple signal in the added output.

The earlier reported preamplifier circuit was modified to provide a higher frequency signal to drive the terminal derippler. The signal is developed by adding the two stator signals without clamping. The resultant signal is proportional to the terminal variations.

The complete preamplifier circuit is shown in Fig. 9.7-3.

The variable capacitors at the input provide a method of electronic balance of the two stator signals, and the high frequency signal viewed on an oscilloscope is very useful to aid in adjusting the balance.

The new preamplifier circuit has a buffer amplifier between the high frequency pickoff and the clamp circuit. This was necessary to isolate the clamp conduction spikes from entering the high frequency circuit.

Reference:

1. Nuclear Physics Laboratory Annual Report, University of Washington (1978), p. 119.

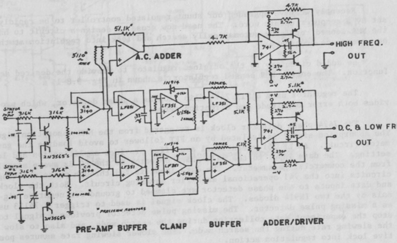

Fig. 9.7-3: Preamp circuit

9.8 Automatic Search and Lock Regulation of the 90° Magnet

H. Fauska

Using an accelerator to measure excitation functions requires that the beam energy be stepped periodically. Measuring ratios of isotopes for radiochronology requires stepping back and forth between different isotope beams. In each case, the accelerator analyzing magnet must be accurately and rapidly varied from one field level to another.

The shunt sensed regulator normally used to control the magnet field has the desired stability, but the iron in the magnet causes problematic errors due to hystersis. The hystersis problem can be solved by using an NMR sensed regulator.

Earlier we had designed an NMR sensed regulator.[1] The regulator takes the NMR resonance signals from the commercially supplied gaussmeter. The regulator controls on a separate coil on the magnet, and therefore the usual crosstalk problems are avoided. We use the originally provided degaussing coil and a separate voltage-varied bipolar power supply. The result is an add-on regulator circuit which is electrically isolated from the shunt regulator, and can be installed on existing magnet regulator systems. The earlier regulator was manually adjusted after each magnet setting.

Recently we have upgraded our shunt regulated controller to be rapidly set by a computer update word. The need now arose to design a circuit to have the NMR sensed regulator automatically search and lock into regulation at the new resonance frequency.

We added circuitry to the original regulator to provide the desired search function. The entire NMR sensed regulator is shown in Fig. 9.8-1.

The regulator uses a TTL 7474 flip flop as a phase detector, which provides both error magnitude and direction sense.

The 7474 phase detector clock is triggered from the NMR absorption signal. The absorption signal is isolated by an FET follower to avoid loading the gaussmeter circuit. An LF 351 operational amplifier provides amplification and level setting. The data input to the 7474 phase detector is the 60 Hz sweep signal from the commercial gaussmeter. The data input is fed through phase shifting circuits into the 741 operational amplifier squaring circuit. Both the clock and data inputs to the phase detector are clamped to ground for negative signals by the two 1N914 diodes. The clock signal is used to trigger a 74123 used as a missing pulse detector. The missing pulse detector provides a signal to stop the experiment data collection during the search mode, and also to slow the slewing rate during the search mode. The slower slewing rate assures positive lock into regulation action.

The phase detector outputs are fed into the inverting and non-inverting inputs of the 741 operational amplifier squaring circuit. The squared output is amplitude limited by the two matched zener diodes. The limited output will have equal time excursions positive and negative if regulation balance exists, and

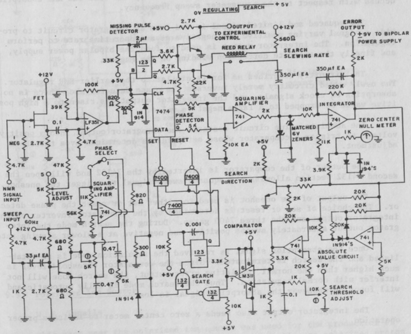

Fig. 9.8-1: NMR sensing magnet regulator

the time positive or negative will be determined by the time the NMR absorption occurs with respect to the gaussmeter sweep frequency.

The squared and limited signal is fed into an integrator circuit to provide a signal varying positive and negative at a proper time rate to perform regulation. The integrator output is used to feed the bipolar power supply, and finally the separate correction winding on the magnet.

The circuitry described so far is similar to the earlier NMR regulator. The newly added circuitry merely reverses the phase detector when there is no absorption or clock signals, and the integrator output has risen to a high positive value or dropped to a large negative value.

The absolute value circuit converts the integrator output into a positive voltage to trigger a comparator whose set point is determined by a threshold adjustment.

The output of the comparator is inverted by the 74132 and will open the second 74132 section allowing the squared sweep signal to trigger the oneshot.

The output of the oneshot is used to either set or reset the phase detector. The choice of set or reset is determined by the transistor inverter on the integrator output and the three 7400 gates. During the search mode the integrator output alternately sweeps positive and negative at a slower slewing rate.

Once the absorption signal is received the regulation mode is re-established and the search is terminated. Since the comparator threshold level is much higher than the normal regulating error output, the search mode will not interfer with normal regulation. Thus the search mode is fully automatic and will function whenever the absorption signal is lost.

The integrator output also feeds a zero center meter to indicate proper operation.

Fig. 9.8-2 is a diagram of the bipolar power supply, which is basically a power operational amplifier.

The regulator holds the magnet field to ± 17 milligauss for proton resonance frequencies of 3 MHz to 40 MHz. The regulating range is limited because the gaussmeter signals have a poor signal-to-noise ratio at the two ends of the regulation range.

The search range is ± .5 MHz.

The search time to lock is 8 to 10 seconds depending on where the search level output is when the absorption signal is received.

Reference:

1. Nuclear Physics Laboratory Annual Report, University of Washington (1970), p. 23.

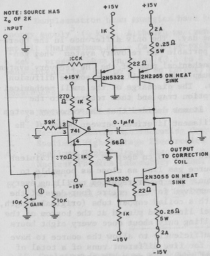

Fig. 9.8-2: Bipolar magnet power supply.

9.9 Polarized Ion Source

W. B. Ingalls

This past year the polarized ion source was used for the production of beams of helium nuclei as frequently as for the production of polarized proton beams. Modifications to the duoplasmatron-charge-exchange region (hereafter referred to as the "cesium box") were implemented to improve the ease of operation of the ion source by experimenters utilizing helium ions, without sacrificing the ability of the ion source to produce polarized proton beams.

There have been two main difficulties associated with the production of helium beams; short filament lifetimes, and high-voltage breakdown both within the duoplasmatron itself and between the extraction and focusing electrodes and the insulators within the cesium box.

Filament Lifetime

It was noticed that there was a marked difference in filament life when the ion source was used to produce ^{3}He beams as opposed to ^{4}He beams. Filament lifetimes during ^{3}He runs are typically three to four days; lifetimes for ^{4}He runs were generally little more than one day. The only difference in the operation of the ion source is the use of a portable ^3He recovery system[1] when generating beams of this ion. The small mechanical pump of the ^3He recovery system is used to replace the ion source forepump and thus all three source diffusion pumps are backed by the recovery system. The discharge of the small mechanical pump is passed through a LN_2 cooled sorption trap and then returned to the source gas input of the duoplasmatron. It was decided that the recovery system trap was the key to the difference in filament lifetimes between beams of ^3He and ^4He.

A stainless steel "U" tube immersed in a 23 cm deep LN_2 filled stainless steel dewar was installed on the ion source gas line as close as possible to the duoplasmatron gas inlet for a ^4He run. The dewar required refilling every three to four hours, but the filament survived for the entire four days of the run. The "U" tube has been replaced with a coiled copper tube (original length, 70 cm) silver soldered to stainless steel lines and placed at the bottom of the LN_2 dewar. The dewar now requires refilling only about once every eight hours and filament lifetimes have increased sufficiently to allow the source to have been successfully started and restarted for five different runs of a total of ten days of running time with no filament recoating or replacement.

High Voltage Breakdown

Cesium which escapes the charge-exchange canal and eventually coats everything within the cesium box has been the source of voltage breakdown problems in the duoplasmatron vicinity. A simple 3.2 mm thick, freon cooled copper plate with a 1.3 cm diameter hole to pass the beam was placed between the cesium canal entrance and the decel electrode. The abatement of voltage breakdown was dramatic. The copper plate was moved to the exit end of the cesium canal and a 2 cm deep, 4 cm ID freon cooled cup which captures any cesium leaving the canal except that which travels along the beam axis was placed between the canal entrance and the decel electrode. Degradation of the voltage holding capabilities of electrodes and insulators by cesium buildup has ceased to be a problem for normal source operation. The cup-shaped trap succeeded in collecting approximately two grams of cesium during the aforementioned ten days of running which would have otherwise deposited itself on electrodes and insulators with all-too-familiar consequences.

Additional Improvements

The cesium box vacuum enclosure was equipped with a stainless steel toggling valve at the beam exit. A commercial[2] gate valve was installed between the cesium box and its diffusion pump. All routine source maintenance can now be performed with minimal impact on the source vacua.

Upgrading of the ion source electronics is now essentially complete. Two RF-regulated high-voltage power supplies were purchased for the einzel lens[3] and the third gap[4] of the acceleration tube.

Duoplasmatron beam energies have been increased to the limit of the beam energy supply[5] (4 kV). Although we cannot reach beam energies high enough to exploit the maximum He^+ - Cs charge-exchange cross section, which occurs at 6 keV,[6] present beam energies (3.5 to 4 keV) have been sufficient to provide beam intensities (up to 2 μA on target) of general interest in our Laboratory.

References:

1. Nuclear Physics Laboratory Annual Report, University of Washington (1978), p. 116.
2. Vacuum Research Manufacturing Company, Model 6"-94577-308
3. Spellman High-Voltage Electronics Corp., Model RHR 5PN30
4. Spellman High-Voltage Electronics Corp., Model RHR 40P30
5. Nuclear Physics Laboratory Annual Report, University of Washington (1976), p. 24.
6. A. S. Schlachter, D. H. Loud, P. J. Bjorkholm, L. W. Anderson, and W. Haeberli, Phys. Rev. 174, 201 (1968).

9.10 Cyclotron Operations and Development

H. Fauska, G. Rohrbaugh, G. Saling, and W. G. Weitkamp

The cyclotron continues to provide beams for various medical research projects described in Sec. 8 of this report. Demand for beam time remains high, and improvements to the machine have consequently been delayed.

The performance of the machine has gradually deteriorated throughout the year; the major symptoms have been increased sparking in the tank and decreased extracted beam intensity. By April 1981, the machine would no longer produce enough beam to fill the needs of some users. These symptons apparently have been caused by a 10 cm long hole in the wall of the west dee at about a 25 cm radius. The hole was burned by the beam, which is not well focused in the central region of the magnet. That the beam might burn a hole in the dee wall was recognized early in the history of conventional cyclotrons,[1] but the condition has taken 30 years to develop in our machine. Repair is in progress.

The machine was run for 1183 hours between April 16, 1980 and April 15, 1981. Other statistics of cyclotron operations are given in Table 9.10-1.

Reference:

1. M. S. Livingston and J. P. Blewett, Particle Accelerators, McGraw-Hill, New York, 1962, p. 150.

Table 9.10-1
Statistics of Cyclotron Operations
April 16, 1980 to April 15, 1981

Activity	Days	Percent
Department of Radiation Oncology		
a. Cancer Therapy	109	46
b. Experimental Biology	3	1
c. Neutron Dosimetry	6	3
Division of Nuclear Medicine		
a. Total Body Calcium	37	16
b. Isotope Production	3	1
Department of Environmental Health	2	1
Scheduled Maintenance	26	11
Unscheduled Maintenance	50	21
TOTALS	236	100

9.11 Sputter Ion Source Development

J. F. Amsbaugh, F. S. Schmidt, D. W. Storm, and W. G. Weitkamp

For several years we have been working on a prototype sputter ion source[1] in order to try out some new ideas and to understand better how the on-line source works. During the year we have (a) completed the study of the Cs^+ beam optics, (b) compared source performance with cone, one-channel, and six-channel sputter targets, (c) completed emittance measurements, and (d) studied the performance of the Cs contact ionizer.

The first step in studying the Cs^+ beam optics is to compare measured and theoretical emittance. We found that 90% of the Cs^+ beam can be delivered through two apertures of 1.5 mm diameter each, separated by 17.5 mm. This gives an emittance less than 126 mm-mrad. Assuming an initial Maxwellian thermal velocity distribution and the diameter of the ionizer, one expects 90% of the beam to occupy 90 mm-mrad. Mismatch of acceptance and emittance shapes, and the effects of aberation and space charge in the Cs lens probably are responsible for this difference.

The development source has provision for changing the recess of the ionizer with respect to its field shaping electrode during source operation. These electrodes form a Pierce-like accelerating field. Transmission through the double aperture was maximized when the ionizer protruded into the electrode and the Cs einzel lens strength was weakened. This configuration provided an initially diverging Cs^+ beam which then traverses the einzel lens at a larger radius. Consequently one would expect increasing aberations but decreasing effects of space-charge expansion on the beam. Checking this with a calculation of the space-charge effects is planned. (See Sec. 9.14 of this report.)

Three different types of sputter target are in use in the Laboratory: the cone, the one-channel pellet, and the six-channel pellet. It is important to see which provides the best beams. The cone is simply a cylinder of the material to be sputtered which has a conical hole with a diameter of 2.4 mm in the center. The two other types rely on the negative ion extraction electrode, biased positive in relation to the ionizer, to reflect the Cs^+ beam onto a pellet of the sputtered material on the downstream side of the target. The one-channel target is made of a cylinder of stainless steel, type 304, with a 6.4 mm diameter Cs channel offset by 4.8 mm from the centerline. The material to be sputtered is pressed into a hole of 1.2 mm diameter. The six-channel targets are constructed of two 1.6 mm thick disks of tantalum with six through holes spaced around a pellet pressed into a seventh hole in the center of one of the disks. The diameter of the pellet is 2.4 mm.

Each type of sputter target was made with two types of graphite, reactor grade graphite and commercial graphite, to assure the variations of beam intensity were independent of the particular target material. The two graphites performed to within 5% of each other with the commercial graphite slightly better.

In conjunction with these tests, three negative ion acceleration geometries were studied: the UNIS, the Bochum,[2] and a "hybrid" of the two. The UNIS style, similar to the commercially marketed UNIS[3] source, has cylindrical electrodes of 32 mm diameter and an acceleration gap of 9.5 mm with the sputtering plane recessed 16.5 mm from the beginning of the gap. The Bochum style has a 20 mm diameter, an acceleration gap of 2.3 mm, and a recess of 2.3 mm. The "hybrid" was the same as the Bochum style except the recess was increased to 15 mm.

The normalized emittance measured for the three target types decreased when the ion source was changed from the UNIS to the Bochum configuration. The factors were 1.4 for the cone and 3.2 for the one-channel target. This comparison was not made for the six-channel target although its emittance area was the same as the cone in the UNIS style case. Beam intensity increased by 7% and 10% for the cone and one-channel respectively, during this reconfiguration. The preliminary investigation of the "hybrid" style showed an increase of 7% to 10% in the normalized emittance and no change in the negative ion beam intensity, as compared with the Bochum case. Thus the study focused on contrasting the UNIS and Bochum electrode geometries. The studies were done at a lower Cs oven temperature of 250°C since the source was often unstable and the output was sometimes unreproducible at high Cs oven temperatures.

The most intense $^{12}C^-$ beam was 7.5 μA from the one-channel target at this reduced Cs oven temperature. The six-channel target yielded 5 μA and the cone target 3.2 μA. The six-channel target did not show an increase in the $^{12}C^-$ yield when the Cs^+ beam was increased from .4 mA to .5 mA as the others did. Visual inspection revealed that the graphite pellet was very hot, with a color temperature of ∿ 800°C. The other targets evidently provided better cooling to the sputter material since they did not show signs of a temperature elevation. This is similar to the observations of Hedges, et al. at Oxford.[4]

The emittance measurements in the vertical plane indicated that the test stand 30° magnet was limiting the beam. A crude set of four steering plates were installed with a length of 15 cm and a separation of 2.54 cm. It was found that the beam intensities increased by 50 to 60 percent; however the emittance measurements showed only a slight increase in area and an increase of about 50 percent in the maximum partial brightness as detected by the analyzer. The electrode alignments were carefully checked with the source up to air using a transit and found to be correct to ± .15 mm. However, the alignments were not checked under operating conditions. The steering effect observed was determined to be caused in part by the orientation of the Cs^+ channel, i.e., a 180° turn in the sputter target required a shift in the steering voltage from +95 V to -12 V. It is unknown at this point whether the Cs channel's perturbation of the acceleration field near the sputtering region or the space charge of the reflecting Cs^+ beam or both are the cause of this negative ion beam deflection. With all of these developments the source produced a maximum of 50 μA of $^{12}C^-$ at a Cs oven temperature of 320°C which is disappointing when compared to 48 μA that the UNIS delivers at the maximum oven temperature of 325°C.

We had observed that the extraction voltage power supply load varied greatly with Cs oven temperature and that at high temperatures this current became excessive to the point of being an arc. We also had noticed that the decel current in the UNIS[5] depended on the age of the ionizer and was a reliable diagnostic for determining when the ionizer would have to be replaced. In the UNIS, this current ranges from less than 10 μA for a new, well degassed ionizer to .2 mA for an old ionizer that should be replaced.

A model that describes a Cs contact ionizer[6] is a plate of tungsten with Cs adsorbed onto it. The ratio of the evaporated ions to evaporated atoms, η, is given by $\eta = 2 \cdot \exp[(\phi - I)kT]$ where I is the ionization potential of the Cs, ϕ is the work function of the ionizer surface, k is Boltzmann's constant, and T is the ionizer temperature. The ionization potential of Cs is 3.89 eV and its electronic work function is 1.81 eV, whereas tungsten's is 4.5 eV. At high Cs oven temperatures the large amount of Cs emerging from the pores in the ionizer reduces the work function of the surface from that of clean W. This increases the neutral fraction evaporating from the ionizer and decreases the positive ion fraction. The positive fraction rapidly approaches zero as the work function of the surface approaches the ionization potential of the Cs. This places a limit on the maximum Cs^+ current which depends on the pore size, the pore density, the Cs diffusion rate to the surface of the ionizer, and the temperature of the ionizer. Any attempt to surpass this Cs current limit by raising the Cs oven temperature will only decrease the ion fraction and increase the neutral fraction. This stream of neutrals then causes source instabilities by lowering the work function of electrodes and shorting insulators.

We also noted that it is possible to "poison" an ionizer by coating its surface with a substance that has a low evaporation rate at the ionizer temperature and a low electronic work function. In the development source part of the Cs^+ beam struck a brass electrode and the Zn and Cu appeared to have "poisoned" a newly installed ionizer in a relatively short time. This type of ionizer failure had been seen a lot in the UNIS before conversion to the reflected Cs beam operation. In the reflected mode, neutral sputtered material from the negative ion production region of the source cannot reach the ionizer.

References:

1. Nuclear Physics Laboratory Annual Report, University of Washington (1980), p. 159.
2. K. Brand, Nucl. Inst. and Meth. 154, 595 (1978).
3. Universal Negative Ion Source Mark VII purchased from Extrion Corporation, Peabody, MA 01960
4. R. E. M. Hedges, J. O. Wand, and N. R. White, Nucl. Inst. and Meth. 173, 409 (1980).
5. Nuclear Physics Laboratory Annual Report, University of Washington (1980), p. 167.
6. G. Brewer, IEEE Spectrum, Vol. 2, No. 8, August 1965, p. 65.

9.12 Emittance Measurements for the Sputter and Direct Extraction Ion Sources

J. F. Amsbaugh and D. W. Storm

The emittance monitor, which was built following the design of Billen[1,2] for use with the sputter source development project, has been modified so that it can be installed in the low energy beam system in place of the klystron buncher. Emittance measurements were made with 3 ion species from the sputter source (UNIS) and with 2 ion species from the direct extraction ion source (DEIS). The measurements were done at several beam energies. It was thought that these measurements would explain the observed mass dependence of the particle transmission of the tandem, which decreases rapidly for heavier mass projectiles, and would provide a basis for predicting the performance of the development source when installed on the tandem.

The emittance monitor was installed to measure the emittance at a position 1.525 m after the sputter source inflection magnet (see Fig. 9.12-1). The L. E. Faraday cup and beam scanner were not available for focusing the ion sources so previously recorded operating source parameters were used and fine tuning was done to maximize the beam at the monitor's Faraday cup with drive voltages off. In this mode of operation it was difficult to know if the ion sources were properly tuned when measurements were made with nonstandard parameters.

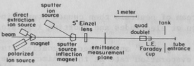

Fig. 9.12-1: Layout of the low energy optical system showing the position of the emittance measurements.

The emittance monitor now uses two slits to define the acceptance of the Faraday cup, after Ames,[3] instead of a circular aperture and slit as before. The slits are .81 mm and .36 mm in width, 25.0 mm in length, and are separated by 457 mm. This defines an acceptance area of .63 mm-mrad. The peak current transmitted through the slits was recorded and from this the maximum partial brightness, MPB, is calculated by the relation MPB = I'/A' in nA/mm-mrad, where I' is the peak current detected by the Faraday cup and A' is the acceptance area of the two slits. We define the two dimensional momentum-normalized emittance as $\varepsilon(f)_n = A(f)\ (E)^{1/2}$. A(f) is the phase space area measured for a fraction, f, of the maximum partial brightness; that is the area of the beam in two dimensional phase space that has a partial brightness greater than 1-f times the maximum. E is the beam energy in MeV. The units are mm-mrad-$(\text{MeV})^{1/2}$. Table 9.12-1 summarizes the results with f=.8 for various ion sources and energies in the horizontal plane. Since the beam brightness distribution appears Gaussian, most of the beam's current is included in this phase space area, A(f=.8). The differences between vertical and horizontal plane measurements were less than the estimated 10% accuracy of this device and did not show any significant shape differences.

The DEIS partial brightness is 6 to 15 times that of the UNIS and its emittance area is at least a factor of 5 smaller. The DEIS normalized emittance area increases with decreasing energy although the large change in the normalized emittance for the proton beam is probably due to poor focusing since source parameters are not well known for that energy. The UNIS in contrast shows an increasing normalized emittance with increasing energy. This could be due to a dependence of the ion ejection energy process on incident sputtering ion energy, or it could be due to the effect of the space charge of the reflecting Cs^+ beam. The reflection voltage may not have been fully optimized. The development sputter ion source (DSIS) shows an increased partial brightness with only a small increase in the normalized emittance. See Sec. 9.11 of this report for more on the DSIS.

These measurements do not conclusively explain the transmission problem of the tandem although the general trend that is seen is qualitatively consistent. It is hoped that the study mentioned above will result in an understanding of this problem and offer a reasonable solution. The measurements did provide an estimate of the performance of the DSIS, i.e., DSIS beams would be approximately twice the UNIS beams.

<u>References</u>:

1. J. H. Billen, Rev. Sci. Instrum. <u>46</u>, 33 (1977).
2. Nuclear Physics Laboratory Annual Report, University of Washington (1979), p. 140.
3. L. L. Ames, Nucl. Inst. and Meth. <u>151</u>, 363 (1978).

Table 9.12-1

Summary of Emittance Measurements

Ion Source	Ion	Energy keV	M.P.B. nA/mm-mrad	ϵ_n(f=.8) mm-mrad-MeV	Area (f=.8) mm-mrad
DEIS	p^-	45.0	986	1.2	5.7
DEIS	p^-	32.7	788	2.4	13.
DEIS	$^{16}O^-$	45.0	425	2.1	9.9
DEIS	$^{16}O^-$	32.7	220	2.2	12.
UNIS	$^{12}C^-$	27.45	63	9.4	57.
UNIS	$^{58}Ni^-$	27.45	7.8	5.3;3.5;16.4	34;21;99
UNIS	Ag^-	27.45	6.3	11.6	70.
UNIS	$^{12}C^-$	32.91	70	14.1	77.
DSIS	$^{12}C^-$	32.1	190	15.9	88.

9.13 Improvements to the Universal Negative Ion Source

J. F. Amsbaugh, F. H. Schmidt, D. W. Storm, and W. G. Weitkamp

During the last year several improvements to the UNIS were implemented to improve performance and to facilitate source operation. These included a new source einzel lens power supply, remote control of some of the source voltages, an increase in the extraction voltage gradient, an automatic source changer, and an interlocked gas manifold.

It was found that a shift in the source einzel lens voltage of 1.6% from the nominal value would produce a 3.7% decrease in the $^{12}C^-$ beam transmitted to the H. E. Faraday cup. The ripple was measured during source operation to be .5%; however the effect of line transients and drift was found to be typically 3% over a 2 hour period, and was thus the major contribution to the instability of the source. This supply was replaced by a Spellman RHR 30N60. The extraction and focus supplies will both be controllable from the control room and remote digital voltage and current readouts will be available soon.

An aluminum insert was installed in the reflection electrode which reduced the diameter of the electrode from 3.17 cm to 1.58 cm and reduced the acceleration gap from 3.80 cm to 1.50 cm. This was done to test the effect of increasing the sputtered ion acceleration electric field strength, and since it increased the transmission through the tandem it has been left in place. Sec. 9.14 of this report discusses more fully this and other extraction geometry details.

A new source wheel has been built using beryllium-copper alloy which was then hardened after machining to prevent the target shell holes from wearing with use. The number of targets was increased from 18 to 20 so that a half revolution of the pinion would rotate the wheel by one target position. A changing device was built which uses a detent to assure accurate positioning with manual or automatic/remote control. The changer can also be controlled by the Texas Instrument programmable controller to cycle between two targets and provide the proper routing signals if needed. The sources can be positioned to ± .02 mm, using a backlash correcting procedure in the T. I. controller.

Finally, since some of the UNIS users introduce gases into the sputter region to increase negative ion yields, a gas manifold is being built to provide gas from supply bottles to a needle valve which is typically at -25 keV. The manifold has provision for three gases with supply line roughing on the house vacuum system. It is interlocked such that if the supply line is pressurized to less than 1.5 atm and the source power is on, an alarm warns the operator and in 5 minutes the source power will be shut off unless the pressure is raised. This prevents the supply line from entering the Geissler region where arcing could destroy the supply line and thus vent the gas to the atmosphere and provide an arc for ignition.

9.14 UNIS Sputter Ion Source - Acceleration Geometry

F. H. Schmidt

For several years now we have been using our standard so-called 6-hole reflection geometry as shown in Fig. 9.14-1.[1] Cs ions pass through a Ta disk containing 6 3/32 in. diameter holes placed symmetrically on a 9/32 diameter circle. They are reflected by a small positive bias on the accelerating, or extraction, electrode. The reflected Cs beam is sharply focused, as from a concave lens, back onto a small "button" of the source material; it is usually also 3/32 in. in diameter.

After some hours of operation, a sputter pattern is produced on the source button consisting of a sharply eroded central core with six lines radiating out

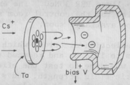

Fig. 9.14-1: Reflection geometry.

from it. We believe that only negative ions originating from the central core are well-enough focused by the low energy beam handling system to pass through the entrance pupil of the tandem beam tube (see Sec. 9.5 of this report for discussion of gridded lens, etc.).

Accelerator Electrode

Fig. 9.14-2 shows the disposition of the electrodes for the negative ion acceleration and Cs^+ ion reflection. A new and "tighter" geometry was achieved by inserting a new electrode into the original one.

The $^{12}C^-$ beam with the new geometry is 40 to 50 percent greater than with the original geometry. The sputter pattern is also reduced in size; the central core is about 1/32 in. in diameter, and the six pointed star is 1/16 in. from tip to tip.

Source Geometry

We have made two experiments using 1/16 in. diameter source buttons (after installation of the new accelerating geometry).

In the first, a 1/16 in. diameter graphite button was substituted for the standard sized 3/32 in. diameter button leaving the six holes for the Cs beam unaltered (3/32 in. diameter on 9/32 diameter B.C.). This source gave the largest beam observed to date - 48 μa of $^{12}C^-$ ions.

In this experiment, we could definitely ascribe the higher output to the smaller source diameter. It may be due to improved cooling, as suggested by work at Oxford.[2] Under identical conditions we obtained:

1/16 in. diameter	190 μA	$^{13}C^{+4}$ (analyzed)
3/32 in. diameter	170 μA	$^{13}C^{+4}$ (analyzed)

In the second experiment, both the source buttom diameter and the Cs holes were made 1/16 in.; the 6 holes were clustered as close as possible to the source button. Our initial results are gratifying. In a short test this

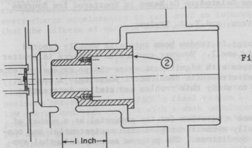

Fig. 9.14-2: New extraction electrode.

source out-performed by about 15 percent several standard sized graphite buttons. The main significance is that, for radiochronology measurements of ^{14}C (see Sec. 9.1 of this report) we can expect to reduce the amount of required sample material by a factor of 4/9.

An experiment was made using several graphite source buttons the surfaces of which were made concave with a radius of 1/16 in. (Our customary button surface is carefully sanded flat to be flush with the surface of the Ta disk.)

These concave surface buttons produced good beams, but there were marked changes in optimum source parameters; the optimum focus voltage changed by 5 to 8 percent, and the optimum reflection voltage shifted by a similar amount. Moreover, the magnetic field of the inflection magnet shifted. Although these changes might appear to be insignificant, they really are not. For example, the focus voltage (for constant extraction potential) has remained within ±1/2% for over a year. The shift in inflection field shows that the beam of negative ions shifts in lateral position due to the curvature of the source. This effect was verified by altering the lateral position of the source button.

We thus conclude that a flat surfaced button which is accurately positioned on the center line of the extraction electrode gives the best reproducible and stable output (see also Sec. 9.1 of this report on radiochronology).

References:

1. Nuclear Physics Laboratory Annual Report, University of Washington (1979), p. 139.
2. R. E. M. Hedges, J. O. Wand, and N. R. White, Nucl. Inst. and Meth. 173, 409 (1980).

9.15 Space Charge Calculations Related to Cs Beams in Sputtered Ion Sources

J. F. Amsbaugh, D. W. Storm, and T. A. Trainor

The effects of space charge in tandem beam optics is usually ignored since beam currents are usually small. However contact Cs ionizers in sputter ion sources can provide Cs^+ beams with significant space-charge expansion, especially in those sources with electrostatic decel-accel focusing. A computer code SPACE is being developed to study this problem and similar interesting problems.

SPACE first solves Laplace's equation for the potential at a number of grid points given a cylindrically symmetric region with equipotential and constant electric field boundary conditions. The program assumes azimuthal symmetry and utilizes a finite-difference approximation equation with a Kutta-

Runge over-relaxation procedure to solve Laplace's equation for the potential. This module of SPACE is a rewritten version of the same module of the code CYSYM.[1] The revision was made to optimize program performance on the NPL VAX.[2] SPACE can write the potential solution on a disk for later use, print the solution, or plot equipotential contours on a Tektronix terminal, with a hardcopy also available. Currently a bug exists in the plotting modules for complex electrode structures; however, since this bug doesn't effect the trajectory module or the trajectory printout, fixing it is a low priority. After SPACE has calculated the potential distribution it is ready to calculate the trajectories through this region.

The mutual repulsion between ions in a beam will result in an acceleration which is not due to the gradient of the previously calculated potential. SPACE assumes the ion charge density is a constant inside the beam and zero outside, and that the beam is "primarily cylindrical". This means the axial component of the space-charge repulsion is ignored whether it is due to sharp changes in beam radius or due to changes in the line charge density which depends on $\dot{z}$. The program calculates the effects of the space charge ignoring the effects of the conducting boundaries conditions of the real problem. With these conditions, the radial acceleration of an ion due to space charge is, by the application of Gauss' law,

$$a_r = eI_o r/2\pi\epsilon_o m\dot{z}\, r_m^2$$

Here r is the radius coordinate for the trajectory, r_m is the maximum radius of the beam, $\dot{z}$ is the axial velocity, I_o is the beam current, and e,m are the charge and mass of the ion respectively. SPACE calculates the radial and axial accelerations due to the gradient of the previously calculated potential using second order central-difference approximations to the partial derivatives. The total radial acceleration is then obtained by adding the radial acceleration due to space charge. The equation of motion in the axial direction is solved for the time it takes to move one grid space in z. Then $\dot{z}$ is averaged over the grid, since the partial derivative of the potential with respect to z is approximated as a constant over the grid. The new radius and radial velocity are calculated using the radial equation of motion and the value of time from the axial equation of motion. Up to ten trajectories can be propagated at one time and the potential field can be scaled. SPACE has the provision for setting the space-charge acceleration to zero over an interval in the potential region so that the effects of various space-charge neutralization schemes can be studied.

The output of SPACE has been compared with the results of Vibran as discussed by Hutter[3,4] for ion beams in field-free regions and for regions of uniform acceleration. The beams ranged in energy from .15 eV to 25 keV, in initial radius from 1 mm to 1 cm, and currents from .43 mA to 5 mA, with accelerating fields from 1.4 kV/cm to 10 kV/cm. The maximum difference in these comparisons corresponded to SPACE's final radium being 3.5% larger for a beam of low energy and high current with a weak accelerating field. The difference is probably due to the radius of the trajectory changing by more than two grids per axial grid, thus overestimating the space-charge acceleration, since this acceleration is proportional to the inverse radius and is averaged over the grid space.

Our polarized ion source typically has a proton beam of 500 eV and a current of 5 mA which is normally space-charge neutralized by electrons from the Cs vapor canal. If the Cs vapor is not present, then excessive space charge expansion of this beam is seen, so this complex electrode geometry will provide another test of SPACE. We will then be able to utilize the program SPACE for the design of intense Cs^+ beam guns, the optics of the Cs^+ beam in sputter ion sources, and other space charge problems.

<u>References</u>:

1. Nuclear Physics Laboratory Annual Report, University of Washington (1972), p. 40.
2. Nuclear Physics Laboratory Annual Report, University of Washington (1980), p. 159.
3. G. E. Vibrans, Tech. Report No. 308, Lincoln Laboratory, 1953.
4. A. Septier, ed., <u>Focusing of Charged Particles</u>, Vol. 2, Academic Press, 1967, p. 13.

---

10. FINAL DESIGN AND CONSTRUCTION OF THE MAGNETIC MOMENTUM FILTER

10.1 Momentum Filter -- Introduction

D. W. Storm

The construction of the large solid angle, isochronous momentum filter is well underway. This system, which was discussed in last year's Annual Report[1], can operate in two modes. In one mode, where only half of the magnets are used, it is a moderately low resolution spectrograph. The resolution will be from .2 to about 1.0% (depending on solid angle). The more interesting operation is as an isochronous momentum filter. In this mode, background particles (e.g., elastically scattered particles) can be removed at the dispersed focus, and the remaining particles will be transported to the final, achromatic focus. The path lengths for all particles of the same momentum are the same (to first order) for this final focus, so the device can be used in coincidence experiments. The solid angle is also appropriate for coincidence measurements, namely about 10 msr. An example of a coincidence experiment for which the momentum filter may be used is a particle-gamma correlation measurement, including measurements with particles at 0°. Non-coincidence experiments include forward angle heavy ion experiments, where the elastically scattered beam usually forms a prohibitive background. Another application is in polarization measurements, where the state of interest is selected at the first focus, and then a thick polarimeter is placed at the final focus. Since the energy of the particles entering the polarimeter has already been determined, the energy resolution of the polarimeter is no longer a concern and a much thicker scatterer than usual can be used to increase the efficiency.

The design of the optics of this system was essentially complete a year ago, and the past year has been devoted to specifying the magnets and having them built. In addition the support structure, the power and cooling, and the control systems were designed and are nearly complete. The design of the scattering chamber and of the rest of the vacuum system is nearing completion, and construction is beginning. The remainder of this section of the report will describe the details of the progress on these subsystems.

Reference:

1. Nuclear Physics Laboratory Annual Report, University of Washington (1980), p. 174.

10.2 Optics and Magnets

D. W. Storm and K. J. Davis

The final design for the momentum filter was fixed during July 1980, and the order for the magnets was placed with ANAC. The dipoles were delivered in December and the quadrupoles in February. The final design is nearly the same as that discussed in last year's Annual Report.[1] However, some adjustments were made in that design to prevent interference between adjacent magnets. The parameters are listed in Table 10.2-1. These parameters produce the required symmetry conditions at the mirror plane, so that the final focus will be (horizontally) achromatic and isochronous. The acceptance of the system is presented in Fig. 10.2-1 and Fig. 10.2-2. The main features of this acceptance are that the solid angle is 12 msr at the central momentum, and 7 msr for an energy range such that E_{max}/E_{min} is 1.5. Of course, for intermediate choices of energy range, the solid angle lies between these values. The resolution of the system is presented in Fig. 10.2-3. The small solid angle resolution is .14% and the resolution at the maximum solid angle is about 1%. In the case where the second half of the system is not used, and one is simply using the first half as a spectrometer, the acceptance is substantially increased. It is expected that the loss of resolution associated with the increased acceptance is not so bad, because a lot of the gain is in the vertical angle acceptance, and the deterioration of resolution occurs mainly with increasing the horizontal angle acceptance. All these calculations have been made using a ray tracing program[2] which carries out numerical integrations of trajectories in magnets which are described with realistic field shape parameters, and the magnet design was specified to correspond to these parameters. At present, we are fitting the actual measured fields to a set of parameters to be used in the program, so we can do ray tracings with the actual fields. Preliminary studies of the measured fields indicate that the performance should be nearly identical to that calculated with the original parameters.

Table 10.2-1
Momentum Filter Parameters

Drift	40 cm
Quadrupole	20 cm × 10 cm bore
Drift	30 cm
Uniform field dipole	ρ = 60 cm, bend = 45° $\alpha_1 = \alpha_2 = -16.8°$
Drift	51 cm
Radially varying field dipole	ρ = 60 cm, bend = -45°, $\alpha_1 = \alpha_2 = -22.5°$ $B = B_0[1 - .272x/\rho - 2.8(x/\rho)^2]$
Drift	40 cm
First focal plane and mirror symmetry plane	
Three magnets identical to the first three in reverse order	

Note: Negative rotation angles for dipole 2 correspond to vertical focusing, since the magnet bends opposite to the conventional direction.

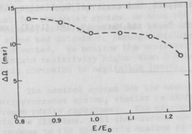

Fig. 10.2-1: Acceptance solid angle of the momentum filter, vs. energy.

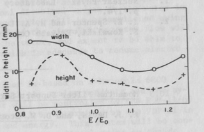

Fig. 10.2-2: Size of final focus for full solid angle, vs. energy.

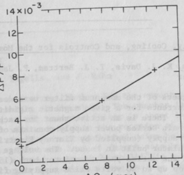

Fig. 10.2-3: Resolution vs. solid angle.

References:

1. Nuclear Physics Laboratory Annual Report, University of Washington (1980), p. 174.
2. J. E. Spencer and H. A. Enge, Nucl. Inst. and Meth. 49, 181 (1967), and S. Kowalski, Private Communication.

10.3 Momentum Filter Support Structure

K. J. Davis, and D. W. Storm

The support structure for the momentum filter is finished and aligned. The six magnets are all supported on a frame which sits on a carriage on the rotating gun mount. Most of the weight of the magnets is born near the outer edge of the rotating floor, and then the carriage transfers this load to the ring track of the gun mount. The base of the gun mount sits on the floor of the basement. The gun mount has been leveled and the axis of rotation of the momentum filter is vertical and true to 0.006 in. at the beam height.

Each individual magnet is supported on three pads which have jack screws for vertical adjustment and roll on a 1.5 in. diameter steel ball to provide horizontal adjustment. The magnets are located horizontally by jacking brackets which are independent of the ball pads.

10.4 Power Supply, Cooling, and Controls for the Momentum Filter

D. W. Storm, K. J. Davis, T. J. Bertram, P. James, T. Van Wechel, and C. L. Wagner

The six magnets of the momentum filter were designed to operate at approximately the same currents for a given magnetic rigidity, so that they could be powered in series. There is an active shunt for each magnet to provide the final adjustment. The main series power supply consists of an adjustable 0 - 285 volt (400 Amp) dc power supply (supplied by Tierney Electric) and a series pass transistor current regulator built in house. The voltage of the dc supply is controlled by SCR's, and the series pass transistor bank (150 2N3055 transistors in parallel) will drop up to 20 volts while supplying fine current regulation. The active shunts (30 2N3055 transistors in parallel) will bypass a set current (up to 40 A). All the set points are controlled by digital to analog converters (DAC's) which are controlled by a microprocessor.

Because the main cooling water for the Laboratory involves an open cooling tower, we decided to cool the momentum filter by a closed loop deionized and dissolved-oxygen free water system. This water is cooled in a heat exchanger by the open tower water. Use of this cooling water will prevent corrosion of the coils in the quadrupole magnets due to oxygen or electrolysis, and will also prevent clogging of cooling lines with deposits. We maintain nitrogen in the expansion tank for the water system, so once the original dissolved oxygen in the water is consumed, no more oxygen will be added. Deionization will be accomplished using a mixed bed deionizer, through which about 10% of the circulating water flow will be diverted. We monitor the resistivity of the water, and expect to be able to maintain resistivity higher than 1 MOhm-cm, which is adequate to reduce electrolytic corrosion to negligible levels.

The control system for the momentum filter is based on a Motorola 6800 microprocessor system, similar to that used with the scaler readouts and the hydrogen parity experiment. The microprocessor will be controlled by the PDP-11/60 via the IEEE bus. All the current set values will be determined by the PDP-11 in response to the operator's desired particle and energy. This system will be connected to a simple data bus (8 data lines and 6 address lines) going to the dc supply voltage control, the main current regulator, the six shunts, and a two byte status register. Each bit of the status register corresponds to one or more sensors which will set the bit if a fault condition occurs: e.g., an over temperature, cooling pressure failure, flow loss, main power off, etc. The current controllers use two byte DAC's and ADC's. The system will select a particular byte for input or output and then transfer the data in the appropriate direction. Once the DAC's are set, the system will monitor the ADC's and the status registers continually. It will maintain the dc power supply voltage so that the voltage drop across the transistor bank is in the desired range, and it will communicate the current values to the PDP-11. In the event of a fault, as indicated by the status register, the microprocessor will shut the current off and inform the PDP-11 of the status.

10.5 Scattering Chamber

D. W. Storm, W. B. Ingalls, and J. Rahn

The design of the scattering chamber for the momentum filter is complete, and construction is proceeding in the shop. The chamber is small, since the edge of the quadrupole magnet of the momentum filter is about 14 inches from the target center. The chamber will rotate with the rotation of the momentum filter over a range of 30°. The rotation is accomplished using bellows on the incoming and outgoing beam lines. There are four different attachment points for the momentum filter, so that a total range of 22 to 145° is available with the exit beam pipe in place. In order to operate at angles less than 22°, the exit beam pipe must be removed, because of interference with the momentum filter. On the side of the chamber away from the momentum filter, there is provision for a large thin window, only 4.5 inches from the target center. This window will permit use of the large NaI or a Ge(Li) detector with as large a solid angle as possible. This feature is especially important for experiments involving coincidence measurements with photons and charged particles. An illustration of the scattering chamber is presented in Fig. 10.5-1.

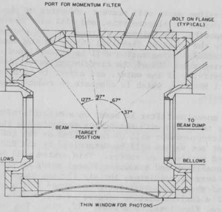

Fig. 10.5-1: Illustration of the scattering chamber for the momentum filter.

The scattering chamber is to be made of aluminum, and it is to be made in a modular fashion. Thus there will be a main box, and the bellows assemblies, thin window, and momentum filter attachments will be separate pieces attached to the box. Since we desire a good vacuum (1.0×10^{-7} Torr), we will make the attachment using metal seals. Appropriate seals for this purpose are aluminum wire seals. Although one might expect that the use of aluminum wire seals on aluminum surfaces would destroy the surface, this is not the case. The aluminum wire is 1100-0 aluminum -- i.e., relatively pure aluminum in an annealed state. The sealing surfaces will be 6061-T6 aluminum, which is a substantially harder alloy, tempered to a hardness near that of mild steel. Tests and previous experience have indicated that such aluminum surfaces will seal repeatedly with wire gaskets without damage to the surface. Of course some components will be stainless steel -- for example, the bellows and associated flanges.

The chamber will be pumped with a CTI cryopump, which will be attached to the bottom of the chamber. There will be a manually operated target changer and detector arm which will be attached to the top of the chamber.

10.6 Momentum Filter Vacuum System

J. F. Amsbaugh, D. W. Storm, and T. A. Trainor

The design of the vacuum ducts and the box for the dispersed focus of the momentum filter is still in preliminary stages, although the conceptual planning is complete. There will be a separate duct in each magnet, and these pieces will be connected with aluminum wire seals. The main material will probably be aluminum. There will be a cryopump, identical to that on the scattering chamber, at the dispersed focus. Both these pumps will operate from the same helium compressor, and the compressor will rotate with the momentum filter.

The box at the dispersed focus will have mechanical feed-throughs for positioning jaws or pins, which will be used to define which magnetic rigidity particles are transmitted to the final focus. There will be five feed-throughs, which could be used for two jaws and three pins, or for any other combination. The box will have provision for a position sensitive detector, so the device can be used as a spectrometer.

There will be a second box at the final focus. This box will be relatively small and will have provision for mounting a solid state detector. There will be no additional pumping at this end of the vacuum system, as the high vacuum requirement results from desire to minimize background resulting from charge changing collisions between heavy ions and residual gas. The actual attenuation of heavy ions is very small, and if the goal of 1.0×10^{-7} Torr is achieved in the first half of the system, the vacuum in the second half will be more than adequate.

---

11. INSTRUMENTATION AND EXPERIMENTAL TECHNIQUES

11.1 Design and Construction of Electronic Equipment

H. Fauska, R. E. Stowell, T. Van Wechel, and C. L. Wagner

The Laboratory's 60 in. scattering chamber required design and construction of a new arm readout system. See Sec. 11.3 of this report.

Improvements were made in controlling the tandem terminal potential by the generating voltmeter. See Sec. 9.7 of this report.

The existing NMR regulator on the Tandem 90° analyzing magnet was modified to allow automatic search and lock regulation. See Sec. 9.8 of this report.

An optical pulser for photomultiplier calibration was designed and constructed. See Sec. 11.2 of this report.

A foil thickness monitor was constructed. See Sec. 11.3 of this report.

Several electronic projects not described elsewhere in this report were designed and/or constructed and include:

a. Several TTL logic probes and pulsers for general laboratory use.
b. An interface box for the DR11C. This currently allows stop, start, clock reset and predetermined count functions from the experiment control box and predetermined count box to access the computer. The experiment control and predetermined count boxes also were modified for this interface.
c. A dead time correction chassis that will handle up to six ADC's. The laboratory BIC (current integrator) is gated by the appropriate ADC busy signals and the outputs are totaled in scalers.
d. A predetermined count chassis for the new scalers. It features a LED readout and a nine decade range.
e. A dual level controller to step the analyzing magnet NMR oscillator. Used in conjunction with the modified NMR regulator (see Sec. 9.8 of this report) one can switch between two selected field strengths.
f. A new cricket chassis for the new scalers. It gives an audible indication of event counting, scaled by a rate of 10^0 thru 10^7.
g. The ADC interface[1] was modified to allow the installation and future use of a Mode III selection (simultaneous coincidence and fast singles). This would be a mixed Mode I, Mode II operation with the same ADC's. The hardware is built but not yet installed.
h. A CAMAC time interlock control chassis was constructed to allow extension of the ADC interface[1] Mode II operation to include various CAMAC modules.
i. A foot controlled speed controller was built for the machine shop to allow accurate slow speed rotational table welding. A second foot control box was built for a needle welder to allow selection of precise welding currents.
j. A router/decoder chassis for a selected ADC on the computer. This allows up to 16 way routes with the available 4 bits of route information.

k. Three microprocessor boards (employing a 6802 CPU) were built for various projects, including an expanded version (buffered) for the momentum filter.

Reference:

1. Nuclear Physics Laboratory Annual Report, University of Washington (1980), p. 183.

11.2 A Precision Optical Pulser for Photomultiplier Tube Calibration

J. G. Cramer, A. G. Seamster, and C. L. Wagner

The precision optical pulser is intended to calibrate the photomultiplier tubes (PMTs) used in the neutrino absorber theory experiment.[1] The pulser employs a light emitting diode (LED) as the light source and a PIN photodiode for precision optical feedback. The LED and PIN diodes are cooled to 5° centigrade by a proportionally regulated thermoelectric module. The temperature regulator is stable to 0.2°, eliminating the problems of LED temperature variations.

The resolution of the pulser, as measured by a PIN photodiode, is about .5% full width at half maximum (FWHM). When the resolution is measured by a PMT the pulser peak has from 2% to 4% FWHM resolution, depending on the illumination levels. The PMT photocathode and multiplier statistics are apparently the limiting factor in this resolution as the resolution improves with increased illumination levels. This suggests that the use of large area PIN or Schottky barrier photodiodes with the necessary high gain electronics might make higher resolution detectors than are available with PMTs.

The optical pulser circuitry uses a fast operational amplifier (op amp) to regulate the LED pulse amplitude. Both LED current and optical feedback are used to control the LED intensity. See Fig. 11.2-1. The optical pulser peak is tuned into the desired part of the pulse height analyzer spectrum by varying the pulse input to the LED drive op amp.

Reference:

1. Nuclear Physics Laboratory Annual Report, University of Washington (1980), p. 5; (1979), p. 7; (1978), p. 6; (1977), p. 3. See also Sec. 1.4 of this report.

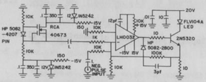

Fig. 11.2-1: Partial schematic of the Light Pulser. The PIN photodiode and LED are on a temperature regulated, thermoelectically cooled coldsink.

11.3 The 60 in. Scattering Chamber Angle Readout System

R. E. Stowell and H. E. Swanson

This chamber has a target holder, two arms, and a bottom table, all movable by external shafts. Mechanical coupling to the respective shafts is by means of anti-backlash gears in the ratio of 1:36; consequently, the available position information is modulo 10 degrees of rotation. Shaft position had been determined using independent optical shaft encoders, but their age and the unavailability of maintenance preclude continued usage.

In the new system, the optical encoders are replaced with resolvers, and these are multiplexed into a commercially available synchro to digital converter (see below). The readout electronics were designed around the same microprocessor circuity used in other NPL readout systems,[1,2] thus placing much of the design task in software. The program keeps track of the selected shaft (arms, table, etc.) and the number of revolutions of the respective resolver. After the initial power-up, each shaft is manually rotated to zero degrees and the revolution counters reset. The actual angle is calculated from the expression;

theta = (rev. counter)*10 + (synchro - 180)/36

where physical zero degrees corresponds to 180 on the resolver shaft, and rev. counter is a signed integer determined from the direction of rotation and the number of zero to 360° crossings incurred.

Angles are displayed in the range of minus to plus 180° on LED displays, and BCD data can be transferred to the data collection computer upon request, via the IEEE instrument bus. Provision was also made to transfer BCD data from 4 additional 10 digit scalers to interface BIC and NMR frequency data to the computer.

Revolution counters are implemented in a section of memory which is powered by battery, and are maintained for at least 24 hours in the event of a power outage.

The system hardware consists of three chassis: (1) the Opto-coupling electronics, (2) the Multiplexer, and (3) the Readout system including four Reeves type R600 resolvers.

The Opto-coupling electronics consist of optically coupled line conditioning ICs (PM 1101s mnfg. by Electrol Corp.) that sense which control relay in the original motor drive controller has been selected.

The multiplexer chassis contains a reed bank that selects which resolver is to be connected to the angle position encoder. The multiplexer sends this information to the microprocessor and through control logic disconnects power drive to all but the selected shaft.

The Readout display chassis contains the synchro to digital converter (North Atlantic Model 8300A), a lab built microprocessor board, control logic, power supplies, and battery backup for the revolution counter memory. The front panel has four 5 digit displays (+/- 180.00°), indicator lights to show the selected shaft and a series of 5 lighted push-buttons to indicate a loss of memory battery power and allow resetting the revolution counters.

References:

1. Nuclear Physics Laboratory Annual Report, University of Washington (1979), p. 39.
2. Nuclear Physics Laboratory Annual Report, University of Washington (1980), p. 190.

11.4 Target Preparation

G. Hinn

The targets listed below have been prepared in the target lab over the past year. Of the 210 targets prepared only the more interesting and non-standard techniques will be described in detail.

Target	Final Form	Method of Preparation	Backing	($\mu g/cm^2$) Thickness
Mo^{100}	metal	Elec. Bombardment	100 μg/C	200
NaF	salt	Vac. Evaporation	20 μg/C	100
$Li^{6}O$	$Li^{6}O$	Vac. Evaporation	S.S.	400-600
$Si^{28}O_2$	$Si^{28}O_2$	Elec. Bombardment	S.S., 10 μg/C	5.50
Si^{30}	Si^{30}	Reduction, E-bomb	S.S.	10^3
Se^{76}	metal	Vac. Evaporation	10 μg/C sandwich	1.5×10^3
Mg^{24}	metal	Reduction, E-bomb	10 μg/C	5.50
N^{15}	melamine	Vac. Evaporation	750 μg gold	400-600
Lu_{nat}	metal	Elec. Bombardment	S.S. collodion	700-800
Hf_{nat}	metal	Elec. Bombardment	collodion	300-400
Hf^{180}	metal	Elec. Bombardment	collodion	300-400
B^{11}	metal	Elec. Bombardment	S.S.	10^3
Be^9,Be^{10}	metal	Reduction, E-bomb	source	10^4
Zn^{64}	metal	Reduction Evaporation	100 μg/C	$10^2 - 10^3$

A. Beryllium

The upgrading of the beryllium evaporator glove box system is now complete (see Sec. 11.8 of this report) with the addition of a Kewaunee Scientific negative pressure radiochemical enclosure. This enclosure contains an analytical balance so that all beryllium oxide powder handling is now totally contained within the system.

This evaporator glove box system was used to produce beryllium metal ion sources from beryllium oxide powder for radiometric dating. Experience has shown that beryllium metal sources produce beams an order of magnitude higher than those produced from beryllium oxide ion sources.[1]

A method has been developed to provide a beryllium metal ion source 2mm in diameter and 0.75mm deep by vacuum reduction evaporation of beryllium oxide contained in a tantalum crucible onto a tantalum ion source disc using magnesium metal as the reductant.[2] The reduction takes place at 600-800°C (1×10^{-3} torr) and the evaporation of the reduced beryllium takes place at 1,400-1,600°C (2×10^{-5} torr).

A 2 to 10 mg deposit of metallic beryllium produced this way has given typical yields of 100 to 800 nA of $^{9}Be^{16}O^{-}$ ions at the low energy cup and 10 to 60 nA of analyzed $^{9}Be^{+3}$ ions measured after the image slits at the detector cup.[1]

B. Silicon-30

It has been difficult to produce oxygen free silicon-30 in the laboratory due to the fact that Oak Ridge supplies silicon-30 normally only as the oxide and charges a great deal to reduce it to its elemental form. Previous attempts at one step reduction evaporations using magnesium metal as the reductant have usually produced brownish contaminated SiO targets.

A two step method has been devised where initially reduction takes place in an enclosed tantalum container under vacuum. Any magnesium oxide remaining after the reduction takes place is removed with 3M HCL. The pure reduced silicon-30 is then evaporated in a second step onto a thin copper backing which is removed with copper etch to produce a thick (1mg/cm^2) self supporting target.

C. Boron-11

A method has been devised to produce thick (1mg/cm^2) Boron-11 targets. Using a copper water cooled hearth and an electron-gun, Boron-11, obtained from Egle-Pritchard, Miami, Oklahoma, can be successfully evaporated onto a thin copper foil which is cooled by a water cooled copper block beam stop. The thin copper backing is then etched off with copper etch to produce a self supporting Boron-11 foil. This method produces some copper contamination in the boron target which can be eliminated by using glass slides with sodium chloride as a release agent. Further work needs to be done to increase uniformity of Boron-11 foils produced by this method.

D. Selenium-76

Selenium foils 600-6000 $\mu g/cm^2$ thick with a 10 $\mu g/cm^2$ carbon coating on both sides were obtained by evaporation. The selenium was converted from the red amorphous state into the more stable gray hexagonal state by floating the target on water and raising the temperature to 80°C. This procedure prevents the target from breaking because of shrinking during conversion.[3]

E. Stripper Foils

In the past few years with the coming on line of the heavy ion facilities at Daresbury and the Holifield heavy ion facility at Oak Ridge and other heavy ion facilities, the subject of long lived carbon stripper foils has come in for extensive study. The group at Daresbury has had a great deal of success and has reported a technique for making cracked ethylene foils[4] which are longer lived than carbon arc produced foils (see Sec. 11.5 of this report). Lifetimes of these foils and standard carbon arc produced foils were further enhanced by a slackening technique also reported by the Daresbury group[5] (see Sec. 11.6 of this report). Combining both of these techniques is supposed to give stripper foils that last up to 25 times longer than the standard stripper foils now in use.[6]

These combined slacked and cracked ethylene foils are now on a production basis and are ready to be tested for longevity in our 40-position tandem foil wheel assembly. The thicknesses of these foils will have been measured in an optical transmission meter (see Sec.11.13 of this report) against standard foils whose thicknesses have been previously measured in the beam.

References:

1. P. M. Grootes, M. Stuiver, G. W. Farwell, T. P. Schaad, and F. H. Schmidt, Radiocarbon 22, 487 (1980).
2. G. M. Hinn, Nucl. Inst. and Meth. (in press).
3. R. Risler, G. Hinn, S. Hoffman, Nucl. Inst. and Meth. (in press).
4. N. R. S. Tait, D. W. L. Tolfree, D. S. Whitmell, and B. H. Armitage, Nucl. Inst. and Meth. 167, 21 (1979).
5. B. H. Armitage, J. D. Hughes, D. S. Whitmell, N. R. S. Tait, and D. W. L. Tolfree, Nucl. Inst. and Meth. 167, 25 (1979).
6. J. L. Gallant, D. Yaraskavitch, N. Burn, A. B. McDonald, and H. R. Andrews, Nucl. Inst. and Meth. (in press).

11.5 Development of Cracked Ethylene Stripper Foils for the Tandem

T. Bertram, G. Hinn and W. Lynch

Research and development of techniques for the production of cracked ethylene stripper foils was begun in September 1979 and successfully completed in November 1980. The project was motivated by the discovery that cracked ethylene foils last longer as stripper foils than do the commercially available amorphous foils. Cracked ethylene foils are produced in a high voltage, low pressure gaseous discharge (glow discharge). It is via plasma (atomic) polymerization of the source gas (ethylene) that carbon polymers precipitate out of the plasma and take part in film growth on the cathode. Important stages of the project completed since last year are: (1) the design and construction of a new glow discharge unit, (2) the determination of the dependence of foil thickness on reaction time, and (3) the determination of the difference in life time between cracked ethylene and amorphous foils.

The new glow discharge unit, which was under construction at the time of last year's report, has been completed and is now in use. It features two 6 in. diameter parallel discs as the electrodes, where the lower disc is the cathode. The anode is suspended from a superstructure and the cathode is mounted on a sliding base for easy handling of substrates. Only the inner surface of each electrode is exposed; the remainder is insulated with teflon to prevent arcing. The inner surface of both anode and cathode is a disposable ferrotype plate (chrome on steel). Thus high quality surfaces are effortlessly and economically achieved.

This unit has proved extremely successful in the production of cracked ethylene foils. Stable discharges are now reproducible, and the dependence of foil thickness on reaction time has been determined. In particular, for a reaction occurring at 3 keV and 60 microns, the growth of 3 $\mu g/cm^2$ and 5 $\mu g/cm^2$ foils require 7.5 seconds and 10.0 seconds respectively. Foil thicknesses were determined by proton elastic scattering in which these foils, together with foils of known thickness, were used as targets. In addition, a device has been designed and constructed which measures the optical transmittance of these foils (see Sec. 11.13 of this report). Thus, foils whose thicknesses and transmittance are known generate a calibration curve, allowing future measurements to be made optically. In particular, 3 $\mu g/cm^2$ and 5 $\mu g/cm^2$ foils have transmittances of 70% and 60% respectively.

A comparison of the lifetime of cracked ethylene foils to that of amorphous foils was done using a 38 MeV ^{28}Si beam (LE current: 10 μA). The lifetime was determined by the ratio of HE cup to LE cup intensities, since this ratio decreases as the foil degenerates. As a control during the test, the HE beam intensity was maintained at a maximum by tuning. Two foils of each type were used. The lifetime criterion was chosen to be the time required for the HE/LE ratio to fall to 70% of its initial value. With respect to this criterion, the cracked ethylene foils were found to last 3.5 times longer than the amorphous foils.

11.6 A Slackening Technique Development for Carbon Stripper Foils

L. Geissel, G. Hinn

Slackened stripper foils have been produced and it has been proven they last longer than conventionally mounted foils.[1] Our laboratory can now produce slackened foils using a design originated at Harwell Laboratories which we have modified.

Due to our laboratory's unique stripper foil wheel design, .015 in. thick material is required for the foil mounts, posing a problem of buckling when the ring diameter is reduced.

The carbon foils to be slackened are mounted on .015 in. thick, 3/8 in. inside diameter, 9/16 in. outside diameter, 2024T4 aluminum. These foil holders are sheared, punched with a 3/8 in. diameter shim punch, then turned on a mandrel in a lathe to 9/16 in. outside diameter. (It is important that the two diameters are concentric to avoid buckling.) Next the rings are annealed in a 775°F furnace for 2 to 3 hours, and allowed to cool in place until they reach 500°F. At this time they will be of hardness "TO" or "dead" soft.

The slackening die, designed to be used in an arbor press, is made of oil hardening drill rod with a highly polished internal taper. Tapering from .750 in. to .498 in. it ends in flat bottom with a 3/8 in. through hole. A spring-loaded pressure pad presses against the aluminum ring, keeping the ring from buckling while the die is being forced over a split micarta collect. It is this forcing or stamping between the micarta and the flat bottom of the die that "coins" the foil holder flat while leaving the foil intact.

This slackening technique has not yet been used in foils mounted in the laboratory's tandem. However, it is possible this procedure, used in conjunction with collodion[2] and cracked ethylene[3] foils could provide longer lasting foils, and savings in both time and money.

References:

1. B. H. Armitage, J. D. H. Hughes, and D. S. Whitmell, Nucl. Inst. and Meth. 167, 25 (1979).
2. Nuclear Physics Laboratory Annual Report, University of Washington (1980), p. 185.
3. Nuclear Physics Laboratory Annual Report, University of Washington (1980), p. 171.

11.7 Construction of a 4-Stage Large Area Multi-Wire Avalanche Counter

K. Lesko, V. Metag, and A. G. Seamster

A position sensitive multi-wire counter has been constructed which features 2 sequential X-Y detectors with 4 independent proportional counter cells. The design was taken directly from that of D. V. Harrach and H. J. Specht.[1]

Improvements include:

a. a modular voltage divider frame which allows the simultaneous use of 2 to 4 separate elements.

b. a wire grid frame which incorporates a permanent electrode opposite the wire side which obsoletes the use of thin foil electrodes.

The assembled active detector, shown in Fig. 11.7-1, is 40 mm thick and is easily accommodated by the standard Heidelberg enclosure. The detector is operated with 10 torr of hexane and an anode voltage of 500-600 volts. Typical position resolution is 0.5 mm, while the time resolution between segments is 250 psec. The completed detector was used for 12 shifts at the SuperHilac. By the strategic replacement of aluminum absorber foils for several of the aluminized mylar entry/exit windows, we were able to monitor the trajectory and energy of a wide range of heavy ions.

Development is underway on an additional segment designed for alpha particle detection, which is currently difficult to do considering the small volume of gas in each element. The new plane incorporates a thin (1/16 to 1/8 in.) sheet of NE-102 plastic scintillator of the same active area. This scintillator will be coupled to a recently developed compact 1.5 in. diameter photomultiplier tube and base assembly supplied by EMI GENCOM. This unit is vacuum compatible and will be located directly behind the last segment of the position counter.

Reference:

1. D. V. Harrach, and H. J. Specht, Nucl. Inst. and Meth. 164, 477 (1979).

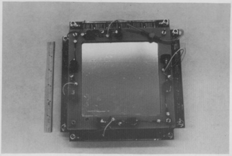

Fig. 11.7-1: Photograph of active multi-element detector stack. Metal scale is 6 inches long.

11.8 Design and Installation of a Closed Beryllium Handling System

L. Geissel and A. G. Seamster

The increased use of beryllium targets and source pellets, primarily for accelerator dating studies, has made it beneficial to upgrade and enlarge our current beryllium evaporator system.[1] The areas requiring major alteration include increased working space and improved venting.

The interior space was doubled by the addition of a commercial stainless steel glove box. This unit was coupled to the original plexiglass enclosure with a baffled port. Weighing and material handling procedures are now done in this new box.

The original venting lines were removed and replaced by a 2 in. Kanaflex system incorporating separate absolute filters and blowers for each enclosure. Negative pressure is maintained in each box and is continuously monitored with a magnehelic gauge. Exhaust is routed to the main radiochemical hood handling system.

Reference:

1. Nuclear Physics Laboratory Annual Report, University of Washington (1978), p. 124.

11.9 Position Sensitive Modifications to a Proton Polarimeter

J. Cramer, A. G. Seamster, W. G. Weitkamp

Experimental constraints, requiring enhanced kinematic information (E,Θ,ϕ), have made it necessary to redesign the gas proportional counters coupled to the polarimeter described previously.[1] Position information is given by both charge division and electron drift time as described by Markham, et al.[2]

Four counter shells were machined from brass and lined with tantalum. High voltage ceramic feedthroughs were installed in opposite vertical ends of each unit. Resistive wire, 158 ohms/cm, was strung between the insulators, just outside the active volume, and attached with conductive paint. Optimum energy and position results were obtained with one atmosphere of P-10, (10% methane - 90% argon), at +1100 volts.

Two counters were mounted in tandem on either side of the scattering cell and backed with a silicon surface barrier detector. Theta (Θ) was determined by a time-of-flight measurement between each set of proportional counters. Phi (ϕ) was determined by combining coincident charge division signals algebraically for each pair. Energy loss values were measured by summing both ends of the wire in each counter. The counters are shown in Fig. 11.9-1.

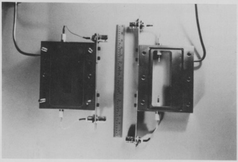

Fig. 11.9-1: Photograph of disassembled counters. Metal scale is 15 cm long.

References:

1. Nuclear Physics Laboratory Annual Report, University of Washington (1979), p. 157.
2. R. G. Markham, S. M. Austin, and H. Laumer, Nucl. Inst. and Meth. 129, 141 (1975).

11.10 Resistive Film Position Sensitive Detector

D. D. Leach and J. G. Cramer

A two-dimension position sensitive detector is under development which is based on a design by Jared, et al.[1] The detector is a parallel-plate gas detector with windows constructed of polypropylene backing with a thin resistive layer of nichrome (NiCr) evaporated on it. Position is determined by charge division of secondary electrons across a NiCr film.

In a previous report we reported[2] a method of evaporating NiCr onto polypropylene. This method used liquid nitrogen cooling to dissipate heat from the film during evaporation. By reducing the required power dissipation, water now adequately cools the film.

Real pulses are now seen from an alpha source but the energy loss in the gas volume is too small to be used for position information. Particles with higher stopping powers must be used to test the position information from this detector.

References:

1. R. C. Jared, et al., Nucl. Inst. and Meth. 150, 597 (1978).
2. Nuclear Physics Laboratory Annual Report, University of Washington (1980), p. 187.

11.11 Bragg Spectrometer

D. D. Leach and J. G. Cramer

Bragg curve spectrometer based on a design of C. R. Gruhn[1] has been constructed. The purpose of this detector is to identify a particle and its energy by giving a signal related to the Bragg energy loss curve of that particle.

The detector is a gas ionization counter which stops the particle in the gas. The secondary electrons drift in the same direction as the initial particle to a Frisch grid and an anode.[2] Because the number of electrons ionized per unit length traveled is proportional to the Bragg curve, the anode current will have the same shape as the Bragg curve in time. The energy and identity are derived from this pulse.

The detector has been tested with a fission fragment source which gave the expected pulse size and shape.

References:

1. Lawrence Berkeley Laboratory, Berkeley, California.
2. O. Bunemann, T. E. Cranshaw, and J. A. Harvey, Can. J. Res. 27, 191 (1949).

11.12 Liquid Inert-Gas Filled Detectors for Energetic Charged Particles and Gamma Rays

J. G. Cramer, C. R. Gruhn[+], and R. Loveman

The goal of this project is the development of new types of detectors for use in nuclear physics and X-ray/γ-ray astronomy through the detailed investigation of the properties of ion chambers filled with ultra-pure liquid inert gases, particularly argon and xenon. This work is being carried out primarily at LBL in collaboration with Dr. C. R. Gruhn. One member of the UW contingent (Loveman) is in residence at LBL working with Dr. Gruhn.

The development of liquid inert gas ionization chambers (L.I.G.I.C.) has moved along two fronts. First, we are trying to develop a liquid xenon gamma detector, and second we are working on the development of a liquid argon charged particle detector.

In attempting to develop the liquid xenon detector, we have encountered difficulties in producing adequately pure liquid xenon. We are working on several schemes to increase the purity of the medium. Work is continuing on several purification schemes.

During the past year, we have built and tested a liquid argon charged particle detector. The chamber is set up as shown in Fig. 11.12-1 and is run as a

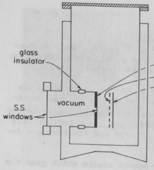

Fig. 11.12-1: Schematic diagram of liquid argon charged particle ionization detector. The interior volume of the detector is filled with ultra-pure liquid argon.

Bragg curve spectrometer. Using this technique we are able to retrieve information on the amount of charge recombination as a function of position in the track. We are finding that for protons the yield of charge as a function of position along the track follows the following formula:

$$\frac{dY}{dx} = \frac{dQ}{dx} \quad \frac{1}{1+k\frac{dQ}{dx}}$$

where Y is yield, Q is the original charge produced and k is a function of the electric field and the medium. This would corroborate preliminary results reported in the last Annual Report[1] that at low fields the charge yield is approximately proportional to track length.

We are continuing studies of the usability of liquid argon as a medium for detectors, including studies of recombination and recombination fluctuations.

References:

\+ Lawrence Berkeley Laboratory, Berkeley, California.
1. Nuclear Physics Laboratory Annual Report, University of Washington (1980), p. 3.

11.13 An Optical Transmittance Meter for Foil Thickness Measurements

T. Bertram, C. L. Wagner

The optical transmittance meter is motivated by the need for a simple procedure to measure the thickness (micrograms per square centimeter) of very thin foils used in nuclear physics research. The circuit was developed for testing the thickness of cracked ethylene foils (see Sec. 11.5 of this report). To measure the thickness of a foil one places the foil in an aluminum block machined to hold the foil and the optical electronics. The transmittance percent is then read on a digital voltmeter. The foil thickness is read from a calibration graph made from foils of known thickness.

The electronics for the transmittance meter has two basic circuits, a precision light emitting diode current regulator and a photodetector amplifier.

11.14 Gas Transfer System for the Zero Degree Beamline

E. G. Adelberger, M. Olson, H. E. Swanson, and R. D. Von Lintig

We have constructed a system to rapidly transfer activated gas from a target cell on the zero degree beamline to a shielded counting cell in Cave 2. The system is designed to facilitate measurements of beta decays with halflives as short as a hundred milliseconds. Location of the detectors in Cave 2 eliminates neutron damage and confusion from direct population of the states under study. The system is patterned after one designed by Hardy, et al.[1], but some improvements involving the target cell configuration and the tubing material have been added. An 8-channel digital timer has been developed to operate the valves and provide synchronous gating signals.

The gas transfer system is depicted in Fig. 11.14-1. Target gas enters the cell through valve 1 after being measured out to correct volume in the ballast area. After the gas has been exposed to the beam for the irradiation period, valves 3 and 2´ open, allowing gas to expand into the evacuated transfer tube and actually shoving the volume of target gas along before an expanding volume of helium from the other ballast volume (through valve 2´). After a transit period of approximately 50 milliseconds, the entrance (valve 5) of the

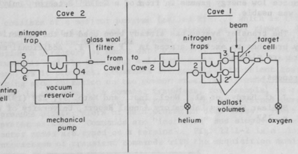

Fig. 11.14-1: The transfer system used to transport target gas from the zero degree beamline to a shielded counting station.

counting chamber closes, counting begins, and the transit line is evacuated. The target cell is refilled and the gas irradiated while counting occurs so that there is almost a one hundred percent duty cycle, except for the transit time.

Some of the experiments for which the transfer system is intended involve production of background or competing reactions, so a capability for trapping and filtering the gas during transit was built in. Fig. 11.14-1 shows the set-up used for studying ^{18}Ne decays. Three liquid nitrogen traps, one containing a molecular sieve material, plus a glass wool filter were used to reduce contaminant activities. The addition of molecular sieve material added about 50 milliseconds to the transit time. This series of traps was found to function extremely effectively, removing essentially all of the directly produced ^{18}F activity.

The relative production or count rate of competing activities can also be controlled by optimizing the irradiation and counting times if the halflives are significantly different. And for beam limited experiments the cycle can be adjusted to optimize the count rate for a given beam intensity. Variation of these cycle features is greatly facilitated by the timer, so that each valve operating period and the gate signals can be adjusted independently at the touch of a dial. The timer also provides signals for sychronizing the beginning of multiscaling or time binning data collection with the beginning of each transfer cycle. The accuracy of the timer is assured by a highly stable oscillator time base and other circuits based upon the design of the polarized ion source spin flip controller.[2] Fig. 11.14-2 is a circuit diagram of the timer.

The efficiency of the system for collecting activated gas in the counting cell is unknown, but appears to be reasonably high. For example, in the case of the ^{18}Ne beta decay experiment, a beam of less than ten nA was required to produce a limiting high count rate in the 3 in. by 3 in. sodium iodide detectors located next to the counting cell. And even with one inch of lead used to attenuate low energy gammas in front of a Ge(Li) detector, only two hundred nA of beam was usable.

The transfer system has already been used in the detection of weak beta decay branches to excited states in ^{18}F and ^{19}F. Additional measurements of this nature are planned.

References:

1. J. C. Hardy, et al., Nucl. Inst. and Meth. 97, 229 (1971).
2. Nuclear Physics Laboratory Annual Report, University of Washington (1977), p. 157.

12.1 Singles Data Acquisition Software

K. Green

Introduction

During the past several years[1] we have developed a new singles data acquisition system replacing a previous system based on an SDS-930 computer. This year we will give an overview of the complete software and hardware system.

The new system is built around a PDP 11/60 minicomputer running the RSX-11M v3.1 operating system. A second processor called the MBD-11 controls CAMAC data acquisition hardware. Secs. 12.5 through 12.8 of this report describe the hardware in detail. For the following discussion refer to Fig. 12.1-1 for a block diagram of the hardware.

The singles acquisition code was locally written. At the time we began development, we could find no acceptable existing code to use. Our design criteria for the singles software were:

a. Rapid implementation of the core routines.
b. Easy extendibility of the system.
c. Accumulation of singles at up to 100 khz, total.
d. Conversational commands which prompt for information not supplied.
e. A flexible system for defaulting elements of commands.
f. Dynamic management of data arrays to minimize wasted memory.
g. High density spooled histogram plotting on the Printronix.
h. A "live" display with light pen interaction for peak analysis.
i. Multiple terminal operation.

Organization of the singles software

The system consists of a monitor program (called RTM...) which is the owner of the data arrays. It is the only program resident at all times. It is responsible for imposing a structure on the common data, regulating access to the data and managing a directory of named data elements. There is no direct communication between it and the user, but only between it and other tasks which need the services it provides. Commands are generally transient tasks and exit after performing some operation on the common area. Background jobs are occasionally spawned in the wake of a command transient, for example, to calculate the average beam energy during a run, or to watch for an external hardware shutdown, or to produce printer plots of data stored in disc files. There is no command interpreter as such. Commands are "installed" and simply run when their three character names are typed on a terminal. Fig. 12.1-2 is a block diagram of the interaction of transient commands with the acquisition monitor and the global common area.

All data acquisition functions are carried out by the MBD, described in more detail in Sec. 12.7 of this report. As an independent processor on the

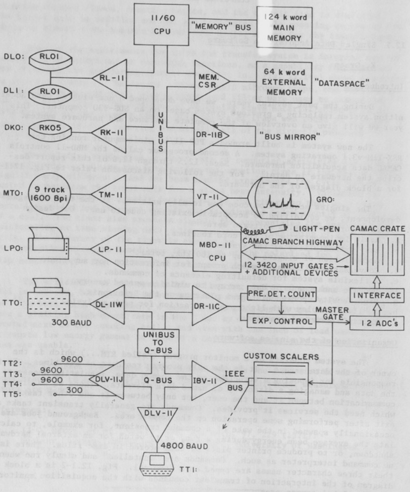

Fig. 12.1-1: System hardware configuration

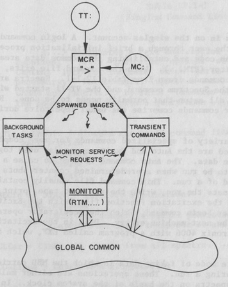

Fig. 12.1-2: Interaction of transient commands with the monitor, MCR and global command. MCR is the RSX-11 command language interpreter. The TT: indicates teletype commands. The "MC:" is a pseudo device with which programs may force commands as if they had been typed by the user.

PDP-11 UNIBUS, it performs channel increments directly into the 11/60 memory arrays. When the MBD starts processing, it is told by the 11/60 which ADC's to read, where to place the results in main memory, what precision each channel is to be (2 or 4 bytes) and what the memory limits of each spectrum are. There is no further communication until the MBD is halted, stopping acquisition. During this time, the 11/60 is generally busy producing printer plots, calculating the average beam energy during the run, and constructing a "live" display on the VT-11. Displays are "live" in the sense that the 11/60 is continuously scaling raw data into the visible image, completing each update in about a second. Visible channels cannot be directly updated on a point by point basis because the 11/60 does not know when the information in a data array is changed by the MBD.

The display is capable of selecting any singles spectrum in the system for viewing, calculating peak areas and errors, showing selected portions of spectra and scaling the data, all through the use of the light pen. Light pen menu items are placed at both the top and the bottom of the screen. The top items generally control the information to be displayed, such as spectrum selection, peak areas and alternate "pages" of system information. The bottom menu controls scaling, windowing and peak definition. The display is completely independent of data acquisition.

Typical operations

To start singles, one logs in on the singles account. A login command file then takes over and leads the user through a brief initialization procedure, loading the MBD acquisition code and establishing the common data area by starting up the acquisition monitor (RTM...). When the command file exits, the system is capable of accepting commands drawn from Table 12.1-1. Spectra are established through the use of the Spectrum command and the VT-11 started with the Display command, completing all setup that normally needs to be done. Begin, End, Plot, Output and Clear commands comprise the usual repertoire during an experiment.

There is also a growing variety of specialized commands for more complex experiments. Most recently added are the Auto and Excita commands, used together in taking excitation function data. The Auto command is used to cause a command file called "auto.cmd" to be run when a predetermined counter shuts down the ADCs, signaling the end of a run. This command file usually contains a sequence of commands to terminate the run, write the run onto tape, print out peak information and update the excitation function file (with the Excita command). Last of all is another Begin command, which the accelerator operator completes when he has reached the next machine energy. Data in the excitation file is displayable on the Tektronix 4006 with a program called EXF, which is automatically started by Excita.

Also added is an alternate mode of taking data in which the MBD carries out a sequence of operations during a run. These operations are either multiscaling of data or routing of spectra on the basis of the system clock. In a typical use of this facility, a target is activated while the beam intensity is multiscaled, after which short lived decays are observed in time routed spectra. The resolution of the clock which is used is 1/60th of a second.

Printouts and plotting

Since most printouts generated by the system take a fairly long time to process, all printer activity is carried out by a background spooling program working from data in disc files. This is to prevent tying up the live data arrays. As soon as the spooler file is written (a matter of a few seconds) the arrays are available for modification. The only restriction on the spooling queue is the amount of file space available on the disc, which is far in excess of usual needs.

The spooling program, called PLOSPL, is capable of a variety of numeric dumps and high density (Printronix) plots, both for 1-dimensional and 2-dimensional spectra. Although the singles software is not currently capable of generating 2-dimensional spectra, the same spooler is used by the multiparameter software (see Sec. 12.2 of this report).

Reference:

1. Nuclear Physics Laboratory Annual Report, University of Washington (1980), p. 191; (1979), p. 160; (1978), p. 129.

Table 12.1-1
Singles Command List

<...> delineates a text description of what is to be supplied. [...] indicates options which may be omitted. Capital letters indicate which parts of keywords are necessary. For example, <spectrum name> could be replaced by GAMMA and /Adc:<...> by /A:3. Omission of all input except the command name invokes a query mode of operation.

AUTo - Enable / disable automatic command file
>AUT /option
/Disable
/Enable
/Toggle

BEGin or STArt - Initiate acquisition.
>BEG /options
/Run:<run number (default: previous+1)>
/Label="<run label to appear on all printouts>"

CLEar - Clear all counts from all spectra.

CONtinue - Continue a stopped run.

DISplay - Start the VT-11 display.

END or STOp - Terminate acquisition.

EXCita - Compute all peak areas and place in an excitation file.
>EXC <file name>/option
/Create
/Append

EXF - Display excitation functions on Tektronix 4006.

INPut - Input a run from data tape.

LET - Spectrum arithmetic (still very simple)
>LET <output spectrum>=<input spectrum 1> [± <input spectrum 2>]

LISt - List the contents of a data tape.

MAG - Data tape utility program.
>MAG [<output device>=]<input device>[/options]
/Full
/Initialize
/List
/Query
/Rewind

NEXt - Input the next run from data tape.

OUTput - Output run to data tape.

PEAks - Print out peak information (spooled).
    >PEA <spectrum name>

PLOt - Plot spectra on line printer (spooled).
    >PLO <spectrum name> [/options]
        /CHannels:<first channel to plot>:<last channel to plot>
        /COmpression:<number of channels to sum>
        /Highdensity
        /LInear
        /LOg
        /Nogrid
        /Range:<value of bottom of counts axis>:<value of top>
        /Standard
        /Top:<value of top of counts axis>
    Defaults are retained from the selections made on the last plot of a spectrum.

PRInt - Print out channels on line printer (spooled).

RELabel - Change run number and/or label of current run.
    >REL /options
        /Run:<run number>
        /Label="<new run label>"

SCAlers - Type out current values of scalers.

SPEctra - Establish, remove or modify spectra.
    >SPE <spectrum name> [/options]
        /Adc:<source adc number, 0 for no adc (default: 0)>
        /Delete
        /Label="<text to appear with printouts of the spectrum>"
        /Precision:<2 or 4 bytes per channel (default: 4)>
        /Routes:<number of routes (default: 1)>
        /Scaler:<adc gate scaler number (default: 0)>
        /Xdimension:<number of channels (default: 512)>

TMR - Construct special MBD command list for multiscaling and clock based routing of spectra.

WINdow - Manually set window channels in spectra.

12.2 Multiparameter Data Acquisition Software

K. Green

Introduction

In contrast with our singles data collection development (outlined in Sec. 12.1 of this report), we were able to import most of the necessary software for multiparameter operations. There are two distinct programs involved. The acquisition code is Lawrence Berkeley Lab's QDA, written by Everett Harvey. The analysis code is Fermilab RSX-Multi. Both codes were initially brought up in (almost) their distributed forms within a very short time of receiving them. The codes had a number of limitations, however, that proved unacceptable in the long run.

2-dimensional histograms

The most severe restriction of Multi was an inability to store 2-dimensional histograms in memory. Multi had no code and no memory space to support this option (Multi has room for only about 7 k words of arrays). The storage limitation can be solved by using RSX-11M's ability to move a 4 k word "window" about in memory, but this operation is far too slow to be useful, taking about 1 msec for each move. Accessing a sizable region of memory, say about 32 k words, would mean the position of the window would always be wrong.

Our solution was to build a piece of hardware to gain access to any word in a 64 k word region in a few microseconds. We call the result a "Bus Mirror" discussed in Sec. 12.5 of this report. The modifications to Multi to support this device were straightforward, involving the substitution of function calls and subroutines for all references to Multi's data array "Dynam". Multi's internal handling of pointers into this array was also altered to prevent a restriction of indices to only positive integers, for a total of 32 k words. The result permitted, at least in theory, access to a total of 64 k words of data array. The conversion was completed in about 2 weeks. A much longer time was spent in adding the support code for the 2-dimensional histograms.

The total amount of memory available for use rose to about 28 k words, this being the largest amount that could be set aside in the 124 k words available in the machine and still support other functions. It was still only just enough for a single histogram of reasonable resolution (128 × 128).

A second solution to the problem was then formulated, again in hardware, in the form of an external 64 k word memory plane. We call it the "Dataspace" memory. It is discussed further in Sec. 12.6 of this report. Basically, it is a standard memory board with the normal addressing logic bypassed in a small piggy-back card. The only modifications to Multi that had to be carried out to take advantage of the new board was in the collection of "Dynam" subroutines which currently accessed the "Bus Mirror". We can now store three 128 × 128 histograms. The fourth histogram which might be expected to fit in the 64 k words of the memory board can't, because Multi puts additional items out there, most notably the dictionary.

Singles under Multi

Because the regular singles software is incompatible with Multi and QDA, a limited singles ability has been built into Multi. Specific histograms can be tagged as "singles". During the beginning of a run, information about these histograms is packaged and transmitted to the microprogrammable branch driver (MBD), which then increments them in the same fashion as in regular singles. The singles code uses a different MBD channel than does the multiparameter code that QDA communicates with. Thus the histogram is incremented independent of Multi. Displaying a singles spectrum causes a static picture to be generated. It must be specifically redisplayed to see the latest information.

Saving histograms for later analysis is not supported under the standard version of Multi. We implemented this capability as a Write command, which causes histogram memory to be dumped into a disc file. The structure of the file permits retention of many runs, up to the limit of storage on the disc. Usually when an event tape must be changed, a standard singles tape is placed on the drive and a singles utility program called MAG is used to append the new runs from the file onto it. The file is then deleted from the disc. Offline analysis programs written for standard singles data tapes can then access Multi histograms as if they were taken by singles. In fact, the singles acquisition system can read these tapes and display the 1-dimensional histograms on the VT-11 display for light pen analysis.

Improved plotting capabilities

The plotting capabilities of Multi were originally limited to a simple character plot, which took a lot of paper and a considerable length of time to complete, during which Multi was completely dead. There was no form of plot at all for 2-dimensional histograms. All of these problems were solved by enhancing the singles spooling program "PLOSPL" and rigging Multi up to use it. Multi's only plotting responsibilities are to collect the options describing how the plotting is to be done, and then dump this information, and the histograms, into a disc file. The file is then sent to PLOSPL which generates a high quality Printronix plot in parallel with continued Multi operation.

Both 1- and 2-dimensional histograms may be plotted or dumped numerically. Both linear and logarithmic plots are supported. 2-dimensional plot channels are represented by a 5 by 5 density symbol.

Analysis speed

As originally installed, data analysis speed was about 10 Hz. A considerable effort has gone into improving analysis speed, resulting in a current speed of 100 to 200 Hz, depending on the type of analysis. There were a number of reasons for the initial poor performance.

The "live" display feature of Multi places an upper limit on the analysis speed, determined solely by the speed of the terminal. An update to the display takes about 10 characters. At 4800 baud this results in a maximum speed of 48 Hz. System overhead in I/O processing makes the situation worse. In fact, with the display on, our measured upper limit was 25 Hz. Since nobody was willing to run with the display off, a check was put in at a point prior to the actual generation of a new update. If the terminal is determined to be busy from a previous operation, the new update is simply omitted. The result is that gaps form in the display of 1-dimensional histograms where the omissions occur. When the display is regenerated due to overflow, the gaps are wiped out. There is no apparent effect on XY scatter plots.

A second loss of analysis speed results from time spent processing the "eval" statements. These are a series of Fortran-like statements describing the operations to be performed on raw event data. The actual time taken by each statement is variable, but is on the average around 1 ms each. Eval statements are so slow because they are interpreted by Multi. The method of interpretation used was as efficient as possible, which left compilation as our only recourse. Modification of Multi to directly produce PDP-11 code for its eval statements turned out to be surprisingly simple. The resulting code array is executed in a small machine language subroutine at roughly 10 times the speed of the interpreter. The subroutine is necessary to provide the variable stacks and access to the Fortran mathematical library. The resulting evaluation is sufficiently fast that it is no longer a noticable effect on the overall event processing.

Our current version appears to require 5 msec for each event fetch and assorted overhead, plus about .3 msec for each histogram. The display has a small (10%) effect presumably due to RSX I/O processing and interrupt handling. Fig. 12.2-1 is a simple model of the timing of Multi's event analysis loop.

Reference:

1. Nuclear Physics Laboratory Annual Report, University of Washington (1980), p. 193.

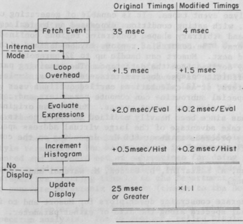

Fig. 12.2-1: A simple model of Multi's event analysis loop.

12.3 Offline Data Analysis on the VAX 11/780

K. Green

Introduction

Several programs now exist for offline multiparameter data analysis on the VAX 11/780. These consist of programs to scan, copy and sort event tapes, define two dimensional gate regions interactively on Tektronix 4010 terminals, form projections of arbitrary regions in a two dimensional space, perform simple arithmetic operations on spectra and plot the resulting one or two dimensional spectra on a Printronix printer/plotter.

Scanning and copying event tapes (A. Lazzarini and K. Green)

Qdascan is used to obtain preliminary information about the contents of an event tape. It lists, for each run on a tape, the run number, title, date and time, total number of events of each unique format pattern and the scaler readouts. This basic information is used for planning subsequent sorting. It gives the user a map of runs on a tape and events of each type. An option allows selection of format patterns to be counted.

Disaster recovery of poor tapes and tape copying is accomplished with Qcopy. Qcopy is a logical copy from tape to tape, with extensive error recovery procedures absent from other analysis programs. Options are provided for discarding or salvaging as much as possible from bad records, discarding singles events from the tape and for concatenating several event tapes together. The error recovery algorithms are designed to maximize salvageable information, while ignoring unreadable and unrecognizable data.

Sorting event tapes (J. Freeman, K. Green, and R. Seymour)

Musort[1] is used to analyze event tapes. It is capable of generating up to 16 spectra simultaneously, with gating conditions expressed as logical equations involving other gates and arbitrary shaped constraint regions confined to the plane of any two parameters. The constraint regions may be defined with the aid of Vaxspan, described next. Musort can handle up to 32 parameters, the first 12 of which are usually derived from the data tape. The remaining parameters are available for definition as pseudoparameters - either as simple combinations of other parameters, or as calculations carried out in a user "special subroutine". The special subroutine can compute parameters and can set logical gate conditions. It also may reject events. Musort was originally written for the 11/60, and has since been heavily modified to optimize its use of the VAX, with changes to take advantage of the large virtual address space available. Sorting generally proceeds at about 800 Hz, depending on the complexity of the events and of the sort.

Spectrum analysis (J. Freeman, A. Lazzarini, D. Gordon, M. Warchol and M. B. Tsang)

Vaxspan is used to generate constraint descriptors for Musort and to form projections of two dimensional spectra along the axis of either parameter. The regions are selected for analysis interactively through the use of the cursor thumbwheels on Tektronix 4010 terminals. A series of points is selected to enclose the region undergoing analysis. The resulting constraint is then written to a file, as are any desired projections.

Arithmetic operations between spectra are accomplished with either Sum1 or Sum2. These programs are capable of stretching, shifting, summing and renormalizing one or two dimensional spectra.

Analysis of singles tapes is carried out with "HP". HP is a calculator program for spectra taken from singles tapes. Its rather unique approach to analysis is to place spectra in "registers" which are handled in a fashion similar to that of an HP calculator. It can perform compressions, shifts, addition, subtraction, plotting and displays on Tektronix 4010 terminals.

Plotting (K. Green)

Printer plotting is carried out by Hist. It is capable of taking one or two dimensional spectra stored in disc files, and producing histograms and density plots on the Printronix printer/plotter. Options exist for selection of ranges of channels, specification of lower and upper cut offs on the plotted values and selection of linear and logarithmic modes of scaling.

Reference:

1. Nuclear Physics Laboratory Annual Report, University of Washington (1979), p. 164.

12.4 Plotting on the VAX

J. Amsbaugh, K. Green, R. Seymour, and M. Warchol

There are a number of software packages available on the VAX to perform Printronix and Tektronix plotting. Calcomp plotting is also possible, currently by carrying floppy discs over to the LSI-11 used in the hydrogen parity mixing experiment.

Tektronix plotting

There are two subroutine packages available for plotting on Tektronix style terminals. The most general is Tektronix PLOT-10. This is a well documented and standard set of subroutines for doing generalized plotting of points, vectors and symbols. Subroutines have been added to perform three dimensional perspective plotting (thanks to the Department of Mechanical Engineering), and to generate Printronix hardcopy (thanks to the Department of Chemistry).

A simpler to use Tektronix display subroutine was locally written for spectrum analysis. The subroutine, called Displa, takes an array of data and peak windows. Plots may be constructed as points, [illegible]es or histograms. Options exist for the interactive scaling and shifting of t[illegible] data being viewed. Peak windows may be altered or defined using the cursor [illegible]mb wheels available on 4010 type terminals.

Printronix plotting

General purpose plotting is performed with a Calcomp and Versatec call-compatible subroutine package supplied by Printronix. It is a two-pass operation, with the application program as the first pass. A second program then takes the files produced and generates a rasterized output. The Tektronix to Printronix plotting is carried out by this package with a specialized application program that takes a raw Tektronix plot file and interprets it, performing the necessary Printronix plot calls.

Simpler one pass subroutines were written to handle both one and two dimensional spectra, producing the laboratory standard plots. One-dimensional histograms are plotted with Histo, which can plot either 1-dimensional histograms or points, allowing selection of channels, plot range and mode (linear or logarithmic). Numeric printout of the data occurs side by side with the plot. Two dimensional plots are produced by Twod, which uses many of the subroutines of Histo. Options are similar to Histo, but no numeric printout occurs. The plot itself is composed of 5 × 5 density symbols.

Standard spectrum files may be printed with a program called Hist, which employs calls to both Histo and Twod to perform the plotting.

Calcomp plotting

Calcomp plotting is currently accomplished by writing a spectrum file on the VAX floppy disc, and carrying it over the hydrogen parity LSI-11 microcomputer. The LSI-11 has a Calcomp interfaced via an IEEE bus. Work is in progress to interface the Calcomp to the VAX. The general purpose Printronix subroutines will be used in conjunction with a Calcomp-specific second pass routine to provide application-independent plotting to either the Printronix or Calcomp.

12.5 The Bus Mirror, A Virtual Storage Expansion Device for a PDP-11

R. Seymour

In its original form, MULTI had a 7000 word histogram storage array, which was inadequate for us. For access to arrays far larger than would fit in a normal PDP-11 program's address space, the RSX-11M operating system has facilities for programs to move logical "windows" through physical memory. These are called "Programmable Logical Address Space" (PLAS) directives. Unfortunately this facility was designed for orderly access, with the program making one call, using 4000 words of information, and then making another call. The call takes slightly longer than a millisecond of real time. This time is spent in the operating system itself, so other programs can not execute until the request is serviced. In MULTI's application, we were asking for totally random access to as much space as possible.

Temporary solutions were tried, including having MULTI freeze the PDP-11's clock to cancel timesharing. MULTI would then directly change the computer's memory management registers to perform the window operation, acquire the desired data, then return the registers to their original state and release the clock. This could be executed in 5 microseconds, but would occasionally cause a system crash for reasons we never understood. At this time, we learned about DEC's DJ-11 device, which is able to move a "window" for programs on one UNIBUS computer through the memory space of another UNIBUS computer. We realized that this idea could be adapted to moving a hardware "window" around on a single UNIBUS. We already knew that a DEC DR-11-B general purpose direct memory access interface could be run in "maintenance" mode whereby it performed program-controlled single-word transfers to any location in low memory. A cheaper version of the DR-11-B, a DECkit-11-D, was purchased and modified to provide features more suited to our use. These features are:

a. 64 k word addressing instead of 32 k word,
b. upper/lower 64 k word bank selection,
c. one-word-only transfers,
d. read-modify-write mode,
e. disabled word-count circuit,
f. disabled interrupt circuit.

The modified unit became known as the "Bus Mirror". It appears to the UNIBUS as three address locations: one for control, one for the address to be read or written, and one for the actual data transfer. The user program sets a direction state in the control register, then the address into the address register. If the operation is a "read", the direct-memory-access transfer occurs before the execution of the next PDP-11 instruction, and the data register will contain valid data when read by the program. If the operation is a "write", the Bus Mirror waits until the program writes to the data register, and then performs the memory modification immediately. The control register can be set for automatic read/write based upon data register activity, but additional circuitry would be required to absolutely prevent logic races. The automatic feature allows X=X+1 operation within the program.

Any program can access the Bus Mirror by mapping the PDP-11's device page addresses to its own address space. This is easily performed under RSX-11M by making that area a known named COMMON area. A Fortran program simply uses the following statement:

```
COMMON /IOPAGE/ CONTROL,ADDRESS,WORD
(all integers), with a corresponding
   COMMON=IOPAGE:RW:7
command to the taskbuilder.
```

The program may then drive the mirror with simple code like:

```
        CONTROL=1          (read)
        ADDRESS=LOCATE     (a channel number,  rhaps)
        LOCAL=WORD         (pulling the resu   rom the mirror)
or:
        CONTROL=2          (write)
        ADDRESS=LOCATE     (where to put it)
        WORD=LOCAL         (sending it to the mirror)
```

MULTI was modified by simply changing all references to the DYNAM array to either function calls for reading or subroutine calls (DYNAMP) for writing to the histogram area. Further modifications had to be made to allow MULTI to use full 16-bit pointers. MULTI had been using negative numbers as flags, but now the 64 k word addressing range required the use of the sign bit as valid information. Therefore specific flags were defined (such as -32768) which would never appear as DYNAM pointers.

The final step in implementing the Bus Mirror was telling RSX-11M to reserve a block of memory for the histogram/Bus Mirror operations. Space requirements for MULTI, QDA and other programs limited that space to 24 k words.

The Bus Mirror served as MULTI's access to its histograms for a number of months, but the users immediately filled the 24 k word space and again demanded more. Squeezing and shuffling allowed test runs with up to 48 k words of space, but no real data runs were possible in this configuration. The only way to enlarge the space available while leaving the programs room to breathe was to move the data entirely out of the UNIBUS's address space. We had sketched out ways for two Bus Mirrors to be wired back-to-back between two UNIBUSes, but kept looking for other ways to perform the memory expansion. The result of that search is described in Sec. 12.6 of this report.

12.6 The DATASPACE Memory Expansion for a PDP-11

R. Seymour

The DATASPACE system provides memory space separate from the PDP-11's normal 124 k word memory. The new space is available only for data; programs cannot be run in it. Programs may access the data by putting the address of the desired datum into an address register and then reading or writing the next PDP-11 address location (data window). That second access will be to/from the dataspace memory, at the address specified by the register. Repeated accesses to/from the same PDP-11 location will continue to point to the same dataspace location. The address register/data window system is similar to the Bus Mirror, but does not require an additional register to define the direction of transfer.

There are 16 address registers available, with provision to expand to 32. This allows simultaneous access by 16 (32) different programs without contention problems. If only 1 register were provided, the programs would have to establish ownership of the dataspace to prevent another program from changing the register before the first one completes its transaction.

The design of the dataspace allows additional banks of 64 k word memory planes, with no practical limit (256 megawords using only one of the spare registers). Slight modification would allow the use of fewer, denser, memory boards. The first implementation does not have the bank-switching circuitry installed.

The 16 address registers occupy every fourth even word address from 760400 (octal) to 760776 in the PDP-11's IOPAGE. The registers are "write-only" PDP-11 memory locations. An attempt to "read" them results in a "non-existant memory" system trap. The data window locations are the next odd word addresses. The bank-switching will be controlled by writing to the next even word address. This will load the bank address. The third word above an address register is reserved for future expansion.

The data window appears as normal PDP-11 memory to the computer. Accessing the data windows as bytes merely retrieves the desired half-word from the data space.

Hardware

The dataspace is built with a modified Plessey PM-S1164A memory board. Additional planes can be other types of memory boards if they provide access to the required signal paths.

The Plessey board includes a parity controller. The circuitry which normally serves to address the parity controller's Control and Status Register (CSR) is changed to provide the address decoding for the address and data registers. PDP-11 address bits A17-A8 are still decoded by the Plessey board to turn on the device-select line for any address around 7604xx.

Address lines A7 and A2 are reserved for future expansion. Lines A6, A5, A4 and A3 serve to select one address register from the address register bank. Line A1 selects between the address registers and the data memory. A2 will select the bank registers if A1 is low.

The address registers exist as memory locations in four 7489 16×4 bit memory chips. The UNIBUS supplies the data which loads them, and their outputs drive the address lines of the dataspace memory board. The memory board then performs normal UNIBUS data transfers directly.

When 7604xx is decoded as an address to be written into, the Plessey board is selected and checks A2 and A1 to determine which function to perform. If it is an address register load, the 7489's write-enable signal feeds a Plessey circuit to give a completion handshake to the UNIBUS. The speed of the 7489 does not require any additional handshake delay.

If the decoded function is a memory read/write, the Plessey's select signal is fed to the memory plane. The Plessey board will also check the UNIBUS's C1 line for write/read selection. The Plessey's normal handshake circuit then treats it as a normal memory access, with full synchronism with refresh and chip response time. The only change the Plessey board sees is that the address information for the access is coming from the 7489s instead of from the UNIBUS address lines. Again, the speed of the 7489s permi[illegible]iding them in the UNIBUS settle times.

Programming

Fortran programs access the dataspace in the same fashion as the Bus Mirror. A named common IOPAGE is defined, with access to the 128th through 255th word above the start of the common area. The program determines which location it wishes to access, and places the address of that word into its assigned address register. The address may range from -32768 through +32767. To write to the dataspace, the data is put into the next word in common above the address. To read from the dataspace, the program simply takes the result from that same data location.

Speed of operation

Based on the Plessey memory specifications, the DATASPACE board can have a register loaded in about 200 ns. It can read or write the data word in slightly less than 500 ns. Since the read/writes are direct to the memory, these are the only times involved. In the Bus Mirror, there was the write to the address register, the write to the direction register, and then an unknown time (depending on bus activity) when the actual DMA transfer occurred. Then the user could read the data register to get the result. The total time involved in a transaction was about 500 ns per register transfer, plus a minimum of 500 ns for the DMA transfer, for a total of at least 2 μs. Compared to direct manipulation of the PDP-11 address registers, the loss was only the 500 ns DMA time.

The net result is that the DATASPACE system should take less than half the time for a single word transfer as does the Bus Mirror. Additional savings are realized by no longer needing the PDP-11 instructions which commanded the direction register.

For the MBD-11, the use of the DATASPACE system could actually add transfer time. This is because the MBD-11 has the ability to directly access any word in PDP-11 memory without using the PDP-11 mapping registers. Therefore we go from a single DMA command to the dual transfer of address followed by data. This possible loss is mitigated by leaving the MBD-11 pointing to the IOPAGE. Under non-dataspace operation, each MBD transfer must be prefaced by a check as to which 64 k word half of the PDP-11 is to receive the data. Then the MBD must set/reset an internal one-bit register to supply that address line. Only then can the MBD instruction for data transfer be issued. If all MBD transactions occur over the DATASPACE, this bit can simply be left on. At worst, the MBD can simply turn it on each time without having to check what the proper state should be. Avoiding the check/set/reset code will save about 2 microseconds of MBD time, at the expense of a 200 ns DMA cycle to load the DATASPACE's address register. The actual savings or loss will be determined by the code generated to suit the application.

Since the DATASPACE memory is directly controlled by the UNIBUS, channel increments may be done with a read-modify-write cycle. This takes only 70 ns, since it avoids the address setup time for the write half of the cycle.

12.7 Singles Data Acquisition Hardware

H. Fauska, R. Seymour, and T. A. Trainor

This is a review of the digital hardware involved in singles data acquisition.[1] In summary, we have a set of ADCs interfaced to a CAMAC crate, which is connected via a small computer to a PDP-11/60 responsible for overall experiment control, display and storage. Software for this system is described in Sec. 12.1 of this report.

A data event is an analog pulse, associated with a half square-wave gating signal (see Fig. 12.7-1). This report will follow the path of an event through the various devices which make up the system.

We measure the pulse with Tracor-Northern TN-1213 200 MHz ADCs. The ADCs are set to ignore analog inputs unless there is a simultaneous gating pulse provided to the coincidence (COINC) inputs.

When a gated pulse is seen, an ADC waits until the analog signal starts to drop in amplitude (peak detection). At that point the ADC grabs the signal to prevent the loss of amplitude with a pulse-stretching circuit. When this circuit is turned on, the ADC issues a signal called Pulse Stretcher Busy (PSB). An overall BUSY signal is started, and the ADC begins the A-to-D conversion at this time. When the conversion is complete, PSB is turned off and a signal called STORE is turned on to tell external electronics that the final result can be stored elsewhere. The BUSY signal remains on, and the ADC remains unable to receive another event until external electronics provide a CLEAR signal. That cancels the existing result and returns the ADC to a waiting-for-analog state.

The result appears on 13 wires as the binary representation of the voltage converted. The ADC front-panel Group Size switch determines the maximum number the ADC will yield for any conversion. The Conversion Gain Switch determines what value a ten-volt signal will generate.

The ADCs are controlled by an NPL-built interface which contains master on/off gating and clearing control, as well as routing bit latches for modifying the ADC results (see Fig. 12.7-2).

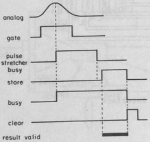

Fig. 12.7-1: ADC pulse timing relationships. "Off" blocks inputs and conversion.

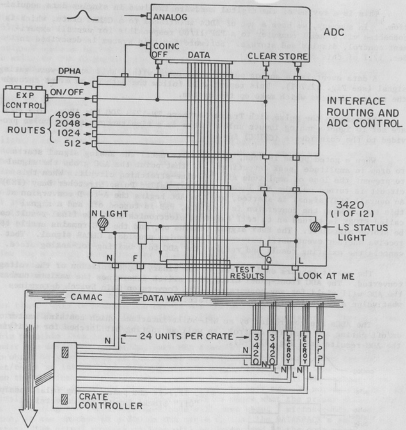

Fig. 12.7-2: ADC interface

The ADC gate is fed into the front panel DPHA BNC connector. It is fed directly to the ADC COINC input, unless blocked on an experiment-wide basis by the experiment controller. The experiment controller is controlled by either the computer or conditions in the outside world (such as a predetermined counter). Front panel switches can select which inputs affect the experiment.

Routing information is presented to separate banks of BNCs (one group for each ADC). The routing information is latched by the leading edge of the event gate. When an ADC is read, an "OR" is performed between its route bits and the ADC result wires. When a 512 route is set, it looks just like the last conversion had the 512 bit active in the channel number. This simple scheme produces nonsense if the group size knob is set higher than the minimum routing input used. If the ADC converts to channel 912, the result cannot be distinguished from a 512-routed channel 400 signal.

The ADC STORE and CLEAR signals just pass on through to the CAMAC crate. They go to a Kinetics Systems 3420 (see Fig. 12.7-2). The 3420 is basically a slightly complicated connector, which resides in a CAMAC crate. All of the CAMAC devices' data lines are in parallel. Only the device selected by the "crate controller" may put its data on the lines.

When the STORE signal arrives, the 3420 passes it on as a CAMAC "Look At Me" (LAM) signal. When the computer reads the ADC result, the 3420 automatically generates an "acknowledge" signal, which clears the ADC, releasing it for the next event. Because of this, we can only read the ADC once. However, we can test for the STORE signal any number of times. The LAM signal can either interrupt the computer or be tested on an individual basis. We test all STOREs sequentially, one every 3 μs. This distributes the deadtimes evenly across all ADCs.

The CAMAC crate is managed, read and tested by a microprogrammable branch driver, the MBD-11. The MBD is a computer in its own right. It has 4 k words of 16-bit 30 ns memory, a central processor, and special provisions for input and output. Fig. 12.7-3 is a simplified view of the MBD. It can control the CAMAC crate, read and write data to the crate and communicate with the PDP-11.

The sole purpose of the MBD is to intelligently connect CAMAC crates to the PDP-11. By being its own computer, the MBD relieves the PDP-11 of much busy

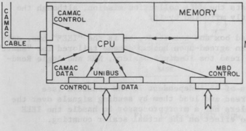

Fig. 12.7-3: Schematic of the MBD-11 microprogrammable bus driver.

work, such as the repetitive testing of the STORE signals. Since it was built with a single goal in mind, it lacks much of the general purpose fast number crunching that the PDP-11 has. But by giving up flexibility, it has gained speed. The actual "computer" integrated circuits are the same as those used by the PDP-11, but the hookup is such that it runs 3 times faster.

The spectra (or histograms) are kept in the PDP-11's memory. During the "start" processing, the PDP-11 tells the MBD-11:

a. which ADCs are active - so that only those will be checked,
b. where the spectra are - where to put the numbers,
c. the spectra limits - so as not to step on other spectra,
d. two or four byte precision - 2 byte to save space, 4 byte for 2×10^9 counts.

The MBD-11 is loaded with a program for singles data acquisition. This report will cover that program, since the rest of the acquisition system views the MBD-11 as a black box. Its flowchart (see Fig. 12.7-4) shows how the MBD loops, waiting for a STORE (LAM). When it is seen, that ADC is read. The result is checked against the group size. If it is too big, it is set to zero. If the spectrum is 4 byte, the result is multiplied by two, to allow two PDP-11 words per channel. That result is then added to the address of that spectrum's zero channel in the PDP-11 memory. That result is the PDP-11 address of the channel which needs to be incremented. The PDP-11 memory is read. The MBD has to wait while the PDP-11 UNIBUS comes up with the result. Then one is added to that result and it is written back into the PDP-11 memory. The MBD is reset to "loop" mode, and the search for LAMs continues. The speed of the MBD-11 allows useful processing to occur during the one-microsecond delays that the CAMAC and UNIBUS require for activity.

The spectrum's channel has now been incremented. The PDP-11 processing that goes on afterwards is discussed in Sec. 12.1 of this report.

A major feature of the PDP-11/60 is its UNIBUS architecture. Any device on the UNIBUS can be accessed by any other device. This is what allows the MBD-11 to directly increment memory. More than that, it lets the MBD read or control other devices as well. In singles we don't use this capability, but in TIME BIN mode and MULTI, we do.

Additional hardware assists the data collection mission, although the analog events may not be directly affected by it.

Just as CAMAC is a defined box and connector, so is the "IEEE" bus, only it doesn't have a box. It is an agreed-upon hookup scheme tailored for "smart" instrumentation. We use it to read the 10-digit scalers, NMR and Angle Readouts.

The scalers are two banks of 16 independent 75 MHz counters (see Fig. 12.7-5). The PDP-11 can read and load them by sending signals over the IEEE bus. Each bank of 16 scalers has a microprocessor to handle the IEEE transactions. It has almost no effect on the actual scaler counting.

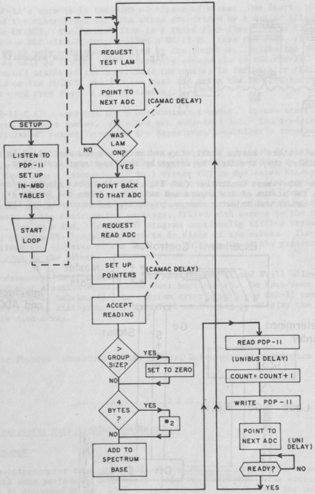

Fig. 12.7-4: MBD flow chart.

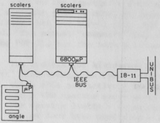

Fig. 12.7-5: IEEE bus schematic.

The scalers' master start/stop and reset are not controlled by the IEEE bus. Rather, they are directly driven by the Experiment Controller.

The Experiment Controller (see Fig. 12.7-6) issues simple go/no-go signals based on the states of its inputs and switches. Among the inputs are beam intensity, tandem and injector energy, predetermined counters, and the PDP-11.

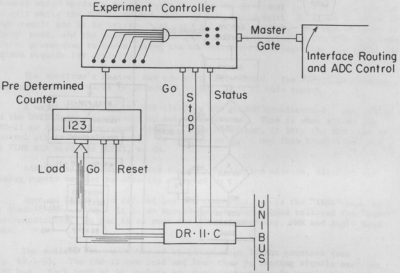

Fig. 12-7-6: Experimental controller schematic.

The PDP-11's vote is in the form of a pair of wires. One Starts the experiment, and the other Stops it. The wires are driven by a set of flip-flops driven by the UNIBUS. The "reset" line is a third flip-flop. These flip-flops are built into a DEC circuit board called a DR-11-C. Like the 3420, it is a "connector" which only acts when selected by the computer. Unlike the 3420, it can talk as well as listen, and is directly accessible to the PDP-11. As shown, the on/off status of the Experiment Controller is fed back to the PDP-11. Because it is on the UNIBUS, the MBD can read and write the DR-11-C too. We have not yet used that feature beyond testing.

The DR-11-C also controls the predetermined counter. It can start, stop, reset and load a target number. We don't use auto-load yet. The predetermined counter's "finished" output is one of the Experiment Controller's inputs.

The final hardware component of note is the VT-11 graphics display processor. This device is another semi-intelligent peripheral riding on the UNIBUS. An image is formed on a (nominally 17 in.) vector CRT by dedicated hardware stepping through a display "list" in the PDP-11's memory. The list contains beam and mode controls, the scaled data for beam positioning, and "jump" instructions to direct the VT-11 to start pulling data from other places in memory. The PDP-11 sets up the skeleton for an image, filled with zeroes in the data areas. Then, during a run, the DISPLAY program continually riffles through the raw spectra, placing VT-11-scaled abstracts in place of the zeroes. The VT-11 hardware follows the dictates of the skeleton, which includes the presentation of the data area on the screen.

The independent co-processing of the MBD-11, PDP-11 and VT-11 allows high data rates without creation of rate-dependent bottlenecks. We have seen instances of the PDP-11 halting (due to program error), with the MBD-11 continuing to update the spectra histograms and the VT-11 continuing to display the last update of its data array.

Reference:

1. Nuclear Physics Laboratory Annual Report, University of Washington (1980), p. 189.

12.8 Multiparameter Data Acquisition Hardware

R. Seymour

The multiparameter data collection system uses the same devices used by singles, with some performing completely different functions. The singles arrangement is discussed in Sec. 12.7 of this report. The changes for multiparameter operation include: coincident gating and lockout by the ADC-to-CAMAC interface, different programs in the MBD-11, use of a Tektronix 4006 instead of the VT-11, and additional memory space for the PDP-11.

During singles operation, the individual ADCs are allowed to run independent of each other. During multiparameter operation the ADCs share a common "master event" gate, while still maintaining their individual DPHA inputs (see Fig. 12.8-1). The master gate is "ANDed" with all DPHAs, thereby preventing an ADC from accepting an analog event without the corresponding master signal.

Once any ADC responds with a Pulse Stretcher Busy (PSB) signal, the master event input is locked off to prevent event pileup. It remains locked until all ADCs showing PSB have been read. When the last ADC has been read, an OR circuit performs the physical clearing of all of the busy ADCs. In singles, each ADC is cleared as it is read. In Multi, an event's ADCs wait until all have been read, and then clear simultaneously. This prevents any member ADC from becoming ready before any other. The OR circuit can also be held in a don't clear state by a CAMAC input, permitting other functions to occur during the lockout period. The interface allows individual selection of either singles or Multi operation for each ADC. Changes are underway to provide for simultaneous singles/Multi operation of any ADC.

The PSBs are presented to an additional CAMAC 3420 called a "format register". The master event gate also sets the "Look At Me" (LAM) signal for this 3420. That LAM starts the MBD-11 code assigned to multiparameter operation.

The MBD-11 code is modified from LBL's MULTI/QDA package. The modifications reflect our hardware configuration, with some speed and location optimizations. The MBD-11 is viewed as a supercomponent, and its software will be described here.

Fig. 12.8-2 is a simplified flow chart of the MBD-11 program. The following description just follows the path down the extreme left of the chart.

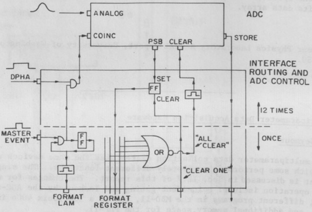

Fig. 12.8-1: ADCDPHA and event gate circuitry

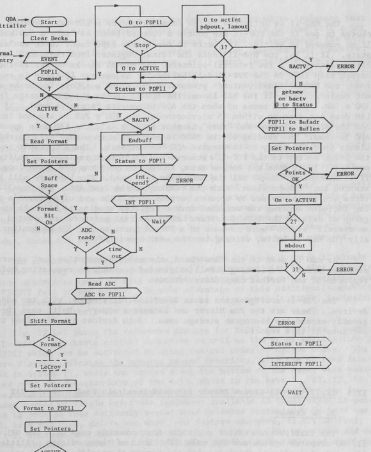

Fig. 12.8-2: Flowchart of the MBD program which collects multiparameter data.

The MBD-11 is activated by the format register's LAM (at "EVENT"). It checks to see if the PDP-11 has posted a command (such as "take a new buffer"). If no command is waiting, it checks to see if the experiment is in an "active" state. If it is, the MBD-11 reads the format register from the CAMAC crate. After setting up a few internal pointers, the MBD-11 checks to see if there is enough room left in the PDP-11 data buffer for an event. If there is enough room, the MBD-11 finally starts processing the event's ADCs. It checks a format register bit. If the bit is on, the MBD-11 checks the CAMAC crate for that ADC's LAM. The LAM comes up when the ADC issues its "store" signal. If the LAM does not come up within 45 microseconds, the ADC's PSB is assumed invalid and the ADC is cleared and "zero" is sent as data. If the LAM does appear, the ADC is read. The reading of the 3420 issues the "acknowledge" signal which clears that ADC entry to the active-ADC "OR" network. The ADC result is sent to the event buffer in the PDP-11's memory. Now the format register is shifted down one bit. If it does not become zero, the MBD-11 performs the above loop again. If it has gone to zero, all the ADCs have been read. The hardware will have started the "common clear" with the reading of the last ADC. Any non-3420 devices are now processed by special purpose code. The end of an event's processing includes sending the original format register reading to head the event's group of data in the PDP-11 buffer. More internal pointers are updated. Then an overall "status" word is sent to a PDP-11 location for QDA to monitor. Finally the MBD-11 halts, waiting for the next event LAM.

As can be seen in the flow chart, the above description just covers the simplest event. Performing PDP-11 originated commands or requesting buffer replacement can further complicate matters.

The PDP-11 configuration is as described for singles, with two added devices. These are the Bus Mirror and Dataspace memory. Multi uses these to greatly expand its histogram storage area. Both devices are described in other sections of this report.

12.9 ZEDIT, a Full-Screen Editor for Z-19 Terminals Used with the VAX

J. G. Cramer

The text/program editor utilities most commonly used with the NPL VAX 11/780 computer system are EDI and TECO. Both of these editing utilities are line-oriented editors which require the typing of specific command codes to move the pointer, add or delete characters, search for character strings, etc. An alternative approach to text/program editing which is growing increasingly popular, particularly with users of dedicated word-processing systems, is the full-screen editor, which "windows" a full screen of text which occurs immediately before and after the present position of the pointer, and which permits insertions, deletions, searches, etc., by means of single keystrokes which operate directly on the text which is imaged on the screen of the terminal.

Recently, the TECO editing utility has been improved to implement text "windowing" in the way described above, when this utility is used with a DEC VT-52 terminal. The latter type of terminal is required because of its many special features (special symbols, reverse scrolling, user-defined function keys, redefinition of keypad operations, etc.) which facilitate the windowing operation. A large TECO macro named VTEDIT[1] has recently become available from the DECUS (the DEC users group) which employs the windowing feature of TECO to provide a very complete full-screen editing utility for VAX and PDP-11 computers, when used with a VT-52 terminal.

Our Laboratory has no VT-52 terminals, but it does have three of the new Zenith/Heathkit Z-19 terminals which provide an almost complete emulation of the VT-52 functions and are considerably less expensive. The principal differences between the VT-52 and the Z-19 are: (a) the Z-19 has five extra user-defined function keys (f1 to f5) which transmit five different escape-code sequences; (b) the Z-19 has an "erase" key which transmits two different escape-code sequences, depending on whether it is operated in the shifted or unshifted mode; (c) when the user-defined keypad mode is activated, the upper nine keys of the numeric keypad will each transmit two different escape codes depending on whether the key is pressed in the shifted or unshifted mode; and (d) the Z-19 does not have separate "arrow" keys on the keypad, as does the VT-52. Instead, these are available as shifted operations of the numeric keypad.

The result of these differences is that the Z-19 can provide 32 single keystroke editing operations (plus delete), as compared with 20 single keystroke editing operations (plus delete) available with a VT-52 terminal operated using the VTEDIT full screen editor. To take advantage of this additional capability, we have extensively modified the VTEDIT macro and renamed it ZEDIT, indicating its adaptation to the Z-19 terminals.

Fig. 12.9-1 shows the reference diagram for ZEDIT and provides a summary of the single keystroke editing functions as well as the other editing functions of ZEDIT which can be activated by using control codes or escape codes. The square diagram indicates the numeric keypad functions, with the shifted functions in braces {}, while the arrows along the bottom of the page, when positioned over the function keys of the Z-19, point to the keys f1, f2, f3, f4, f5, erase, blue, red, and white, respectively. Note in particular that the increased number of single keystroke functions available in ZEDIT makes it possible to provide four extremely useful word-oriented operations: forward one word, back one word, delete one word, and restore one word, (i.e., shift-1, shift-3, shift-5, and shift-6 on the keypad). Moreover, the up-screen and down-screen operations (shift-7 and shift-9) make possible very rapid paging through a file, one screen-load at a time.

The scientific text-processing system[2] used in our Laboratory employs several control characters for special purposes. In particular the control characters A and B are used to form superscripts and subscripts, the control characters D, E, F, and T for placing a vector arrow, tilde, bar, or caret, respectively, over a given character, and the control characters P, G, and L to indicate that the preceeding character is to be interpreted as a special symbol, that the terminal bell is to be sounded, and that a form feed is to be inserted,

Fig. 12.9-1: ZEDIT Reference Diagram

KEYBOARD LAYOUT AND SPECIAL CODES FOR ZEDIT

```
         KEYPAD
                                               CONTROL & ESCAPE CODES
+-------------------------------+            ^R     = Append*
:   "7"    :   "8"    :   "9"    :          ^Uq     = Execute Macro in Q-reg "q"
:  Open    :  Page*   :  Mark/   :          ^V[:]q  = Load & Delete Q-reg "q"+*
:  line*   :          :  quote*  :          ^Wq     = Get Q-reg "q" Contents
:{^Screen}:   {^}*   :{vScreen}:           ^X[:]q  = Load Q-reg "q"+*
+----------+----------+----------+          <esc>F = Repaint Screen/Set Line*
:   "4"    :   "5"    :   "6"    :          <esc>G = Global Search
:   Up     :  Delete  : Delete/  :          <esc>I = Move Word(s) next line
:  Line*   :  char*   : restore  :          <esc>K = Set Left Margin
:  {<}*    :{Dl Wrd}*:  {>}*    :           <esc>O = Set Delimiters
+----------+----------+----------+          <esc>X = Execute Learned Sequence
:   "1"    :   "2"    :   "3"    :          <esc>Y = Yank Page*
:  Top of  :  Bottom  :  Start   :          <esc>Z = Learn Mode
:  page+*  : of page  : of line  :        <esc>/a = Insert ASCII Code for "a"
:{< Word}*:   {V}*   :{> Word}*:
+----------+----------+----------+                      EXITs
:   "0"    :   "."    : "ENTER"  :              f4 = ZEDIT => VMS, Save File
:  Down    :  Search  :  Search  :        <esc>-^Z = ZEDIT => VMS, Kill File
:  line    :  again*  :   args   :      ^C and ^Z = ZEDIT => TECO
:          :          :          : MI<esc><esc> = TECO => ZEDIT
+----------+----------+----------+              f3 = Save & Resume ZEDIT at Top
                                           <esc>1f3 = Save & Resume ZEDIT Here

         DELETE = Delete character before cursor*
         BACKSPACE = Go to End of Line*
```

The keypad commands shown in braces {operation} are "upper-case" commands which require the shift key to be held down when the the keypad key is struck.

The commands which are labelled with an asterisk (*) take an optional numerical argument [n] which is entered as:

ESCAPE [-] <digits> <function key(s)>

The commands which are labelled with a plus sign (+) operate from the present position of the cursor to the Mark (as set by keypad key 9), provided that the mark has been set.

NOTE: Since ZEDIT is a TECO macro, certain errors will cause a default to TECO, which will respond with an asterisk (*). To restore ZEDIT control when this happens, type: MI$$

```
=================== F U N C T I O N   K E Y S ===================

Help   Sho-All   Prot    Exit    Del<=    Kill    Cut    TECO   Paste
 :        :        :       :       :     {Del=>}   :       :      :
 V        V        V       V       V        V      V       V      V
```

respectively. It was therefore necessary to further modify VTEDIT so that these control characters were transmitted verbatim rather than used to signify editing functions, as was the case in the original implementation.

One serious weakness of VTEDIT, as provided by DECUS, was that the file specification procedures were very clumsy and difficult to teach to new users unfamiliar with TECO. To overcome this problem, a DCL command file ZEDIT.COM was written to provide a convenient DCL interface to ZEDIT. This command file has been installed in the system under the name ZED*IT, and provides the capabilities of inline file specification, "oldfile newfile" file specification, automatic creation of a new file with a previously unused name, and remembering the name of the last file edited, so that it does not need to be respecified on the next call of ZEDIT. A listing of ZEDIT.COM is given in Fig. 12.9-2.

The detailed user's manual provided by DECUS as a part of the VTEDIT package[1] has been extensively revised to provide a 35 page user's manual for ZEDIT. This document is resident on the disc of the VAX 11/780 as file [200004.UTIL]ZEDIT.DOC, and may be listed on the VAX line printer by interested users. The ZEDIT editor is an extremely powerful one, because it makes a large fraction of the editing capabilities of TECO available to the user without the burden of learning the extensive set of operation codes which must be memorized in order to use TECO effectively. It is much easier to teach to beginners because the single keystroke functions provide all the edit functions needed by any but the most sophisticated users.

References:

1. "VTEDIT, Keypad Text Editor and Corrector for TECO-11, User's Manual", March 26, 1980 version by MHB, Copyright 1979 & 1980, Digital Equipment Corporation (unpublished).
2. Nuclear Physics Laboratory Annual Report, University of Washington (1980), p. 207.

Fig. 12.9-2: A Listing of ZEDIT.COM

```
$ !                       ZEDIT.COM
$ !   Interfaces ZEDIT.TEC Z-19 Terminal Editor
$ !       to the VAX/VMS Operating System.
$ !
$ ON CONTROL_Y THEN GOTO FINISH
$ SET MESSAGE/NOFACILITY/NOIDENTIFICATION/NOSEVERITY/NOTEXT
$ ISW:=0
$ JSW:=0
$ ZOUT:='P2'
$ ZIN:='P1'
$ IF ZIN.NES."" THEN GOTO NEXT
$ ON ERROR THEN GOTO ASK
$ JSW:=1
$ OPEN/READ GET 'F$USER()'ZEDIT.SAV
$ READ GET ZIN
$ CLOSE GET
$ WRITE SYS$OUTPUT "Resuming editing of file ''ZIN'."
$ GOTO NEXT
$ ASK:
$ INQUIRE ZIN "What File? (NAME.TYP) "
$ NEXT:
$ IF ZOUT.EQS."" THEN ZOUT:='ZIN'
$ OPEN/WRITE SAV 'F$USER()'ZEDIT.SAV
$ WRITE SAV "''ZOUT'"
$ CLOSE SAV
$ PURGE 'F$USER()'ZEDIT.SAV
$ ON ERROR THEN GOTO MARK
$ RENAME 'ZIN' *
$ GOTO MAKE
$ MARK:
$ ISW:=1
$ WRITE SYS$OUTPUT "File named ''ZIN' not found."
$ IF JSW.EQS."1" THEN ISW:=0
$ IF JSW.EQS."1" THEN GOTO ASK
$ WRITE SYS$OUTPUT "Creating new file."
$ MAKE:
$ OPEN/WRITE ZFIL TEMP.TEC
$ IF ISW.EQS."0" THEN WRITE ZFIL "ER''ZIN'$$"
$ WRITE ZFIL "EW''ZOUT'$$"
$ WRITE ZFIL "EI[200004.UTIL]ZEDIT$$"
$ CLOSE ZFIL
$ SET MESSAGE/FACILITY/IDENTIFICATION/SEVERITY/TEXT
$ ASSIGN/USER SYS$COMMAND SYS$INPUT
$ MCR MUN TEMP
$ FINISH:
$ SET MESSAGE/FACILITY/IDENTIFICATION/SEVERITY/TEXT
$ DELETE TEMP.TEC;*
```

13. APPENDIX

13.1 Nuclear Physics Laboratory Personnel

Faculty

Eric G. Adelberger, Professor
John S. Blair, Professor
David Bodansky, Professor; Chairman, Department of Physics
John G. Cramer, Professor
George W. Farwell, Professor
I. Halpern, Professor
Albert J. Lazzarini, Research Assistant Professor
Eric B. Norman, Research Assistant Professor
Fred H. Schmidt, Professor
Kurt A. Snover, Research Associate Professor
Thomas A. Trainor, Research Associate Professor
Robert Vandenbosch, Professor; Director, Nuclear Physics Laboratory
William G. Weitkamp, Research Professor; Technical Director, Nuclear Physics Laboratory

Research Staff

Konrad Aniol, Research Associate[1]
Mohan Doss, Research Associate
David H. Dowell, Research Associate
Munther M. Hindi, Research Associate
Pitsa Ikossi, Research Associate[2]
Eberhard Kuhlmann, Research Associate[3]
Zhaoyou Liu, Visiting Scientist[4]
Volker Metag, Research Associate[5]
Rudolph Risler, Research Associate[6]

Senior Professional Staff

Harold Fauska, Research Electronics Supervisor, Assistant Technical Director, Nuclear Physics Laboratory[7]
Derek Storm, Senior Research Scientist

Predoctoral Research Associates

Norman L. Back
Hyoung C. Bhang[8]
Timothy E. Chupp
Keith J. Davis
Salvador Gil
Kyoung Dong Hahn[9]
David W. Holmgren
C. David Hoyle
Zafar Iqbal
Kevin T. Lesko

Dat-Kwong Lock
Robert Loveman
William G. Lynch[10]
Amlan Ray
Man-Yee B. Tsang[10]
Richard D. Von Lintig

Research Assistants

Gerald Feldman
Mahbubul Khandaker

Professional Staff

John F. Amsbaugh, Research Scientist
Kelly C. Green, Research Scientist
Gervas M. Hinn, Research Scientist
William B. Ingalls, Research Engineer
Donald D. Leach, Research Scientist
Alan G. Seamster, Research Scientist
Richard J. Seymour, Computer Systems Engineer
Rod E. Stowell, Electronics Engineer
H. Erik Swanson, Research Scientist

Technical Staff

Carl E. Linder, Engineering Technician
Georgia J. Rohrbaugh, Accelerator Technician
George E. Saling, Accelerator Technician[7]
Louis L. Geissel, Instrument Maker Leadman, Student Shop
Gustav E. Johnson, Instrument Maker
Hendrik Simons, Instrument Maker Leadman
Peter W. Wiest, Accelerator Operator[6]
Allen L. Willman, Instrument Maker Supervisor

Administrative Staff

Julie L. Anderson, Accounting Assistant
Joan Dinkelspiel, Administrative Secretary[9]
Dianne S. Hulford, Administrative Secretary[9]
Judith C. Nyman-Schaaf, Administrative Secretary

Part Time Staff

Gregory Anderson[11]
Harvey Bennett
Tim Bertram
Dean Corcoran
Alberto Ferreira
Jack Freeman
Eric Geissel[9]
Steve Holmes
Kevin Kiersky[9]
Hwi Yong Kim[9]
Steven Lamoreaux
Barbara Lewellen
Bill Merryfield[9]
Gholam-Reza Mowla[9]
Christine Olason[9]
Mark Olson[9]

John Orth	Richard Stoner
Leslie Pence[9]	Minh Tang[9]
David Peterson[9]	Timothy Van Wechel
Charlotte Pine[9]	Christopher Wagner
Mark Pleas	Mark Warchol[9]
Jerome Rahn[9]	Michael Wittenberg[9]
Winston Saunders[9]	

---

1. Present Address: University of British Columbia, Vancouver, British Columbia, Canada
2. Present Address: Shell Oil Company, New Orleans, Louisiana
3. Present Address: Ruhr-Universität Bochum, Bochum, West Germany
4. Permanent Address: Lanzhou, Gansu, Republic of China
5. Present Address: Max-Planck-Institut fur Kernphysik, Heidelberg, West Germany
6. Present Address: Medical Radiation Physics, University of Washington
7. Retired; currently part-time employee
8. Completed Ph.D. degree. Present Address: University of Colorado, Boulder, Colorado
9. No longer associated with the Nuclear Physics Laboratory
10. Completed Ph.D. degree. Present Address: Michigan State University, East Lansing, Michigan
11. This promising young physicist was killed in a bicycle accident in January, 1981 while on his way to work at the Laboratory.

13.2 Ph.D. Degrees Granted, Academic Year 1980-81

Man-Yee B. Tsang:	Coincidence Study of $^{27}Al(^{16}O,^{12}C\alpha)^{27}Al$ at 65 MeV
William G. Lynch:	Deviations From Rutherford Scattering in Sub-Coulomb Heavy-Ion Elastic Scattering
Hyoung Chan Bhang:	Analyzing Powers in the Inelastic Scattering of Protons to the Continuum

---

13.3 List of Publications

Papers Published:

"A Technique for Measuring Parity Non-Conservation in Hydrogenic Atoms," E.G. Adelberger, T.A. Trainor, E.N. Fortson, T.E. Chupp, D. Holmgren, M.Z. Iqbal, and H.E. Swanson, Nucl. Inst. and Meth. 179, 181 (1981).

"Investigation of the Electric Quadrupole Strength in ^{13}N Using the $^{12}C(p,\gamma)^{13}N$ Reaction," R.W. Helmer, M.D. Hasinoff, J.E. Bussoletti, K.A. Snover, and T.A. Trainor, Nucl. Phys. A336, 219 (1980).

"Energy Dependence in $^{12}C + ^{28}Si$ Elastic Scattering," G.R. Satchler, M.L. Halbert, R.G. Stokstad, R.M. DeVries, D.A. Goldberg, and J.G. Cramer, Nucl. Phys. A346, 179 (1980).

"$^{26}Al^{g}$ Production Cross Sections from the $^{26}Mg(p,n)^{26}Al$ Reaction," E.B. Norman, K.T. Lesko, T.E. Chupp, and P. Schwalbach, Nucl. Phys. A357, 228 (1981).

"$^{12}C + ^{12}C$ Intermediate Structures Correlated Among Elastic and Reaction Channels," E.R. Cosman, R. Ledoux, A. Lazzarini, Phys. Rev. C21, 2111 (1980).

"Dominance of Strong Absorption in $^{9}Be + ^{28}Si$ Elastic Scattering," M.S. Zisman, J.G. Cramer, D.A. Goldberg, J.W. Watson, and R.M. DeVries, Phys. Rev. C21, 2398 (1980).

"The Radial Sensitivity of Elastic Scattering," J.G. Cramer, and R.M. DeVries, Phys. Rev. C22, 91 (1980).

"Charge Distributions for the $^{86}Kr + ^{139}La$ System at 505, 610, and 710 MeV," P. Dyer, M.P. Webb, R.J. Puigh, R. Vandenbosch, T.D. Thomas, and M.S. Zisman, Phys. Rev. C22, 1509 (1980).

"Angular Momentum Dependent Level Density Limitation to Fusion," R. Vandenbosch, and A. Lazzarini, Phys. Rev. C23, 1074 (1981).

"Cross Sections Relevant to Gamma-Ray Astronomy: Proton Induced Reactions," P. Dyer, D. Bodansky, A.G. Seamster, E.B. Norman, and D.R. Maxon, Phys. Rev. C23, 1865 (1981).

"Generalized Absorber Theory and the Einstein-Podolsky-Rosen Paradox," J.G. Cramer, Phys. Rev. D22, 362 (1980).

"Non-Resonant Behavior of the Yield of the $^{28}Si\ 2^{+}$ (Ex = 1.78 MeV) State via the $^{12}C + ^{28}Si$ Reaction," R. Vandenbosch, D.-K. Lock, A. Lazzarini, K. Lesko, and V. Metag, Phys. Rev. Lett. 46, 5 (1981).

"$0^{+} \rightarrow 0^{-}\ \beta^{+}$ Decay of ^{18}Ne and the Determination of F_{π}," E.G. Adelberger, C.D. Hoyle, H.E. Swanson and R.D. Von Lintig, Phys. Rev. Lett. 46, 695 (1981).

"Correlation of Aligned Angular Momentum with Scattering Angle and Energy Loss in Deeply Inelastic Collisions," A. Lazzarini, V. Metag, A.G. Seamster, R. Vandenbosch, and R. Loveman, Phys. Rev. Lett. 46, 988 (1981).

"Enrichment of ^{14}C and Sample Preparations for Beta and Ion Counting," P.M. Grootes, M. Stuiver, G.W. Farwell, T.P. Schaad, and F.H. Schmidt, Radiocarbon 22, 487 (1980).

"Radiometric Dating with the University of Washington Tandem Van de Graaff Accelerator," G.W. Farwell, T.P. Schaad, F.H. Schmidt, M.Y.B. Tsang, P.M. Grootes, and M. Stuiver, Radiocarbon 22, 838 (1980).

"Parity Violation in Hydrogen at Seattle," T.A. Trainor, Proceedings of International Workshop on Neutral Current Interactions in Atoms Cargese, September, 1979, W.L. Williams, ed., p. 231.

"Giant Resonance Effects in Radiative Capture," K.A. Snover, Proceedings of the Giant Multipole Resonance Topical Conference, Oak Ridge, Tennessee, October, 1979, F.E. Bertrand, ed., Harwood Academic Publishers, 1980, p. 229.

"Elastic and Inelastic Scattering of Polarized Protons Through Isobaric Analog Resonances in ^{207}Bi and ^{209}Bi", N.L. Back, H.C. Bhang, J.G. Cramer, T.A. Trainor, and R. Von Lintig, in Polarization Phenomena in Nuclear Physics-1980, G.G. Ohlsen, et al., eds., AIP Conference Proceedings No. 69, 1981, p. 505.

"Depolarization in the Inelastic Scattering of Protons from Copper," W.G. Weitkamp, T.A. Trainor, I. Halpern, H. Bhang, and S.K. Lamoreaux, ibid., p. 511.

"A Proposal for a New Tandem at the University of Washington", W.G. Weitkamp, Proceedings of S.N.E.A.P. 80, University of Wisconsin, 1980, p. 93.

"An Improved Two-loop Voltage Regulation System for an FN Tandem," T.A. Trainor, ibid., p. 195.

"Recent Improvements on Generating Voltmeters," H. Fauska, ibid., p. 203.

"Nucleosynthesis of Odd-Odd Nuclei", E.B. Norman, in Progress in Particle and Nuclear Physics, Vol. 6, D. Wilkinson, ed., Pergamon Press (Oxford), 1981, p. 285.

Papers Submitted or in Press:

"Production of Optically Thin Free-Standing Oil Films from the Edge of a Rotating Disc," J.G. Cramer, D.F. Burch, R. Rodenberg, and P.B. Cramer, submitted to Nucl. Inst. and Meth.

"Neutron Particle-Hole Electric Dipole States in ^{206}Pb, ^{207}Pb, and ^{208}Pb," P.A. Dickey, Nucl. Phys. A, to be published.

"On the Half-Life of ^{180}Ta," E.B. Norman, submitted to Phys. Lett. B.

"The $1/2^+ \rightarrow 1/2^-$ Beta Decay of ^{19}Ne and the Parity Nonconserving NN Force," E.G. Adelberger, M.M. Hindi, C.D. Hoyle, H.E. Swanson, and R.D. Von Lintig, submitted to Phys. Rec. C.

"A Search for a Fusion L-Window in the ^{16}O + ^{16}O System at E_{cm}=34 MeV," A. Lazzarini, H. Doubre, K. Lesko, V. Metag, A. Seamster, R. Vandenbosch, B. Merryfield, Phys. Rev. C, to be published.

"The Structure of ^{18}Ne," A.V. Nero, E.G. Adelberger, and F.S. Dietrich, submitted to Phys. Rev. C.

"Generalized Absorber Theory and the Arrow of Time", J.G. Cramer, submitted to Phys. Rev. D.

"Reduction Evaporation of BeO to Provide a Beryllium Metal Sample For Accelerator Radiometric Dating," G.M. Hinn, Proceedings of the Ninth World Conference of the International Nuclear Target Development Society, Gatlinburg, TN, October, 1980, to be published.

"Production of Carbon Coated Selenium-76 Targets," R. Risler, G. Hinn, S. Hoffman, ibid.

"An Improved Two-Loop Beam Energy Stabilization for an FN Tandem," T.A. Trainor, Proceedings of the Third International Conference on Electrostatic Accelerator Technology, Oak Ridge, TN, April, 1981, to be published.

"Investigation of Periodic Acceleration Tube Discharge With a Capacitive Pickup Array," ibid.

"An NMR Magnet Regulator Circuit Providing Search and Lock Regulation Circuitry for Electrostatic Accelerator Bending Magnets," H. Fauska, ibid.

"Speed Optimizations for Fermilab MULTI," K. Green, Second Topical Conference on Computerized Data Acquisition in Particle and Nuclear Physics, May, 1981, to be published.

"The University of Washington Nuclear Physics Data Collection System," K. Green and R. Seymour, ibid.

"Memory Expansion Hardware for PDP-11 Computers," R. Seymour, ibid.

Invited Papers and Talks:

"^{26}Al: A New Clue to the Early History of the Solar System," E.B. Norman, Bull. Am. Phys. Soc. 26, 17 (1981).

"Parity Violation in Nuclear Systems," E.G. Adelberger, Bull. Am. Phys. Soc. 26, 38 (1981).

"K-Shell Ionization with Sticky Nuclei," J.S. Blair, Bull. Am. Phys. Soc. 26, 601 (1981).

"New Results on the Spectroscopy and Dynamics of Fission," V. Metag, Nucl. Phys. A354, 271c (1981).

"Radiative Capture Studies of the Electromagnetic Decays of Highly Excited States," K.A. Snover, Proceedings of the 1980 RCNP Symposium on Highly Excited States in Nuclear Reactions, May 1980, H. Ikegami, ed., Osaka University, p. 447.

"Weak Interaction of Atoms, Nuclei, and Particles," E.G. Adelberger, Gordon Research Conference on Nuclear Structures, 1980.

"Polarization Techniques and Experimental Tests of Fundamental Symmetries in Nuclear Physics," E.G. Adelberger, Polarization Phenomena in Nuclear Physics 1980, AIP Conference Proceedings, No. 69, p. 1367.

"Polarized Proton Radiative Capture Studies of Giant Resonances," K.A. Snover, ibid., p. 321.

"Search for a Fusion L-Window in $^{16}O + ^{16}O$," A. Lazzarini, American Chemical Society, Div. of Nuclear Chemistry and Technology, Atlanta, GA, March, 1981, to be published.

Contributed Abstracts:

"Experimental Energy and Mass Survey of π^+ Inelastic Scattering to the Continuum," K. Aniol, D. Chiang, I. Halpern, D. Storm, et al., Bull. Am. Phys. Soc. 25, 505 (1980).

"Nucleus-Nucleus Total Reaction Cross Sections and the Geometrical Limit," R. DeVries, N. Digiacomo, J. Peng, W. Sondheim, J. Sunier, C. Gruhn, H. Wiemann, J. Cramer and R. Loveman, Bull. Am. Phys. Soc. 25, 506 (1980).

"Elastic and Inelastic Scattering of Polarized Protons from ^{206}Pb and ^{208}Pb," N.L. Back, J.G. Cramer, T.A. Trainor, R.D. Von Lintig, and H.C. Bhang, Bull. Am. Phys. Soc. 25, 520 (1980).

"Using Inelastic Scattering Data to Determine True Absorption Probabilities for Pions in Nuclear Matter," D. Chiang, I. Halpern, and G.A. Miller, Bull. Am. Phys. Soc. 25, 559 (1980).

"Magnetic Dipole Decays to the Excited 0^+ (6.05 MeV) and 3^- (6.13 MeV) States in ^{16}O," P.G. Ikossi, K.A. Snover, E.G. Adelberger, and K.T. Lesko, Bull. Am. Phys. Soc. 25, 577 (1980).

"Studies of Levels in ^{25}Al and ^{29}P Fed in the β^+ Decays of ^{25}Si and ^{29}S," P.G. Ikossi, C.D. Hoyle, E.G. Adelberger, and K.A. Snover, Bull. Am. Phys. Soc., 25, 578 (1980).

"A Very Efficient Lyman-α Detector for Fast Metastable Hydrogen Beam Studies," T.A. Trainor, K.J. Davis, and E.N. Fortson, Bull. Am. Phys. Soc. 25, 583 (1980).

"E2 Strength in the GQR Region in Radiative Alpha Capture into ^{28}Si and ^{58}Ni," K.A. Snover, E. Kuhlmann, K.J. Davis, G. Feldman, P.G. Ikossi, and M. Hindi, Bull. Am. Phys. Soc. 26, 537 (1981).

"$1/2^+ \rightarrow 1/2^-$ β^+ Decay of ^{19}Ne," E.G. Adelberger, M.M. Hindi, C.D. Hoyle, H.E. Swanson, and R.D. Von Lintig, Bull. Am. Phys. Soc. 26, 537 (1981).

"$0^+ \rightarrow 0^-$ β^+ Decay of ^{18}Ne and the Determination of f_π," R.D. Von Lintig, E.G. Adelberger, C.D. Hoyle, H.E. Swanson, Bull. Am. Phys. Soc. 26, 537 (1981).

"Relativity, Nuclear Polarizability, Atomic Screening and Vacuum Polarization in Sub-Coulomb Heavy Ion Elastic Scattering," W.G. Lynch and J.G. Cramer, Bull. Am. Phys. Soc. 26, 553 (1981).

"Deviations from Rutherford Scattering with Sub-Coulomb Heavy Ions," M.B. Tsang, W.G. Lynch, H. Bhang, J.G. Cramer, R.J. Puigh, and T. Bertram, Bull. Am. Phys. Soc., 26, 554 (1981).

"Parity Violation in Hydrogen: Systematics Studies with a New Two-Cavity, Coaxial Measurement Scheme," T.A. Trainor, E.G. Adelberger, T.E. Chupp, D.W. Holmgren, M.Z. Iqbal, and H.E. Swanson, Bull. Am. Phys. Soc. 26, 589 (1981).

"A Method of Normalization to a Standard Source for Van de Graaff-based Radiochronology Measurements," F.H. Schmidt, G.W. Farwell, land P.M. Grootes, Bull. Am. Phys. Soc. 26, 593 (1981).

"University of Washington Nuclear Physics Laboratory Momentum Filter," D.W. Storm, K.J. Davis, and T.A. Trainor, Bull. Am. Phys. Soc. 26, 594 (1981).

"Beam Position Stabilizer-chopper for a Fast Metastable Hydrogen Atomic Beam," T.A. Trainor, and D.W. Holmgren, Bull. Am. Phys. Soc. 26, 603 (1981).

"Analyzing Power of Protons Inelastically Scattered to the Continuum," H. Bhang, I. Halpern and T.A. Trainor, Bull. Am. Phys. Soc., 26, 635 (1981).

"K-shell Ionization in Heavy-Ion Collisions," J.S. Blair, Proceedings of the International Conference on Nuclear Physics, Berkeley, (1980), p. 392.

"Angular Momentum Dependent Level Density Limitations to Fusion," R. Vandenbosch and A.J. Lazzarini, ibid., p. 568.

"Nuclear 'Time-Delay' and X-Ray-Proton Coincidences Near a Nuclear Scattering Resonance," P. Dyer, K.A. Snover, T.A. Trainor, and J.S. Blair, ibid., p. 838.

"$^{26}Al^{g,m}$ Production Cross Sections from the $^{26}Mg(p,n)^{26}Al$ and $^{23}Na(\alpha,n)^{26}Al$ Reactions," E.B. Norman, K.T. Lesko, P. Schwalbach, and T.E. Chupp, ibid., p. 881.

Other Publications by the Members of the Laboratory and Other Laboratory Research:

"Mechanism of Pion Absorption in Complex Nuclei," K.G.R. Doss and W.R. Wharton, Phys. Rev. C22, 1219 (1980).

"β^+ Decay of ^{67}As," M.J. Murphy, C.N. Davids, and E.B. Norman, Phys. Rev. C22, 2204 (1980).

"Inelastic π^+ Scattering from ^{12}C and Si at Low Energies", J.F. Amann, P.D. Barnes, K.G.R. Doss, S.A. Dytman, R.A. Eisenstein, J.D. Sherman, and W.R. Wharton, Phys. Rev. C23, 1635 (1981).

$^{12}C + ^{12}C$ Intermediate Structures Correlated Among Elastic and Reaction Channels", E.R. Cosman, R. Ledoux, A. Lazzarini, Phys. Rev. C21, 2111 (1980).

"Direct Observation of a High Spin $^{12}C + ^{8}Be$ Cluster State in $^{20}Ne^+$," M.M. Hindi, J.H. Thomas, D.C. Radford, and P.D. Parker, Phys. Lett. 99B, 33 (1981).

"The (π^+,p) and (π^+,d) Reactions on Light Nuclei," K.G.R. Doss, et al., submitted to Phys. Rev. C.

"A Study of the Reaction $^{28}Si(p,\gamma)^{29}P$," S.T. Lim, M.D. Hasinoff, D.F. Measday, T.J. Mulligan, and K. Ebisawa, submitted to Nucl. Phys.

Employees by above numbers:

1) Ray; 2) Pleas; 3) Swanson; 4) Corcoran; 5) Adelberger; 6) Lamoreaux; 7) Chupp; 8) Iqbal;
9) Vandenbosch; 10) Weitkamp; 11) Hoyle; 12) Leach; 13) Amsbaugh; 14) Holmgren; 15) Dowell;
16) Wagner; 17) Wiest; 18) Von Lintig; 19) Ingalls; 20) Cramer; 21) Callahan; 22) Van Wechel;
23) Nyman-Schaaf; 24) Doss; 25) Anderson; 26) Lesko; 27) Schmidt; 28) Ferreira; 29) Kuan;
30) Linder; 31) Murano; 32) Rohrbaugh; 33) Back; 34) Norman; 35) Stowell; 36) Storm;
37) Kellogg; 38) Gil; 39) Davis; 40) Khandaker; 41) Liu; 42) Lock; 43) Lazzarini; 44) Snover